Formulation of a thermosetting biocomposite based on poly (furfuryl alcohol) and cellulose for 3D printing

Khaoula Bouzidi

THÈSE

Pour obtenir le grade de

DOCTEUR DE L'UNIVERSITE GRENOBLE ALPES

Spécialité : **Matériaux, Mécanique, Génie Civile, Electrochimie**

Arrêté ministériel : 25 mai 2016

Présentée par

Khaoula BOUZIDI

Thèse dirigée par **Davide BENEVENTI, DR**, CNRS
Codirigée par **Didier CHAUSSY, Pr,** Grenoble INP et co-encadrée par **Roberta BONGIOVANNI**, **Pr**, Politecnico di Torino

Préparée au sein du **Laboratoire Génie des Procédés Papetiers (LGP2)**

dans **l'École Doctorale Ingénierie – Matériaux, Mécanique, Environnement, Energétique, Procédés, Production**

Formulation d'un biocomposite thermodurcissable à base de l'alcool polyfurfurylique et de cellulose pour le procédé d'impression 3D.

Formulation of a thermosetting biocomposite based on poly(furfuryl alcohol) and cellulose for 3D printing.

Thèse soutenue publiquement le **9 Février 2022**,
devant le jury composé de :

Monsieur Davide BENEVENTI
DIRECTEUR DE RECHERCHE, CNRS, Directeur de thèse
Madame Christine CHIRAT
PROFESSEUR, Grenoble INP, Examinatrice et Présidente
Monsieur Antoine LE DUIGOU
MAITRE DE CONFERENCES, Institut de Recherche Dupuy de Lôme, Rapporteur
Madame Alice MIJA
PROFESSEUR, Université de Nice Institut de chimie, Rapporteure
Monsieur Naceur BELGACEM
PROFESSEUR, Grenoble INP, Membre Invité
Monsieur Didier CHAUSSY
PROFESSEUR, Grenoble INP, Co-directeur de thèse, Membre Invité
Madame Roberta BONGIOVANNI
PROFESSEUR, Politecnico di Torino, Membre Invité
Monsieur Alessandro GANDINI
ANCIEN PROFESSEUR DES UNIVERSITES, Membre Invité

" Il ne suffit pas d'atteindre le succès.. l'important est de continuer à réussir"

Hannibal

Remerciements-Aknowledegments

Il y a exactement 1 an j'ai commencé à écrire les premières lignes de mon premier chapitre (sur le même bureau) avec 50 onglets ouverts dans mon moteur de recherche et une infinité de fichiers PDF. Ce manuscrit m'a semblé si difficile à écrire de jour comme de nuit parfois, encore éveillée à 5 heure du matin plongé dans cet écrit. Il y a eu des hauts, des bas, des moments de motivation et d'inspiration ainsi que des moments de doute. Aujourd'hui, Je couronne enfin ces 325 pages et les 3 ans et 3 mois de thèse avec ces lignes de remerciements. Comme quoi les débuts sont difficiles mais avec la volonté et la persévérance tout est possible.

Mes premiers remerciements s'adressent aux membres du jury qui m'ont fait l'honneur d'évaluer mon travail : Pr. Alice Mija, Dr. Antoine Le duigou, Pr. Naceur Belgacem et Pr. Christine Chirat. Je vous remercie pour votre disponibilité et pour votre implication. Ce fut un plaisir de discuter avec vous et d'avoir votre expertise sur mon travail de thèse.

Je remercie profondément mes deux directeurs de thèse Dr. Davide Beneventi et Pr. Didier Chaussy de m'avoir fait confiance pour mener à bien ce projet. Davide merci pour tous tes conseils et tes encouragements. Merci de m'avoir impliqué dans tous les aspects du projet sans pour autant me laisser me soucier des problèmes administratifs que tu as toujours pu résoudre tout seul. Merci aussi pour ta confiance dans mes idées et de m'avoir laissé gérer le projet et prendre des décisions ce fut un plaisir de travailler à tes côtés. Didier je te remercie d'avoir été là quand j'avais besoin de toi, de ton expérience et de ton sens de l'organisation. Tu as assuré un très bon équilibre dans cette équipe de projet puisque tu as toujours su donner des conseils précis et de bien m'encadrer surtout pendant ma dernière ligne droite de thèse. Malgré tes occupations et tes responsabilités pendant la direction du labo tu étais toujours présent quand il le fallait. Roberta je te remercie aussi pour tes réponses et tes encouragements même depuis un autre pays.

Je voudrais remercier plus particulièrement Pr. Alessandro Gandini pour tout ce qui a apporté pour ce projet. Une chose est sûre, cette thèse n'aurait jamais été pareille sans vos conseils et votre assistance. La chimie n'a jamais été mon point fort et encore moins la chimie des furanes mais votre patience et passion pour la science (même avec un membre cassé !) ont été

suffisants pour que je comprenne tous ces spectres RMN et les réactions de réticulation. Je vous serai à jamais reconnaissante pour l'aide et l'encouragement que vous m'avez apporté.

Un grand merci à la région Auvergne Rhône Alpes et l'UGA qui ont financé ce projet et qui ont permis de le prolonger dans le contexte sanitaire particulier. Grâce à eux, j'ai pu finir ma thèse sereinement. Je voudrais également remercier nos différents collaborateurs industriels et académiques. Merci à Qualup pour leurs aide et intérêt pour le développement de l'imprimante et surtout leur patience malgré les difficultés administratives rencontrées. Merci à Emmanuel Flahaut pour nous avoir fourni les nanotubes de carbone et son expertise. Merci au Cermav pour les belles images au MEB et à tous les autres laboratoires qui m'ont aidé à réaliser des tests dans leurs locaux avec un accueil toujours chaleureux. Je cite donc Isterre, Nanobio, LEPMI et CMTC.

Je ne peux pas oublier le personnel scientifique, technique, administratif et informatique de notre cher laboratoire qui m'ont toujours soutenu et aidé. Je voudrais remercier en particulier Chu qui j'ai sollicité pendant toute ma thèse et je l'ai embêté avec mes moules et mes pièces bizarres mais surtout pour m'avoir laissé finir mes expériences après 19h. Je remercie ensuite Cécile, Maxime Mikael et Nadège pour leurs disponibilités. Je pense en particulier à Cécile Sillard qui a toujours étais là pour me former et trouver de l'azote liquide. Merci à Maxime Terrien pour les longues heures passées sur la nouvelle DMA et ta patience. Enfin merci à Denis Curtil pour sa disponibilité malgré ses engagements pour nous avoir aidé avec toutes nos idées parfois un peu exotiques. Je tiens aussi à remercier Giulia Lannello pour son implication et motivation pendant son stage malgré tous les obstacles. Ce fut un plaisir de travailler avec vous tous.

Qui dit LGP2 et vie de laboratoires, dit un beau groupe des doctorants et post doctorants soudés (bon aller je rajoute aussi les ingénieurs qui monopolisent LGP2 dernièrement). Merci à vous tous pour tous les moments partagés. Je n'oublierai jamais nos pause-café à 16h et nos discussions parfois futiles et parfois profondes et scientifiques. Je n'oublierai pas votre soutien pour la préparation de la soutenance et vos remarques toujours constructives et bienveillantes. Nos soirées BIM et nos afterwork dans le PPM seront à jamais gravés dans ma mémoire. Je remercie en particulier mes collègues de bureau Fanny, Amélie, et Myriam j'ai eu de la chance

de pouvoir partager mes journées avec vous dans le C104 (la vue de notre bureau sur Belledonne aide aussi hein !). Un grand merci à Malek pour son soutien pendant toutes mes années de thèse mais surtout pendant la soutenance, merci aussi pour les heures de rälement dans ton bureau.

Une thèse de doctorat n'est pas uniquement le fruit d'un travail scientifique et ne se fait pas seulement entre les murs d'un laboratoire et sur un campus. Une thèse c'est aussi le résultat des expériences cumulées et grâce au soutien apporté au quotidien et pendant des longues années d'études. Ainsi je voudrais remercier mes amis extérieurs au labo pour leur soutien. Je remercie en particulier Nahla ma « compagnon de route » tu as toujours été à mes côtés pour me soutenir et m'encourager.

Enfin, le plus grand des mercis à ma grande famille. Je suis incapable de vous remercier assez pour tout ce que vous avez fait (et vous continuez à faire) pour moi. Un paragraphe, une page voire un autre mémoire de 300 pages ne serait suffisant pour exprimer ma profonde gratitude. Cette thèse et tous mes succès passés et futurs sont dédiés à ma chère maman Halima Bouzidi qui malgré tous les défis de la vie a su me donner tout ce dont j'ai besoin…une affection profonde et un amour pur. Tu es une femme forte, douce et intelligente et tes sacrifices ne seront jamais en vain. Je remercie chacun de mes oncles, mes tantes et mes cousins qui sont certes (très) nombreux mais qui ont tous d'une façon ou d'une autre une influence positive sur ma vie personnelle et mon cursus académique. Je voudrais tout de même exprimer mes profonds remerciements à mes deux sœurs Intiss(ar) et Tess(nime).

Table of content

Glossary

ABS	Acrylonitrile butadiene styrene
AM	Additive Manufacturing
ASTM	American Society for Testing and Materials
BC	Bacterial cellulose
CNC	Cellulose Nanocrystal
CNT	Carbon nanotubes
DIW	Direct Ink writing
DMA	Dynamic mechanical analysis
DP	Degree of Polymerization
DSC	Differential Scanning Calorimetry
DWCNT	Double-walled carbon nanotube
EC	Electrical conductivity
FA	Furfuryl alcohol
FDM	Fused deposition modeling
FFF	Fused filament fabrication
FRP	fiber-reinforced plastics
FTIR	Fourier transform infrared spectroscopy
LDM	Liquid deposition modeling
LOM	Laminated Object Manufacturing
MFC	Micro Fibrillated Cellulose
MWCNT	Multi-walled carbon nanotube
NFC	Nano Fibrillated Cellulose
NMR	Nuclear magnetic resonance spectroscopy
PE	Polyethylene
PEEK	Polyether ether ketone
PFA	Poly(furfuryl alcohol)
PLA	Polylactic acid
PP	Polypropylene
SEM	Scanning electron microscope
SLA	Stereolithography
SLM	Selective laser melting
SLS	Selective laser sintering

SWCNT	Single-walled carbon nanotube
Tg	Glass transition
TGA	Thermogravimetric analysis

General introduction

Additive manufacturing, also referred to as 3D printing or additive fabrication, is a revolutionary manufacturing technology receiving a significant interest in recent years. It is indeed revolutionary and also evolutionary, provoking manufacturers to reconceptualize the approach used to develop, produce and design objects. Due to its adaptability and controllable parameters, a myriad of applications is possible. What is more, in a time where environmental concerns are increasing, this process has low consumables, offers customizable object geometry using the same machines, and is also cost-effective (Yang et al., 2020).

More recently, the increasing use of 3D printing has been promoted by a series of research and development works conducted over the last several decades. As one can see in Figure A-0-1, the number of publications dealing with additive manufacturing has been increasing since 2000 to reach over 45,000 publications by 2020. A closer look at these publications suggests that the majority of the references displayed by the scientific database, *scifinder,* were patents. This trend highlights the innovation capacity of additive manufacturing and also the growing interest this new fabrication process generated among scientists. For instance, composite printing is one of the less explored tracks. However, it can enable the development of high performance materials outstanding conventional single-phase materials. On the same graph in Figure A-0-1, the evolution of publication numbers dealing with 3D printing of composite is following the same tendency as that of additive manufacturing with almost 30% of the total publication mentioning composite. However, biocomposite additive manufacturing is not yet fully explored representing less than 0.5% of published papers.

Therefore, a handful of researchers are focusing their attention on the development and study of new biocomposites to fill this gap (Kariz et al., 2016; Kucherov et al., 2017; Li et al., 2017; Montalvo Navarrete et al., 2018). Combining bio-based thermoplastics with natural fillers and natural fibers has been studied, highlighting that natural fillers can effectively increase the mechanical performances of most thermoplastics used in fused filament fabrication (Nguyen et al., 2018; Tao et al., 2017). Moreover, polymers derived from the vegetal biomass are interesting candidates for the development of novel printing ‘inks’ by direct ink writing as it is one of the more abundant resources in nature (Liu et al., 2019). For instance, the use of cellulose was studied by several researchers and it has been shown to be highly interesting in tissue engineering and many other bio-medical applications. However, several challenges emerged such as poor/no shape fidelity and a high process cost (Wang et al., 2018).

On another note, alongside the evolution of direct ink writing as a reliable additive manufacturing technique, the use of thermosetting polymers as matrix offering better thermal stability and high mechanical performances has been recently considered as a viable option (Peerzada et al., 2020).

Despite the high performance of these composite materials, the most commonly used materials are fossil based. Therefore, the use of bio-based thermosetting resin and natural fillers remains rather unexplored.

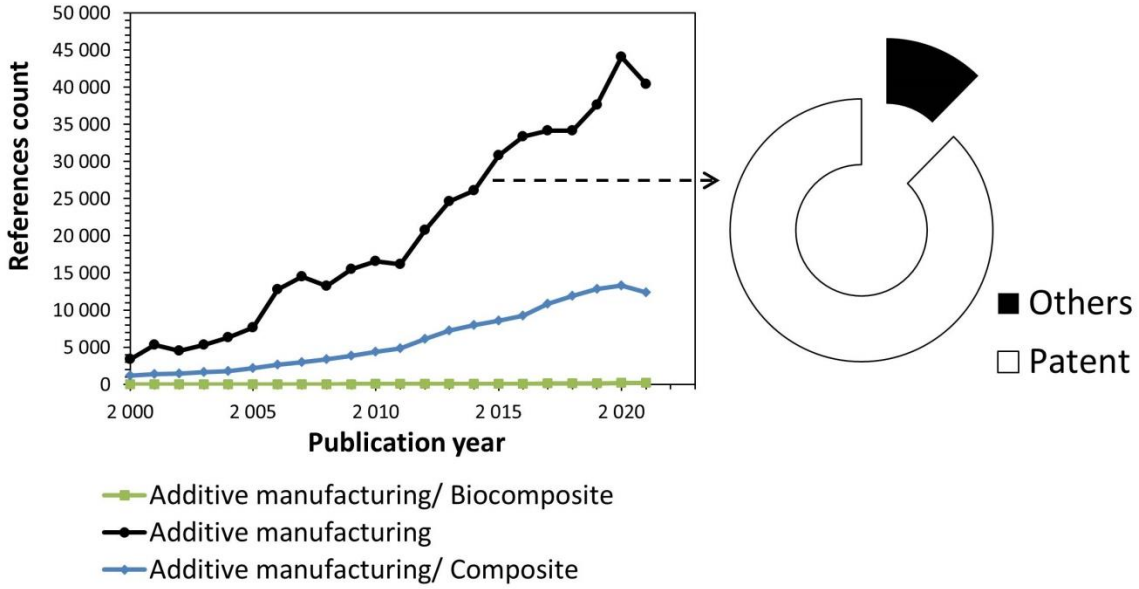

Figure A-0-1: The evolution of publications number concerning additive manufacturing, composite in additive manufacturing and biocomposite in additive manufacturing over the 2 last decades found in the database of scifinder. Source: Scifinder, 2021

In due course, the work conducted in this PhD project proposed the development of a biocomposite with the use of a bio-based thermosetting resin alongside cellulose. This would enable the development of a fully biomass-based composite with high thermal stability conferred by the matrix and adequate shape fidelity. The experimental approach and main findings obtained during this PhD project are presented in 5 chapters.

The thesis begins with a literature review in Chapter 1, which evaluates the current state of the art of additive manufacturing by material extrusion and more specifically composite material manufacturing and their ensuing performances. This chapter ends with an explication of the production and polymerization of the thermosetting resin used in this work, i.e. poly(furfuryl alcohol), and its use in composites production.

The used materials and methods are detailed in Chapter 2, where a detailed description of the commercial products is provided along with the employed characterization techniques and conditions.

To gain a better insight on the composition of used polymers, they were analyzed and the ensuing results are displayed in Chapter 3.

Chapter 4 is dedicated to the development, characterization and optimization of composite slurries for direct ink writing. The first part of this chapter exposes the results of the development of a structural ink and the characteristics of the ensuing cured composite. The second part deals with the development of a functional ink yielding electrically conductive prints.

Chapter 5 is dedicated to the study of the process. In the first part of this chapter, a general study to understand the curing and solidification step of the used polymer was conducted. In the second part, the effect of different printing parameters on the mechanical performances and printability are investigated.

For a clear and quick overview of the thesis content, the general layout and structure are displayed in Figure A-0-2, where the different questions answered by the respective chapters are highlighted.

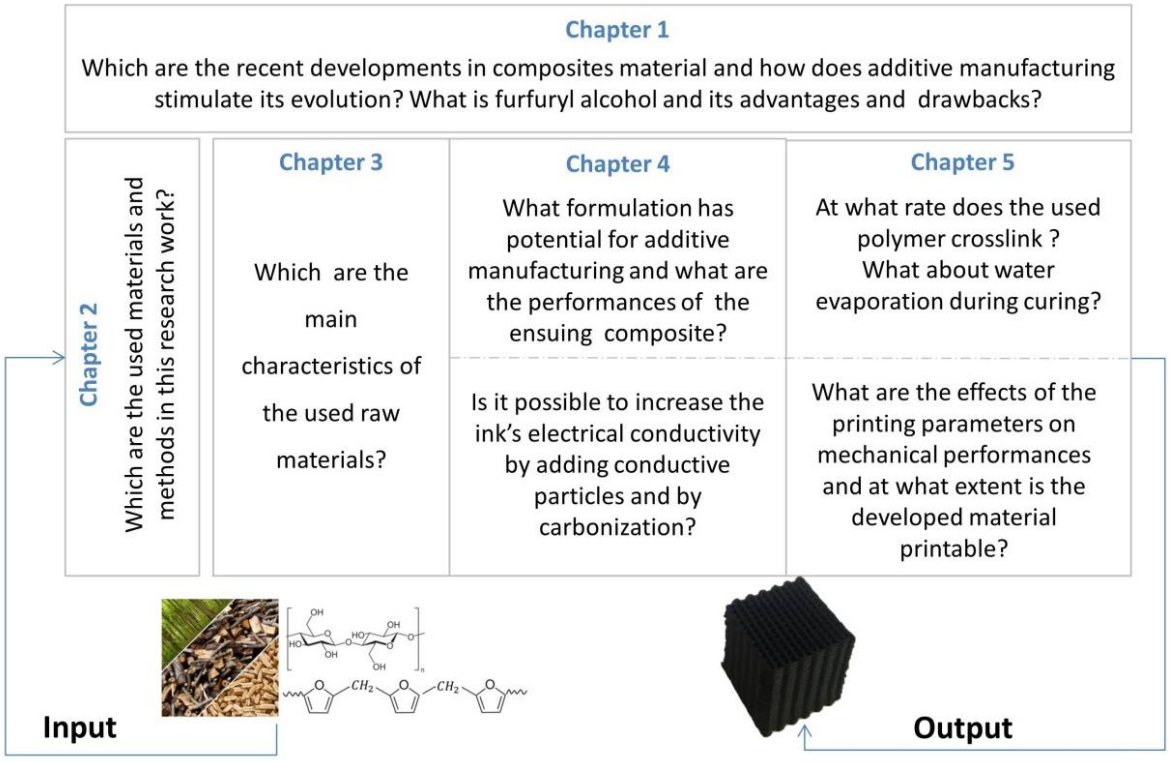

Figure A-0-2: Schematic representation of the manuscript organization.

References

Kariz, M., Sernek, M., Kuzman, M.K., 2016. Use of wood powder and adhesive as a mixture for 3D printing. European Journal of Wood and Wood Products 74, 123–126. https://doi.org/10.1007/s00107-015-0987-9

Kucherov, F.A., Gordeev, E.G., Kashin, A.S., Ananikov, V.P., 2017. Three-Dimensional Printing with Biomass-Derived PEF for Carbon-Neutral Manufacturing. Angewandte Chemie International Edition 56, 15931–15935. https://doi.org/10.1002/anie.201708528

Li, V.C.-F., Dunn, C.K., Zhang, Z., Deng, Y., Qi, H.J., 2017. Direct Ink Write (DIW) 3D Printed Cellulose Nanocrystal Aerogel Structures. Scientific Reports 7, 8018. https://doi.org/10.1038/s41598-017-07771-y

Liu, J., Sun, L., Xu, W., Wang, Q., Yu, S., Sun, J., 2019. Current advances and future perspectives of 3D printing natural-derived biopolymers. Carbohydrate Polymers 207, 297–316. https://doi.org/10.1016/j.carbpol.2018.11.077

Montalvo Navarrete, J.I., Hidalgo-Salazar, M.A., Escobar Nunez, E., Rojas Arciniegas, A.J., 2018. Thermal and mechanical behavior of biocomposites using additive manufacturing. Int J Interact Des Manuf 12, 449–458. https://doi.org/10.1007/s12008-017-0411-2

Nguyen, N.A., Barnes, S.H., Bowland, C.C., Meek, K.M., Littrell, K.C., Keum, J.K., Naskar, A.K., 2018. A path for lignin valorization via additive manufacturing of high-performance sustainable composites with enhanced 3D printability. Science Advances 4, eaat4967. https://doi.org/10.1126/sciadv.aat4967

Peerzada, M., Abbasi, S., Lau, K.T., Hameed, N., 2020. Additive Manufacturing of Epoxy Resins: Materials, Methods, and Latest Trends. Industrial & Engineering Chemistry Research 59, 6375–6390. https://doi.org/10.1021/acs.iecr.9b06870

Tao, Y., Wang, H., Li, Z., Li, P., Shi, S.Q., 2017. Development and Application of Wood Flour-Filled Polylactic Acid Composite Filament for 3D Printing. Materials 10, 339. https://doi.org/10.3390/ma10040339

Wang, Q., Sun, J., Yao, Q., Ji, C., Liu, J., Zhu, Q., 2018. 3D printing with cellulose materials. Cellulose 25, 4275–4301. https://doi.org/10.1007/s10570-018-1888-y

Yang, J., An, X., Liu, L., Tang, S., Cao, H., Xu, Q., Liu, H., 2020. Cellulose, hemicellulose, lignin, and their derivatives as multi-components of bio-based feedstocks for 3D printing. Carbohydrate Polymers 250, 116881. https://doi.org/10.1016/j.carbpol.2020.116881

1 State of the art

Chapter content

1.1 Composite materials

1.1.1 Generalities

Composite materials are defined as a combination of several macro or micro components that differ in size, morphology, composition and that are not soluble one in another (Smith, 1986). A more recent definition considers composite materials as the result of a consolidated mixture of two or more macro, micro, or nano components after optimal processing. The components can have different morphology, size, and chemical composition. One constituent plays the role of the matrix while the other constituents provide reinforcement or special functionalities “ex-situ” or “in-situ” (Pech-Canul and Valdez-Rodriguez, 2015). The author here eliminates the “insolubility” restriction as one can identify many composite materials with components that are soluble in the matrix or the creation of new components in-situ.

Composites are not new materials; they have been created by humans for 5,000 to 6,000 years. In ancient Egypt, in some parts of Asia and Africa, and America, composite materials based on wattle and daub were used in building monuments and structures. Composites in more advanced form were used by Mongols around 1200 AD especially in the fabrication of more performant reinforced bows which helped the empire to spread across Asia (Todd, 2019).

Composite as we know today were first used in the 20th century with the invention of plastics and in particular with the discovery of glass fibers in 1935. By 1945, over 3 million kg of glass fiber were used in composites, essentially for military uses because of wartime. The advantages of composites especially fiber-reinforced plastics (FRP), such as their lightweight and corrosion resistance, allowed them to spread and gain the interest of other markets like transportation, automobile, and construction (Ngo, 2020).

In general, a composite material is constituted of two components:

- The first is the discontinuous phase usually fibrous or in form of particles and provides mechanical strength (or other functions depending on the use). This component is called fillers.

- The second is the continuous phase which is in the case of FRP a polymer that plays the role of binder and provides also efforts distribution and protects fillers from the external environment. This component is called the matrix.

In addition to these two main regions, we can add the interphase region or also known as the interface which also plays an important role in the composite final properties (Cantwell and Morton, 1991; Kalpakjian and Schmid, 2002).

Any material can be used as a matrix but the most used matrices are ceramics, metals, and polymers. In reality, the vast majority of matrices are polymer-based by either using thermoplastics or thermosetting which present very different properties (Haddout, n.d.; Ngo, 2020). The classification into thermoplastics and thermosets defines the processability of material in respect to temperature changes (Swallowe, 1999).

Thermoplastics can be melted and flow when heating because of either exceeding the glass transition temperature (T_g) or because of crystal melting. This makes the thermoplastics easily shaped and processed as they maintain the desired shape by dropping the temperature below their melting point to obtain a glass-like solid. This process can be repeated many times but as these materials melt and solidify repeatedly they can lose some of their properties hence the limitation of recyclability of these thermoplastics (Jones, 1998; Swallowe, 1999).

Thermosets on the other hand, are materials that can be transformed from a liquid to a solid state after undergoing chemical changes and reactions called curing or crosslinking reactions. The uncured liquid state is due to the small unlinked molecules forming the uncured resin, these molecules are called monomers. The curing reaction can be triggered by a thermic treatment (heat, radiation) or by physio-chemical treatment by introducing a catalyst or a hardener. During this reaction, monomers would polymerize forming longer molecules called macromolecules or chains which crosslink to form a three-dimensional network causing the material solidification. Unlike thermoplastics, this solidification or crosslinking step is irreversible and the solid-state is permanent causing a permanent deterioration of the material under high temperature (Jones, 1998; Ngo, 2020; Swallowe, 1999).

Broadly, thermoplastics are considered as linear or branched polymers, and thermosets as rigid crosslinked molecules. Interestingly, these two polymer-based materials can have extremely varied and different mechanical and physico-chemical properties which are summarized in Table 1-1. The manufacturing of composite and the matrix choice is based on these properties related to the final use of the composite. Both thermoplastics and thermosets have their places in the market, dominated by thermosets with a 60% of the composites market (Haddout, n.d.; Swallowe, 1999).

Table 1-1: comparison between Thermoplastics and thermosets (Haddout, n.d.; Ngo, 2020).

	Thermosets	Thermoplastics
Wettability	Easy	Difficult
Resistance to high temperature	More resistant to high temperature	Limited resistance to high temperature
Recyclability	Not possible	Possible
Cost	Cost-effective	More expensive
Stocking	Needs refrigeration and has a limited shelf life	Unlimited shelf life
Shock resistance	Limited	Good

Currently, thermosets count for roughly 75% of plastics mass used in matrices versus 25% for thermoplastics (Biron, 2018). The former polymers are classified into polyester resins, epoxy resins, vinyl ester resins, phenolic, polyurethane, and other high-performance resins like cyanate esters. When it comes to the latter polymers we can classify them by their use:

- Commodities use: Polyethylene (PE), Polypropylene (PP), polyvinyl chloride (PVC), and polystyrene (PS).
- Technical thermoplastics: Polyamide (PA), polyacrylics (PMMA), polyacetal (POM), polycarbonate, polyphenylene oxide (PPO), or polyphenylene ether (PPE) and thermoplastic polyesters (PET).
- Specialties thermoplastics: polysulfone (PSU), polyphenylene sulfide (PPS), fluoroplastics, polyetheretherketone (PEEK), polyetherimide (PEI), and polyamide-imide.

Nowadays, we can find many plastic materials on the market The properties and cost of some of the most commonly used plastics are summarized in Table 1-2.

As for fillers, we can find the use of different fibers and particles, and perhaps the most used and the most efficient are glass fibers, carbon fibers, and aramids fibers. Recently, besides these synthetic fibers, one start also noticing the use of natural fibers which are less efficient but their environmental impact makes them attractive especially in recent years.

Composite materials offer many advantages over conventional materials such as steel or aluminum. Perhaps the most obvious one is the high strength to weight ratio easily noticeable in Table 1-2 of different possible matrices with a specific strength ranging from 40 to 100 MPa·cm^3/g against around

60 MPa·cm^3/g for the steel. The mechanical performances of these plastics can be considerably increased by coupling them with fibers such as glass fiber and carbon fibers making the strength reach until 500 MPa (Çeçen et al., 2008). This is definetly an asset for the aerospace and transport industry. Composites have also good fatigue properties and corrosion resistance and high anisotropy. Coupled with these assets, an easier and more cost-effective manufacturing process makes FRP more attractive. Composites, like conventional materials, have limits that depend on the used matrix, filler, and the compatibility between them. More general known drawbacks of FRP, comparing to more conventional materials, are limited fire resistance, recycling issues, limited resistance under heat, and their response to localized impact loading (Cantwell and Morton, 1991; S et al., 2017).

Table 1-2: Properties of some plastic matrices (Biron, 2018; Haddout, n.d.; Ngo, 2020).

Polymer	Name	Density (kg/m^3)	Young's modulus (MPa)	Strength (MPa)	Specific strength (MPa·cm^3/g)	Price (€/kg)
Thermosets	Epoxide	1220	5200	121	99	16.0
	Polyester	1300	3800	88	68	2.3
	Vinyl ester	1200	3500	81	68	2.8
	Polyimide	1217	3450	80	66	75
	Phenolic	1350	3000	70	52	2.0
Thermoplastics	Polyamide	1130	1900	70	62	3.8
	Polyester	1310	2800	55	42	
	Polyetheretherketone	1300-1500	3600	92-95	73	75.0
	Polycarbonate	1100	2300	60	55	6.0
	Acrylonitrile butadiene styrene (ABS)	1100	2100	47	43	2.2
	Polylactic acid (PLA)	1200	1100-3600	59-72	60	15.0

Furthermore, these multi-component materials make the reuse or recycling very challenging due to the difficulty in separating different components even when using thermoplastic (La Mantia and Morreale, 2011; Netravali and Chabba, 2003). Unfortunately, this makes these materials environmentally unfriendly. Moreover, plastic, the base materials of most composites, is a fossil-based material that is non-renewable (La Mantia and Morreale, 2011; Marsh, 2008).

1.1.2 Biocomposites in virtue of a growing interest in sustainability

As discussed previously, the majority of plastic matrices and fibers used in FRP are not renewable and has a high environmental impact. This issue was starting to be more conspicuous in the last 20 years. Thusly, scientific researcher started to get more interested in finding bio-based substitutes to petroleum-based polymers traditionally used in composite manufacturing. These fully or partially bio-based composites referred to as biocomposites or 'green composites' have a lower impact on the environment and are renewable. 'Greener' substitutes can have limited mechanical properties comparing to traditional FRP, especially when compared to glass and carbon fibers. However, these materials can be great candidates for manufacturing secondary and tertiary structures (packaging, panels, casing, etc.) (La Mantia and Morreale, 2011; Netravali and Chabba, 2003).

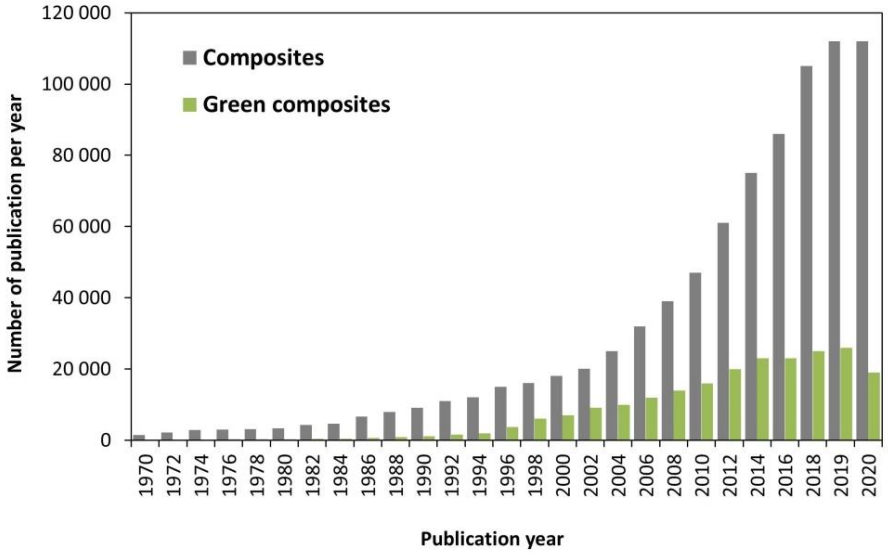

Figure 1-1: The evolution of publications number concerning composites and green composites over the 5 last decades. Source: Scifinder, 2021

As we can see in Figure 1-1, the scientific interest in composites has never declined over the years and especially during these last 5 years. On the other hand, researchers only started giving green composite a chance in the late nineties, and ever since the publications number on environmentally-friendly composites kept increasing. However, the ratio between the research concerning composites in general and those concerning green composites is decreasing in this last decade despite the raising environmental consciousness among consumers, manufacturers, and governments. To increase the potential of the use of natural fibers and matrices, researchers need to develop enhanced green composites with better mechanical properties and with a wider range of applications (Misra et al., 2011). Nonetheless, as ambitious as this may be, it is a difficult task, especially when using natural fibers with complex structures.

1.1.2.1 Natural fibers for 'greener' composites

Carbon dioxide neutrality of natural fibers that grow in crop fields and their renewable nature provide good potentials to use them as reinforcement in FRP (Ilcewicz et al., 1988). Natural fibers, as their name suggests, can be found in nature but from different sources, it may be plants, animals, or minerals. According to literature reviews, plant fibers are the most popular among the natural fibers in fiber-reinforced composites (Akil et al., 2011). Lignocellulosic fibers can also be subdivided according to their origin from the plant itself. It is also possible to find a more general classification into wood-fibers and non-wood fibers. Therefore, nature provides a wide range of natural fibers classified in Figure 1-2 alongside some examples of the most used fibers in composites.

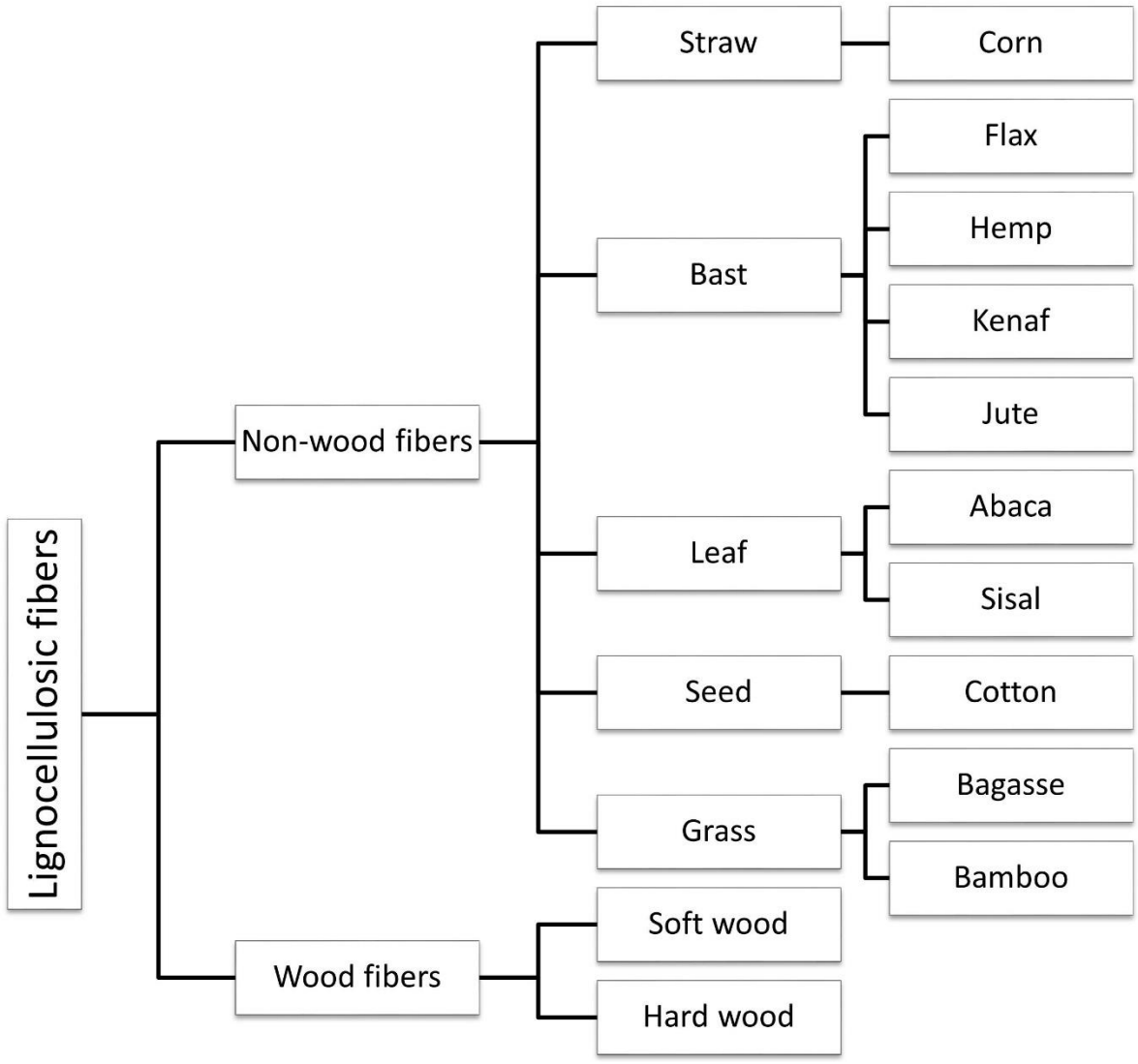

Figure 1-2: A general classification of lignocellulosic fibers adapted from (Akil et al., 2011).

These fibers are designed by nature and have a rather complicated structure. Structure-wise, these fibers are considered like natural composite themselves; the reinforcement component is the crystalline cellulose micro-fibrils and the matrix is the amorphous lignin and hemicellulose. Composition-wise, they are composed (except for cotton) of cellulose, lignin, and hemicelluloses as the main constituents along with waxes and some water-soluble compounds. From a chemical point of view, cellulose (the main constituent) is a linear polysaccharide generated from the repetition of β-D-glucopyranose monomers that are covalently linked through acetal functions (Abdul Khalil et al., 2012). Figure 1-3 shows a summary of the different forms of cellulose usable in composite reinforcement such as macro-sized fibers, microfibrillated cellulose (MFC), cellulose nanocrystal (CNC), nanofibrillated cellulose (NFC), or bacterial cellulose (BC) (Games, 1985).

Throughout the bibliographic research, one can notice that the most used lignocellulosic fibers in green composites development are essentially the bast fibers. One of the reasons for this growing interest is their cost, sustainability, and low density. Indeed Natural fibers are also significantly lighter than glass, with a density of 1.15-1.50 g/cm³ against 2.4 g/cm³ for glass fiber (Pickering, 2008). Kenaf fibers, for example, were largely used in the reinforcement of thermoplastics thanks to their toughness and high aspect ratio. For instance, kenaf was added to PE (Chen and Porter, 1994; Maldas and Kokta, 1995; Verma and Shukla, 2018), to PP (Deka et al., 2013; Sukri et al., 2012), and to PLA (Ben et al., 2007; Chen et al., 2017) which provided an enhancement in the mechanical properties of these different thermoplastics. Furthermore, these bast fibers were added to several thermosetting polymers recently such as poly(furfuryl alcohol) (PFA) (Deka et al., 2013) and epoxy (Krishna and Kanny, 2016). Flax fibers are also largely used in composites reinforcement for thermoplastics (Modniks et al., 2012; Wang et al., 2019a), thermosets (Bagheri et al., 2013; Coroller et al., 2013), and biodegradable matrices (Liu et al., 2006; Xia et al., 2016). Studies showed that these fibers have good specific mechanical properties which have the potential to replace glass fibers as reinforcement in composite (Coroller et al., 2013; Dittenber and GangaRao, 2012). However, their incompatibility with these matrices can result in a poor fiber/matrix adhesion (Modniks et al., 2012) yet it has been proven that adequate chemical treatment can limit this issue (Chandrasekar et al., 2017; Modniks et al., 2012; Xia et al., 2016). Jute fibers are one of the most abundant bast fibers worldwide that can be valorized in composite reinforcement (Alves et al., 2010). Nevertheless, these fibers as well suffer from the same limits as flax fibers and many studies have been conducted to overcome these challenges by performing surface chemical modifications (Corrales et al., 2007; Mohanty et al., 2000, 2004; Sinha and Rout, 2009).

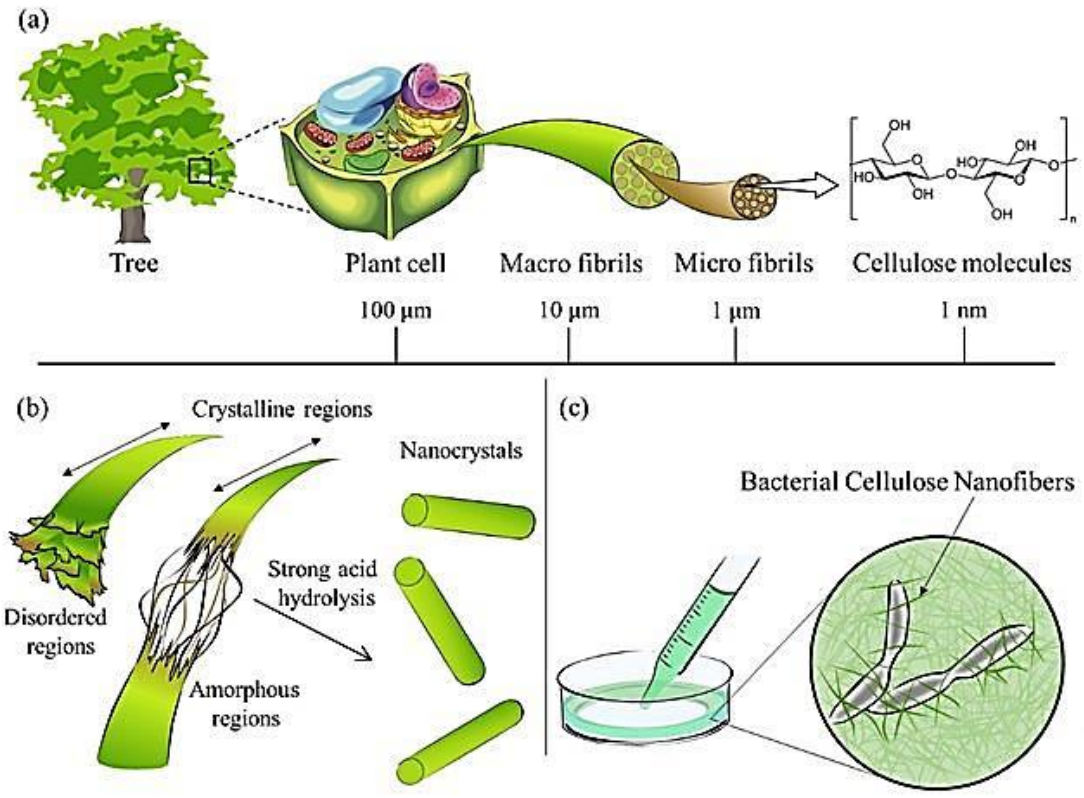

Figure 1-3: Schematic illustration of (a) the supramolecular organization of cellulose (b) the reaction between cellulose and strong acid to obtain cellulose nanocrystals and (c) bacterial cellulose nanofibers. (Miyashiro et al., 2020).

More recently, the use of cellulose nanofibers has overstepped natural fiber-reinforced composite. These nanofibers (10-60 nm) can be extracted from any natural plant-based fibers using different methods. The high stiffness of nanofibers can make the development of high performances bio-based composite possible. Scientist believing in the potential of these nano/micro-sized natural fibers started their investigation 25 years ago (Favier et al., 1995).

Composites with natural fibers reinforcement offer many advantages like a low machine abrasion, a low density, a lower cost, and renewability (Wambua et al., 2003). Yet the main motivation to use natural fibers in composite manufacturing is their positive impact on the environment (Mansor et al., 2015).

On the other hand, these naturally-produced fibers have non-uniform dimensions and mechanical properties which make the design of composite challenging. Another major drawback of the use of cellulosic fibers is their polarity. Their hydrophilic nature makes the adhesion with the hydrophobic matrix lower. Moreover, cellulosic fibers' polarity leads to high moisture sorption (Mehta et al.,

2004). Another considerable limitation to the use of natural fibers in composites is their limited thermal stability and thus they cannot be processed over 200°C (Akil et al., 2011).

1.1.2.2 Natural matrices for 'fully green' composites

For better sustainability, polymers produced from natural raw material were used along natural fibers to process fully green composites (Wambua et al., 2003). In the literature, we can find many studies and reviews on bio-based polymers such as starch, furan resins, and epoxy. Many others are still under investigation and development (Doroudgarian, 2016). In Table 1-3, a non-exhaustive list of commercially available bio-based thermoset resins is presented.

Table 1-3: Examples of commercially available thermosetting resins. Adapted from (Doroudgarian, 2016).

Trade name	Raw material	Manufacturer
Palapreg® ECO	Unsaturated polyester (55% bio-based)	DSM
ENVIROLITE	Unsaturated polyester and soy oil (25% bio-based)	Reichhold
Envirez®	Unsaturated polyester and soybean oil (18% bio-based)	Ashland
Biorez furfuryl resin	Furfuryl alcohol from biomass	Tranfurans chemicals
Furolite	Furfuryl alcohol from biomass	Tranfurans chemicals
LAIT-X/POLLIT	Lactic-acid-based	JVS-Polymers Ltd

Lately, research in bio-based composites has intensified and many countries start to consider the potential of these materials. The European Union, in particular, has been funding many research projects namely, ANACOMPO, ECOFINA, BIOCOMP, and WOODY aiming to explore more the potential of green composites (Doroudgarian, 2016).

Natural oils are used as a feedstock for many thermosetting resins thanks to their availability and low cost. After several chemical modifications, these oils can yield different resins such as polyesters, polyamides, polyurethanes, and epoxy resins (Llevot, 2017; Xia et al., 2013).

For instance, epoxidized vegetable oil is largely used to replace or to toughen fossil-based thermosetting resins, and soybean and castor oils are the most used (Liu et al., 2006; Llevot, 2017; Xia et al., 2013). Furan-based resins are also a possible matrix to produce bio-based composites as they are produced from biomass and more particularly agricultural waste. These resins and more

particularly furfuryl alcohol polymers will be explained and further detailed in section 1.3 (p.63) of this chapter.

Notwithstanding their renewability, these composites undergo the same end-of-life treatment as the fossil-based ones because of the no-degradability of the matrix and the difficulty to separate the encapsulated natural fibers. These composites unfortunately can only be downcycled but a chemical modification is possible to make them biodegradable or to make the crosslinking reversible (Netravali and Chabba, 2003; Quirino et al., 2021).

More recently, research of a 'truly green' composite increased. These materials are composed of natural biodegradable fibers and natural biodegradable resin thus at their end of life (usually short life cycle) these composites can be composted.

For instance, Biopol, a commercial poly(hydroxybutyrate-co-hydroxyvalerate) resin from Monsanto company, was used in green composite development. Biopol was combined with natural fibers such as pineapple and henequen for a composite with good mechanical properties with Young's modulus of 3 GPa in the longitudinal direction (Luo and Netravali, 2003, 1999a, 1999b). Moreover, this biodegradable resin was also successfully combined with jute fabric which resulted in 80% enhancement in tensile properties (Khan et al., 1999). Starch is another promising material for biodegradable and available thermoplastic matrices which was used combined with hemp and bamboo fibers and resulted in excellent flexural properties and high tensile strength (Takagi and Ichihara, 2004). The critical limit to the use of these plastics is their water sensitivity and poor mechanical performance. To overcome these limits, starch is usually used blended with other thermoplastics (Averous and Boquillon, 2004).

Recently, protein-based thermosettings are gaining the attention of the research community. Soy protein in particular has been used as a feedstock for biodegradable matrices. For instance, wood fibers were mixed with soy protein for the production of biocomposite by hot compression molding. Mechanical properties of these composites turn out to be even more efficient than PE/wood fibers composite (Netravali and Chabba, 2003). By the same token, composites with soy protein isolate and chopped ramie fibers yielded composite with an improved strength (Lodha and Netravali, 2002).

Lactic acid, the main monomer of PLA, was first isolated in 1780 from milk by the Swedish chemist Scheele. PLA is aliphatic polyester made from a-hydroxy acids. This thermoplastic is not only bio-based (made from renewable waste) but biodegradable as well. Furthermore, PLA has good mechanical properties compared to other biodegradable polymers and can be easily processed by using common techniques such as extrusion and injection molding (Kaplan, 1998). This aliphatic polyester starts to chemically decompose at 200 °C and has a low T_g temperature of only 55°C (Spinu

et al., 1996). In the literature, we can find many biodegradable composites based on PLA matrices. For instance, up to 30% of chopped flax fibers were added to PLA yielding a composite similar to that of polyester/glass fibers in terms of mechanical properties (Bodros et al., 2007). In another study, a plasticizer was added to PLA/ flax fibers composite and was found that despite the enhancement of mechanical properties with the addition of flax fibers the plasticizer harmed these properties (Oksman et al., 2003). Kenaf fiber is also a good candidate for the production of high performances PLA-based composites. It was reported that kenaf fibers' addition improved the storage modulus and thermal properties of the composite and its mechanical properties with Young's modulus of 6.3 GPa with 70% kenaf reinforcement (Nishino et al., 2003).

1.1.3 Different manufacturing techniques

Composite materials are very different composites need different manufacturing techniques. The first developed manufacturing processes were manual techniques. However, as the industry grows and composites start to get popular in many markets, a massive production was needed. Thusly, the development of different manufacturing techniques was essential to cope with this industrial growth. The method choice mainly depends on the materials, the part design, and the final use.

Manual techniques

The hand lay-up or wet lay-up method is an open contact molding technique. The resin is impregnated manually into a textile structure (woven, non-woven, knitted) after laying it in a mold coated with mold release and the number of these fiber layers depends on the desired thickness. Rollers and brushes are often used in the impregnation step to minimize air bubbles in the composite. The structure is then left to cure at room temperature before adding more layers if needed. Instead of impregnating the fibrous structures with the resin manually, it is also possible to use a pre-impregnated fibers called 'prepeg'. (Elkington et al., 2015)

The spray lay-up is another similar method where workers use a handgun to spray simultaneously resin and chopped fibers on the mold. The final step is to compact the thick layer with rollers and wait until it is cured at room temperature.

Autoclave processing (Compression molding)

It is a close molding technique by placing the material manually or robotically in the mold. The two halves of the mold are then closed and pressure is applied to impregnate the resin into the fibers and especially to eliminate voids in the composite (Tatara, 2017). Heat can also be applied with a varied

amount depending on the composite size and thickness. However, in some cases, the heating is not required and the pressure is applied at room temperature, we talk here about cold press molding.

Vacuum-assisted method (The vacuum bagging technique)

Prepregs with viscous resin are placed in a mold in the desired sequence topped with a film layer, air bleed layer, blocked film layer, breath layer, and then the vacuum bag layer. A vacuum is then applied to make the resin (even with high viscosity) liquefy and drawn for uniform impregnation. The vacuum will also help to remove the trapped air in the mold (Pearce et al., 1998).

Injection molding

This is another close molding process used more commonly for thermoplastics filled with chopped fibers but can be also used with thermosets. This process has been used for over 150 years (Frizelle, 2016). The fibers and pellets go through a funnel-shaped hopper with a screw into a heated barrel for liquefaction. The molten polymer is then injected in a closed mold until solidification. This is one of the fastest manufacturing processes (Balasubramanian et al., 2018).

Resin transfer molding (RTM)

In this method, the two halves of the mold are treated with a releaser, and the dry reinforcement is placed in the lower half before closing the mold. The thermosetting resin along with a catalyst is pumped into the mold at low pressure. The used resin usually has low viscosity for a quicker injection before reaching the gel point. This technique has been used for natural fibers-based composites (O'Dell, 1997).

Pultrusion

The name of this technique comes from the combination of the words pull and extrusion and is a continuous fabrication method highly automated. In this process, continuous fibers are pulled through a die that contains a resin bath. The resin is cured in the die and the final shape of the composite, usually in form of bars, is given by the die's shape. This technique is largely used for synthetic composites and was also successfully used for natural fibers such as kenaf (Zamri et al., 2016), kenaf/glass (Hashemi et al., 2016), and jute/glass (Uawongsuwan et al., 2015).

Filament winding

This is another example of a highly automated continuous fabrication. This technique is used to produce circular-shaped components using filaments winding process on an open cylindrical mold called a mandrel. The continuous fibers are pulled from the creel and impregnated in a resin bath before being wounded in the rotating mandrel. The fibers are equally distributed along the mold.

Additive manufacturing

Additive manufacturing (AM), also known as 3D printing, is an uprising technology in the manufacturing techniques introduced more than 20 years ago. This technology is also used in composite manufacturing not only for thermoplastics but also for thermosetting polymers. An introduction to this technology and scientific progress in composite production using this technology will be presented and detailed in section 1.2 (p.40).

A comparison of different manufacturing processes for composites production is presented in Table 1-4 (Balasubramanian et al., 2018). The images included in Table 1-4 are taken from a recent book by (Ngo, 2020).

Table 1-4: Comparison between composite manufacturing techniques.

Technique	Constituent materials	Advantages	Limits	Illustration
Manual techniques	Prepeg/ Textile fabric + Thermosetting resin	-Design flexibility -Minimum equipment investment -Low Tooling cost	-Labor-intensive -One-tooled surface -Quality related to operator's skill	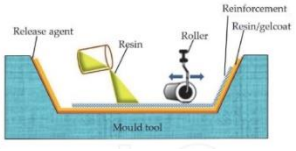

Technique	Constituent materials	Advantages	Limits	Illustration
Injection molding	Thermoplastic + Chopped fibers	-High volume production -Fast production -Low labor cost -Design flexibility	-Limited fiber length -High tooling cost	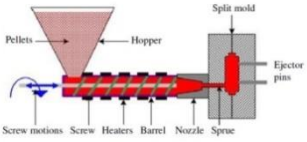
Compression molding	Prepegs Thermosets/ Thermoplastics + Chopped fiber/ Textile fabric	- Excellent mechanical and chemical properties -Excellent surface finish	-High labor cost -Slower process time -Not suitable for complex molds	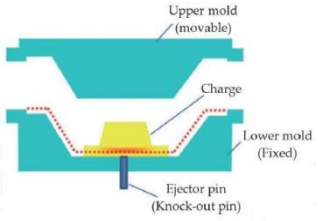
RTM	Prepegs Thermosets + Textile fabric	-Good finishing surface -Faster production cycles	-Requires good tools or great skill -Resin-rich edges	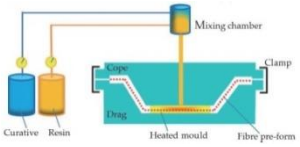
The vacuum bagging technique	Prepegs Theromosets+ Textile fabric	-Good interlayer adhesion -Good mechanical properties	- Many used tools - Low viscosity resin needed	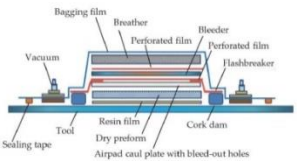

Technique	Constituent materials	Advantages	Limits	Illustration
Pultrusion	Continuous fibers + Thermosets	-Low void content -Continuous production -Low labor requirements	-High tooling cost -Limited cross-section components	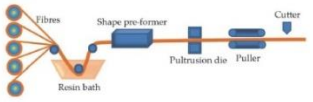
Filament winding	Continuous fibers + Thermosets	-High fiber volume -Oriented Fibers -Fast automated production	-Limited product shapes -High tools cost	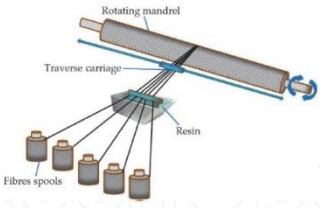
Additive manufacturing	Thermoplastics/ Thermosets or any kind of matrix + Continuous or chopped fibers or particles	-Automated process -Tailored product properties -Cost-effective Complex designs production	-Slow production -Limited printable materials -Limited fillers size	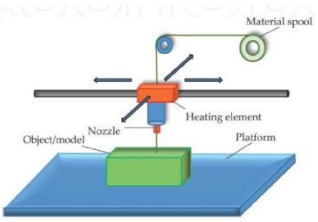

1.1.4 Conclusions

To conclude, nowadays, composite materials are widely used in different sectors, owing to the scientific research contribution and development of new efficient materials and manufacturing techniques. The majority of the used materials are petroleum-based which does not align with the recent increasing environmental concerns. Accordingly, many research and development projects were launched in these last two decades to find a natural and renewable substitute to synthetic composites, however many challenges appeared when using natural feedstocks. Hence, the presence of these composite on the market is still humble thus more research and development are needed to overcome its limits. New developments are also being done in the manufacturing techniques to produce more efficient and eco-friendly materials such as additive manufacturing. This new technology is gaining more popularity these last years and should be fully exploited in composites production.

1.2 Composites and additive manufacturing

1.2.1 Additive manufacturing - overview

According to ISO standard (ASTM 52900:2015) "*AM is the process of joining materials to make parts from 3D model data, usually layer upon layer, as opposed to subtractive manufacturing and formative manufacturing methodologies*". AM is also referred to as layer manufacturing or freeform fabrication. Usually, objects are fabricated according to three main techniques either by subtraction, by combination, by deformation, or by combining more than one technique. When using these classic techniques, the material loss is so important and more than one machine is needed which demands more workers more maintenance, and more costs. Furthermore, the time which is the main capital in the industry, is not optimized adding to that all the complicated logistics and production management. Meanwhile, the use of AM is different; the object is built layer by layer using one machine with almost zero material loss. AM methods can be different but the main common point is the fact of adding layer by layer the material according to the object pattern to obtain a solid 3D fabricated object. The main steps of AM are summarized in Table 1-5.

Table 1-5: A summary of AM main steps (Zhang et al., 2015).

				
The step	Designing	Slicing and adjustments	Building	Post-processing
The output	STL file	G-code	3D printed object	Final object
		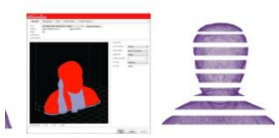		

Despite the recent popularity of 3D printing, this technology has existed for almost four decades during which it has been improved and developed for larger use. The engineer Chuck Hull is the author of the first patent in AM explaining the stereolithography (SLA) technique in 1984, which as a matter of fact, was also the origin of the STL designation of the files used nowadays for the 3D printers. In this US4575330B1 patent, Chuck Hull described how to build an object from an ultraviolet (UV) ray-sensitive material by successive layering and curing (Charles W, 1989). The engineer called the machine a 'Stereolithography Apparatus' and then the very first 3D printer, called SLA-250, was developed in 1988 by the 3D Systems Startup. One more patent has been deposited in 1989 by Scott and Lisa Crump, the creators of Stratasys company, for the development of the Fused Deposition Modeling (FDM) printer. The FDM® printing technique is based on the deposition of layers of a melted thermoplastic. This technique has rapidly gained its place in the market. In 1993, Massachussets Institute of Technology developed a new 3D printer based on a new technique called Three Dimensional Printing (3DP) which enables object building by depositing a thin layer of powder and jetting a few drops of glue according to the object pattern. This technique did not stay in the lab-scale since enterprise Z Corporation (later redeemed by 3D Systems) has fabricated the first 3DP machines for industry use.

Until 2006, Stratasys, 3D Systems, Z Corporation were the leaders of the 3D-printers market. These companies developed and sold many AM machines that made this technology more popular and used especially for rapid prototyping in the industry. In 2007, in Europe, several achievements took place such as the elaboration of the online service for public users to 3D print. A timeline of some key achievements in AM is presented in Figure 1-4.

In 2012, according to the Economist magazine, this technology was considered the third industrial revolution (The Economist, 2012). Indeed, AM size market is growing rapidly and steadily to pass from less than $5 Billion in 2014 to over $12 Billion in 2020 (Wohlers, 2021). AM market has been growing with an average growth of 27.4% over the previous 10 years but in the most recent Wohlers Associates' report, 3D printing market only grew by 7.5% (was expected to be $15.8 billion in 2019) which was still considered to be satisfactory owing to the impact of COVID-19 crises (Wohlers, 2021). In 2018, this new manufacturing technology was used the most to build end-use parts and functional prototypes as we can see in Figure 1-5 (Wohlers, 2019). Despite the recent low growth rate, another report forecasted a $51 billion market size by 2030 with a larger share for end-use parts (Research, 2021).

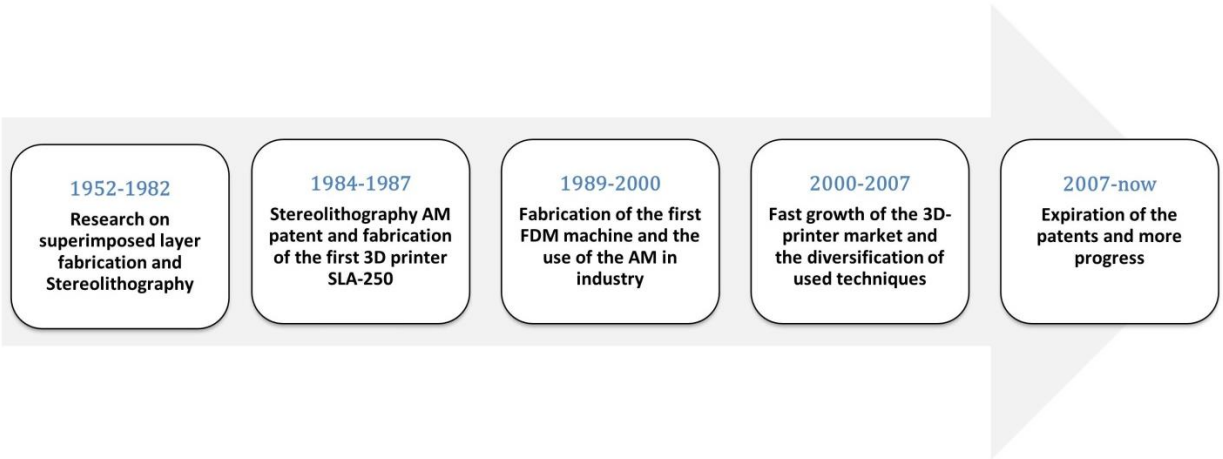

Figure 1-4: General timeline of important events in AM.

As a consequence of the rapid growth of AM popularity these last years and by dint of the development of new methods and techniques, many new terminologies have appeared. Thus, the ASTM decided to give a clear classification and universal terminologies for the different techniques. We list below a short description of the main used methods.

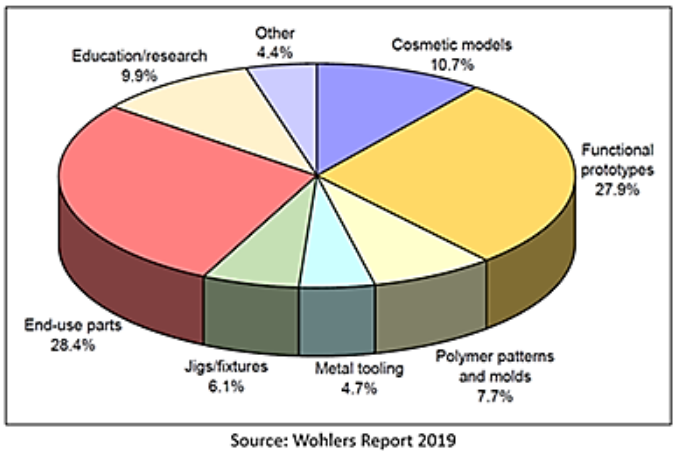

Figure 1-5: Circle chart of the share of the industrial application of AM in 2018 (Wohlers, 2019).

1.2.2 Different available techniques in AM

1.2.2.1 Material extrusion

The main technique is Fused Filament Fabrication (FFF) where a thermoplastic filament is melted after heating the nozzle until the melting temperature of the used plastic. Formerly, the liquefied plastic is deposited according to the coordinates on the GCode generated to print the specific object. Next, the plastic is cooled at room temperature to solidify before depositing the next layer. This technique is the most used for personal 3D printers thanks to its simplicity, yet a very precise configuration of the height, thickness, and filament orientation is required for a successful printing without weakening the mechanical properties of the object (Mohamed et al., 2015; Sood et al., 2010). Under the same category, we can also find cold material extrusion, also called direct ink writing (DIW) or Liquid Deposition Modeling (LDM) (Lewis, 2006), largely used in bioprinting using gels and pastes instead of molten plastic.

1.2.2.2 Powder bed fusion

This method consists of depositing layers of a very thin powder of polymers, metal, or ceramics on a platform and then a source of thermal energy selectively fuses the thin particles according to the desired pattern. This action is repeated for the next layers. Powder bed fusion is similar to the bed jet binding where the particles are assembled with glue jetting. After building the object the excess powder is eliminated and further processing is performed if necessary. The object is determined by the size distribution and the packing density of the used powder which are the main factors of a successful printing (Utela et al., 2008). Moreover, the difference between the Selective Laser Sintering (SLS) and Selective Laser Melting (SLM) should also be highlighted; in the first case the material choice is larger and the high temperature will make only the surface of the particle melt and fuse whereas in the latter case the particles are melted and fused which limits the material choice (aluminum, steel) but also results in better mechanical properties (Lee et al., 2017). The main interest of this method is its simple process with no required post-processing, decent resolution, and mechanical properties along with a variety of raw materials. However, this method has many challenges like the impossibility to build closed hollow cavities, as illustrated in Figure 1-6. Moreover, when using some material, the speed of laser scanning can be too high to melt correctly the particles which can lead to high porosity and fragile structure. Dust generation is another issue of this technique.

1.2.2.3 Binder jetting

Binder jetting, or 3DP, is one of the oldest methods of AM. This method has the same principle as powder bed fusion but instead of using a laser, the particles are glued by jetting a liquid binder. In this case, the essential parameters to control for good manufacturing are the binder rheology, deposition speed, and powder-binder interaction (Wang et al., 2017). The porosity is higher than the other methods leading to fragile objects and also poor surface finish.

1.2.2.4 Sheet lamination

Laminated object manufacturing (LOM) is based on the use of sheets of various materials such as paper, ceramics, polymers, and metallic sheets. This technique is also based on a layer-by-layer building by spreading the sheet and then cutting it precisely using either a mechanical cutter or laser according to the desired pattern. Then, the platform is lowered by one layer height and another fresh layer is bonded to the latter and the cycle is repeated until the object is built. After the building, post-processing is required to remove the rest of the non-used material (that beneficially insured the structure support) which can be recycled afterward (Gibson et al., 2010). LOM is recommended for the simple objects and is also time-effective however this technique is not recommended for the complex shape as the elimination of laminates becomes complex and time-consuming besides the low surface quality.

1.2.2.5 Vat photo-polymerization

Stereolithography (SLA) is the very first AM method used. This method is based on layer-per-layer solidification of photo-curable monomers using a light source. After the selective crosslinking of the photopolymer vat, the platform is lowered by a thin layer to repeat the process several times until the object is built. At the end of the printing, the object should then be finished by washing it with a solvent and further crosslink it in a UV oven. SLA is considered one of the most precise AM methods. Another benefit of this method is the possibility to print large objects. However, like all the AM methods, the SLA has numerous drawbacks like its high cost and process complexity. The very limited material choice is also a major limitation of this method in addition to the low manufacturing speed.

1.2.2.6 General remarks and comparaison of available techniques in AM

Despite the common principle of manufacturing by adding layer-by-layer material, every AM is different as it needs its specific materials and has its limitations. So, the right AM technique should be chosen depending on the object structure, its application, and the budget tolerance. In Figure 1-6, the structural limitations of every technique are revealed where one can notice that evry technique

has its limitations in terms of design structure and geometry. The availability of material currently used for this manufacturing technology is still limited as we can find mainly thermoplastics, photo-curable monomers, some metals powders and alloys, ceramics, and paper. Despite all of these limitations, AM is still an object of development and researchers are working to overcome these challenges to offer more materials and to optimize its techniques. 3D printing has multiple benefits to offer. First of all, personal product customization becomes easy and possible even in the biggest companies where large series production is no longer a necessary condition to make profits. Moreover, the manufacturing cost is significantly decreased thanks to the use of merely one machine instead of using many that consume a lot of energy and need specific skills and human resources. In addition, the necessity of outsourcing, transport can be considerably reduced (Berchon and Luyt, 2014; Horvath, 2014; Kamran and Saxena, 2016). Furthermore, AM is a great technology to optimize the material used with a significant waste reduction. A summary of these different techniques along with their main benefits and limits is presented in Table 1-6.

Table 1-6: Summary of the main AM methods (Ngo et al., 2018).

Method	Materials	Technique	Object	Benefits	Drawbacks
SLA Stereolithography	-Photoactive resin -Hybrid polymer-ceramics	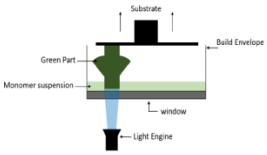		- Precise and high quality -Surface quality	-Limited material -Expensive -Slow printing
SLS/SLM Laser Sintering and Selective Laser Melting	-Metals and alloys -Limited polymers	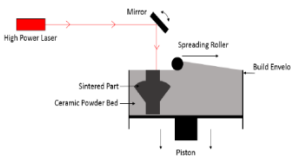		-Good resolution High quality -Fine mechanical performance	-Slow printing -Expensive

Method	Materials	Technique	Object	Benefits	Drawbacks
3DP Binder jetting	-Ceramic -Polymers	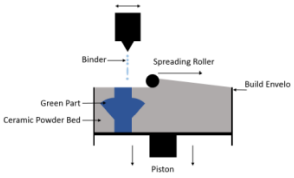	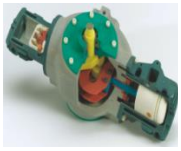	-Good resolution -Variety of material Possibility of using colors	- High porosity -Weak mechanical performance -Poor surface finish
FFF Fused Filament Fabrication	-Thermoplastic filament -Thermoplastic reinforced with fibers filaments	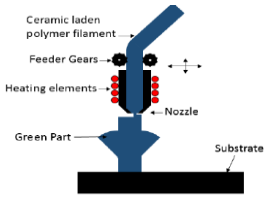	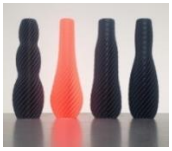	-Low cost -Simplicity	- Layer-by-layer finish -Weak mechanical properties
LOM Laminated Object Manufacturing	-Paper -Ceramics -Metal rolls -Polymers	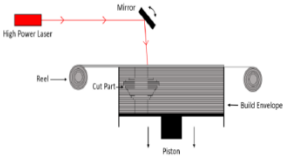		-Vast range of materials -Low cost	-Bad surface finishing - Post-processing complication -Material waist

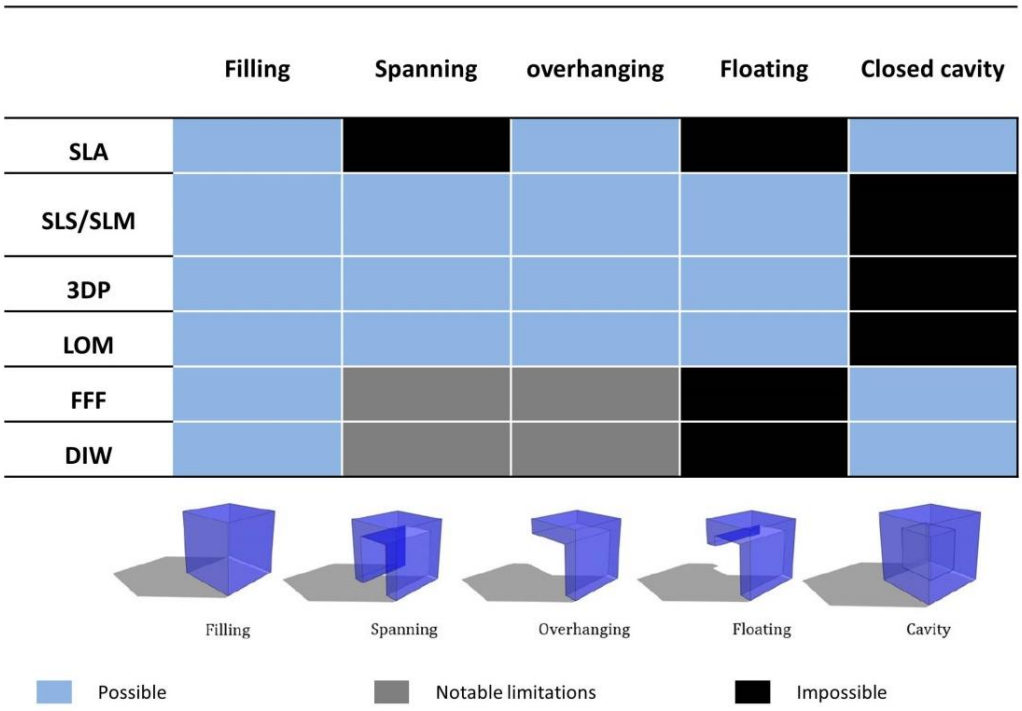

Figure 1-6: Structural limitations of different AM methods (Feilden, 2017).

1.2.3 Composites in AM by material extrusion

1.2.3.1 An overview

Before tackling the composite additive manufacturing state of the art, we will start with an overview of the steps involving AM by extrusion and its forms for a better understanding of the research challenges.

Based on the extrusion type, the printable material, or also called 'ink', can be divided into three main categories (Godoi et al., 2016):

- Hot-melt extrusion: thermoplastics whose solidification takes place after a phase change (solidification).
- Gel extrusion: their extrusion can be either at room temperature or higher temperature but their shape maintenance is due to a phase change after gelation.
- Cold extrusion: for this type of ink, the extrusion, and the deposition take place at ambient temperature and no phase transition occurs for supporting the printed structure. In this case, rigorous rheological behaviors are required so the material can be extrudable, easily flows through the nozzle, and resists deformations after printing to form a self-supporting structure.

Depending on the used material, the extrusion can take place either at high temperature using a liquefier as described before or at room temperature when the used material is not a thermoplastic. We can find different extruder systems on the market for the FFF (high-temperature extrusion) or DIW (ambient temperature extrusion).

In the FFF 3D printer available on the market two types of extruder systems can be distinguished:

- The pinch roller system is the most used. The pinch roller pushes the filament toward the liquefier with a constant linear speed. To ensure a constant flow rate, the adherence between the pinch roller and the plastic filament should be perfect and without any slipping.

- Another less popular extruder system is the screw-driven technique used for the pellets. The screw drives the melted pellet and pushes the molten rod through the nozzle.

In the case of cold extrusion, we can distinguish three extrusion systems to push the material through the nozzle, as illustrated in Figure 1-7-(c) (Sun et al., 2018):

- Screw-driven system with a stepper motor where the material is pushed by the rotation of the screw. The flow rate is regulated by the stepper motor and the material is initially stored in a syringe and pushed with pneumatic pressure until it comes in contact with the screw. This technique is largely used for concentrated suspensions and pastes (W. Li et al., 2017).
- The pneumatic extrusion technique is wildly used in bio-inks and food extrusions (Siqueira et al., 2017). The driving force of the ink in this system is a compressed gas (commonly the air). This system can be used for large inks types (Hölzl et al., 2016) but is still limited to material with low viscosity at the extrusion shear rate, and with low yield stress. This extrusion technique is simple and easy to use but the flow is not instantly controlled because of the compressed gas.
- The piston system is a syringe with a plunger connected to a step motor that controls the extrusion and the flow rate as shown in Figure 1-7-(a). This system is used in many commercial printers (such as Choc Creator). Contrarily to the pneumatic solution this technique allows a rapid adjustment of the extrusion rate.

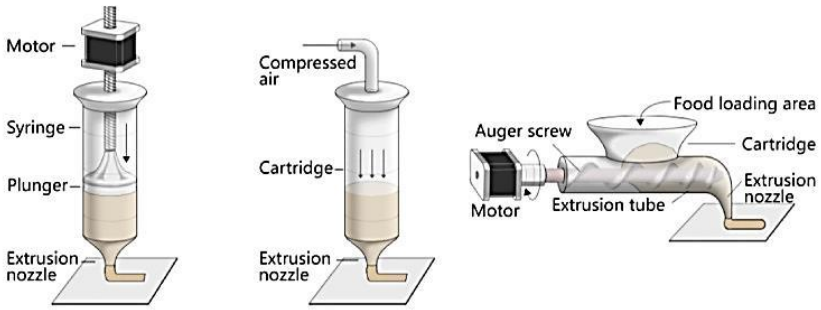

(a) Syringe-Based Extrusion (b) Air Pressure Driven Extrusion (c) Screw-Based Extrusion

Figure 1-7: Extruder for cold extrusion (Sun et al., 2018).

Independently to the used type of extrusion, AM by extrusion process passes by 4 main steps;

(i) Material preparation: this step is depending on the nature of the material. For instance, in the case of FFF the material is usually fed as a filament with a normalized diameter. The extrusion can also take place at ambient temperature in the case of ceramic, bio-inks, and many other formulations that should be compatible with AM requirements. In the latter case, the material preparation is complex because the formulation should have convenient rheology, should be homogeneous, and with no air bubbles.

(ii) Extrusion step: This is a crucial step in which the main objective is to insure a continuous and homogeneous rod flow through the nozzle. This step not only depends on the material nature but also on the extrusion system and the nozzle morphology.

(iii) Layers deposition: The quality of the raster deposition highly depends on the previous steps and the process parameters chosen by the user which will be detailed later.

(iv) Solidification: this is the last step before any eventual post-processing. The solidification step once again depends on the nature of the used material. The solidification of the melted thermoplastics takes place by simple cooling to room temperature while in the case of other pastes and suspensions this step can be more complicated and needs more control. The consolidation can be achieved by air drying, polymers crosslinking, or freeze-drying.

The final properties of the printed object are not only depending on the used material but also the hardware specifications such as the extruder type which usually is not controlled by the user, (Kuznetsov et al., 2019). However, there are many parameters, presented in detail below, that can be controlled by the user through the software that generates the GCode.

- Air gap: the air gap is the distance between the deposited roads. This air gap can be either positive in the case where the roads do not touch or positive when they are overlapped. This parameter can also affect the dimensional accuracy and mechanical performance of the printed object. A negative air gap can reduce the porosity and improve the bonding between the roads (Rodriguez et al., 2000).
- Build orientation and raster orientation: the build orientation depends on how the object is placed on the printing platform in the X-Y-Z space. This parameter has a major effect on the mechanical performances as well as on the dimensional accuracy (Alafaghani et al., 2017; Raju et al., 2010; Chacón et al., 2017; Panda et al., 2009). The raster orientation which is the deposit inclination with respect to the X-axis is also one of the parameters affecting the tensile strength. It has been proved that an angle of 45/-45° (Kung et al., 2018; Rinanto et al., 2018) and 0/90° (Leite et al., 2018) is the best for improving tensile properties. However, the effect of this parameter should be further studied especially for specimens printed in the same direction (0°).
- Extrusion temperature: The temperature of the liquefier is fixed mainly according to the used material. This parameter can influence the quality of the printed part. As the road leaves the nozzle from the heated liquefier to the printing environment, it solidifies. Hence, the material is subjected to thermal stresses that might distort the printed part and thus affect the shape fidelity and the mechanical performances (Alafaghani et al., 2017).
- Infill density: is defined as the fraction of the space occupied by the material in a layer over the total internal surface of the layer. The infill excludes the shells, which is also considered an important parameter that can affect tensile and compressive strengths (Croccolo et al., 2013). This parameter affects directly the properties of the printed part, especially its mechanical performances. The lower is the infill density, the higher is the porosity in the final object, and the poorer are the mechanical performances (Mahmood et al., 2017; Raju et al., 2019).
- Road width is the distance between the edges of deposited rods. Although this parameter can be fixed on the software, it cannot be less than 1.2 to 1.5 times the nozzle diameter when printing with thermoplastics (Agarwala et al., 1996) and certainly not less than the nozzle's diameter.
- Layer thickness is the height of one layer and is another parameter constrained by the nozzle dimension. The layer thickness cannot be more than the nozzle diameter and usually is chosen to be less. This parameter influences the printing resolution. Thinner layers improve

the surface roughness and the dimensional accuracy but increase the built time (Agarwala et al., 1996; Han et al., 2003; Sood et al., 2009; Alafaghani et al., 2017). The layer thickness influence also the tensile properties, it is believed that thin slices improve tensile strength (Deng et al., 2018; Leite et al., 2018; Li et al., 2018) but certain researchers proved the contrary (Tontowi et al., 2017).

- Printing speed: is the extruder movement speed in the XY plane expressed by mm/s which also affects the dimensional accuracy of the printed part and directly affects the building time (Anitha et al., 2001; Sood et al., 2009).

1.2.3.2 Composite manufacturing by hot-melt extrusion

According to a report published by Statista in 2020, FFF is the most used 3D printing technology in 2018. FFF is also the most common personal 3D printer thanks to its simplicity and cost-effectiveness and its office-friendly environment. However, 3D printed parts using this technique suffers from poor mechanical properties. Therefore, the idea of reinforcing the polymer with nanoparticles, short fibers, or continuous fibers was imposed to improve mechanical, thermal, and electrical properties. Plentiful research works have been carried out since last two decades to print quality products through FFF by using composite materials which have been the subject of many reviews these last years (Mohan et al., 2017; Parandoush and Lin, 2017; Mazzanti et al., 2019; Kabir et al., 2020; Penumakala et al., 2020; Wickramasinghe et al., 2020; Angelopoulos et al., 2021; Mogan et al., 2021; Lee et al., 2021; Krajangsawasdi et al., 2021; Mazurchevici et al., 2021). Hereby is an overview of composite printing by FFF highlighting the diverse types of fillers (continuous, discontinuous, natural, Nano-sized) that can be used and their mechanical properties.

1.2.3.2.1 Continuous fibers-reinforcing phase

Continuous fibers reinforcement offers significant improvement in mechanical properties compared to discontinuous fibers. However, this technique is still challenging 3D manufacturers and researchers in the development of a standard paradigm. In 2016, the team of Matsuzaki published in the scientific journal *Nature* an innovative technique for in-nozzle impregnation of continuous fiber within a thermoplastic matrix. In this study, PLA was used as the matrix while carbon fibers, or twisted yarns of natural jute fibers, were used as reinforcements. PLA reinforced with carbon fibers exhibited a net enhancement in mechanical properties with 500% amelioration in tensile modulus and 400% in tensile strength. Despite the increase of mechanical properties with the use of natural fibers, their impact stays limited comparing to carbon fibers. Moreover, comparing the continuous carbon-fiber composites with composite fabricated with discontinuous fillers using FFF or other

printing techniques, one can notice that this innovative technique showed a superior Young's modulus and strengths as we can see on the graph in Figure 1-8 (Matsuzaki et al., 2016). In fact, continous carbon-fiber composite outperform the filled and unfilled composite produced by different techniques in terms of strength with values approaching 250 MPa.

To overcome the poor matrix-carbon fiber bonding, carbon fibers were processed to enhance adhesion between the two phases. The produced composite had improved mechanical and thermal properties (N. Li et al., 2016). This trend of mechanical properties enhancement was supported with many other studies using PLA (Tian et al., 2016), ABS (Ning et al., 2015), and Nylon (Dickson et al., 2017; Klift et al., 2016) but it was also found that high fiber content eventually deteriorated the mechanical performances because of the increasing porosity.

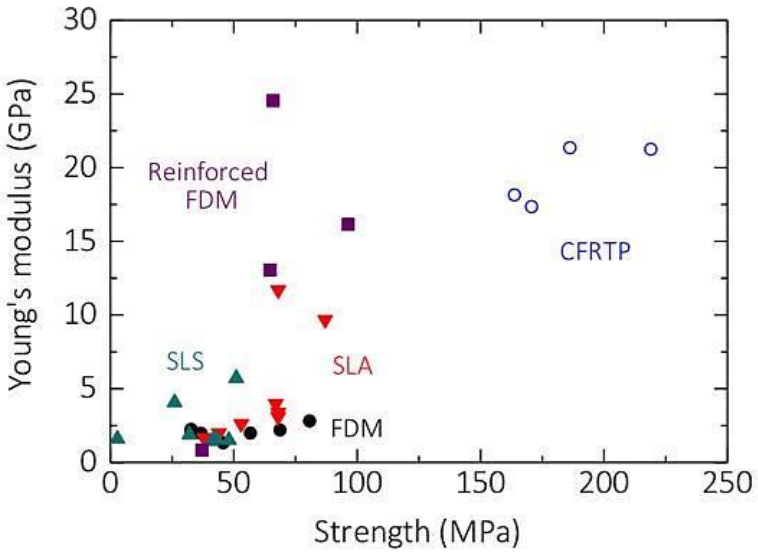

Figure 1-8: Young's moduli and strengths of continuous carbon-fibers composites (CFRTP) with composites fabricated by FFF, SLS, and SLA (Matsuzaki et al., 2016).

1.2.3.2.2 Short fibers and particles - reinforcing phase

Short fibers, macro, and nanoparticles were also added to enhance mechanical properties or to add specific functionalities such as thermal and electrical conductivity. Examining the literature, one can notice that the most used fibers are carbon fibers which enhanced the mechanical performances of thermoplastic matrices such as ABS (Ning et al., 2015; Tekinalp et al., 2014), PLA (Ferreira et al., 2017), and PEEK (Han et al., 2019; P. Wang et al., 2020). Despite an improvement in mechanical properties, the adhesion between the two phases was poor and fiber pull-out from the matrix was highlighted by SEM analysis (Figure 1-9). On one hand, it was found that the average size of the triangular channels between the rods decreases with the presence of carbon fibers as compared to neat matrices which can be attributed to the decrease in die-swell. On the other hand, voids inside

the rods increased. This porosity caused a limited mechanical properties improvement compared to compressed molded composites. Furthermore, nanoparticles with a high specific surface, such as graphene nanoplatelets (Caminero et al., 2019; Y. Wang et al., 2020; Yaragalla et al., 2021) and carbon nanotubes (Berretta et al., 2017; Gonçalves et al., 2018), were combined with many thermoplastics in order to develop high-performance nanocomposites.

In general terms, the incorporation of nanoparticles improved the mechanical and thermal properties and changed the mechanical behavior of thermoplastic from brittle to ductile. However, the improvement in the performances of these nanocomposites starts to decline when adding a large quantity of nano-fillers because of the creation of aggregates due to the dispersion difficulties of these nano-sized particles. Another commonly reported phenomenon is the alignment of fibers and nanoparticles in the printing direction as a consequence of shearing in the nozzle during extrusion. This alignment makes the printed parts anisotropic with tunable properties. In Figure 1-9, one can notice the shear-induced alignment of carbon fibers on the cross-section SEM images of the printed composites.

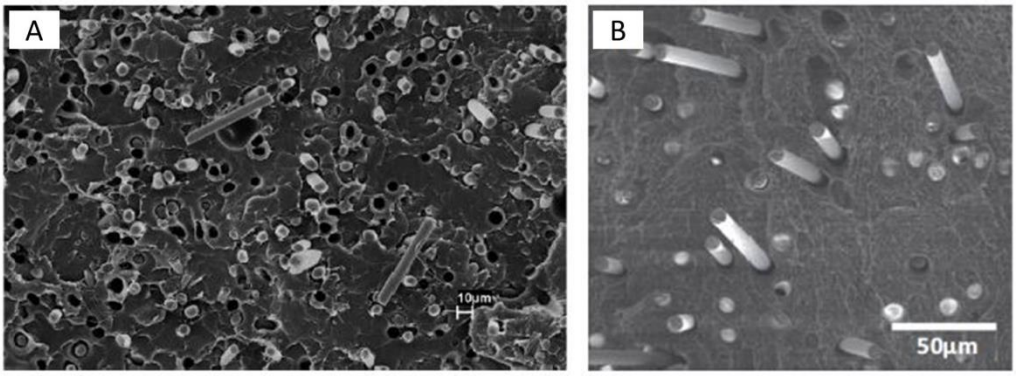

Figure 1-9: SEM micrographs of carbon fibers in (A) PLA matrix (Ferreira et al., 2017) and (B) ABS matrix (Tekinalp et al., 2014) highlighting fibers pullout and the resulting pores.

1.2.3.2.3 Natural fillers for composites produced by the FFF technique

Thermoplastics were also combined with natural fibers for greener or fully bio-based composites when blended with PLA. The use of bio-based fibers could be a great substitute for fossil-based fibers to enhance the performances of many matrices. However, the use of these natural fibers with a rather complex structure raises some challenges such as higher porosity, visible in Figure 1-10, and higher water uptake which leads to swelling and defects in the dimensional stability sought in 3D printed parts (Le Duigou et al., 2016; Torrado Perez et al., 2014). On the other hand, when flax fibers were blended with PP the shrinkage upon solidification decreased by more than 80% (Stoof and Pickering, 2018).

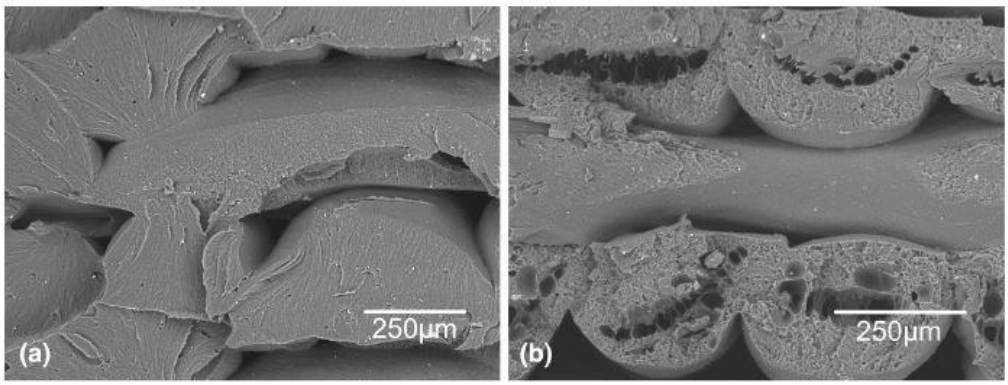

Figure 1-10: SEM images of the fractures of (a) ABS and (b) ABS and jute fibers (Torrado Perez et al., 2014).

In addition to natural fibers, some works have been conducted to valorize bio-refinery byproducts to blend them in 3D printing filament to boost their performances and their environmental impact. For instance, lignin was added to ABS and Nylon which increased the stiffness and decreased the melt viscosity making it a good material for 3D printing by melt extrusion (Nguyen et al., 2018). In another study, 25 wt% of wood hemicellulose were blended to PLA to produce a fully green composite filament for 3D printing. The added hemicellulose slightly improved the thermal properties of the resulting composite but no significant improvement in mechanical performances was reported. Nevertheless, the authors stressed the importance of hemicelluloses active sites which may be used as carriers or molecular anchors to introduce tuned functionality (Xu et al., 2018a). Different composites developed in the last 5 years for 3D printing by hot-melt extrusion are summarized in Table 1-7 with a focus on their mechanical properties. As one can notice, adding fillers to thermoplastics has significantly improved mechanical properties but their effect on thermal properties is rarely reported. With no surprise, PLA was the most used matrix thanks to its easy printability. When reinforcing this plastic with short fiber the maximum stiffness was 7.5 GPa and the strength was 67 MPa. The composite tested with ABS and PP had stiffness under 3 GPa and a maximum strength of 65 MPa.

The major limitation to the use of thermoplastics is their weak thermal stability and low T_g which led to the development of more technical thermoplastic such as PEEK. These costly and highly performant plastics can only be printed by heating the nozzle over 350°C which makes the printing process rather complicated. As highlighted previously in Table 1-1, thermosets are more resistant to high temperature, have better wettability without being over-priced. In the next section, recent studies for the development of 3D printing inks using thermosetting resin will be presented.

Table 1-7: A summary of thermoplastics and fillers used for 3D printing of composites and their mechanical properties.

Matrix	Fillers	Mechanical properties	Reference
PP Tensile modulus= 1 ±0.6 GPa Tensile strength= 26 ±9 MPa	30 wt% Glass fibers	Young's modulus= 1.25 GPa Tensile strength= 34.5 MPa	(Carneiro et al., 2015)
	30 wt% flax fibre	Young's modulus= 2.8 GPa Tensile strength= 39 MPa	(Stoof and Pickering, 2018)
ABS Tensile modulus= 2.5 ±1 GPa Tensile strength= 33 ±5.5 MPa Tg= 96-110°C	7.5 wt% Carbon fiber	Young's modulus= 2.5 GPa Tensile strength= 42 MPa	(Ning et al., 2015)
	40 wt% short carbon fiber	Young's modulus= 14 GPa Tensile strength= 65 MPa	(Tekinalp et al., 2014)
	5 wt% Jute	Young's modulus= 1.5 GPa Tensile strength= 26 MPa	(Torrado Perez et al., 2014)
	5 wt% TiO_2	Young's modulus= 1.7 GPa Tensile strength= 32 MPa	(Torrado Perez et al., 2014)
PLA Tensile modulus= 2.9 ±0.6 GPa Tensile strength= 44 ±10 MPa Tg= 53-60°C	Continuous carbon fiber	Young's modulus= 20 GPa Tensile strength= 175 MPa	(Matsuzaki et al., 2016)
	Continuous jute yarn	Young's modulus= 5 GPa Tensile strength= 55 MPa	(Matsuzaki et al., 2016)
	30% glass fibers	Young's modulus= 2.34 GPa Tensile strength= 15.8 MPa Tg= 50.6°C	(Vinyas et al., 2019)
	2 wt% modified graphite nanoplatelets	Young's modulus= 1.75 GPa Tensile strength= 67 MPa Tg= 63 °C	(Y. Wang et al., 2020)
	15 wt% short carbon fibers	Young's modulus= 7.5 GPa Tensile strength= 53.4 MPa	(Ferreira et al., 2017)
	Graphene nano-platelets	Young's modulus= 3.6 GPa Tensile strength= 63.2 MPa	(Caminero et al., 2019)
	20% of wood hemicellulose	Flexural modulus= 3.5 GPa	(Xu et al., 2018b)
	15 wt% recycled wood fibers	Young's modulus= 2.2 GPa Tensile strength= 20 MPa	(Le Duigou et al., 2016)

Matrix	Fillers	Mechanical properties	Reference
Nylon® Tensile modulus= 1 ±0.5 GPa Tensile strength= 41 ±7 MPa	Kevlar continuous fiber	Young's modulus= 9 GPa Tensile strength= 81 MPa	(Melenka et al., 2016)
PEEK Tensile modulus= 4 ±0.1 GPa Tensile strength= 105 ±6.5 MPa Tg= 143°C	1 wt% graphene nanoplatelets	Young's modulus = 2.6 GPa Tensile strength = 140 MPa Tg= 168°C	(Yaragalla et al., 2021)
	3 wt% MWCNT and 1 wt% Graphene nanopelets	Young's modulus= 3.6 GPa Tensile strength= 95 MPa	(Gonçalves et al., 2018)
	5 wt% carbon nanotubes	Tensile strength= 55 MPa	(Berretta et al., 2017)
	5 wt% Carbon fiber	Young's modulus= 7.4 GPa Tensile strength= 101 MPa	(Han et al., 2019)
	5 wt% Carbon fiber	Tensile strength= 94 MPa Flexural strength= 155 MPa	(P. Wang et al., 2020)

1.2.3.3 Composites manufacturing by cold and gel extrusion

1.2.3.3.1 Additive manufacturing of bio-based composites by extrusion

The new definition of composites material, explained in section 1.1.1 (p.24), is vague and includes any material containing a polymeric phase and fillers. By simple bibliographic research for bio-based composites in 3D printing, one can notice that the absolute majority of these materials are developed for biomedical applications and the most used material is cellulose in form of CNC, NFC, and MFC. These nano-sized cellulosic fillers are usually produced at low concentration (<5 wt%) in water which forms a hydrogel largely used in 3D printing by extrusion (bio-printing), especially for tissue engineering. The reason behind the popularity of MFC hydrogel in 3D printing is their convenient rheological behavior for AM because it has a shear-thinning and thixotropic behavior facilitating respectively the extrusion and the shape maintaining (Abouzeid et al., 2018; Håkansson et al., 2016; Sultan and P. Mathew, 2018). However, for the solidification of the printing parts, the hydrogels are usually combined with biopolymers to ensure the consolidation of the material by crosslinking such as alginate (Abouzeid et al., 2018; Leppiniemi et al., 2017; Markstedt et al., 2015)

and chitosan (He et al., 2016). The combination of the hydrogel and these biopolymers enables a successful 3D printing of scaffolds as shown in Figure 1-11-A and Figure 1-11-B. Although MFC hydrogel is a very interesting candidate for AM of biomaterials, its high water content (up to 98 wt %) harms the shape maintenance after drying. As we can see in Figure 1-11-C2, after air-drying the water evaporates leaving a shapeless fibers residue. Air drying is not an option when printing hydrogels so the most used technique is freeze-drying for shape maintenance and the generation of a porous structure ideal for tissue engineering (Figure 1-11-C1). Freeze-drying is an expensive technique that is worth using for high-performance and high-impact materials such as biomaterials. However, in order to use cellulose fibers in more general applications, it is obvious that water content has to be limited. Accordingly, recent studies have been conducted to develop cellulose-based 'inks' for AM by extrusion with higher cellulose content and limited water load. A paste based on high content enzymatically fibrillated cellulose nanofibers was used for AM by extrusion. Indeed, the high cellulosic content limited the shrinkage upon drying but cracking of the printed parts was resulted from water evaporation. Moreover, clogging in the nozzle (1.2 mm) was reported when extruding fibrous pastes with high solid content (Klar et al., 2019). The approach of increasing cellulose content was also used to formulate a paste based on softwood microfibers combined with carboxymethyl cellulose which played the role of a matrix and also lubricant to limit nozzle clogging.

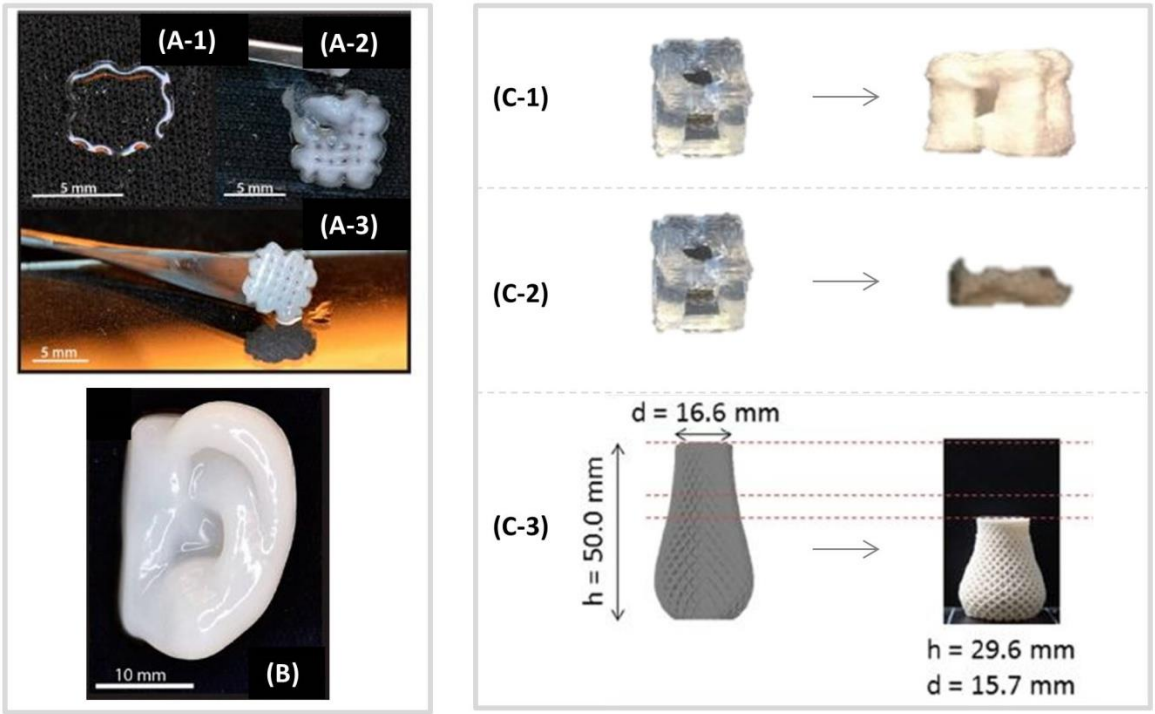

Figure 1-11: Printed parts of (A1) 3% alginate and (A2) 2.5% cellulose nanofibers (A3) cellulose nanofibers and alginate. (B) human ear 3D printed with alginate and cellulose (Håkansson et al., 2016; Markstedt et al., 2015). Photographs of printed parts: MFC hydrogel after freeze-drying (C1) and after air drying (C2) (Håkansson et al., 2016) and of high content cellulose paste after air drying (Thibaut et al., 2019).

The paste's overall solid content was over 40 wt% which further limited shrinkage and deformation of the printed parts. However, the fibers' anisotropic shrinkage upon drying was still important as we can notice in Figure 1-11-C3 (Thibaut et al., 2019). These bio-based printed materials exhibited good mechanical performances compared to thermoplastics but the major limitation is unsurprisingly their water and humidity sensors (Le Duigou et al., 2019). Nevertheless, this limitation can also be a big advantage for the recycling step.

Some other approaches were also proposed such as the combination of wood powder with an adhesive mixture which presented many limitations and needs more optimization (Kariz et al., 2016). Another approach consisting of printing a solution of cellulose acetate by extrusion and solidification by solvent evaporation was adopted (Pattinson and Hart, 2017).

1.2.3.3.2 Thermosetting-resin-based composites

Thermoset polymers exhibit superior thermal, chemical, and mechanical stability, making them more adequate for demanding applications comparing to thermoplastics and cellulosic materials. However, 3D printing of crosslinkable polymers is still limited to photocurable resins because thermosetting resins do not have rapid solidification after extrusion. As mentioned previously in the DIW technique the ideal 'ink' should exhibit shear-thinning and thixotropic behaviors. Thus, thermoset polymers are usually never printed alone but in a combination with fillers which play the role of rheology modifiers. When printing thermoset polymers by DIW, the most important step is the formulation and preparation of the ink. Indeed, tuning the rheological parameters is important to make the thermosetting feedstock printable.

In a study published in 2017, epoxy resin was mixed with 30 wt% alginate that played the role of thickener and rheology tuner (Yield shear stress 2000 Pa) and dimethyl methyl phosphonate for increasing the solid load. The purpose of this study was to find the universal property and printing parameters for AM of thermoset by extrusion. The authors reported that the first important parameter is the rheological behavior of the extrudate which has to be pseudoplastic. Alginate powder transformed the Newtonian behavior of the pure resin to a shear-thinning ink and also increased the yield stress. The effect of different extrusion and printing parameters such as nozzle height and extrusion rate was studied with respect to the cross-section geometry. A new parameter called nozzle critical height was reported that results in an extruded line with a near 90° contact angle (Shang et al., 2017). In 2015, Compton and his team (Compton, 2015) have already mixed epoxy resin with nano-clay and SiC whiskers particles to make it printable. The nanoparticles addition modified the rheology by increasing the viscosity and the shear-thinning abaility of the slurries to

yield a suitable ink for AM. As we can see in Figure 1-12, nanoclay platelets provided the shear thinning, stiffness, and the yield strength required for 3D printing. As for SiC whiskers, they provided additional stiffness and yield strength to the ink and acted as effective structural reinforcement in the final composite.

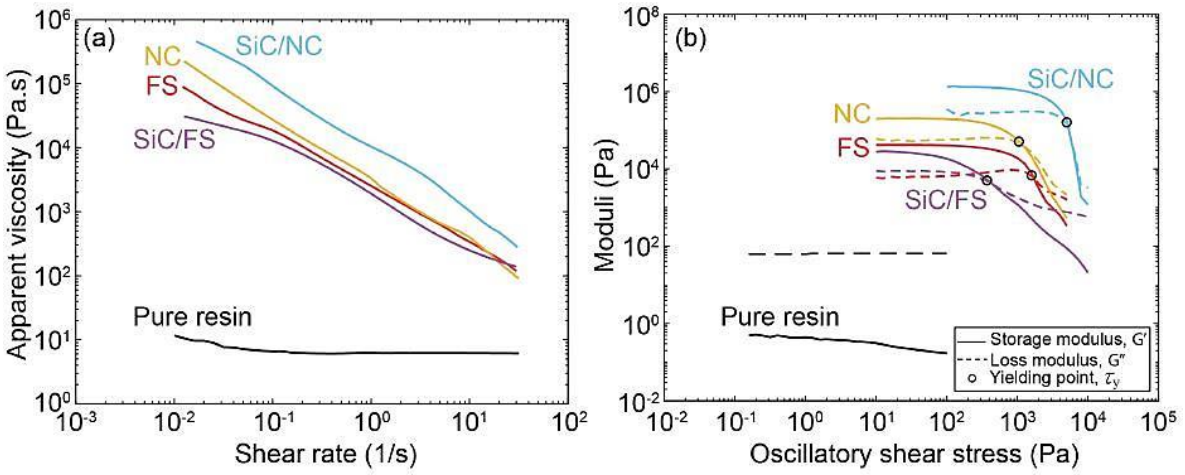

Figure 1-12: Effect of particle addition on resin rheology. (a) Curves of viscosity function of shear rate and (b) Storage and loss moduli function of shear stress (Compton, 2015).

Furthermore, and in the same reported work, less than 4 vol% of carbon fibers were added which enhanced Young's modulus to reach 25 GPa. It was also found that during extrusion, high aspect ratio fillers become highly aligned, resulting in superior properties along the print direction as we can clearly see in Figure 1-13. The shear inducing anisotropy of printed parts due to high aspect ratio particles alignment in the extrusion direction is a relatively old discovery compared to AM history (Peng et al., 1999). This approach was more explored for 3D printing of structures with specific stiffness by mimicking balsa cell walls. Carbon fibers were added to epoxy which made the material stiffer with Young's modulus of 57 GPa (Malek et al., 2017).

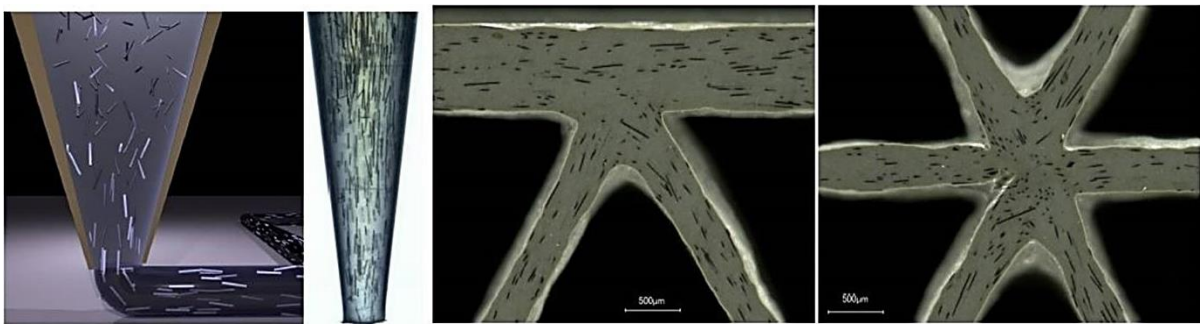

Figure 1-13: Shear-induced alignment of carbon fiber visible in printed rods (Compton, 2015).

In 2018, graphene flakes were blended with epoxy resin to 3D print electrically conductive material. It was found that besides increasing electrical conductivity, graphene particles modified the viscosity

to enable the AM of the thermoset polymers. However, the printability of the ink was limited thus a low concentration of nanoclay was added to further increase the yield stress of the ink. The resulting composite was as strong as neat casted epoxy (flexural strength 80 MPa) and stiffer (flexural modulus 4.8 GPa) (Compton et al., 2018). Once again, the same research team conducted a recent study to investigate the effects of filler morphology, nozzle size, and print speed on the mechanical anisotropy in 3D printed epoxy composites. 10 wt% of fumed silica and nanoclay pellets were added to epoxy resin and successfully modified the rheology to obtain a printable ink (yield shear stress of about 1000 Pa) with preference to nanoclay in the case of multi-fillers composites. In this study, it was also demonstrated that SiC whisker insured a better enhancement in mechanical properties with flexural strength values up to 215 MPa and a 4 GPa flexural modulus while fumed silica composite had 107 MPa flexural strength and a 3.1 GPa modulus. Furthermore, the mechanical properties of these composites containing high-aspect-ratio fillers (like nanocalay and unlike fumed silica) display pronounced dependence on both nozzle size and print speed (Hmeidat et al., 2020). An attempt to 3D print continuous carbon fiber with epoxy resin was also made and inspired by the FFF process. The printed material exhibited high mechanical properties over-performing composites of thermoplastic and continuous carbon fiber. The elastic modulus and tensile strength of these composites reached respectively 162 GPa and 793 MPa (Hao et al., 2018).

Usually, when manufacturing composite the porosity is not desired but in some applications such as regenerative medicine or sensors, voids are essential. Accordingly, in a recent study, porous printed structures of different thermosets were developed by tuning the rheology with sacrificial particles such as sodium chloride. The added particles play a double role of rheology modifier to enable the printing of the structure and also as porosity precursors as they will be removed after curing of thermosets by water dissolving and freeze-drying (Lei et al., 2019).

In recent years, AM of thermoset polymers gained more popularity and many techniques were developed to tune the rheology and to enhance mechanical performances. However, the major limitation of these resins is their non-recyclability. Accordingly, some researchers developed a recyclable 3D printing approach for thermally cured polymers by using a recyclable vitrimer epoxy by solvent dissolution (Shi et al., 2017) and Diels-Alder reversible thermoset (Yang et al., 2017). To tune the rheology of the vitrimer epoxy, 18 wt% of nanoclay were added and the blend was precured to increase the viscosity. The printed parts had limited mechanical properties with tensile modulus and strength respectively 11 MPa and 6 MPa.

Besides of epoxy, many other thermoset polymers were also used to bestow higher performances to the printed part. For instance, cyanate ester resin was an ideal candidate for DIW of high thermal performance composite (Chandrasekaran et al., 2018). Indeed, the printed composites (containing 20 wt% silica nanoparticles) exhibited excellent thermo-oxidative stability up to 420°C and high T_g temperature. Furthermore, owing to its high char residue the printed part was carbonized and yielded a stiff carboneous material while conserving its original printed structure. More recently in the frame of a master's degree thesis (Stellato, 2020), a fully bio-based printed composite was developed based on a blend of PFA resin and lignin. The ink was prepared by blending 74% of PFA with 18% lignin and 7 % fumed silica which played the role of rheology modifier. In this work, the curing and consolidation step was conducted in-situ by loading two different feedstocks of the curing agent and the ink. Afterward, the two feedstocks are mixed in the extrusion head and the crosslinking of the thermoset starts as soon as the material is extruded and deposited. This in situ curing technique, illustrated in Figure 1-14, was also reported before by (Rios et al., 2018) without mentioning the used polymer. The temperature of curing and the catalyst ratio were carefully chosen and optimized to avoid the foaming of the furanic resin. The printed furan-based material had flexural modulus and strength respectively 3.8 GPa and 88 MPa.

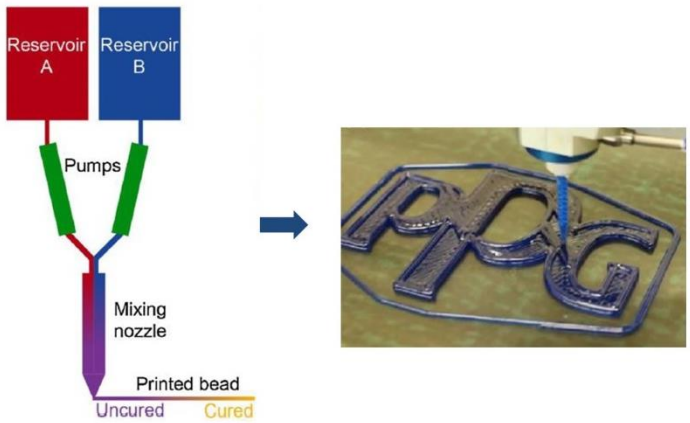

Figure 1-14: Schematic of the printing process for reactive polymers (Rios et al., 2018).

1.2.3.4 Conclusions

Notwithstanding, additive manufacturing of polymer composites has known significant developments in recent years, it is still not ready for larger industrial use. Several limitations of this technology need to be overcome such as the poor material choice. The polymer selection for composites additive manufacturing is limited to printable materials. Currently, the majority of 3D-printed composites are thermoplastic-based owing to the easy process of hot-melt extrusion by the FFF technique. However, these materials have low T_g and poor thermal properties which do not meet

the various requirements of industry application. To overcome this limitation, recently, 3D printable inks were developed for additive manufacturing of thermoset polymers composites. These 'inks' are composed of synthetic thermosetting polymers blended with macro or nano-sized particles essential for making the material printable. The thermal and mechanical properties of these materials can be further tuned by reinforcing them with fibers or carbon-based particles. Despite the complexity of the formulation step to obtain a printable material, especially in the absence of a clear definition of 'printability', these composite exhibited promising mechanical and thermal properties using a cost-effective manufacturing process and raw materials. In the state of the art, there is still a major focus on epoxy resin and carbon fibers yielding an efficient yet petroleum-based composite. More research on the development of more eco-friendly and sustainable materials with good mechanical and thermal properties for the 3D printing of composite should be done.

1.3 PFA - an economic and bio-based polymer with high thermal performances

1.3.1 PFA structure polymerization and properties

As discussed previously, sustainability gained a large interest in the manufacturing of products due to the dwindling of fossil resources. The use of bio-based polymers along with natural fibers is the key to shift towards materials with a carbon-neutral footprint. One such bio-based and available polymer is PFA. In this section, the production and the polymerization steps of this renewable polymer will be reviewed.

1.3.1.1 Furfural monomers - one of the bases of furan polymers

1.3.1.1.1 Source and synthesis of furfural

For a better understanding of the preparation and properties of the PFA macromolecules, is wiser to deal with the synthesis and production of the furfural molecule, i.e the precursor of the monomer which represents the base of the used material in the present project.

For the sake of terminologies, it is worth mentioning that furfur is actually a Latin word that means bran (Fink, 2013). Furfural molecule is not a recent discovery as it was first isolated in the early 19th century by Döbereiner when producing formic acid. However, industrial production only started in the early 20th century (Dunlop and Peters, 1953). Manufacturers were and still are very interested in the production of this molecule because of the availability and the cost-effectiveness of the raw materials and the production process. Indeed, this molecule can be readily produced from any agricultural and forest waste containing pentoses. Therefore corn cobs, oat, and rice hulls, sugarcane bagasse, cotton seeds, olive husks, wood chips can all be used as a feedstock for the production of this monomer (Choura et al., 1996; Gandini, 1997). 2-furancarboxaldehyde, more commonly called furfural, is produced from hemicellulose and more specifically from pentoses. These polymeric pentoses (pentosans) are hydrolyzed to break them down into small units. These monosaccharide units, such as xylose, will be the base for the synthesis of furfural molecules. A general overview is presented in Figure 1-15.

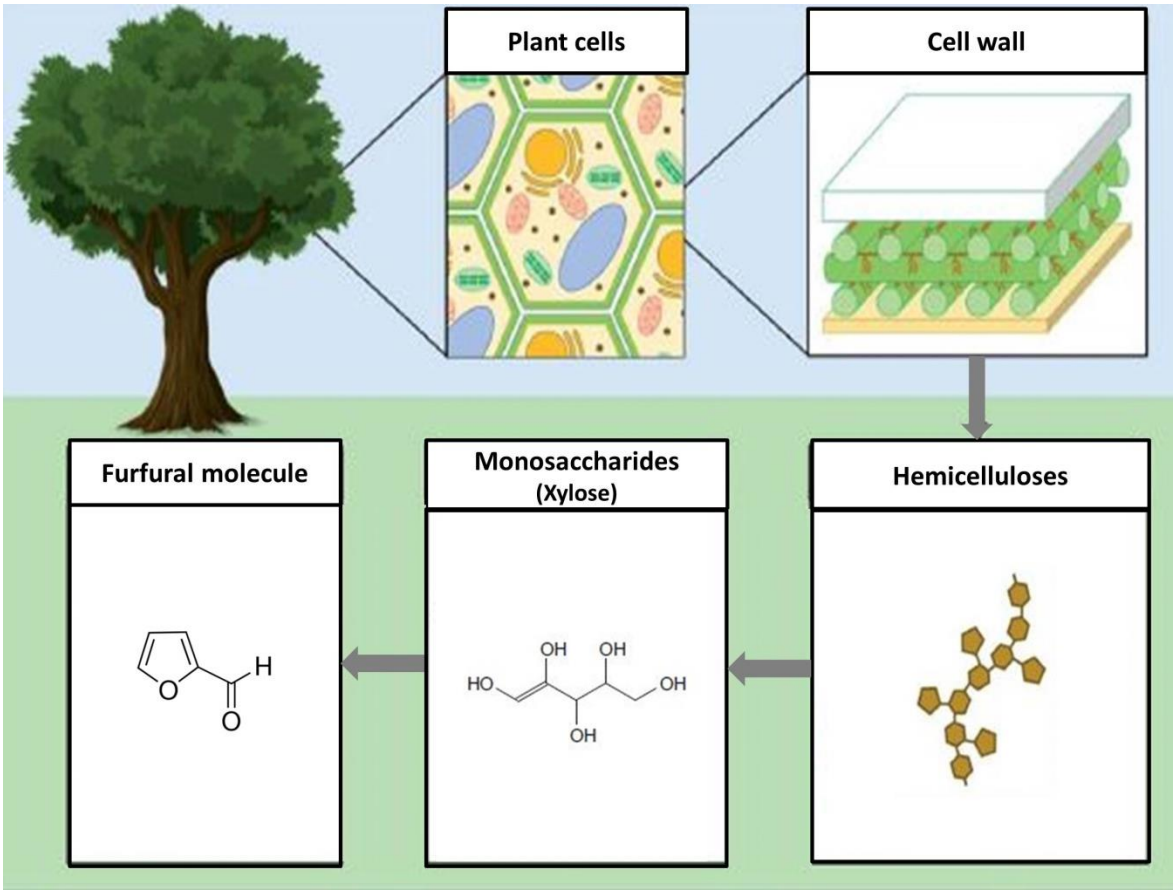

Figure 1-15: General overview of furfural production from biomass feedstock. Adapted from (Istasse and Richel, 2020).

After hydrolysis of xylane (pentosan), the resulted xylose (monosaccharide) is progressively dehydrated and then cyclized to give the furfural molecule (Gandini, 1997). The reactions included in this step are schematized in Figure 1-16.

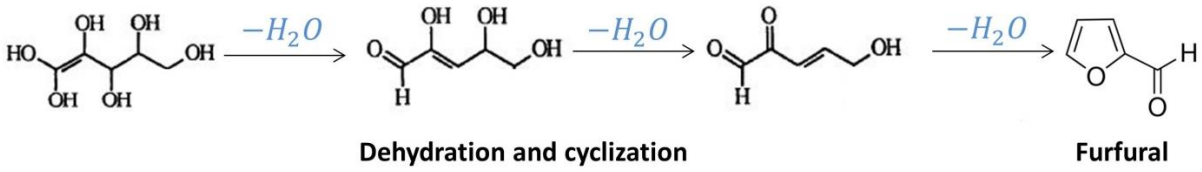

Figure 1-16: Dehydration of xylose to produce furfural.

1.3.1.1.2 Industrial production of furfural

There are two processes for furfural production, either a one-stage or two-stage process. In the one-step process the depolymerization of pentosans by acid and the dehydration of the resulted pentoses, happen simultaneously in a single reactor. The two-stage process starts first with the dissolution of pentosans in the mild condition in one reactor. Then, in another reactor, the pentoses are dehydrated to yield furfural (Machado et al., 2016; Mesa et al., 2014).

The first furfural production was a two-stage process originally developed by Quaker Oats Technology. The hydrolysis step is performed in an aqueous acid batch of sulphuric or phosphoric acid (2.2 wt%) and with steam at 153°C. After the second stage of cyclodehydration, furfural is recovered by steam stripping from the solution. This process has many drawbacks such as high effluent production and high energy consumption for a low furfural yield (Dashtban, 2012).

Many studies have been carried out to improve furfural production to develop a more environmentally friendly process. For further reading, Mehdi Dashtban has published a detailed review treating this subject (Dashtban, 2012).

These drawbacks and environmental concerns led to the closing of many furfural production plants. Nevertheless, the furfural global market size is in constant growth with about $479 million in 2019 and is expected to grow by 6.2% from 2020 to 2027 according to Grand View Research online data (Grand view research, 2020). China is the leading producer with over 200,000 ton/year in 2005 using corncobs as feedstock. Dominican Republic is also another major actor in the furanic production with 40,000 tons per year of furfural produced from sugarcane bagasse which is transformed to furfuryl alcohol by Transfurans Chemicals in Belgium (Istasse and Richel, 2020).

By simple chemical reactions, it is possible to obtain many derivatives of furfural (Gandini, 1997). However, the majority of furfural is industrially converted into furfuryl alcohol (FA) because the latter has found many applications. Polymerization and brunching mechanisms as well as the usage of this industrialized product will be summarized in the following section.

1.3.1.2 Furfuryl alcohol (FA)

1.3.1.2.1 The synthesis of furfuryl alcohol from furfural

FA is made from furfural by reduction with hydrogen as shown in Figure 1-17. FA can be further converted into 2,5-bis(hydroxymethyl)furan (BHMF) by formylation as illustrated in Figure 1-17 (Gandini, 1997).

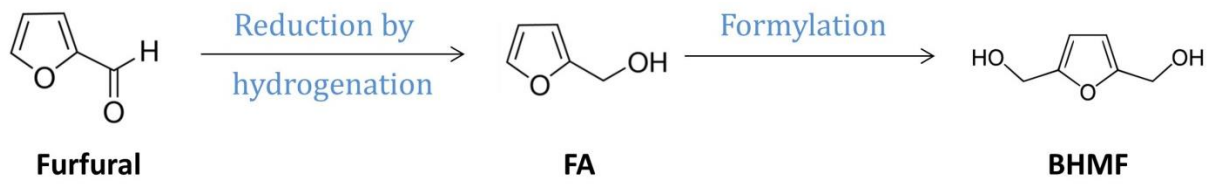

Figure 1-17: Yielding FA and BHMF from Furfural.

This molecule is majorly used in form of polymer or oligomer of poly(furfuryl alcohol). The polymerization requires an acid catalyst and leads to a black crosslinked solid material. To understand the reactions involved in the formation of this network, many studies have been conducted since 1953.

When in contact with an acidic medium FA goes through a polymerization process in which the first step is a condensation reaction. The condensation reaction can take place following two paths as illustrated in the simplified schema in Figure 1-18. In reaction [1], the condensation occurs between the OH of one monomer with the free hydrogen (H5) atom in the furan ring of another monomer to eliminate one water molecule. In this case, the structure is called head-to-tail and yields a methylene bridge between furan rings. When following reaction [2], the hydroxyl group of one monomer condensates with the same group of another monomer with the elimination of one molecule of water. This structure is called head-to-head and yields an ether moiety between the two monomers. Generally, reaction [1] is more frequent, so that in the ensuing oligomers it is more probable to find methylene bridges because the reaction is faster and under strongly acidic conditions the ether moieties can lose a formaldehyde molecule to revert to the former moiety, as shown in Figure 1-18. Therefore, in the macromolecular structures methylene bridges are in general much more frequent than their ether counterparts (Choura et al., 1996; Gandini, 1997).

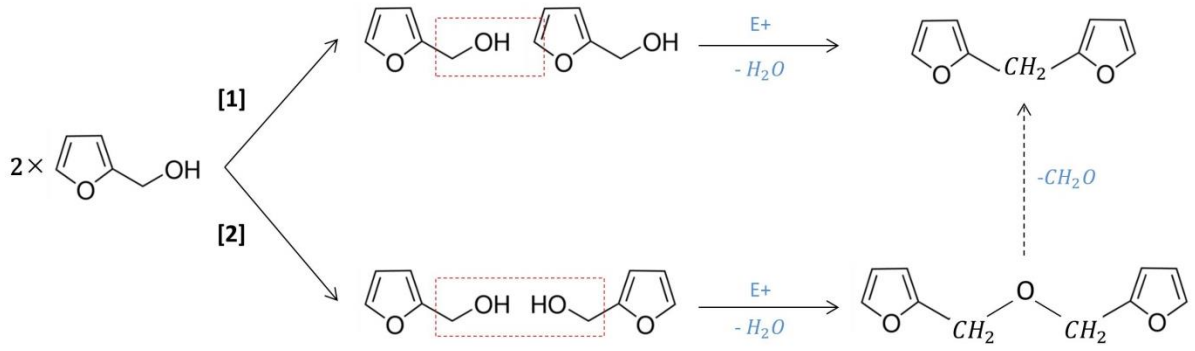

Figure 1-18: Acid-catalyzed condensation of furfuryl alcohol.

1.3.1.2.2 Crosslinking of FA - Puzzles of a complex structure collected over years

Condensation reactions can only lead to a linear structure and do not explain the crosslinking of this polymer. In fact, the condensation reactions discussed above, would lead to a colorless thermoplastic material. The polymerization of FA instead yields a yellowish resinous oligomeric compound when the reaction is stopped at its early stages. As the reaction evolves, the material starts to develop a darker color and higher viscosity until turning into a black solid product (Gandini, 1997; Iroegbu and

Hlangothi, 2018). Therefore, the PFA structure and the involved crosslinking reactions are more complex than a simple linear polycondensation.

This complex structure has puzzled chemists for decades. As analysis techniques evolve, scientists had more data and hence more information about the structure emerged. The first investigation was conducted in 1953 where the linear structure by condensation, discussed before, was explained and the crosslinking was associated with the formation of methylene bridges thanks to the formaldehyde released after the reversion of di-methylene ether moieties into methylene. A simplified illustration of this structure is given in Figure 1-19 (Dunlop and Peters, 1953).

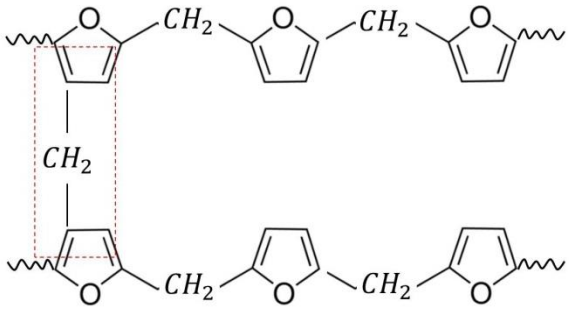

Figure 1-19: Crosslinking by Methylene Bridge.

A decade later, thanks to the use of FTIR spectroscopy, a furan ring-opening, as shown in Figure 1-20, was identified after the detection of γ-diketones (Conley and Metil, 1963).

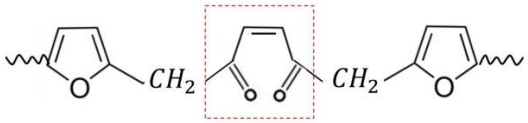

Figure 1-20: Furan ring opening.

In 1971, a paper was published proposing a polymerization pathway for the termination of the chains when using alumina catalysts (Wewerka, 1971). Over a decade later, a new analysis using ^{13}C-NMR, confirmed the ring-opening and the crosslinking through methylene bridges as suggested back in the fifties. The published work also confirmed the lack of di-methylene ether bridges comparing to their methylene counterparts (Chuang et al., 1984). In addition to ^{13}C-NMR, ^{1}H-NMR was used in analyzing furfuryl acetate structure. This study identified for the first time aside reaction leading to a conjugated structured as represented in Figure 1-21 (Buchwalter, 1985).

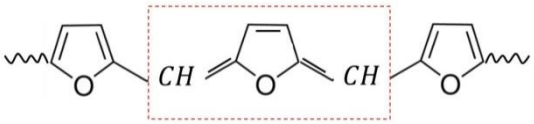

Figure 1-21: Conjugated structure of PFA.

In 1996, a systematic study was conducted using different model compounds and using FTIR spectroscopy and ^{1}H-NMR for polymer characterization. This study confirmed the linear polymerization and formation of methylene bridges as the first phase of curing. The second phase according to the research group involved many side reactions in particularly the conjugation of the furan-methylene chain which is at the origin of the coloration of the cured product. Authors attributed the brunching to Diels-Alder reactions between conjugated and unconjugated chains as highlighted in Figure 1-22 (Choura et al., 1996).

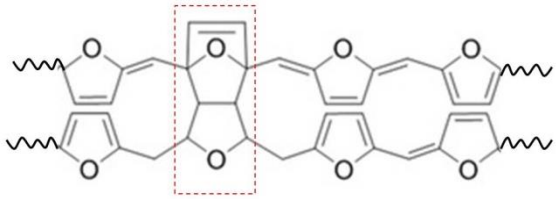

Figure 1-22: Diels-Alder reaction interchains. adapted from (Falco et al., 2018).

Over the last two decades, many analysis techniques were used such as chemo-rheological kinetics (Guigo et al., 2007a) Attenuated total reflectance (ATR), FTIR spectroscopy (Barsberg and Thygesen, 2009), Raman spectroscopy (Kim et al., 2013), and ^{13}C solid-state NMR spectroscopy (Falco et al., 2018). These studies mainly confirmed the structures revealed before with some more specifications about their frequencies.

More recently, a new study investigated this complicated structure of PFA by complementing ^{13}C-NMR, FTIR, and UV-Raman spectroscopies with spectra modeling. The author confirmed again the presence of most of the structures mentioned before but their NMR analysis showed a limited signal for the conjugated and the Diels-Alder structures. This study suggested for the first time a new structure resulting from the furan ring opening and the linear structure presented in Figure 1-23. This new structure was supported by ^{13}C-NMR and FTIR techniques (Tondi et al., 2019).

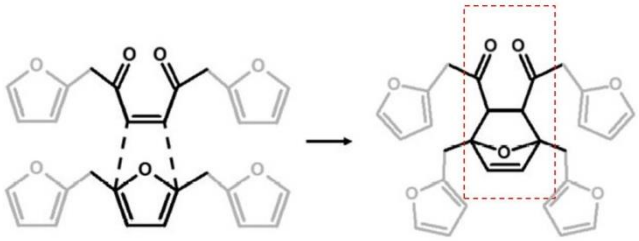

Figure 1-23: New Diels-Adler reaction suggested by (Tondi et al., 2019).

This rather complicated structure confers to the cured plastic interesting properties and assets. These Furanic macromolecules have no functional groups. Therefore, the crosslinked material has outstanding alkali resistance, solvent resistance, and good corrosion resistance to inorganic acid. Another well-known asset of PFA is its good heat resistance, low inflammability, and low smoke release (Gandini, 1997). The crosslinked material can indeed be used at 120°C to 140°C for a long time and in some cases at 180°C (Wang et al., 2011). However, its oxidation resistance is poor because of the possible furan ring-opening under certain conditions. Another limitation to the use of PFA is its brittleness which requires the utilization of plasticizer or blending it with other polymers. In the literature, one can find the usage of this product in numerous and different areas, such as the historical metal cores, fragrances production, and of course composites.

1.3.1.2.3 Some applications of furfuryl alcohol monomer and polymer

FA is historically often used in the foundry as a binder for the fabrication of molds and cores. This still holds nowadays, as in 2019 foundry industry monopolized FA market share by over 80% (Grand view research, 2020). What makes this furanic binder popular in the foundry industry is its lower volatile organic compound, less formaldehyde, and less smoke release during casting comparing to phenolic urethane thermosets (Fink, 2013). Preservation, or as commonly called “furfurylation” of wood is another usage of low-viscosity FA. This furanic compound is a great eco-efficient substitute to toxic and hazardous compounds such as salts of copper (Goldstein and Dreher, 1960; Lande et al., 2008). FA is also used in form of polymers for the fabrication of resins. Thanks to their excellent resistance to corrosive chemicals these resins find applications as cementitious grouts, coating, impregnating materials, and sealants (Schmitt, 1974). FA can also be used in its liquid state as a solvent serving as a cleanser, paint softener, or dye dispersant for textile applications (Pizzi and Mittal, 2003).

Pyrolysis of PFA and the ensuing materials gained also much interest in many applications such as carbon/carbon composites (brakes and clutches, rocket motors, heatshield, aero-engine components), electrodes, etc... The pyrolysis process was studied by many researchers (Wang et al., 1997; Zarbin et al., 2002) and it was found that until 300°C the condensation and crosslinking

reactions dominated. When exceeding 350°C, loss of hydrogen and oxygen led progressively to carbonization which is accomplished at about 900°C (Gandini, 1997).

FA finds also use in many different fields such as flavoring and fragrances (Centi and Perathoner, 2013), pharmaceuticals (Mohamed et al., 2017), and rocket fuels (Kulkarni et al., 2009). As mentioned previously, cured PFA has excellent fire resistance properties and low smoke emission but is a brittle material. Accordingly, this polymer would be a good matrix to use combined with different fillers providing it with better mechanical properties and different functionalities. Indeed, this was the idea of some research groups who used PFA as a matrix for composites which will be further detailed in the next section.

1.3.2 PFA -based composites

1.3.2.1 PFA as a precursor for carbon matrix

Under inert conditions, PFA can be carbonized. At a low temperature of 200-500°C, chaotic structures of amorphous carbon and aromatic microdomains are formed leading to large pores. Under higher temperature and longer thermal treatment, the aromatic microdomains enlarge and rearrange. Therefore, the structure becomes more ordered and the pores shrink as illustrated in the conceptual model in Figure 1-24 (Mariwala and Foley, 1994). Furthermore, the electrical conductivity of the resulting PFA-derived carbon increases when increasing the carbonization temperature. At above 850°C the pyrolysis yields a highly conductive material (Wang et al., 1997).

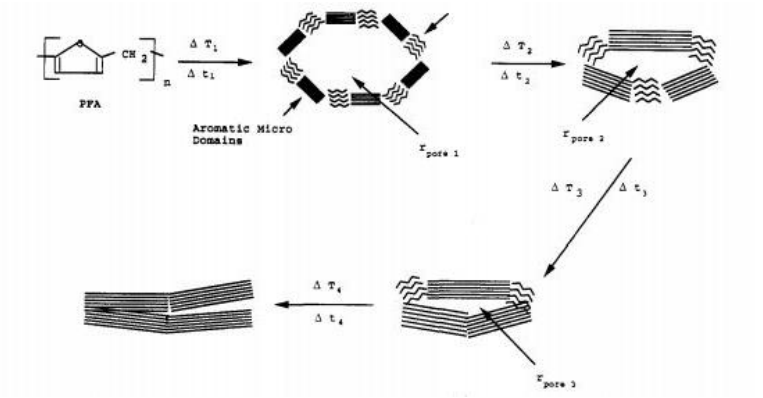

Figure 1-24: Conceptual model for adsorptive structure evolution in PFA-derived carbon (Mariwala and Foley, 1994).

Accordingly, PFA was used as a precursor for many carbon-based composites. A nanocomposite of carbon and silica was prepared by using a sol-gel process to obtain mesoporous carbon. The precursor was prepared using tetraethyl orthosilicate in the presence of FA followed by the polymerization of FA and its subsequent carbonization. The removal of the silica framework from

such nanocomposite led to the formation of porous carbon. The size of the pores was directly influenced by the sol-gel reaction conditions (Kawashima et al., 2000). PFA was also used as precursors for the fabrication of films with high electrical conductivity (sheet resistances 13 Ω/sq). PFA resin was mixed with 1 wt% of graphene and FA microspheres, obtained after emulsion polymerization, were mixed with graphene oxide to yield porous film. This porous film was then selectively carbonized according to the desired pattern. This carbonaceous porous film was demonstrated to be an excellent material for the fabrication of micro-supercapacitors with a maximum capacitance of 16.0 mF/cm² at 0.05 mA/cm². The micro-supercapacitor had also an impressive life cycle, hence it could retain up to 97.4% of its capacitance after 10000 cycles. This PFA/graphene oxide composite has many potential uses especially in wearable electronics (Hawes et al., 2019).

1.3.2.2 Lignocellulosic fillers

As discussed before, recently the interest in composites based on renewable materials has grown because of greater environmental awareness. When coupling PFA with natural fillers in particularly lignocellulosic fillers we can obtain a fully biomass-based composite. One popular natural fiber used in green composites is flax fiber and which was unsurprisingly combined with PFA. Examples include the use of PFA as copolymer in cellulose acetate butyrate. The copolymers mixture was added to a flax nonwoven mat to reach a 50 wt% fiber fraction. The well-impregnated flax mat thanks to the effect of FA was cured by compression molding following many curing steps to release byproduct from FA poly-condensation and thus avoid foaming and possible defects of the composite. High pressure of about 2.2 MPa had to be applied and temperature cycles up tol 155 °C had to be used for a long time which makes the manufacturing rather complicated and energy-consumer. The ensuing composite had an improved storage modulus compared to the neat matrices and the addition of 25 wt% thermoplastic improved the stiffness of PFA at temperatures higher than 80°C. Changes in mechanical properties were evaluated for different PFA fractions in the matrix phase of the composite and it was found that the thermosetting resin promoted the increase of both stiffness and strength at rupture to reach respectively 12.2 GPa and 95 MPa when adding 100 wt% PFA against 4 GPa and 70 MPa without PFA. However, these improveming were at the expense of impact strength. Nevertheless, in this study, the impact of the reinforcement with flax nonwoven fibers was not evaluated as compared to neat matrices (Toriz et al., 2003).

In a similar approach, humins were combined with PFA which enhanced the mechanical properties thanks to the plasticization role of humins (Pin et al., 2014). In another study, aligned natural fiber textiles, randomly oriented natural-fiber textiles, and glass fiber textiles have been hand laid up and

impregnated with a commercial furan resin to form prepregs. The composite prepregs were cured into composite plates by compression molding. During compression molding, the mold was lifted several times to evaporate the water resulting from the poly-condensation. The curing process lasted less than 8 min, since the prepregs were precured for 8 hours, and 2 MPa pressure was applied. The approximate void content in the different composites was measured with a µCT scanner, and it was found that the aligned flax fibers composites had the highest void content spatially compared to glass fiber composites which could be caused by the unfilled lumen of natural fibers as shown in the SEM image in Figure 1-25. Accordingly, the specific Young's modulus of glass fiber and aligned flax fiber composites were similar of respectively 12.4 GPa·m^3/kg and 11.4 GPa·m^3/kg except for strength which was higher for composite with the synthetic fibers. Moreover, the authors showed that the sensitivity of fiber orientation to load angle was less in the case of flax fibers comparing to glass fibers. These interesting mechanical properties of the fully green composite were explained with a high matrix fiber adhesion owing to a similar chemical composition between the two phases. The fire resistance properties were also evaluated and contrary to the glass fibers base composites the fully natural composite was ignited but the burning rate was low revealing good fire retardance (Pohl et al., 2011).

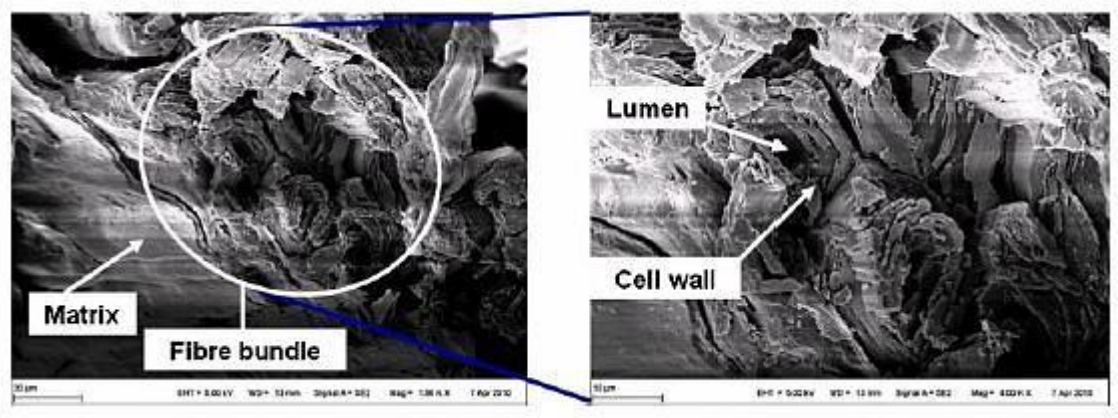

Figure 1-25: Images (SEM) of flax fiber non-crimp composite fracture area (Pohl et al., 2011).

As one can notice, voids in composite, created because of the morphology of natural fibers and of steam bubbles released during curing, present a major challenge in the development of PFA-based green composite. In another study presented in the *15th European conference on composite materials*, aligned flax fibers were impregnated by PFA and were cured using vacuum molding and casting which was found to be not possible because of the boiling of water solvent as shown in Figure 1-26. The elimination of solvent was reported to be quasi-impossible because of the exponential increase of viscosity. It was found that a low-temperature cure to prevent the exothermal peak from exceeding the boiling point of the solvent could stop the foaming of the resin as visible in Figure

1-26-D. The adapted technique was found to be a beta-stage compression molding which insured good mechanical properties with a tensile strength of 211 MPa (Crossley et al., 2012).

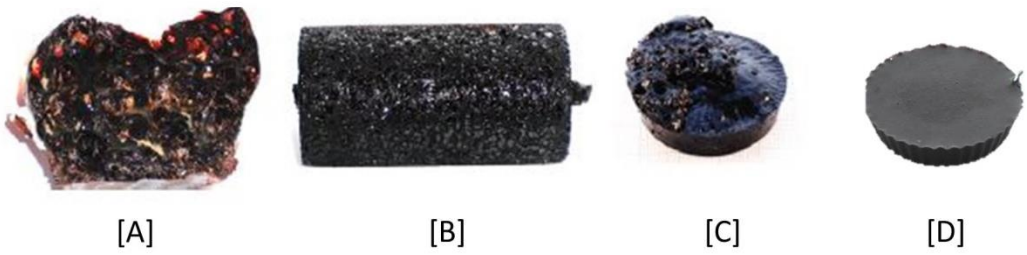

Figure 1-26: Foaming during cure of furan resin samples at [A] 150°C ambient pressure, [B] 140°C RTM closed mold pressure tested to 8 bar and [c] 140°C 6 bar autoclave [D] 60°C at 1°C/min (Crossley et al., 2012).

The development of more eco-friendly materials is also interesting to the European countries which have launched a European program project called BIOCOM for the development of high-performance composites. In the frame of this project, an adapted PFA commercial resin for the composite was developed by Transfurans Chemicals. This natural matrix was combined with flax woven textile and glass fibers for the fabrication of vehicle panels. These composites were manufactured using the vacuum bag technique and compression molding for the consolidation step. By characterizing mechanical properties it was found that Young's modulus of the composite with glass fibers and flax fibers were similar (7.2 GPa and 8.5 GPa respectively) but the tensile strength of the latter was 30% lower than the former. In virtue of their end-use, the mechanical properties were also evaluated after aging in different fluids and it was shown that the use of natural fibers caused a drop in mechanical performances with a remarkable loss in stiffness caused by their hydrophility with more than 50% drop in Young's modulus after mmersion in water (Giannis et al., 2008).

In another study, 0% to 20 wt% of bleached kenaf fibers were added to the PFA matrix. The optimum properties of the green composites were achieved by 20 wt% fiber loading which showed significant increments in tensile strength (310%), storage modulus (123%), and flexural strength (48%) compared to neat PFA. In addition, the introduction of kenaf fibers improved thermal stability with an increase in storage modulus values. Mechanical properties were also reevaluated after boiling-water absorption. These mechanical performances were retained up to 83% for tensile, 89% for flexural, and 82% for impact strength (Deka et al., 2013). When used with low fractions, PFA or FA can also be used for reinforcement of cellulosic fibers such as microfibrillated lignocellulose (MFCL) (Lems et al., 2019) and bamboo fibers (Wang et al., 2019b). In both cases, it was found that the furfurylation of the lignocellulosic fibers enhances mechanical and thermal performances especially when the PFA fraction approaches 50 wt%. On the other hand, the authors mentioned a degradation of the mechanical properties of the cellulosic material caused by the use of acidic catalyst which

should have been avoided (Wang et al., 2019b). Furthermore, it was proven that cellulosic fibers containing a higher amount of residual noncellulosic polymers had better wetting and better compatibility with FA during the in-situ polymerization (Lems et al., 2019).

To replace the use of bast fibers with more sophisticated fibers, the use of high tenacity rayon fibers was considered (Malaba and Wang, 2015). In this research work aligned rayon fibers were compressed to form sheets and then PFA resin was added. The composite was cured by mold compression with a fibers mass fraction ranging from 51 to 75%. First of all, the study of the laminate cracking behavior revealed the two materials to be compatible as a composite system but the matrix-fibers adhesion deteriorated at fibers fraction as high as 75 wt%. Moreover, for composite with not more than 64% fibers, the mechanical and thermal properties enhanced which make them a lighter substitute to glass fibers. Despite the long curing process and the pressure used, porosity in these composites was really high (38% for 51 wt% of fibers) which believed to be caused by steam bubbles during curing. The voids volume decreased when adding more fibers to reach 13%. In spite of the sustainability of this bio-based composite rayon fibers are artificial and not fully natural fibers and undergo a polluting production process which might harm the overall environmental impact of this composite. Bio-based nanocomposites of PFA and 2 wt% freeze-dried sisal whiskers were prepared by an in-situ polymerization method. After the dispersion of nanofibers by sonication a “resinification” was conducted at 85°C and then the composite was cured in open mold by gradually increasing curing temperature. The nanocomposite had improved viscoelastic properties by increasing the storage modulus of PFA. However, thermal stability studied by TGA was almost unchangeable compared to neat matrix (Ahmad et al., 2013). Recently, Menager et al. reported a first approach for preparing a fully bio-based composite using micro (50-200 µm) and macro (2-4 mm) particles of cork (Menager et al., 2019). PFA insured a good wetting of the empty cork cells which was observed by SEM images and also testified with lower water absorption. Moreover, cork incorporation enhanced thermal stability and improved the rigidity of the matrix by increasing the storage modulus. Tensile modulus and strength were optimized with 25 wt% added cork powder. In fact, cork powder over-performed cork granules by making the material more rigid owing to a higher density (storing more energy per unit of volume).

1.3.2.3 PFA and fillers

Among the most widely used fillers added to thermosetting resins, we can find carbon nanotubes (CNT) multi-walled (MWCNT), single-walled (SWCNT), or double-walled (DWCNT). These nanomaterials were also added to PFA to achieve different functions and properties. For instance, MWCNT with diameter distribution of 100-300 nm and length of about 10 µm were dispersed in PFA

resin with ultrasonication for 30 min. MWCNT concentration in the polymer ranged from 5 to 15 wt%. To characterize the resulting material, the PFA-MWCNT mixture along with an acidic curing agent was either poured in a plastic tray for the production of bulk specimens or in the doctor blade apparatus for the fabrication of film specimens. It was found that composites prepared with the doctor blade technique had a preferentially aligned MWCNT in the blading direction as clearly visible in field emission scanning electron microscope (FE-SEM) micrographs in Figure 1-27. Unsurprisingly, this alignment of the nanotubes caused an anisotropic electrical conductivity with an electrical conductivity parallel to the blading direction of 10^{-5} S/m which is 4 orders of magnitude higher than in the perpendicular direction and 6 orders of magnitude higher than the bulk specimen. However, this electrical conductivity in the two directions converged to the magnitude order as MWCNT concentration gets high (15 wt%). Furthermore, when using the doctor blade technique, there was a slight tilting of the nanotubes in film creating additional contacts between nanotubes resulting in higher electrical conductivities in the film than in the bulk (Lanticse et al., 2006).

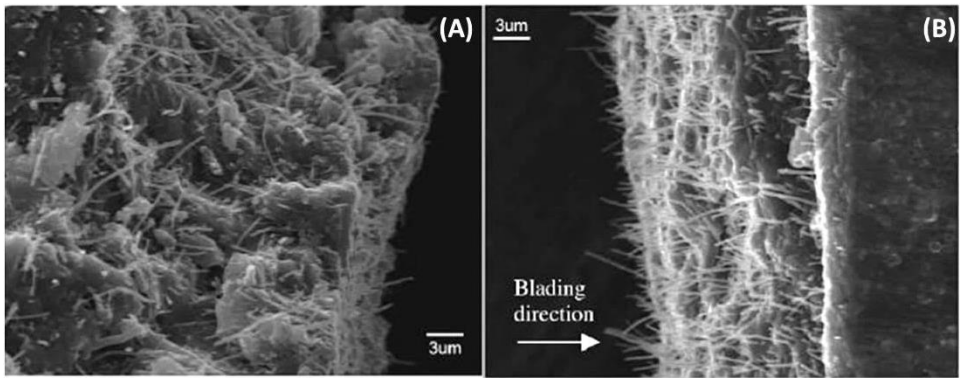

Figure 1-27: FE-SEM micrographs of the cross-sections of (A) bulk (B) the film viewed at the direction perpendicular to the blading direction (Lanticse et al., 2006).

Besides improving electrical conductivity, MWCNT were also used to improve the tribological properties of PFA composite coatings by mean of functionalization by grafting FA onto their surface. The used MWCNT had a diameter of 8 nm and length of 50 nm and they were first oxidized to obtain MWCNT-COOH then treated with thionyl chloride to obtain MWCNT-COCl which were treated with FA to finally obtain MWCNT-FA. After this grafting, it was found that the overall dispersion of these nanotubes was enhanced. It was also reported that the functionalization of the MWCNT reduced friction and anti-wear ability of the poly(furfuryl alcohol) composite coatings which were explained by the self-lubrication property of MWCNTs and the dispersion enhancement (X. H. Men et al., 2008). The same research group has also successfully modified MWCNT by perfluorooctanoic acid (PA) to obtain fluorocarbon-modified MWCNTs. PFA/MWCNT films were then prepared with a superhydrophobic surface. This hydrophobicity was attributed not only to the low surface energy of the fluorocarbon-modified MWCNTs but also to the roughness structures on the surfaces. This

hydrophobicity was confirmed with water contact angle and water sliding angle measurements. And the surface morphology was evaluated with FE-SEM (X.-H. Men et al., 2008).

Moreover, fully bio-based nanocomposites were prepared using PFA as a matrix and cellulose whisker and montmorillonite clay as nano-fillers. These nanocomposites were prepared by dispersing nanoparticles in FA then in-situ polymerized. The polymerization was catalyzed by the fillers because of their acidic character. These fillers improved the thermal stability of the plastic matrix. For instance, the addition of 0.8 wt% of cellulose whiskers increased the onset of degradation by 80°C while the addition of montmorillonite clay increased the residual weight above 400°C (Pranger and Tannenbaum, 2008). In another work later in 2021, the researchers confirmed the results of their first work and explained the better thermal stability of cellulose fillers as compared to montmorillonite clay by a stronger matrix–nanoparticles interaction. The same research group evaluated the mechanical properties of bio-based composites with added cellulose whiskers. This composite had a limited stiffness with an elastic modulus of about 1 GPa and over 30 MPa breaking strength (Pranger et al., 2012). In addition to organic nanoparticles, inorganic nanofillers were also used combined with PFA to yield a nanocomposite with high thermal stability. A hybrid material based on the dispersion of silica in PFA was prepared. The nanoparticles of silica were homogeneously dispersed in the furanic matrix which outputs an improvement of the T_g temperature and the overall thermal stability thanks to the confinement of furanic chains. By detecting and analyzing volatile organic compounds during thermal degradation, the authors proposed a multi-step degradation pathway for the neat PFA. According to their analysis, this degradation starts first by the scission of methylene and methyne links then at a higher temperature the scission of the furanic links starts (Guigo et al., 2009).

An overview of the composites developed with PFA highlighting their mechanical and thermal properties is presented in Table 1-8. According to this data, one can notice that PFA has been mainly coupled either with CNT or with different classes of natural non-wood fibers such as flax, sisal, and bamboo. These composites were manufactured using different methods but compression is always applied and if not PFA was used to produce thin films pobably due to high porosity content which this resin can generate when manufacturing bulk structures. In terms of mechanical properties, it was reported that the neat PFA has a stiffness below 1 GPa (tensile mode) and tensile strength of about 10 MPa (Deka et al., 2013; Kherroub et al., 2015). After the addition of continuous reinforcing phase, for instance, aligned flax fiber woven textile, the stiffness of the resulting composite reached a value of 25 GPa and its strength attained 211 MPa. However, when adding discontinuous filler we notice a limited improvement in Young's modulus which remains under 2 GPa but a considerable

improvement in the strength of about 400% compared to the neat polymer. In terms of thermal properties, the results can be quite dispersed depending on the used polymer and filler with a T_g ranging from 80°C to over 130°C and a storage modulus over 1 GPa at 160°C in some cases. The addition of some of these fillers (especially nanoparticles) served to confer the polymer with new properties such as electrical conductivity, long wear life, and superhydrophobic surface.

Table 1-8: A summary of research work on PFA-based composites and their mechanical and thermal properties.

Composite	Manufacturing	Mechanical properties	Thermal properties	Functionality	Reference
25 to 40% silica (removed after pyrolysis) in PFA	Cured at 120°C for 2 h then carbonized at rate 2.5 °C/min to 800°C under N_2 flow.	N.A	N.A	Mesoporous carbon	(Kawashima et al., 2000)
50 wt% Flax fibers mat and PFA	Compression molding under 2.2 MPa at 150°C	Young's modulus= 12.2 GPa Rupture strength= 95 MPa	Storage modulus= 1 GPa at 160°C Tg= 105°C	N.A	(Toriz et al., 2003)
5 to 15 wt% of MWCNT in PFA	Open-air curing at 60°C and post-curing at 160°C	N.A	N.A	Electric conductivity 10^{-5} S/m at 5 wt% and 10 S/m at 15 wt%	(Lanticse et al., 2006)
fluorocarbon-modified MWNTs and PFA	Spray and film curing at 70, 120, and 180°C for 3 h	N.A	N.A	superhydrophobic surfaces	(X. H. Men et al., 2008)

Composite	Manufacturing	Mechanical properties	Thermal properties	Functionality	Reference
0.8 wt% MWCNT-FA in PFA	Spray coating and curing at 70°C for 12 h, at 120°C for 1 h and 170°C for 1 h	N.A	N.A	Long wear life and low friction coefficient	(X.-H. Men et al., 2008)
Furan/ 60 wt% flax fibers mat	Vacuum bag applied to the prepregs then cured in an oven for 15 minutes at 150°C.	Young's modulus= 8.5 GPa Tensile strength= 64 MPa	N.A	N.A	(Giannis et al., 2008)
About 20% Silica in PFA	Open air molding at 160°C for 2 h	Storage modulus=1 GPa at 25°C	Char residue at 700°C >60 wt% Storage modulus= 0.1 GPa at 160°C Tg= 130°C (80°C neat PFA)	N.A	(Guigo et al., 2009)
57 wt% Flax fibers non-woven and PFA	Compression molding of prepregs under 2 MPa pressure at 150°C	Young's modulus= 9 GPa Rupture strength= 48 MPa	The burning rate of 22 mm/min	N.A	(Pohl et al., 2011)
0.75 wt% Cellulose whiskers and PFA	Open-air film curing at 130°C for 75 min and then at 210°C for 105 min	Young's modulus= 1 GPa Rupture strength= 32 MPa	Char residue at 800°C 50 wt%	N.A	(Pranger et al., 2012)nger et al., 2012)

Composite	Manufacturing	Mechanical properties	Thermal properties	Functionality	Reference
Aligned flax fiber woven textile and PFA prepeg	Compression molding of prepreg at 140°C	Young's modulus= 25 GPa Tensile strength= 211 MPa	N.A	N.A	(Crossley et al., 2012)
2 wt% freeze-dried sisal whisker in PFA	Open-air molding at 70°C, 100°C and 150°C	Storage modulus= 2.1 GPa at 25°C (1.4 GPa neat PFA)	50 wt% chat residue at 800°C Tg= 70°C (75°C neat PFA) Storge modulus= 10 MPa (6 MPa neat PFA)	N.A	(Ahmad et al., 2013)
20 wt% bleached kenaf fibers with PFA	Compression molding under 7 MPa pressure at 60°C for 4 h, 80°C for 4 h at 110°C for 1 h	Young's modulus= 1.25 GPa (Neat PFA 0.75 GPa) Flexural modulus= 4.6 GPa Tensile strength= 42 MPa (Neat PFA 10 MPa) Impact strength= 60 J/m	Storage modulus= 0.5 GPa at 150°C Tg= 95°C Char residue at 800°C 45 wt% (55 wt% neat PFA)	N.A	(Deka et al., 2013)

Composite	Manufacturing	Mechanical properties	Thermal properties	Functionality	Reference
64 wt% High tenacity rayon with PFA	Sheets of aligned fibers wetted with PFA and molded by compression under 10 MPa and for 31 h	Young's modulus= 5.5 GPa Tensile strength= 120 MPa Flexural modulus= 5.9 GPa Flexural strength= 75 MPa	Tg=122°C (90°C Neat PFA) Storage modulus= 1.5 GPa at 160°C (Neat PFA 0.3 GPa) 35 wt% Char residue at 600°C	N.A	(Malaba and Wang, 2015)
PFA resin or PFA microspheres with 1 wt% graphene oxide	Laser-Induced Carbonization	N.A	55 wt% char residue at 800°C	Conductive material with a sheet resistance of 13 Ω/sq/ Supercapacitor with a capacitance of 16.0 mF/cm² at 0.05 mA/cm².	(Hawes et al., 2019)
Up to 50 wt% FA reinforcing MFC-L gel	Freeze-drying for a porous material	Compression modulus= 1 MPa Compression strength= 0.21 MPa	20 wt% char residue at 800°C	Foams for thermal insulation and packaging Applications.	(Lems et al., 2019)

Composite	Manufacturing	Mechanical properties	Thermal properties	Functionality	Reference
25 wt% of cork powder (50-200 µm) and PFA	Compression molding under 1 MPa pressure at 160°C	Young's modulus= 180 MPa Tensile strength= 6.5 MPa	Storage modulus= 0.8 GPa at 160°C	N.A	(Menager et al., 2019)
Up to 30 wt% FA reinforcing bamboo fibers	Impregnation under pressure followed by curing at 120°C for 5 h	Modulus of elastic= 6 GPa Modulus of rupture= 15 GPa	20 wt% char residue at 800°C	N.A	(Wang et al., 2019c)

1.3.2.4 How green is PFA?

Although it is true that PFA is a fully renewable and bio-based resin, the production of furfural and FA, as already explained, seems to be an energy-consuming process and generating polluting wastes. One cannot abstain from considering the actual environmental impact of such production. In 2015 a life Assessment Analysis (LCA) was conducted to quantify the impact of furfural and furfuryl alcohol production from corncob by identifying the main pollution processes and substances (Hong et al., 2015). According to this LCA, the corncob production, transport, and electricity consumption stages had the greatest impact on the environment because of direct heavy metal, phosphate, and phosphorus emissions. After data analysis, the authors suggest increasing furfural yield, optimizing wastewater and electricity consumption efficiencies, and decreasing corncob transport distance for more cost-effective and eco-friendly production. A comparative LCA study between a PFA-based composite and a fossil-based matrix using natural fibers for reinforcement would be interesting to compare the real environmental impact enhancement of the use of this kind of bio-based resins.

1.3.3 Conclusions

In short, furfural is a cheap and sustainable utility chemical. Its manufacturing is simple and calls upon large variety agriculture wastes available in every part of the world. This chemical is described

by David Win Tin as “Gold from Garbage (Win, 2005). Furfural is mostly used to produce furfuryl alcohol used in various applications in different fields. The production of bio-based composites is among these applications. When combined with natural fibers and fillers this polymer can yield a fully green composite and one can find many examples in the literature. However, compared with this polymer benefits, its use in composites stays humble. The reason behind this poor exploitation might be the unclear understanding of its curing process during which many defects can occur such as voids creation. Nevertheless, this polymer confers excellent properties sought-after in composites such as thermal stability, low smoke release, fire resistance, and resistance to chemical attacks.

1.4 Chapter Conclusions

To conclude, composites are interesting materials used in many sectors which can be engineered according to their final use by selecting the adapted matrix and fillers. As environmental concerns are increasing and the fossil resources are dwelling, the need for more eco-friendly and sustainable materials starts to be a priority for their futur use. Many research projects have been conducted to replace the synthetic fibers and plastic usually used in composite production with natural feedstocks such as biomass. Despite the promising enhancement in mechanical properties of the composites, many challenges were faced when using natural fibers such as poor fiber/matrix adhesion, humidity sensitivity, and high porosity. Recently, various research works are being done for composite production using innovative additive manufacturing technology. The majority of these printed composites were produced using the fused filament fabrication by blending thermoplastics with continuous or short fiber. This technique enabled a rather simple way for composite printing but the matrices choice is limited to thermoplastics. Thermoplastic printed composites had greater mechanical properties in respect to the neat polymers used in FFF (until x50 better) but their thermal properties remain limited to the matrix thermal stability which can rarely be used under temperature exceeding 100°C. Although some printing filament with high thermal stability exit on the markets they are usually overpriced and skill-demanding.

To overcome these limits, composites using thermosets polymers were printed with the DIW technique by tuning the rheology with nano and macroparticles. These thermosetting composites exhibited higher thermal properties and significant mechanical properties enhancement. However, the most used polymers were petroleum-based and non-sustainable. A schematic summary of the state of art presented in this chapter is presented in Figure 1-28.

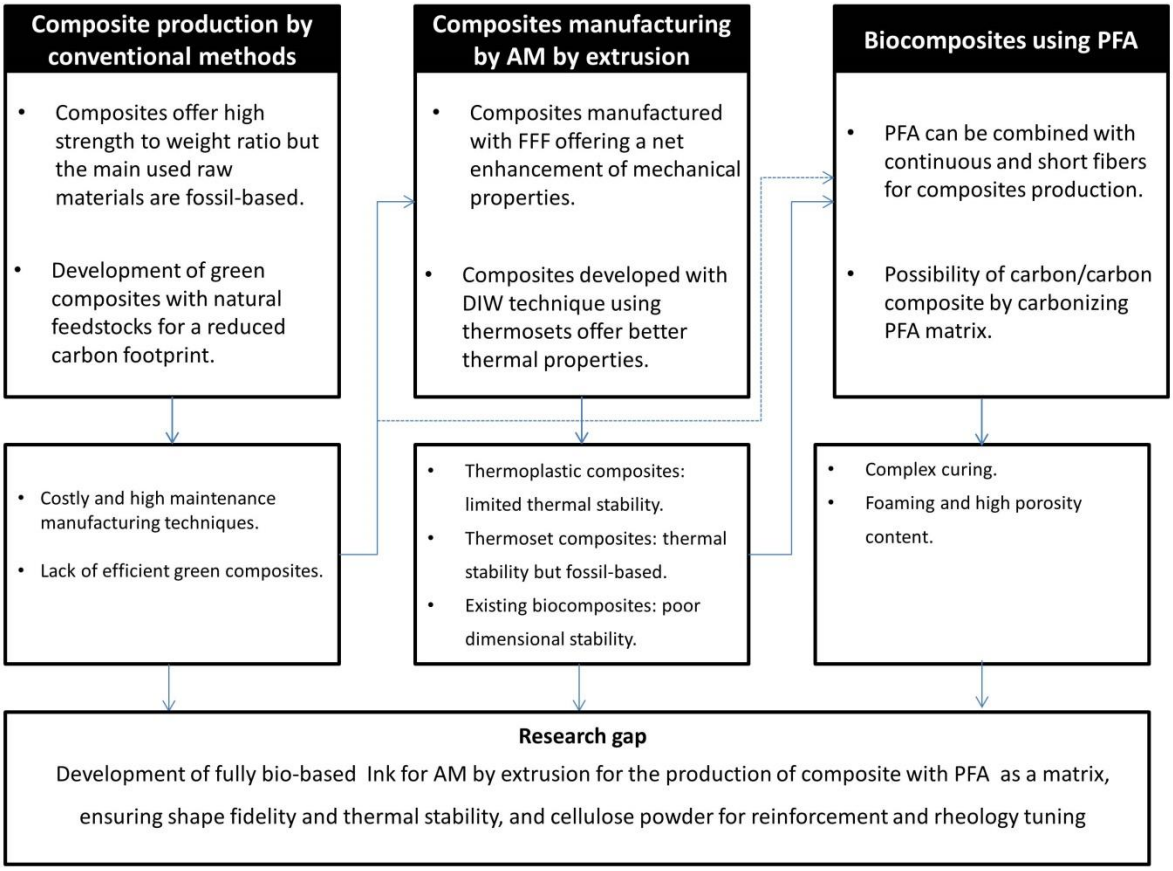

Figure 1-28: State of the art: key facts and limitations.

1.5 References

Abdul Khalil, H.P.S., Bhat, A.H., Ireana Yusra, A.F., 2012. Green composites from sustainable cellulose nanofibrils: A review. Carbohydr. Polym. 87, 963–979. https://doi.org/10.1016/j.carbpol.2011.08.078

Abouzeid, R.E., Khiari, R., Beneventi, D., Dufresne, A., 2018. Biomimetic Mineralization of Three-Dimensional Printed Alginate/TEMPO-Oxidized Cellulose Nanofibril Scaffolds for Bone Tissue Engineering. Biomacromolecules 19, 4442–4452. https://doi.org/10.1021/acs.biomac.8b01325

Agarwala, M.K., Jamalabad, V.R., Langrana, N.A., Safari, A., Whalen, P.J., Danforth, S.C., 1996. Structural quality of parts processed by fused deposition. Rapid Prototyp. J. 2, 4–19. https://doi.org/10.1108/13552549610732034

Ahmad, E.E.M., Luyt, A.S., Djoković, V., 2013. Thermal and dynamic mechanical properties of bio-based poly(furfuryl alcohol)/sisal whiskers nanocomposites. Polym. Bull. 70, 1265–1276. https://doi.org/10.1007/s00289-012-0847-2

Akil, H.M., Omar, M.F., Mazuki, A.A.M., Safiee, S., Ishak, Z.A.M., Abu Bakar, A., 2011. Kenaf fiber reinforced composites: A review. Mater. Des. 32, 4107–4121. https://doi.org/10.1016/j.matdes.2011.04.008

Alafaghani, A., Qattawi, A., Alrawi, B., Guzman, A., 2017. Experimental Optimization of Fused Deposition Modelling Processing Parameters: A Design-for-Manufacturing Approach. Procedia Manuf., 45th SME North American Manufacturing Research Conference, NAMRC 45, LA, USA 10, 791–803. https://doi.org/10.1016/j.promfg.2017.07.079

Alves, C., Ferrão, P.M.C., Silva, A.J., Reis, L.G., Freitas, M., Rodrigues, L.B., Alves, D.E., 2010. Ecodesign of automotive components making use of natural jute fiber composites. J. Clean. Prod. 18, 313–327. https://doi.org/10.1016/j.jclepro.2009.10.022

Angelopoulos, P.M., Samouhos, M., Taxiarchou, M., 2021. Functional fillers in composite filaments for fused filament fabrication; a review. Mater. Today Proc., International Conferences & Exhibition on Nanotechnologies, Organic Electronics & Nanomedicine 37, 4031–4043. https://doi.org/10.1016/j.matpr.2020.07.069

Anitha, R., Arunachalam, S., Radhakrishnan, P., 2001. Critical parameters influencing the quality of prototypes in fused deposition modelling. J. Mater. Process. Technol., part 1: containing papers presented at international conference on advances in materials processing technology 118, 385–388. https://doi.org/10.1016/S0924-0136(01)00980-3

Averous, L., Boquillon, N., 2004. Biocomposites based on plasticized starch: thermal and mechanical behaviours. Carbohydr. Polym. 56, 111–122. https://doi.org/10.1016/j.carbpol.2003.11.015

Bagheri, Z.S., El Sawi, I., Schemitsch, E.H., Zdero, R., Bougherara, H., 2013. Biomechanical properties of an advanced new carbon/flax/epoxy composite material for bone plate applications. J. Mech. Behav. Biomed. Mater. 20, 398–406. https://doi.org/10.1016/j.jmbbm.2012.12.013

Balasubramanian, K., Sultan, M.T.H., Rajeswari, N., 2018. Manufacturing techniques of composites for aerospace applications, in: Sustainable Composites for Aerospace Applications. Elsevier, pp. 55–67. https://doi.org/10.1016/B978-0-08-102131-6.00004-9

Barsberg, S., Thygesen, L.G., 2009. Poly(furfuryl alcohol) formation in neat furfuryl alcohol and in cymene studied by ATR-IR spectroscopy and density functional theory (B3LYP) prediction of vibrational bands. Vib. Spectrosc. 49, 52–63. https://doi.org/10.1016/j.vibspec.2008.04.013

Ben, G., Kihara, Y., Nakamori, K., Aoki, Y., 2007. Examination of heat resistant tensile properties and molding conditions of green composites composed of kenaf fibers and PLA resin. Adv. Compos. Mater. 16, 361–376. https://doi.org/10.1163/156855107782325203

Berchon, M., Luyt, B., 2014. L'impression 3D Ed. 2. Eyrolles.

Berretta, S., Davies, R., Shyng, Y.T., Wang, Y., Ghita, O., 2017. Fused Deposition Modelling of high temperature polymers: Exploring CNT PEEK composites. Polym. Test. 63, 251–262. https://doi.org/10.1016/j.polymertesting.2017.08.024

Biron, M., 2018. Chapter 6 - Thermoplastic Composites, in: Biron, M. (Ed.), Thermoplastics and Thermoplastic Composites (Third Edition), Plastics Design Library. William Andrew Publishing, pp. 821–882. https://doi.org/10.1016/B978-0-08-102501-7.00006-0

Bodros, E., Pillin, I., Montrelay, N., Baley, C., 2007. Could biopolymers reinforced by randomly scattered flax fibre be used in structural applications? Compos. Sci. Technol. 67, 462–470. https://doi.org/10.1016/j.compscitech.2006.08.024

Buchwalter, S.L., 1985. The polymerization of furfuryl acetate in acetonitrile. J. Polym. Sci. Polym. Chem. Ed. 23, 2897–2911. https://doi.org/10.1002/pol.1985.170231202

Caminero, M.Á., Chacón, J.M., García-Plaza, E., Núñez, P.J., Reverte, J.M., Becar, J.P., 2019. Additive Manufacturing of PLA-Based Composites Using Fused Filament Fabrication: Effect of Graphene Nanoplatelet Reinforcement on Mechanical Properties, Dimensional Accuracy and Texture. Polymers 11, 799. https://doi.org/10.3390/polym11050799

Cantwell, W.J., Morton, J., 1991. The impact resistance of composite materials — a review. Composites 22, 347–362. https://doi.org/10.1016/0010-4361(91)90549-V

Carneiro, O.S., Silva, A.F., Gomes, R., 2015. Fused deposition modeling with polypropylene. Mater. Des. 83, 768–776. https://doi.org/10.1016/j.matdes.2015.06.053

Çeçen, V., Sarikanat, M., Yildiz, H., Tavman, I.H., 2008. Comparison of mechanical properties of epoxy composites reinforced with stitched glass and carbon fabrics: Characterization of mechanical anisotropy in composites and investigation on the interaction between fiber and epoxy matrix. Polym. Compos. 29, 840–853. https://doi.org/10.1002/pc.20458

Centi, G., Perathoner, S., 2013. Chapter 16 - Catalytic Transformation of CO2 to Fuels and Chemicals, with Reference to Biorefineries, in: Triantafyllidis, K.S., Lappas, A.A., Stöcker, M. (Eds.), The Role of Catalysis for the Sustainable Production of Bio-Fuels and Bio-Chemicals. Elsevier, Amsterdam, pp. 529–555. https://doi.org/10.1016/B978-0-444-56330-9.00016-4

Chacón, J.M., Caminero, M.A., García-Plaza, E., Núñez, P.J., 2017. Additive manufacturing of PLA structures using fused deposition modelling: Effect of process parameters on mechanical properties and their optimal selection. Mater. Des. 124, 143–157. https://doi.org/10.1016/j.matdes.2017.03.065

Chandrasekar, M., Ishak, M.R., Sapuan, S.M., Leman, Z., Jawaid, M., 2017. A review on the characterisation of natural fibres and their composites after alkali treatment and water

absorption. Plast. Rubber Compos. 46, 119–136. https://doi.org/10.1080/14658011.2017.1298550

Chandrasekaran, S., B. Duoss, E., A. Worsley, M., P. Lewicki, J., 2018. 3D printing of high performance cyanate ester thermoset polymers. J. Mater. Chem. A 6, 853–858. https://doi.org/10.1039/C7TA09466C

Charles W, H., 1989. Priority to US06638905. US4575330B1.

Chen, H.-L., Porter, R.S., 1994. Composite of polyethylene and kenaf, a natural cellulose fiber. J. Appl. Polym. Sci. 54, 1781–1783. https://doi.org/10.1002/app.1994.070541121

Chen, P.-Y., Lian, H.-Y., Shih, Y.-F., Chen-Wei, S.-M., Jeng, R.-J., 2017. Preparation, characterization and crystallization kinetics of Kenaf fiber/multi-walled carbon nanotube/polylactic acid (PLA) green composites. Mater. Chem. Phys. 196, 249–255. https://doi.org/10.1016/j.matchemphys.2017.05.006

Choura, M., Belgacem, N.M., Gandini, A., 1996. Acid-Catalyzed Polycondensation of Furfuryl Alcohol: Mechanisms of Chromophore Formation and Cross-Linking. Macromolecules 29, 3839–3850. https://doi.org/10.1021/ma951522f

Chuang, I.S., Maciel, G.E., Myers, G.E., 1984. Carbon-13 NMR study of curing in furfuryl alcohol resins. Macromolecules 17, 1087–1090. https://doi.org/10.1021/ma00135a019

Compton, B., 2015. 3D printing of composites with controlled architecture 30.

Compton, B.G., Hmeidat, N.S., Pack, R.C., Heres, M.F., Sangoro, J.R., 2018. Electrical and Mechanical Properties of 3D-Printed Graphene-Reinforced Epoxy. JOM 70, 292–297. https://doi.org/10.1007/s11837-017-2707-x

Conley, R.T., Metil, I., 1963. An investigation of the structure of furfuryl alcohol polycondensates with infrared spectroscopy. J. Appl. Polym. Sci. 7, 37–52. https://doi.org/10.1002/app.1963.070070104

Coroller, G., Lefeuvre, A., Le Duigou, A., Bourmaud, A., Ausias, G., Gaudry, T., Baley, C., 2013. Effect of flax fibres individualisation on tensile failure of flax/epoxy unidirectional composite. Compos. Part Appl. Sci. Manuf. 51, 62–70. https://doi.org/10.1016/j.compositesa.2013.03.018

Corrales, F., Vilaseca, F., Llop, M., Gironès, J., Méndez, J.A., Mutjè, P., 2007. Chemical modification of jute fibers for the production of green-composites. J. Hazard. Mater., " Selected papers of the proceedings of the 5th European Meeting on Chemical Industry and Environment, EMChIE 2006 " held in Vienna, Austria, 3-5 May 2006 144, 730–735. https://doi.org/10.1016/j.jhazmat.2007.01.103

Croccolo, D., De Agostinis, M., Olmi, G., 2013. Experimental characterization and analytical modelling of the mechanical behaviour of fused deposition processed parts made of ABS-M30. Comput. Mater. Sci. 79, 506–518. https://doi.org/10.1016/j.commatsci.2013.06.041

Crossley, R.J., Schubel, P.J., Stevenson, A., Moreira, M., 2012. The development and processing of a sustainable fully bio derived polyfurfuryl alcohol matrix flax fibre prepreg 8.

Dashtban, M., 2012. PRODUCTION OF FURFURAL: OVERVIEW AND CHALLENGES. J--J. Sci. Technol. For. Prod. Process. 2, 44–53.

Deka, H., Misra, M., Mohanty, A., 2013. Renewable resource based “all green composites” from kenaf biofiber and poly(furfuryl alcohol) bioresin. Ind. Crops Prod. 41, 94–101. https://doi.org/10.1016/j.indcrop.2012.03.037

Deng, X., Zeng, Z., Peng, B., Yan, S., Ke, W., 2018. Mechanical Properties Optimization of Poly-Ether-Ether-Ketone via Fused Deposition Modeling. Materials 11, 216. https://doi.org/10.3390/ma11020216

Dickson, A.N., Barry, J.N., McDonnell, K.A., Dowling, D.P., 2017. Fabrication of continuous carbon, glass and Kevlar fibre reinforced polymer composites using additive manufacturing. Addit. Manuf. 16, 146–152. https://doi.org/10.1016/j.addma.2017.06.004

Dittenber, D.B., GangaRao, H.V.S., 2012. Critical review of recent publications on use of natural composites in infrastructure. Compos. Part Appl. Sci. Manuf. 43, 1419–1429. https://doi.org/10.1016/j.compositesa.2011.11.019

Doroudgarian, N., 2016. High performance bio-based composites : mechanical and environmental durability. TDX Tesis Dr. En Xarxa.

Dunlop, A.P., Peters, F.N., 1953. The furans. Reinhold Publishing Corporation, New York.

Elkington, M., Bloom, D., Ward, C., Chatzimichali, A., Potter, K., 2015. Hand layup: understanding the manual process. Adv. Manuf. Polym. Compos. Sci. 1, 138–151. https://doi.org/10.1080/20550340.2015.1114801

Falco, G., Guigo, N., Vincent, L., Sbirrazzuoli, N., 2018. Opening Furan for Tailoring Properties of Bio-based Poly(Furfuryl Alcohol) Thermoset. ChemSusChem 11, 1805–1812. https://doi.org/10.1002/cssc.201800620

Favier, V., Canova, G.R., Cavaillé, J.Y., Chanzy, H., Dufresne, A., Gauthier, C., 1995. Nanocomposite materials from latex and cellulose whiskers. Polym. Adv. Technol. 6, 351–355. https://doi.org/10.1002/pat.1995.220060514

Feilden, E., 2017. Additive Manufacturing of Ceramics and Ceramic Composites via Robocasting. https://doi.org/10.13140/RG.2.2.29343.25765

Ferreira, R.T.L., Amatte, I.C., Dutra, T.A., Bürger, D., 2017. Experimental characterization and micrography of 3D printed PLA and PLA reinforced with short carbon fibers. Compos. Part B Eng. 124, 88–100. https://doi.org/10.1016/j.compositesb.2017.05.013

Fink, J.K., 2013. Chapter 7 - Furan Resins, in: Fink, J.K. (Ed.), Reactive Polymers Fundamentals and Applications (Second Edition), Plastics Design Library. William Andrew Publishing, Oxford, pp. 203–215. https://doi.org/10.1016/B978-1-4557-3149-7.00007-3

Frizelle, W.G., 2016. Injection Molding Technology. pp. 191–202. https://doi.org/10.1016/B978-0-323-39040-8.00010-9

Games, K., 1985. Wood. Chemistry, Ultrastructure, Reactions. Von D. Fengel und G. Wegener. de Gruyter, Berlin 1984. X111, 613 S., geb. DM 245.00. – ISBN 3-11-008481-3. Angew. Chem. 97, 361–361. https://doi.org/10.1002/ange.19850970446

Gandini, A., 1997. Furans in polymer chemistry. Prog. Polym. Sci. 22, 1203–1379. https://doi.org/10.1016/S0079-6700(97)00004-X

Giannis, S., Arnold, E., Hoydonckx, H.E., Weager, B.M., Martin, R.H., 2008. Development of high performance bio-composites based on furan bio-resins for vehicle panels. 13th Eur. Conf. Compos. Mater. 10.

Gibson, I., Rosen, D.W., Stucker, B., 2010. Sheet Lamination Processes, in: Gibson, I., Rosen, D.W., Stucker, B. (Eds.), Additive Manufacturing Technologies: Rapid Prototyping to Direct Digital Manufacturing. Springer US, Boston, MA, pp. 223–252. https://doi.org/10.1007/978-1-4419-1120-9_8

Godoi, F.C., Prakash, S., Bhandari, B.R., 2016. 3d printing technologies applied for food design: Status and prospects. J. Food Eng. 179, 44–54. https://doi.org/10.1016/j.jfoodeng.2016.01.025

Goldstein, I., Dreher, W., 1960. Stable Furfuryl Alcohol Impregnating Solutions. Ind. Eng. Chem. 52, 57–58. https://doi.org/10.1021/ie50601a039

Gonçalves, J., Lima, P., Krause, B., Pötschke, P., Lafont, U., Gomes, J.R., Abreu, C.S., Paiva, M.C., Covas, J.A., 2018. Electrically Conductive Polyetheretherketone Nanocomposite Filaments: From Production to Fused Deposition Modeling. Polymers 10, 925. https://doi.org/10.3390/polym10080925

Grand view research, 2020. Global Furfuryl Alcohol Market Size Report, 2020-2027 [WWW Document]. URL https://www.grandviewresearch.com/industry-analysis/furfuryl-alcohol-market (accessed 5.12.21).

Guigo, N., Mija, A., Vincent, L., Sbirrazzuoli, N., 2007. Chemorheological analysis and model-free kinetics of acid catalysed furfuryl alcohol polymerization. Phys. Chem. Chem. Phys. 9, 5359–5366. https://doi.org/10.1039/B707950H

Guigo, N., Mija, A., Zavaglia, R., Vincent, L., Sbirrazzuoli, N., 2009. New insights on the thermal degradation pathways of neat poly(furfuryl alcohol) and poly(furfuryl alcohol)/SiO2 hybrid materials. Polym. Degrad. Stab. 94, 908–913. https://doi.org/10.1016/j.polymdegradstab.2009.03.008

Haddout, A., n.d. Cours Les Matériaux composites à matrices polymériques 76.

Håkansson, K.M.O., Henriksson, I.C., Vázquez, C. de la P., Kuzmenko, V., Markstedt, K., Enoksson, P., Gatenholm, P., 2016. Solidification of 3D Printed Nanofibril Hydrogels into Functional 3D Cellulose Structures. Adv. Mater. Technol. 1, 1600096. https://doi.org/10.1002/admt.201600096

Han, W., Jafari, M.A., Seyed, K., 2003. Process speeding up via deposition planning in fused deposition-based layered manufacturing processes. Rapid Prototyp. J. 9, 212–218. https://doi.org/10.1108/13552540310489596

Han, X., Yang, D., Yang, C., Spintzyk, S., Scheideler, L., Li, P., Li, D., Geis-Gerstorfer, J., Rupp, F., 2019. Carbon Fiber Reinforced PEEK Composites Based on 3D-Printing Technology for Orthopedic and Dental Applications. J. Clin. Med. 8, 240. https://doi.org/10.3390/jcm8020240

Hao, W., Liu, Y., Zhou, H., Chen, H., Fang, D., 2018. Preparation and characterization of 3D printed continuous carbon fiber reinforced thermosetting composites. Polym. Test. 65, 29–34. https://doi.org/10.1016/j.polymertesting.2017.11.004

Hashemi, F., Tahir, P.M., Madsen, B., Jawaid, M., Majid, D., Brancheriau, L., Juliana, A., 2016. Volumetric composition and shear strength evaluation of pultruded hybrid kenaf/glass fiber composites. J. Compos. Mater. 50, 2291–2303. https://doi.org/10.1177/0021998315602948

Hawes, G.F., Yilman, D., Noremberg, B.S., Pope, M.A., 2019. Supercapacitors Fabricated via Laser-Induced Carbonization of Biomass-Derived Poly(furfuryl alcohol)/Graphene Oxide Composites. ACS Appl. Nano Mater. 2, 6312–6324. https://doi.org/10.1021/acsanm.9b01284

He, J.-X., Tan, W.-L., Han, Q.-M., Cui, S.-Z., Shao, W., Sang, F., 2016. Fabrication of silk fibroin/cellulose whiskers–chitosan composite porous scaffolds by layer-by-layer assembly for application in bone tissue engineering. J. Mater. Sci. 51, 4399–4410. https://doi.org/10.1007/s10853-016-9752-7

Hmeidat, N.S., Pack, R.C., Talley, S.J., Moore, R.B., Compton, B.G., 2020. Mechanical anisotropy in polymer composites produced by material extrusion additive manufacturing. Addit. Manuf. 34, 101385. https://doi.org/10.1016/j.addma.2020.101385

Hölzl, K., Lin, S., Tytgat, L., Vlierberghe, S.V., Gu, L., Ovsianikov, A., 2016. Bioink properties before, during and after 3D bioprinting. Biofabrication 8, 032002. https://doi.org/10.1088/1758-5090/8/3/032002

Hong, Jingmin, Zhou, J., Hong, Jinglan, 2015. Environmental and economic impact of furfuralcohol production using corncob as a raw material. Int. J. Life Cycle Assess. 20, 623–631. https://doi.org/10.1007/s11367-015-0854-2

Horvath, J., 2014. Mastering 3D Printing. Apress. https://doi.org/10.1007/978-1-4842-0025-4

Ilcewicz, L.B., Keary, P.E., Trostle, J., 1988. Interlaminar fracture toughness testing of composite mode I and mode II DCB specimens. Polym. Eng. Sci. 28, 592–604. https://doi.org/10.1002/pen.760280908

Iroegbu, A.O., Hlangothi, S.P., 2018. Effects of the Type of Catalyst on the Polymerisation Mechanism of Furfuryl Alcohol and its Resultant Properties. Chem. Afr. 1, 187–197. https://doi.org/10.1007/s42250-018-0017-5

Istasse, T., Richel, A., 2020. Mechanistic aspects of saccharide dehydration to furan derivatives for reaction media design. RSC Adv. 10, 23720–23742. https://doi.org/10.1039/D0RA03892J

Jones, R.M., 1998. Mechanics Of Composite Materials. CRC Press.

Kabir, S.M.F., Mathur, K., Seyam, A.-F.M., 2020. A critical review on 3D printed continuous fiber-reinforced composites: History, mechanism, materials and properties. Compos. Struct. 232, 111476. https://doi.org/10.1016/j.compstruct.2019.111476

Kalpakjian, S., Schmid, S.R., 2002. Manufactura, ingeniería y tecnología. Pearson Educación.

Kamran, M., Saxena, A., 2016. A Comprehensive Study on 3D Printing Technology 6, 6.

Kaplan, D.L. (Ed.), 1998. Biopolymers from Renewable Resources, Macromolecular Systems - Materials Approach. Springer-Verlag, Berlin Heidelberg. https://doi.org/10.1007/978-3-662-03680-8

Kariz, M., Sernek, M., Kuzman, M.K., 2016. Use of wood powder and adhesive as a mixture for 3D printing. Eur. J. Wood Wood Prod. 74, 123–126. https://doi.org/10.1007/s00107-015-0987-9

Kawashima, D., Aihara, T., Kobayashi, Y., Kyotani, T., Tomita, A., 2000. Preparation of Mesoporous Carbon from Organic Polymer/Silica Nanocomposite. Chem. Mater. 12, 3397–3401. https://doi.org/10.1021/cm000435l

Khan, M.A., Ali, K.M.I., Hinrichsen, G., Kopp, C., Kropke, S., 1999. Study on Physical and Mechanical Properties of Biopol-Jute Composite. Polym.-Plast. Technol. Eng. 38, 99–112. https://doi.org/10.1080/03602559909351562

Kim, T., Assary, R.S., Kim, H., Marshall, C.L., Gosztola, D.J., Curtiss, L.A., Stair, P.C., 2013. Effects of solvent on the furfuryl alcohol polymerization reaction: UV Raman spectroscopy study. Catal. Today, Operando IV: The 4th International Congress on Operando Spectroscopy 205, 60–66. https://doi.org/10.1016/j.cattod.2012.09.033

Klar, V., Pere, J., Turpeinen, T., Kärki, P., Orelma, H., Kuosmanen, P., 2019. Shape fidelity and structure of 3D printed high consistency nanocellulose. Sci. Rep. 9, 3822. https://doi.org/10.1038/s41598-019-40469-x

Klift, F.V.D., Koga, Y., Todoroki, A., Ueda, M., Hirano, Y., Matsuzaki, R., 2016. 3D Printing of Continuous Carbon Fibre Reinforced Thermo-Plastic (CFRTP) Tensile Test Specimens. Open J. Compos. Mater. 06, 18. https://doi.org/10.4236/ojcm.2016.61003

Krajangsawasdi, N., Blok, L.G., Hamerton, I., Longana, M.L., Woods, B.K.S., Ivanov, D.S., 2021. Fused Deposition Modelling of Fibre Reinforced Polymer Composites: A Parametric Review. J. Compos. Sci. 5, 29. https://doi.org/10.3390/jcs5010029

Krishna, K.V., Kanny, K., 2016. The effect of treatment on kenaf fiber using green approach and their reinforced epoxy composites. Compos. Part B Eng. 104, 111–117. https://doi.org/10.1016/j.compositesb.2016.08.010

Kulkarni, S.G., Bagalkote, V.S., Patil, S.S., Kumar, U.P., Kumar, V.A., 2009. Theoretical Evaluation and Experimental Validation of Performance Parameters of New Hypergolic Liquid Fuel Blends with Red Fuming Nitric Acid as Oxidizer. Propellants Explos. Pyrotech. 34, 520–525. https://doi.org/10.1002/prep.200800061

Kung, C., Kuan, H.-C., Kuan, C.-F., 2018. Evaluation of tensile strength of 3D printed objects with FDM process on RepRap platform, in: 2018 1st IEEE International Conference on Knowledge Innovation and Invention (ICKII). Presented at the 2018 1st IEEE International Conference on Knowledge Innovation and Invention (ICKII), pp. 369–372. https://doi.org/10.1109/ICKII.2018.8569166

Kuznetsov, V.E., Tavitov, A.G., Urzhumtcev, O.D., 2019. Hardware Factors Influencing Interlayer Bonding Strength of Parts Obtained by Fused Filament Fabrication. https://doi.org/10.20944/preprints201905.0108.v1

La Mantia, F.P., Morreale, M., 2011. Green composites: A brief review. Compos. Part Appl. Sci. Manuf. 42, 579–588. https://doi.org/10.1016/j.compositesa.2011.01.017

Lande, S., Eikenes, M., Westin, M., Schneider, M.H., 2008. Furfurylation of Wood: Chemistry, Properties, and Commercialization, in: Development of Commercial Wood Preservatives, ACS Symposium Series. American Chemical Society, pp. 337–355. https://doi.org/10.1021/bk-2008-0982.ch020

Lanticse, L.J., Tanabe, Y., Matsui, K., Kaburagi, Y., Suda, K., Hoteida, M., Endo, M., Yasuda, E., 2006. Shear-induced preferential alignment of carbon nanotubes resulted in anisotropic electrical conductivity of polymer composites. Carbon 44, 3078–3086. https://doi.org/10.1016/j.carbon.2006.05.008

Le Duigou, A., Castro, M., Bevan, R., Martin, N., 2016. 3D printing of wood fibre biocomposites: From mechanical to actuation functionality. Mater. Des. 96, 106–114. https://doi.org/10.1016/j.matdes.2016.02.018

Lee, C.H., Padzil, F.N.B.M., Lee, S.H., Ainun, Z.M.A., Abdullah, L.C., 2021. Potential for Natural Fiber Reinforcement in PLA Polymer Filaments for Fused Deposition Modeling (FDM) Additive Manufacturing: A Review. Polymers 13, 1407. https://doi.org/10.3390/polym13091407

Lee, H., Lim, C.H.J., Low, M.J., Tham, N., Murukeshan, V.M., Kim, Y.-J., 2017. Lasers in additive manufacturing: A review. Int. J. Precis. Eng. Manuf.-Green Technol. 4, 307–322. https://doi.org/10.1007/s40684-017-0037-7

Lei, D., Yang, Y., Liu, Z., Chen, S., Song, B., Shen, A., Yang, B., Li, S., Yuan, Z., Qi, Q., Sun, L., Guo, Y., Zuo, H., Huang, S., Yang, Q., Mo, X., He, C., Zhu, B., M. Jeffries, E., Qing, F.-L., Ye, X., Zhao, Q., You, Z., 2019. A general strategy of 3D printing thermosets for diverse applications. Mater. Horiz. 6, 394–404. https://doi.org/10.1039/C8MH00937F

Leite, M., Fernandes, J., Deus, A.M., Reis, L., Vaz, M.F., 2018. Study of the influence of 3D printing parameters on the mechanical properties of PLA. https://doi.org/10.25341/D4988C

Lems, E.-M., Winklehner, S., Hansmann, C., Gindl-Altmutter, W., Veigel, S., 2019. Reinforcing effect of poly(furfuryl alcohol) in cellulose-based porous materials. Cellulose 26, 4431–4444. https://doi.org/10.1007/s10570-019-02348-6

Leppiniemi, J., Lahtinen, P., Paajanen, A., Mahlberg, R., Metsä-Kortelainen, S., Pinomaa, T., Pajari, H., Vikholm-Lundin, I., Pursula, P., Hytönen, V.P., 2017. 3D-Printable Bioactivated Nanocellulose–Alginate Hydrogels. ACS Appl. Mater. Interfaces 9, 21959–21970. https://doi.org/10.1021/acsami.7b02756

Lewis, J.A., 2006. Direct Ink Writing of 3D Functional Materials. Adv. Funct. Mater. 16, 2193–2204. https://doi.org/10.1002/adfm.200600434

Li, H., Wang, T., Sun, J., Yu, Z., 2018. The effect of process parameters in fused deposition modelling on bonding degree and mechanical properties. Rapid Prototyp. J. 24, 80–92. https://doi.org/10.1108/RPJ-06-2016-0090

Li, N., Li, Y., Liu, S., 2016. Rapid prototyping of continuous carbon fiber reinforced polylactic acid composites by 3D printing. J. Mater. Process. Technol. 238, 218–225. https://doi.org/10.1016/j.jmatprotec.2016.07.025

Li, W., Ghazanfari, A., Leu, M.C., Landers, R.G., 2017. Extrusion-on-demand methods for high solids loading ceramic paste in freeform extrusion fabrication. Virtual Phys. Prototyp. 12, 193–205. https://doi.org/10.1080/17452759.2017.1312735

Liu, Z., Erhan, S.Z., Akin, D.E., Barton, F.E., 2006. “Green” Composites from Renewable Resources: Preparation of Epoxidized Soybean Oil and Flax Fiber Composites. J. Agric. Food Chem. 54, 2134–2137. https://doi.org/10.1021/jf0526745

Llevot, A., 2017. Sustainable Synthetic Approaches for the Preparation of Plant Oil-Based Thermosets. J. Am. Oil Chem. Soc. 94, 169–186. https://doi.org/10.1007/s11746-016-2932-4

Lodha, P., Netravali, A.N., 2002. Characterization of interfacial and mechanical properties of "green" composites with soy protein isolate and ramie fiber. J. Mater. Sci. 37, 3657–3665. https://doi.org/10.1023/A:1016557124372

Luo, S., Netravali, A.N., 2003. A study of physical and mechanical properties of poly(hydroxybutyrate-co-hydroxyvalerate) during composting. Polym. Degrad. Stab. 80, 59–66. https://doi.org/10.1016/S0141-3910(02)00383-X

Luo, S., Netravali, A.N., 1999a. Interfacial and mechanical properties of environment-friendly "green" composites made from pineapple fibers and poly(hydroxybutyrate-co-valerate) resin. J. Mater. Sci. 34, 3709–3719. https://doi.org/10.1023/A:1004659507231

Luo, S., Netravali, A.N., 1999b. Mechanical and thermal properties of environment-friendly "green" composites made from pineapple leaf fibers and poly(hydroxybutyrate-co-valerate) resin. Polym. Compos. 20, 367–378. https://doi.org/10.1002/pc.10363

Machado, G., Leon, S., Santos, F., Lourega, R., Dullius, J., Mollmann, M.E., Eichler, P., 2016. Literature Review on Furfural Production from Lignocellulosic Biomass. Nat. Resour. 7, 115–129. https://doi.org/10.4236/nr.2016.73012

Mahmood, S., Qureshi, A.J., Goh, K.L., Talamona, D., 2017. Tensile strength of partially filled FFF printed parts: experimental results. Rapid Prototyp. J. 23, 122–128. https://doi.org/10.1108/RPJ-08-2015-0115

Malaba, T., Wang, J., 2015. Unidirectional Cordenka Fibre-Reinforced Furan Resin Full Biocomposite: Properties and Influence of High Fibre Mass Fraction. J. Compos. 2015, e707151. https://doi.org/10.1155/2015/707151

Maldas, D., Kokta, B.V., 1995. Composite Molded Products Based on Recycled Thermoplastics and Waste Cellulosics. II. Kenaf Fiber-Recycled PE Composites. J. Reinf. Plast. Compos. 14, 458–470. https://doi.org/10.1177/073168449501400504

Malek, S., Raney, J.R., Lewis, J.A., Gibson, L.J., 2017. Lightweight 3D cellular composites inspired by balsa. Bioinspir. Biomim. 12, 026014. https://doi.org/10.1088/1748-3190/aa6028

Mansor, M.R., Salit, M.S., Zainudin, E.S., Aziz, N.A., Ariff, H., 2015. Life Cycle Assessment of Natural Fiber Polymer Composites, in: Hakeem, K.R., Jawaid, M., Y. Alothman, O. (Eds.), Agricultural Biomass Based Potential Materials. Springer International Publishing, Cham, pp. 121–141. https://doi.org/10.1007/978-3-319-13847-3_6

Mariwala, R.K., Foley, H.C., 1994. Evolution of Ultramicroporous Adsorptive Structure in Poly(furfuryl alcohol)-Derived Carbogenic Molecular Sieves. Ind. Eng. Chem. Res. 33, 607–615. https://doi.org/10.1021/ie00027a018

Markstedt, K., Mantas, A., Tournier, I., Martínez Ávila, H., Hägg, D., Gatenholm, P., 2015. 3D Bioprinting Human Chondrocytes with Nanocellulose–Alginate Bioink for Cartilage Tissue Engineering Applications. Biomacromolecules 16, 1489–1496. https://doi.org/10.1021/acs.biomac.5b00188

Marsh, G., 2008. Composites that grow in fields. Reinf. Plast. 52, 16–22. https://doi.org/10.1016/S0034-3617(08)70369-2

Matsuzaki, R., Ueda, M., Namiki, M., Jeong, T.-K., Asahara, H., Horiguchi, K., Nakamura, T., Todoroki, A., Hirano, Y., 2016. Three-dimensional printing of continuous-fiber composites by in-nozzle impregnation. Sci. Rep. 6, 23058. https://doi.org/10.1038/srep23058

Mazurchevici, A.D., Nedelcu, D., Popa, R., 2021. Additive manufacturing of composite materials by FDM technology: A review. Indian J. Eng. Mater. Sci. IJEMS 27, 179–192.

Mazzanti, V., Malagutti, L., Mollica, F., 2019. FDM 3D Printing of Polymers Containing Natural Fillers: A Review of their Mechanical Properties. Polymers 11, 1094. https://doi.org/10.3390/polym11071094

Mehta, G., Mohanty, A.K., Misra, M., Drzal, L.T., 2004. Effect of novel sizing on the mechanical and morphological characteristics of natural fiber reinforced unsaturated polyester resin based bio-composites. J. Mater. Sci. 39, 2961–2964. https://doi.org/10.1023/B:JMSC.0000021492.61235.00

Melenka, G.W., Cheung, B.K.O., Schofield, J.S., Dawson, M.R., Carey, J.P., 2016. Evaluation and prediction of the tensile properties of continuous fiber-reinforced 3D printed structures. Compos. Struct. 153, 866–875. https://doi.org/10.1016/j.compstruct.2016.07.018

Men, X.H., Zhang, Z.Z., Song, H.J., Wang, K., Jiang, W., 2008. Functionalization of carbon nanotubes to improve the tribological properties of poly(furfuryl alcohol) composite coatings. Compos. Sci. Technol. 68, 1042–1049. https://doi.org/10.1016/j.compscitech.2007.07.008

Men, X.-H., Zhang, Z.-Z., Song, H.-J., Wang, K., Jiang, W., 2008. Fabrication of superhydrophobic surfaces with poly(furfuryl alcohol)/multi-walled carbon nanotubes composites. Appl. Surf. Sci. 254, 2563–2568. https://doi.org/10.1016/j.apsusc.2007.08.084

Menager, C., Guigo, N., Wu, X., Vincent, L., Sbirrazzuoli, N., 2019. “Green” composites prepared from polyfurfuryl alcohol and cork residues: Thermal and mechanical properties. Compos. Part Appl. Sci. Manuf. 124, 105473. https://doi.org/10.1016/j.compositesa.2019.105473

Mesa, L., Morales, M., González, E., Cara, C., Romero, I., Castro, E., Mussatto, S.I., 2014. Restructuring the processes for furfural and xylose production from sugarcane bagasse in a biorefinery concept for ethanol production. Chem. Eng. Process. Process Intensif. 85, 196–202. https://doi.org/10.1016/j.cep.2014.07.012

Misra, M., Ahankari, S.S., Mohanty, A.K., Nga, A.D., 2011. 11 - Creep and fatigue of natural fibre composites, in: Zafeiropoulos, N.E. (Ed.), Interface Engineering of Natural Fibre Composites for Maximum Performance, Woodhead Publishing Series in Composites Science and Engineering. Woodhead Publishing, pp. 289–340. https://doi.org/10.1533/9780857092281.2.289

Miyashiro, D., Hamano, R., Umemura, 2020. A Review of Applications Using Mixed Materials of Cellulose, Nanocellulose and Carbon Nanotubes. Nanomaterials 10, 186. https://doi.org/10.3390/nano10020186

Modniks, J., Poriķe, E., Andersons, J., Joffe, R., 2012. Evaluation of the apparent interfacial shear strength in short-flax-fiber/PP composites. Mech. Compos. Mater. 48, 571–578. https://doi.org/10.1007/s11029-012-9301-7

Mogan, J., Sandanamsamy, L., Halim, N.A., Harun, W.S.W., Kadirgama, K., Ramasamy, D., 2021. A review of FDM and graphene-based polymer composite. IOP Conf. Ser. Mater. Sci. Eng. 1078, 012032. https://doi.org/10.1088/1757-899X/1078/1/012032

Mohamed, B.S., Périgaud, C., Mathé, C., 2017. Revaluation of biomass-derived furfuryl alcohol derivatives for the synthesis of carbocyclic nucleoside phosphonate analogues. Beilstein J. Org. Chem. 13, 251–256. https://doi.org/10.3762/bjoc.13.28

Mohamed, O.A., Masood, S.H., Bhowmik, J.L., 2015. Optimization of fused deposition modeling process parameters: a review of current research and future prospects. Adv. Manuf. 3, 42–53. https://doi.org/10.1007/s40436-014-0097-7

Mohan, N., Senthil, P., Vinodh, S., Jayanth, N., 2017. A review on composite materials and process parameters optimisation for the fused deposition modelling process. Virtual Phys. Prototyp. 12, 47–59. https://doi.org/10.1080/17452759.2016.1274490

Mohanty, A.K., Khan, M.A., Hinrichsen, G., 2000. Surface modification of jute and its influence on performance of biodegradable jute-fabric/Biopol composites. Compos. Sci. Technol. 60, 1115–1124. https://doi.org/10.1016/S0266-3538(00)00012-9

Mohanty, S., Nayak, S.K., Verma, S.K., Tripathy, S.S., 2004. Effect of MAPP as a Coupling Agent on the Performance of Jute–PP Composites. J. Reinf. Plast. Compos. 23, 625–637. https://doi.org/10.1177/0731684404032868

Netravali, A., Chabba, S., 2003. Composites get greener. Mater. Today - MATER TODAY 6, 22–29. https://doi.org/10.1016/S1369-7021(03)00427-9

Ngo, T.-D.), 2020. Introduction to Composite Materials. https://doi.org/10.5772/intechopen.91285

Ngo, T.D., Kashani, A., Imbalzano, G., Nguyen, K.T.Q., Hui, D., 2018. Additive manufacturing (3D printing): A review of materials, methods, applications and challenges. Compos. Part B Eng. 143, 172–196. https://doi.org/10.1016/j.compositesb.2018.02.012

Nguyen, N.A., Barnes, S.H., Bowland, C.C., Meek, K.M., Littrell, K.C., Keum, J.K., Naskar, A.K., 2018. A path for lignin valorization via additive manufacturing of high-performance sustainable composites with enhanced 3D printability. Sci. Adv. 4, eaat4967. https://doi.org/10.1126/sciadv.aat4967

Ning, F., Cong, W., Qiu, J., Wei, J., Wang, S., 2015. Additive manufacturing of carbon fiber reinforced thermoplastic composites using fused deposition modeling. Compos. Part B Eng. 80, 369–378. https://doi.org/10.1016/j.compositesb.2015.06.013

Nishino, T., Hirao, K., Kotera, M., Nakamae, K., Inagaki, H., 2003. Kenaf reinforced biodegradable composite. Compos. Sci. Technol., Eco-Composites 63, 1281–1286. https://doi.org/10.1016/S0266-3538(03)00099-X

O'Dell, J.L., 1997. Natural Fibers in Resin Transfer Molded Composites 6.

Oksman, K., Skrifvars, M., Selin, J.-F., 2003. Natural fibres as reinforcement in polylactic acid (PLA) composites. Compos. Sci. Technol., Eco-Composites 63, 1317–1324. https://doi.org/10.1016/S0266-3538(03)00103-9

Panda, S.K., Padhee, S., Sood, A.K., Mahapatra, S.S., 2009. Optimization of Fused Deposition Modelling (FDM) Process Parameters Using Bacterial Foraging Technique. Intell. Inf. Manag. 01, 89. https://doi.org/10.4236/iim.2009.12014

Parandoush, P., Lin, D., 2017. A review on additive manufacturing of polymer-fiber composites. Compos. Struct. 182, 36–53. https://doi.org/10.1016/j.compstruct.2017.08.088

Pattinson, S.W., Hart, A.J., 2017. Additive Manufacturing of Cellulosic Materials with Robust Mechanics and Antimicrobial Functionality. Adv. Mater. Technol. 2, 1600084. https://doi.org/10.1002/admt.201600084

Pearce, P.J., Arnott, D.R., Camilleri, A., Kindermann, M.R., Mathys, G.I., Wilson, A.R., 1998. Cause and effect of void formation during vacuum bag curing of epoxy film adhesives. J. Adhes. Sci. Technol. 12, 567–584. https://doi.org/10.1163/156856198X00795

Pech-Canul, M.I., Valdez-Rodriguez, S., 2015. UPDATING THE DEFINITION AND CONCEPTS IN THE FIELD OF COMPOSITE MATERIALS.

Peng, J., Lin, T.L., Calvert, P., 1999. Orientation effects in freeformed short-fiber composites. Compos. Part Appl. Sci. Manuf. 30, 133–138. https://doi.org/10.1016/S1359-835X(98)00110-9

Penumakala, P.K., Santo, J., Thomas, A., 2020. A critical review on the fused deposition modeling of thermoplastic polymer composites. Compos. Part B Eng. 201, 108336. https://doi.org/10.1016/j.compositesb.2020.108336

Pickering, K., 2008. Properties and Performance of Natural-Fibre Composites. Elsevier.

Pin, J.-M., Guigo, N., Mija, A., Vincent, L., Sbirrazzuoli, N., van der Waal, J.C., de Jong, E., 2014. Valorization of Biorefinery Side-Stream Products: Combination of Humins with Polyfurfuryl Alcohol for Composite Elaboration. ACS Sustain. Chem. Eng. 2, 2182–2190. https://doi.org/10.1021/sc5003769

Pizzi, A., Mittal, K.L. (Eds.), 2003. Handbook of adhesive technology, 2nd ed., rev.expanded. ed. M. Dekker, New York.

Pohl, T., Bierer, M., Natter, E., Madsen, B., Hoydonckx, H., Schledjewski, R., 2011. Properties of compression moulded new fully biobased thermoset composites with aligned flax fibre textiles. Plast. Rubber Compos. 40, 294–299. https://doi.org/10.1179/1743289810Y.0000000017

Pranger, L., Tannenbaum, R., 2008. Biobased Nanocomposites Prepared by In Situ Polymerization of Furfuryl Alcohol with Cellulose Whiskers or Montmorillonite Clay. Macromolecules 41, 8682–8687. https://doi.org/10.1021/ma8020213

Pranger, L.A., Nunnery, G.A., Tannenbaum, R., 2012. Mechanism of the nanoparticle-catalyzed polymerization of furfuryl alcohol and the thermal and mechanical properties of the resulting nanocomposites. Compos. Part B Eng. 43, 1139–1146. https://doi.org/10.1016/j.compositesb.2011.08.010

Quirino, R.L., Monroe, K., Fleischer, C.H., Biswas, E., Kessler, M.R., 2021. Thermosetting polymers from renewable sources. Polym. Int. 70, 167–180. https://doi.org/10.1002/pi.6132

Raju, M., Gupta, M.K., Bhanot, N., Sharma, V.S., 2019. A hybrid PSO–BFO evolutionary algorithm for optimization of fused deposition modelling process parameters. J. Intell. Manuf. 30, 2743–2758. https://doi.org/10.1007/s10845-018-1420-0

Raju, T.N. *d R., Ramach, V., Raju, R., 2010. An experimental investigation on surface quality and dimensional accuracy of FDM components.

Research, L., 2021. Lux Research Forecasts the 3D Printing Market Will Reach $51 Billion in 2030 [WWW Document]. URL https://www.luxresearchinc.com/press-releases/lux-research-forecasts-the-3d-printing-market-will-reach-51-billion-in-2030 (accessed 5.18.21).

Rinanto, A., Nugroho, A., Prasetyo, H., Pujiyanto, E., 2018. Simultaneous Optimization of TensileStrength, Energy Consumption and Processing Time on FDM Process Using Taguchi and PCR-TOPSIS, in: 2018 4th International Conference on Science and Technology (ICST). Presented at the 2018 4th International Conference on Science and Technology (ICST), pp. 1–5. https://doi.org/10.1109/ICSTC.2018.8528667

Rios, O., Carter, W., Post, B., Lloyd, P., Fenn, D., Kutchko, C., Rock, R., Olson, K., Compton, B., 2018. 3D printing via ambient reactive extrusion. Mater. Today Commun. 15, 333–336. https://doi.org/10.1016/j.mtcomm.2018.02.031

Rodriguez, J.F., Thomas, J.P., Renaud, J.E., 2000. Characterization of the mesostructure of fused-deposition acrylonitrile-butadiene-styrene materials. Rapid Prototyp. J. https://doi.org/10.1108/13552540010337056

S, P., Km, S., K, N., S, S., 2017. Fiber Reinforced Composites - A Review. J. Mater. Sci. Eng. 06. https://doi.org/10.4172/2169-0022.1000341

Schmitt, C.R., 1974. Polyfurfuryl Alcohol Resins. Polym.-Plast. Technol. Eng. 3, 121–158. https://doi.org/10.1080/03602557408545025

Shang, J., Li, X., Wang, R., Wang, Z., 2017. Rheological and Printable Behavior of Epoxy Resin-based Materials for Extrusion 3D Printing Applications. 폴리머 41, 874–881. https://doi.org/10.7317/pk.2017.41.5.874

Shi, Q., Yu, K., Kuang, X., Mu, X., K. Dunn, C., L. Dunn, M., Wang, T., Qi, H.J., 2017. Recyclable 3D printing of vitrimer epoxy. Mater. Horiz. 4, 598–607. https://doi.org/10.1039/C7MH00043J

Sinha, E., Rout, S.K., 2009. Influence of fibre-surface treatment on structural, thermal and mechanical properties of jute fibre and its composite. Bull. Mater. Sci. 32, 65. https://doi.org/10.1007/s12034-009-0010-3

Siqueira, G., Kokkinis, D., Libanori, R., Hausmann, M.K., Gladman, A.S., Neels, A., Tingaut, P., Zimmermann, T., Lewis, J.A., Studart, A.R., 2017. Cellulose Nanocrystal Inks for 3D Printing of Textured Cellular Architectures. Adv. Funct. Mater. 27, 1604619. https://doi.org/10.1002/adfm.201604619

Smith, W.F., 1986. Principles of materials science and engineering.

Sood, A.K., Ohdar, R.K., Mahapatra, S.S., 2010. Parametric appraisal of mechanical property of fused deposition modelling processed parts. Mater. Des. 31, 287–295. https://doi.org/10.1016/j.matdes.2009.06.016

Sood, A.K., Ohdar, R.K., Mahapatra, S.S., 2009. Improving dimensional accuracy of Fused Deposition Modelling processed part using grey Taguchi method. Mater. Des. 30, 4243–4252. https://doi.org/10.1016/j.matdes.2009.04.030

Spinu, M., Jackson, C., Keating, M.Y., Gardner, K.H., 1996. Material Design in Poly(Lactic Acid) Systems: Block Copolymers, Star Homo- and Copolymers, and Stereocomplexes. J. Macromol. Sci. Part A 33, 1497–1530. https://doi.org/10.1080/10601329608014922

Stellato, J.A., 2020. Renewable Monomers for 4D Printing (Thesis).

Stoof, D., Pickering, K., 2018. Sustainable composite fused deposition modelling filament using recycled pre-consumer polypropylene. Compos. Part B Eng. 135, 110–118. https://doi.org/10.1016/j.compositesb.2017.10.005

Sukri, S.M., Suradi, N.L., Arsad, A., Rahmat, A.R., Hassan, A., 2012. Green composites based on recycled polyamide-6/recycled polypropylene kenaf composites: mechanical, thermal and morphological properties. J. Polym. Eng. 32, 291–299. https://doi.org/10.1515/polyeng-2012-0016

Sultan, S., P. Mathew, A., 2018. 3D printed scaffolds with gradient porosity based on a cellulose nanocrystal hydrogel. Nanoscale 10, 4421–4431. https://doi.org/10.1039/C7NR08966J

Sun, J., Zhou, W., Yan, L., Huang, D., Lin, L., 2018. Extrusion-based food printing for digitalized food design and nutrition control. J. Food Eng., 3D Printed Food – Design and Technology 220, 1–11. https://doi.org/10.1016/j.jfoodeng.2017.02.028

Swallowe, G.M. (Ed.), 1999. Mechanical Properties and Testing of Polymers, Polymer Science and Technology Series. Springer Netherlands, Dordrecht. https://doi.org/10.1007/978-94-015-9231-4

Takagi, H., Ichihara, Y., 2004. Effect of Fiber Length on Mechanical Properties of “Green” Composites Using a Starch-Based Resin and Short Bamboo Fibers. JSME Int. J. Ser. Solid Mech. Mater. Eng. 47, 551–555. https://doi.org/10.1299/jsmea.47.551

Tatara, R.A., 2017. 14 - Compression Molding, in: Kutz, M. (Ed.), Applied Plastics Engineering Handbook (Second Edition), Plastics Design Library. William Andrew Publishing, pp. 291–320. https://doi.org/10.1016/B978-0-323-39040-8.00014-6

Tekinalp, H.L., Kunc, V., Velez-Garcia, G.M., Duty, C.E., Love, L.J., Naskar, A.K., Blue, C.A., Ozcan, S., 2014. Highly oriented carbon fiber–polymer composites via additive manufacturing. Compos. Sci. Technol. 105, 144–150. https://doi.org/10.1016/j.compscitech.2014.10.009

The Economist, 2012. The third industrial revolution. The Economist The Economist.

Thibaut, C., Denneulin, A., Rolland du Roscoat, S., Beneventi, D., Orgéas, L., Chaussy, D., 2019. A fibrous cellulose paste formulation to manufacture structural parts using 3D printing by extrusion. Carbohydr. Polym. 212, 119–128. https://doi.org/10.1016/j.carbpol.2019.01.076

Tian, X., Liu, T., Yang, C., Wang, Q., Li, D., 2016. Interface and performance of 3D printed continuous carbon fiber reinforced PLA composites. Compos. Part Appl. Sci. Manuf. 88, 198–205. https://doi.org/10.1016/j.compositesa.2016.05.032

Todd, J., 2019. What is the Definition of a Composite Material? [WWW Document]. ThoughtCo. URL https://www.thoughtco.com/what-is-a-composite-820406 (accessed 4.22.21).

Tondi, G., Cefarin, N., Sepperer, T., D'Amico, F., Berger, R., Musso, M., Birarda, G., Reyer, A., Schnabel, T., Vaccari, L., 2019. Understanding the Polymerization of Polyfurfuryl Alcohol: Ring Opening and Diels-Alder Reactions. Polymers 2019, 2126. https://doi.org/10.3390/polym11122126

Tontowi, A., Ramdani, L., Erdizon, R., Baroroh, D., 2017. Optimization of 3D-Printer Process Parameters for Improving Quality of Polylactic Acid Printed Part. Int. J. Eng. Technol. 9, 589–600. https://doi.org/10.21817/ijet/2017/v9i2/170902044

Toriz, G., Arvidsson, R., Westin, M., Gatenholm, P., 2003. Novel cellulose ester–poly(furfuryl alcohol)–flax fiber biocomposites. J. Appl. Polym. Sci. 88, 337–345. https://doi.org/10.1002/app.11730

Torrado Perez, A.R., Roberson, D.A., Wicker, R.B., 2014. Fracture Surface Analysis of 3D-Printed Tensile Specimens of Novel ABS-Based Materials. J. Fail. Anal. Prev. 14, 343–353. https://doi.org/10.1007/s11668-014-9803-9

Uawongsuwan, P., Yang, Y., Hamada, H., 2015. Long jute fiber-reinforced polypropylene composite: Effects of jute fiber bundle and glass fiber hybridization. J. Appl. Polym. Sci. 132. https://doi.org/10.1002/app.41819

Utela, B., Storti, D., Anderson, R., Ganter, M., 2008. A review of process development steps for new material systems in three dimensional printing (3DP). J. Manuf. Process. 10, 96–104. https://doi.org/10.1016/j.jmapro.2009.03.002

Verma, R., Shukla, M., 2018. Characterization of Mechanical Properties of Short Kenaf Fiber-HDPE Green Composites. Mater. Today Proc. 5, 3257–3264. https://doi.org/10.1016/j.matpr.2017.11.567

Vinyas, M., Athul, S., Harursampath, D., Nguyen Thoi, T., 2019. Experimental evaluation of the mechanical and thermal properties of 3D printed PLA and its composites. Mater. Res. Express 6, 115301. https://doi.org/10.1088/2053-1591/ab43ab

Wambua, P., Ivens, J., Verpoest, I., 2003. Natural fibres: can they replace glass in fibre reinforced plastics? Compos. Sci. Technol., Eco-Composites 63, 1259–1264. https://doi.org/10.1016/S0266-3538(03)00096-4

Wang, P., Zou, B., Ding, S., Huang, C., Shi, Z., Ma, Y., Yao, P., 2020. Preparation of short CF/GF reinforced PEEK composite filaments and their comprehensive properties evaluation for FDM-3D printing. Compos. Part B Eng. 198, 108175. https://doi.org/10.1016/j.compositesb.2020.108175

Wang, R.-M., Zheng, S.-R., Zheng, Y.-P., 2011. 3 - Matrix materials, in: Wang, R.-M., Zheng, S.-R., Zheng, Y.-P. (Eds.), Polymer Matrix Composites and Technology, Woodhead Publishing Series in Composites Science and Engineering. Woodhead Publishing, pp. 101–548. https://doi.org/10.1533/9780857092229.1.101

Wang, X., Jiang, M., Zhou, Z., Gou, J., Hui, D., 2017. 3D printing of polymer matrix composites: A review and prospective. Compos. Part B Eng. 110, 442–458. https://doi.org/10.1016/j.compositesb.2016.11.034

Wang, Y., Deng, L., Xiao, Z., Li, X., Fan, Y., Li, C., 2019a. Preparation and properties of bamboo/polymer composites enhanced by in situ polymerization of furfuryl alcohol [WWW Document]. https://doi.org/info:doi/10.1166/mex.2019.1550

Wang, Y., Deng, L., Xiao, Z., Li, X., Fan, Y., Li, C., 2019b. Preparation and properties of bamboo/polymer composites enhanced by in situ polymerization of furfuryl alcohol. Mater. Express 9, 712–722. https://doi.org/10.1166/mex.2019.1550

Wang, Y., Deng, L., Xiao, Z., Li, X., Fan, Y., Li, C., 2019c. Preparation and properties of bamboo/polymer composites enhanced by in situ polymerization of furfuryl alcohol. Mater. Express 9, 712–722. https://doi.org/10.1166/mex.2019.1550

Wang, Y., Lei, M., Wei, Q., Wang, Yanmei, Zhang, J., Guo, Y., Saroia, J., 2020. 3D printing biocompatible l-Arg/GNPs/PLA nanocomposites with enhanced mechanical property and thermal stability. J. Mater. Sci. 55, 5064–5078. https://doi.org/10.1007/s10853-020-04353-8

Wang, Z., Lu, Z., Huang, Y., Xue, R., Huang, X., Chen, L., 1997. Characterizations of crystalline structure and electrical properties of pyrolyzed polyfurfuryl alcohol. J. Appl. Phys. 82, 5705–5710. https://doi.org/10.1063/1.366434

Wewerka, E.M., 1971. Study of the γ-alumina polymerization of furfuryl alcohol. J. Polym. Sci. [A1] 9, 2703–2715. https://doi.org/10.1002/pol.1971.150090923

Wickramasinghe, S., Do, T., Tran, P., 2020. FDM-Based 3D Printing of Polymer and Associated Composite: A Review on Mechanical Properties, Defects and Treatments. Polymers 12, 1529. https://doi.org/10.3390/polym12071529

Win, D., 2005. Furfural - Gold from Garbage. AU J Technol 8.

Wohlers, A., 2021. Wohlers report 2021 3D prinitng and additive manufacturing: Global state of the industry.

Wohlers, A., 2019. Wohlers report 2019 3D prinitng and additive manufacturing: Global state of the industry [WWW Document]. URL https://wohlersassociates.com/2019report.htm (accessed 5.18.21).

Xia, X., Liu, W., Zhou, L., Hua, Z., Liu, H., He, S., 2016. Modification of flax fiber surface and its compatibilization in polylactic acid/flax composites. Iran. Polym. J. 25, 25–35. https://doi.org/10.1007/s13726-015-0395-3

Xia, Y., Quirino, R.L., Larock, R.C., 2013. Bio-based Thermosetting Polymers from Vegetable Oils. J. Renew. Mater. 1, 3–27. https://doi.org/10.7569/JRM.2012.634103

Xu, W., Pranovich, A., Uppstu, P., Wang, X., Kronlund, D., Hemming, J., Öblom, H., Moritz, N., Preis, M., Sandler, N., Willför, S., Xu, C., 2018a. Novel biorenewable composite of wood polysaccharide and polylactic acid for three dimensional printing. Carbohydr. Polym. 187, 51–58. https://doi.org/10.1016/j.carbpol.2018.01.069

Xu, W., Wang, X., Sandler, N., Willför, S., Xu, C., 2018b. Three-Dimensional Printing of Wood-Derived Biopolymers: A Review Focused on Biomedical Applications. ACS Sustain. Chem. Eng. 6, 5663–5680. https://doi.org/10.1021/acssuschemeng.7b03924

Yang, K., Grant, J.C., Lamey, P., Joshi-Imre, A., Lund, B.R., Smaldone, R.A., Voit, W., 2017. Diels–Alder Reversible Thermoset 3D Printing: Isotropic Thermoset Polymers via Fused Filament Fabrication. Adv. Funct. Mater. 27, 1700318. https://doi.org/10.1002/adfm.201700318

Yaragalla, S., Zahid, M., Panda, J.K., Tsagarakis, N., Cingolani, R., Athanassiou, A., 2021. Comprehensive Enhancement in Thermomechanical Performance of Melt-Extruded PEEK Filaments by Graphene Incorporation. Polymers 13, 1425. https://doi.org/10.3390/polym13091425

Zamri, M.H., Osman, M.R., Akil, H.M., Shahidan, M.H.A., Mohd Ishak, Z.A., 2016. Development of green pultruded composites using kenaf fibre: influence of linear mass density on weathering performance. J. Clean. Prod. 125, 320–330. https://doi.org/10.1016/j.jclepro.2016.03.026

Zarbin, A.J.G., Bertholdo, R., Oliveira, M.A.F.C., 2002. Preparation, characterization and pyrolysis of poly(furfuryl alcohol)/porous silica glass nanocomposites: novel route to carbon template. Carbon 40, 2413–2422. https://doi.org/10.1016/S0008-6223(02)00130-6

Zhang, L., Dong, H., El Saddik, A., 2015. From 3D Sensing to Printing: A Survey. ACM Trans. Multimed. Comput. Commun. Appl. 12, 1–23. https://doi.org/10.1145/2818710

2 Materials and methods

Chapter content

2.1 Chapter introduction

To fulfill the PhD project goals many materials, processes, and characterization methods were used and will be detailed in this chapter to provide essential information before tackling the results discussed in the following chapters. This chapter is divided into 5 main sections related to the composite's production phase (Figure 2-1):

- Section 2.2: Description of the used commercial materials in the development and optimization of the composites.

- Section2.3: Detailing the slurry preparation step with an overview of the different tested formulations.

- Section2.4: Explication of the composite production step including a description of the used 3D printer, the software, the bulk composite molding, and the curing process.

- Section 2.5: Description of the carbonization step of the cured composites.

- Section2.6: A general description of the used characterization methods and techniques. This section is divided into 4 subsections:

    - Description of the methods and apparatus used in the characterization of the raw commercial polymers.
    - Explication of rheological methods used in the characterization of different developed uncured pastes.
    - Description of the methods used in the characterization of the curing process.
    - Explication of the different techniques employed in the characterization of mechanical properties, thermal stability, dimensional stability, morphology, and electrical conductivity of the cured/carbonized final composite.

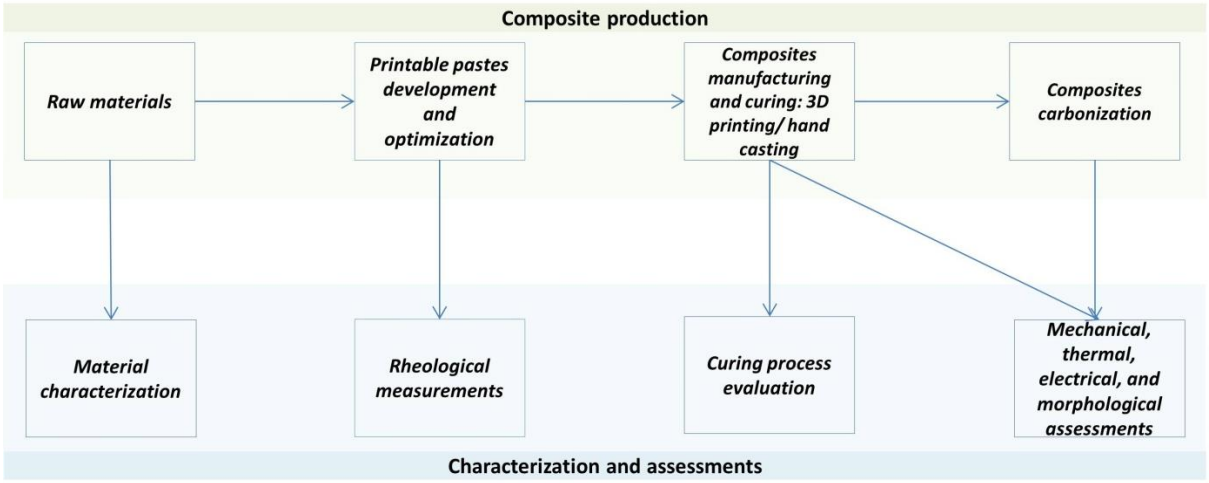

Figure 2-1: General layout of the project's approach.

2.2 Cellulose powder and fibers

In this project, the used cellulose is a commercial product by *CFF* from their *Technocel® pure series* and was kindly supplied by *Rossow Industry*. The mainly used cellulose is the finest powder in this product line, known under the trade name *Technocel® FM8*. According to the supplier's datasheet, this cellulose has a powdery aspect, with over 99.5% purity, and 80% whiteness. Moreover, the particle size was reported to be between 6-12 µm and the specific density 1.5 g/cm^3. The density was further confirmed by experimentally measuring the apparent density of cellulose pellets (obtained by powder compression at 1.2 GPa) which is in line with solid cellulose density values. According to the supplier's information, the water content of this powder is vaguely determined to be below 8 wt% and was experimentally measured to be 4.58 ±0.05 wt% using the standard method to determine the dry content of paper, board, and pulps (ISO 638:2008). The *Technocel®200*, made of 300 µm long fibers, was also used in some preliminary tests. According to the little information provided by the supplier and the limited information published, the used raw material is wood fibers (hardwood) which were cleansed, bleached and hot steam dried before ending up in the *CFF* production sites in Germany. The fibers are then milled multiple times and, if necessary, finely milled and sieved to reach the desired particle size (LG Hemija, 2017). A more detailed characterization of the cellulose morphology, size distribution, and structure will be presented in the next chapter.

2.2.1 Carbon nanotubes

Two sources of Carbon NanoTubes (CNT) were used during this project. First, for preliminary tests, DWCNT were kindly provided by *Centre Interuniversitaire de Recherche et d'Ingénierie des Matériaux* of Toulouse, France (DWCNT-L). These CNT were synthesized at a lab-scale by a catalytic chemical vapor deposition method using a removable MgO-based catalyst (Flahaut et al., 2003). In Figure 2-2-A one can see the CNT bundles thanks to the high-resolution transmission electron microscopy image provided by Dr. Flahaut Emmanuel. The length of these CNT was in the range of 100 µm and their average external diameter of 2 µm (Flahaut et al., 2003). As lab-scale production of CNT is limited, for further experimentation, a larger quantity of commercial CNT was purchased from *Nanoamor (TX, USA).*

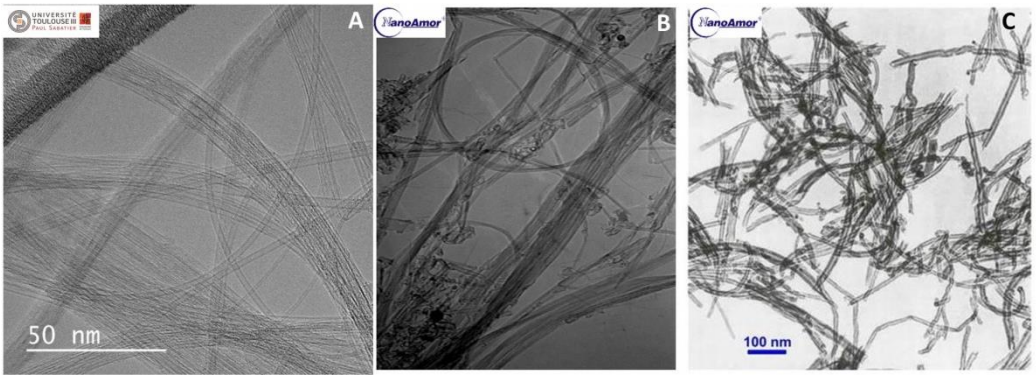

Figure 2-2: HRTEM image of (A) DWCNT produced in lab-scale (Flahaut et al., 2003), (B) commercial DWCNT, and (C) commercial MWCNT short (Nanoamor, 2021).

Different types and morphologies of CNT were used to select the most suitable, their main characteristics, given by the supplier, are listed in Table 2-1. The form factor, defined as the ratio between the length and diameter, ranged from 33 to 2500 and their bulk electrical conductivity (EC) given by the supplier is estimated to be 100 S/cm. The EC was experimentally measured by the 4 probes technique on a thin layer of CNT and was found to be in line with the supplier's indications. The morphological difference between the short and long CNT is visible on the TEM photos published by the supplier (Figure 2-2-B and Figure 2-2-C).

Table 2-1: The commercial CNT characteristics.

Labeled	Supplier's reference	Internal diameter (nm)	External diameter (nm)	Length (nm)	Aspect ratio L/d	EC (S/cm)
SWCNT	1283YJ		1-2	5000-30000	2500	>100
DWCNT	1280YJD	1-3	2-4	50000	1250-2500	>100
MWCNT 1	1229YJ	5-10	20-30	10000-30000	333-1500	>100
MWCNT 2	1233YJ	5-15	30-80	<10000	125-333	>100
MWCNT Gr	1223YJ	5-15	30-80	<10000	125-333	>100
MWCNT short	1235YJS	3-5	8-15	500-2000	33-250	>100

2.2.2 Graphene aggregate and graphite powder

Some other nano and micro conductive particles were tested during the present thesis such as graphene and graphite (Figure 2-3). Graphene nanoplatelets were supplied in form of powder by *Strem Chemicals (MA, USA)*. These are sub-micron platelet aggregates with a diameter smaller than 2 µm, a thickness of few nanometers and an apparent density ranging from 0.2 to 0.4 g/cm^3. These

particles have a specific surface area of around 750 m^2/g and EC of the order of 10^5 S/cm (STREM, 2021).

The graphite powder, known under the trade name *TIMCAL TIMREX® SLP 30*, was supplied by *Timcal Group (Bodio, Switzerland)* consists, according to the technical datasheet, of more than 99.5% graphite with a bulk density of 2.2 g/cm^3. According to the analysis found in the literature, the size of the analyzed particles was 90% below 31 µm (Ghimbeu et al., 2013).

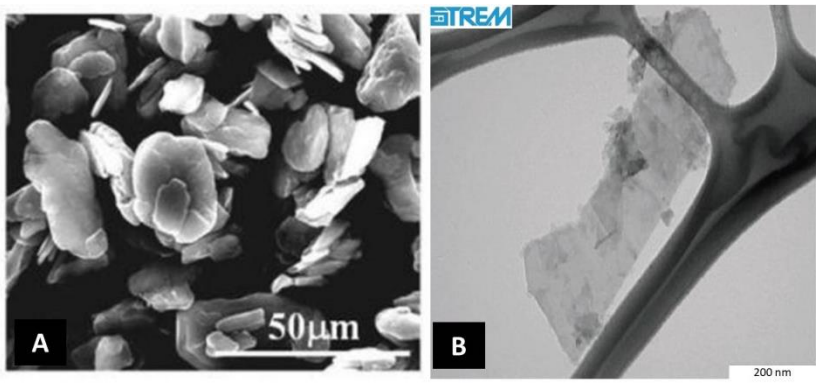

Figure 2-3: (A) SEM picture of TIMCAL TIMREX® SLP 30 (Ghimbeu et al., 2013) and (B) TEM picture of a nearly transparent platelet of graphene (STREM, 2021).

2.2.3 Poly(furfuryl alcohol) polymer

The main polymer matrix used in this project is a commercial poly(furfural alcohol) resin known under the trade name *Furolite* (i.e. Furolite 050915A RF-2ST) that was kindly supplied by *Transfurans Chemicals (Geel, Belgium).* On the market, it is possible to encounter different PFA resins and Furolite was selected for its pH neutral nature (pH 4-5) which was developed to be compatible with cellulosic fillers (Arnold et al., 2011). Indeed, the action of acids can cause hydrolysis in cellulose chains thereby degrading the fiber's mechanical properties (Thygesen et al., 2007).

According to the supplier's datasheet, this PFA resin contains between 5 and 7.5 wt% water and less than 1% of the FA free monomers. To determine the exact water content, around 15 g of the *Furolite* were placed in a vacuum oven at 60°C and left for 120 h to eliminate water. When the resin mass was stabilized the water content was calculated as the difference between the initial and final mass and it was found to be 7.5 wt%. The apparent density of the Furolite is 1.21 g/cm^3. The apparent viscosity given by the producer is below 5 Pa·s, i.e.3.8 ±0.3 Pa·s as experimentally determined.

Preliminary tests aimed at identifying the PFA/water miscibility limit (carried out by preparing several aqueous solutions and centrifuging them for 20 min at 4020 rpm) showed phase separation when the water content was higher than 24 wt%. Therefore, it was concluded that the resin could be

diluted with water up to 24 wt% (including the catalyst). Moreover, the supplier's information claim that the polymer can be stored for a long time (days/months) at temperatures between 20°C and 25°C without risking its polymerization, and according to the literature, the shelf life of this kind of resin can reach 18 months at room temperature (Behzadfar et al., 2019). The viscous uncured *Furolite* resin has a brownish color, shown in Figure 2-4, and is stored in a plastic container in a bunker where the temperature hardly exceeds 25°C even on the hottest days.

A latent hardener that will only catalyze the curing reaction at hot temperature was opted for the resin crosslinking. This latent catalyst will prevent the untimely crosslinking of the formulations and prevent the use of strong acid catalysts that would attack the cellulosic fillers. This latent hardener is a salt-based latent catalyst (*M 1448*) which consists of a 65 wt% aqueous solution of (2-hydroxyethyl) ammonium nitrate (*Wiz chemicals*). It has a density of 1.2 g/cm^3 and a boiling temperature of 100°C.

Figure 2-4: Photos of the used viscous PFA resin (left) and the catalyst (right).

2.2.4 Other chemicals

In addition to distilled water, for dilution and cleansing purposes some organic solvents were used such as denatured ethanol C_2H_6O at 99% (boiling point 78.4°C) and acetone C_3H_6O (boiling point 56°C) (PubChem, 2021).

2.3 Ink preparation- Formulation step

2.3.1 Paste mixing method

The slurries or 'pastes' were prepared by first adding the catalyst to the resin and manually mixing the two fluids. The mixture was then poured into a planetary mixer (*KitchenAid 5KSM3311X*) and the cellulose powder was gradually added for 5 min while mixing at 120 rpm. The slurry was further blended for 15 minutes at 180 rpm and then 5 min at 200 rpm. The resulted paste is then manually loaded in 55 cm^3 syringes with precaution to avoid creating any air bubbles and voids. These

cartridges are sealed and then placed in a refrigerator at 4-5°C before further processing. An illustration of the different slurry preparation steps is given in Figure 2-5. The mixing time was fixed based on microscopic visualization of the slurry homogeneity. Further mixing can help the vaporization of water however in the present study the mixing was limited to 30 min.

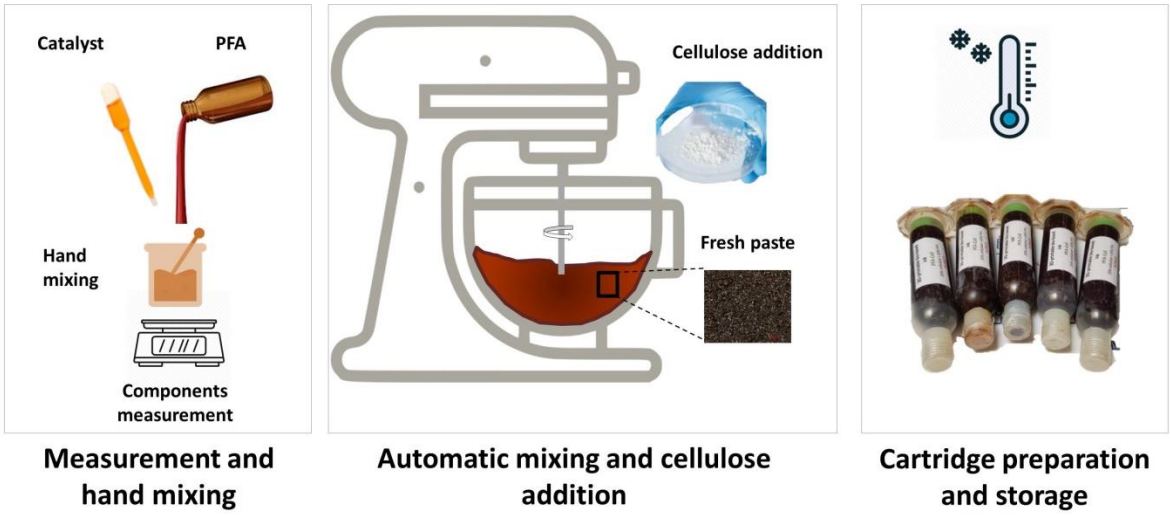

Figure 2-5: Illustration of the paste preparation method.

In this study, different formulations were tested with different cellulose fractions and water content. As a first step, preliminary formulations were tested using different fiber morphology, different solvent content, and different resin/cellulose ratios. After a better definition of the concentration ranges of every component, more formulations were prepared with and without added water. All tested formulations are placed on the Ternary diagram in Figure 2-6.

The preliminarily tested formulation zone highlighted in the red triangular zone and the detailed weight ratio of the components are detailed in Table 2-2. Cellulose weight fraction ranged from 10 wt% to 32 wt% and solvent from at least 19 wt% to 28 wt%. Two different solvents were tested, water and ethanol to compare their effect on drying and solidification of the slurries

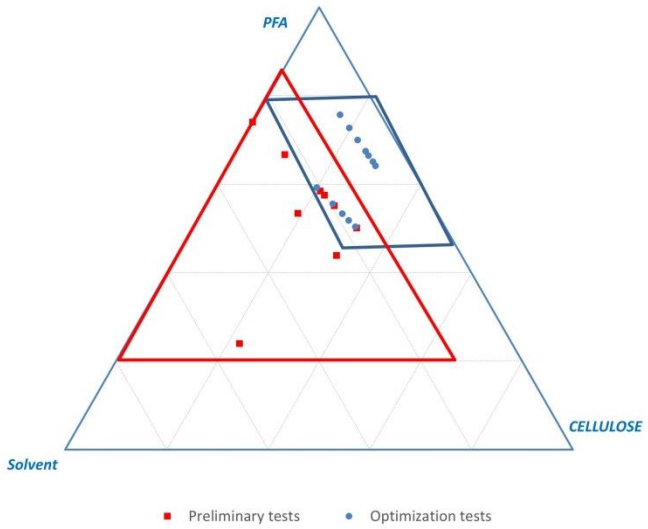

Figure 2-6: Ternary diagram with weight fraction (wt%) of cellulose, solvent, and PFA resin. The red zone is presenting the preliminary testing area and the blue is the optimization zone formulation. On the top is presenting 100 wt% of PFA on the right 100 wt% cellulose and the left 100 wt% solvent.

Table 2-2: Preliminary testing formulations.

Formulation	PFA wt%	Solvent wt%	Cellulose wt%
IF-01-L	58.42	20.53	21.05
IF-01	58.42	20.53	21.05
IF-02	53.37	27.40	19.23
IF-03	55.11	19.36	25.53
IF-04	43.82	24.61	31.58
IF-04-E	43.81	24.61	31.58
IF-05-E	53.37	27.40	19.23
IF-06	76.60	23.40	0.00
IF-07	68.94	21.06	10.00

After the preliminary tests, more formulations were prepared to optimize and study the effect of cellulose addition on the 'ink'. These formulations are in the blue zone in Figure 2-6. First formulations set was conducted with PFA resin diluted with 25% water (the dilution limit of PFA) yielding solvent weight fraction in the formulation ranging from 15 to 19% and the cellulose weight fraction was between 20 and 32%. The respective weight fractions of this set of formulations are detailed in Table 2-3.

Thereafter, a new set of formulations without any added water are done and detailed in Table 2-4 containing from 6 to 7.5 wt% of water content depending on the PFA polymer content and cellulose content from 16 to 29 wt%. The latter formulations were the most studied and characterized in the present study. The weight (W) fractions of the cured composite were calculated considering that during the crosslinking 100% of water was evaporated (both added and condensation water). Although it has been reported in the literature that only half of the water is supposed to evaporate, the water content in the slurries is low (under 7.5 wt%), which allows neglecting the weight contribution of residual water in case of a partial evaporation (Domínguez and Madsen, 2014).

Table 2-3: Optimization of paste composition with 25% resin dilution.

	Slurry component by weight			Slurry component by volume			Composite by weight	
Formulation	PFA wt%	Solvent wt%	Cellulose wt%	PFA vol%	Solvent vol%	Cellulose vol%	PFA wt%	Cellulose wt%
PFA-Cell20-A	61.28	18.72	20.00	62.52	20.44	17.04	74.75	25.25
PFA- Cell25-A	57.44	17.55	25.01	59.15	19.34	21.51	68.93	31.07
PFA- Cell28-A	55.16	16.85	28.00	57.11	18.68	24.21	65.56	34.44
PFA- Cell30-A	53.61	16.38	30.01	55.73	18.22	26.05	63.31	36.69
PFA- Cell32-A	52.07	15.91	32.02	54.33	17.77	27.90	61.10	38.90

Table 2-4: Optimization of the formulation without added water.

	Slurry component by weight			Slurry component by volume			Composite by weight	
Formulation	PFA wt%	Solvent wt%	Cellulose wt%	PFA vol%	Solvent vol%	Cellulose vol%	PFA wt%	Cellulose wt%
PFA-Cell16-B	76.60	7.40	16.00	81.84	4.95	13.20	82.22	17.78
PFA- Cell19-B	73.65	7.12	19.23	79.23	4.79	15.98	78.72	21.28
PFA- Cell22-B	70.93	6.85	22.22	76.78	4.64	18.58	75.51	24.49
PFA- Cell25-B	68.39	6.61	25.00	74.47	4.51	21.03	72.55	27.45
PFA- Cell28-B	66.03	6.38	27.59	72.30	4.37	23.33	69.81	30.19
PFA- Cell29-B	65.14	6.29	28.57	71.46	4.32	24.21	68.77	31.23

2.3.2 CNT suspensions preparation

CNTs were received in powder form; hence a suspension preparation step was needed. In this work, we chose to prepare the suspension using ethanol as carrier liquid for optimal dilution of the PFA resin and an easier solvent evaporation. Suspensions of 1 wt% of CNT in ethanol were prepared by hand stirring with added dispersant agent provided by the supplier which is a mixture of nonionic surfactants in polymerized form (*Nanoamor 8011YJ, USA*). The dispersant was added at different concentrations following the supplier's recommendations depending on the used CNT type and morphology. The dispersion of these nanoparticles was carried out at first with sonication. This ultrasonic treatment was applied by introducing a titan base probe powered by a *Branson 250* ultrasounds generator. All the suspensions were sonicated in discontinues mode for 30 min with 10 min intervals to avoid over-heating. Moreover, the suspensions were covered and placed in an ice bath to limit solvent vaporization. Afterward, the CNT suspensions were further homogenized using an ultra-turrax for 5 min at 10,000 rpm, the speed and duration were limited to prevent CNT breakage. The resulted 1% CNT suspensions were then stored in well-sealed bottles to prevent any solvent evaporation for further use. A visual illustration of the suspension preparation process is presented in Figure 2-7.

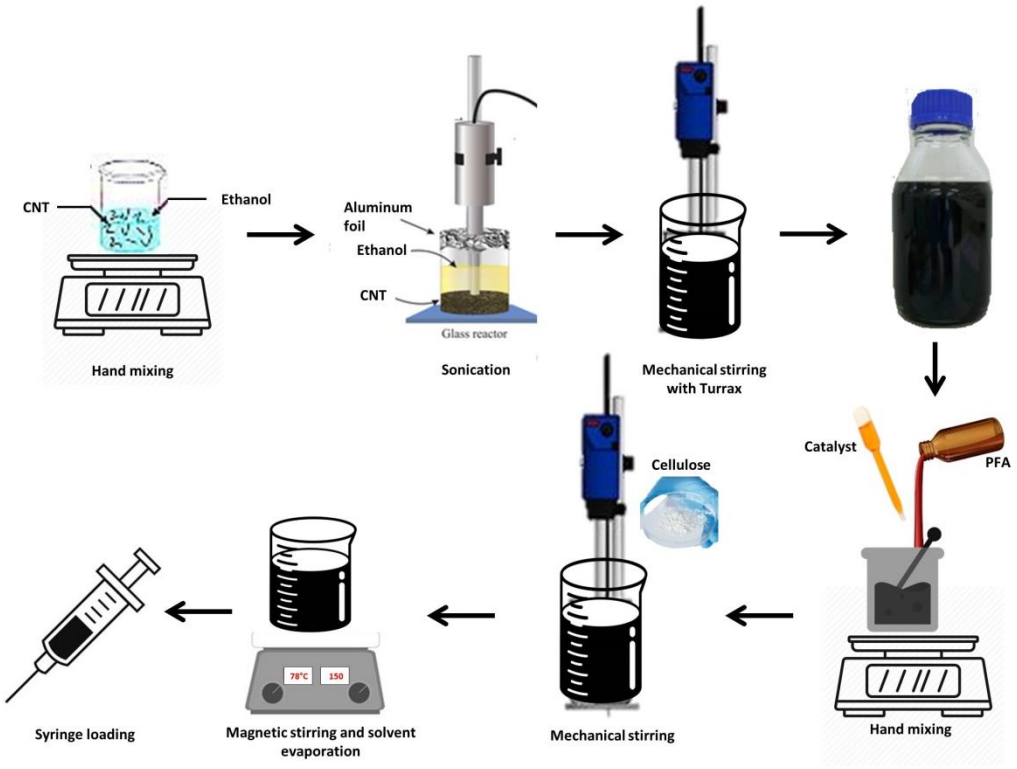

Figure 2-7: Illustration of CNT/PFA/Cellulose mixing and preparation.

2.3.3 Electrically conductive ink formulations

To prepare printable inks with suitable electrical conductivity several conductive fillers were added into the PFA resin. First, graphite and graphene powders were directly added with different concentrations to PFA resin and the cellulose powder was then added when needed. Therefore, CNT-based formulations were prepared using the previously prepared CNT-ethanol suspensions. To do so, PFA resin and catalyst were added to CNT and then hand mixed. The cellulose was gradually added while mixing using the ultra-turrax at 7000 rpm for 10 min. The mixture is then placed on a hot plate with magnetically continuous stirring. The hot plate temperature was fixed at 78°C to evaporate the excess solvent.

The different prepared formulations are displayed on the zoomed Ternary diagram in Figure 2-8.

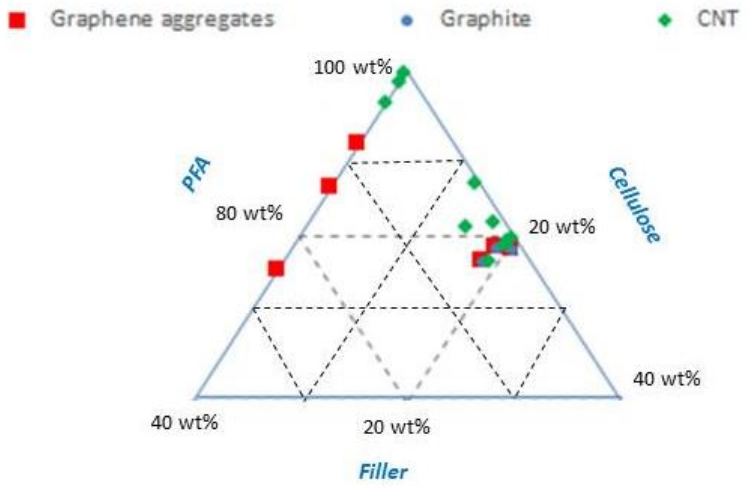

Figure 2-8: Ternary diagram with weight fraction (wt%) of conductive fillers (graphene aggregates in red, graphite in blue, and CNT in green), cellulose, and PFA resin.

For comparison reasons, similar formulations were prepared using graphene and graphite powders. The preliminary formulation prepared using the DWCNT-L adding different cellulose and CNT concentrations. For further optimization, CNT supplied by Nanoamor were used, and different formulations using either DWCNT or MWCNT-short were prepared with different concentrations of conductive fillers and cellulose. These formulations will allow to study the effect of CNT morphology and concentration and cellulose addition on the ink rheology and electrical conductivity. The formulations contained from 1% to 24% of nanoparticles (graphene, graphite, CNT) and from 0 to 21 wt% of cellulose powder. The detailed formulations are listed in Table 2-5.

Table 2-5: Conductive formulations detailed weight ratios and fillers type.

Filler type	Formulation reference	PFA	Fillers	Cellulose
Graphene aggregates	Gr-9	91.0	9.0	0.0
Graphene aggregates	Gr-14	86.0	14.0	0.0
Graphene aggregates	Gr-24	76.0	24.0	0.0
Graphene aggregates	Gr-1.3	78.2	1.3	20.5
Graphite Powder	G-1.3	78.2	1.3	20.5
Graphene aggregates	Gr-2.5	78.3	2.5	19.1
Graphite Powder	G-2.5	78.3	2.5	19.1
Graphene aggregates	Gr-4.7	76.7	4.7	18.6
Graphite Powder	G-4.7	76.7	4.7	18.6
DWCNT-L	DWCNT-1	86.10	0.65	13.25
DWCNT-L	DWCNT-2	81.52	1.18	17.30
DWCNT-L	DWCNT-3	79.30	1.20	19.50
DWCNT	DCNT-4-19	76.5	4.0	19.5
MWCNT-Short	MCNT-4-19	76.5	4.0	19.5
DWCNT	DCNT-4-15	81	4.0	15.0
MWCNT-Short	MCNT-4-15	81.0	4.0	15.0
DWCNT	DCNT-4	96.0	4.0	0.0
MWCNT-Short	MCNT-4	96.0	4.0	0.0
DWCNT	DCNT-1.5-19	79.0	1.5	19.5
MWCNT-Short	MCNT-1.5-19	79.0	1.5	19.5
DWCNT	DCNT-1.5	98.5	1.5	0

Filler type	Formulation reference	PFA	Fillers	Cellulose
MWCNT-Short	MCNT-1.5	98.5	1.5	0
DWCNT	DCNT-0.5-19	80.0	0.5	19.5
MWCNT-Short	MCNT-0.5-19	80.0	0.5	19.5
DWCNT	DCNT-0.5	99.5	0.5	0.0
MWCNT-Short	MCNT-0.5	99.5	0.5	0.0

2.4 Composite manufacturing– Process step

2.4.1 Bulk composite molding

To study the effect of cellulose addition and the overall composite behavior and characteristics, bulk composites specimens were prepared. First, the cold slurries were placed in an oven at 50°C for 5 min to decrease their viscosity and facilitate their processing. The biocomposites were prepared using a simple hand casting in open poly(tetrafluoroethylene) molds. The molding was done manually and without any additional constraints, yet avoiding creating any voids because of the sticky nature of the slurries. The used open molds are designed for every specific specimen shape. Although in the literature the PFA-based composites are usually molded under pressure to limit the porosity and the foaming, in this study, we aimed for a simple hand casting with no applied pressure to be able to compare with printed composites which are cured under ambient pressure.

2.4.2 3D printing by cold extrusion

2.4.2.1 The used modified 3D printer

The main used machine for additive manufacturing is a commercial 3D printer *Artillery sidewinder (China)*. The printing platform moves in the Y-axis whereas the printing head moves in x and z axes. This printer is designed for fused filament printing and was upgraded with a Direct Ink Writing (DIW) extruder fabricated by *WASP (Lombardia, Italy)* originally designed for clay extrusion and compatible with many concentrated pastes. This extruder was fixed on the printing head thanks to a designed support which can be easily eclipsed and when needed disconnected when needed (Figure 2-9-1).

The paste formulation is fed to the extruder using a pressure syringe of 55 cm^3 with a modified straight Luer taper with an internal diameter of 4 mm to avoid constrictions and flow direction

change (faced in the original syringe system). The paste is fed thanks to air pressure applied with a plastic plunger and the adapter (Figure 2-9-2).

The WASP extruder is composed of an Archimedes screw-driven device, an extruder body tipped with a cylindrical barrel where the screw can rotate thanks to the action of a step motor. At the end of the barrel, there is an interchangeable nozzle with different outlet diameters. The X-ray tomography images of the nozzles revealed an inner shape with two successive constrictions from a diameter of approximately 5 mm to the final outlet diameter of 1.2-0.5 mm (Thibaut, 2020) (Figure 2-9-3). According to the supplier's information, this extruder can apply up to 40 bars of pressure to the paste.

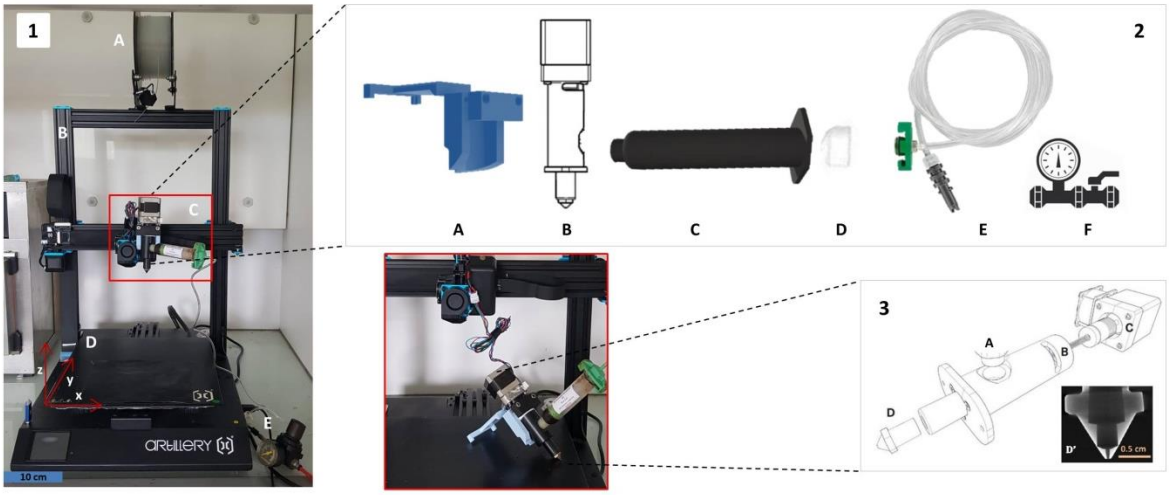

Figure 2-9: Photo of the modified 3D-printed Artillery sidewinder and the WASP extruder.

The different described parts in the printer and the printing head are shown in Figure 2-9 and the designation of the spare part is detailed in Table 2-6.

Table 2-6: Modified DIW 3D-printer spare parts designation.

image	Part number	Description	Supplier
1	A	PLA filament coil	
	B	Printer chassis	Artillery
	C	Extruder head	Artillery
	D	Platform (printing bed)	Artillery
	E	Manometer	
2	A	Extruder support	3D Printed and designed in LGP2

image	Part number	Description	Supplier
	B	DIW extruder	WASP
	C	Pressure syringe 55 cm^3	Doseurope (modified)
	D	Plastic plunger	Doseurope
	E	Dispensing syringe adapter	Doseurope
	F	Compressed air outlet	
3	A	Cavity for material introduction	WASP
	B	Extruder body	WASP
	C	Step motor with screw-driven device	WASP
	D	Steel nozzle	WASP
	D'	X-ray Computed Tomography (XCT) scan of the nozzle	

2.4.2.2 Slicing software

Slicer software is properly named as it virtually "cuts" the 3D digital model into 2D layers which will be later printed by the 3D printer. In other words, the slicer software is our tool to communicate with the machine and the used language is G-code. In this work the used slicer was *Simplify 3D*. The inputs of this software are; (i) the CAD models in format *.stl*, (ii) different printing parameters introduced by the user, and (iii) information about the used printer and material. The single output of the software is a digital file with detailed instructions in form of G-code commands. The G-code commands define the x,y,z tracks coordinates, printing speed, and the extrusion flow of the materials. The extrusion flow is an important parameter that must be controlled and verified to have a coherent printing with continued well-aligned roads. The extrusion flow calculated by the software is directly related to the road's width, the layer's height, and the printing speed. The needed material volume per unit of time is then translated to a linear velocity of the plastic filament fed to the extrusion head (length per unit of time) which is calculated based on its diameter (usually 1.75 mm). As in our work the used extrusion head is an Archimedes screw pump, a relation between the linear extrusion velocity and the rotation speed of the extruder was determined and an extrusion correction factor was determined after performing several extrusion calibrations on the used pump which will be detailed in chapter 5.

As mentioned before, the user can program several printing parameters, illustrated in Figure 2-10, such as;

- Nozzle diameter.
- Layer height: the thickness of the layer deposited by nozzle tip.
- Road width: is the width of the material bead used for rasters. The value of raster width varies based on nozzle tip size.
- Raster angle: refers to the angle of the raster pattern with respect to the X-axis on the bottom part layer.
- Infill percentage: is the percentage of the layer area covered with the deposited material.
- Outline Overlap: is the percentage of the distance of superposition between the outlines and the infill roads.
- Outline Shell: the number of outlines.

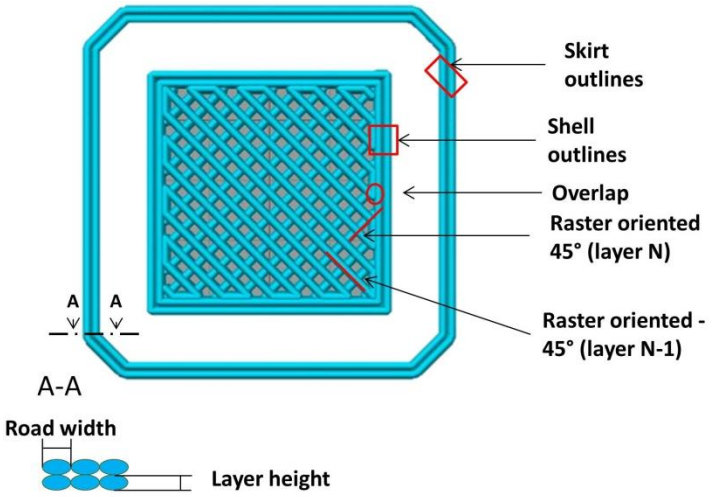

Figure 2-10: Simulation of printed cube done with Simplify3D.

2.4.2.3 Optimization of flow extrusion and printing parameters

Ink formulation is an important step to obtain a printable materials but an adaptable 3D printer with optimized printing parameters and calibrated extrusion flow is also a primordial variable for successful printing.

2.4.2.3.1 Extrusion flow calibration

As mentioned previously in section 2.4.2 (p.120), the FFF commercial printer was upgraded with a DIW extruder suitable for paste extrusion. On the other hand, the software is designed for managing the extrusion flow of a conventional thermoplastic extruder fed with a continuous filament with

known diameter. In the case of volumetric/screw pumps, the filament diameter must be provided in couple with the calibration factor just to allow the slicer to correlate the volume flow of extruded material with the pump angular speed. The calibration should be done for a specific material, using a specific nozzle and extruder head. In the present study, the calibration is done on the PFA-Cell28-B formulation using 0.72, 1 and 1.2 mm nozzle diameters. Using the software control panel, or by directly coding an extrusion command (G1 Ex Fy) it is possible to fix the number of revolutions and the rotation speed of the screw pump to obtain its characteristic flow curve by weighing the mass of extruded material when varying the rotation speed with a constant number of revolutions and fluid feed pressure. The mass flow can be calculated and therefore the volume flow can be concluded based on the paste's density (measured according to the method described in 2.6.2.1 p.130). To do so, the rotation speed ranged from 25 rpm to 400 rpm, and for extrusion velocity, the extruded filament was weighed. Every mass measurement was repeated at least 3 times and weighed to within ±0.0001 g. The calculation details will be detailed further in chapter 5.

2.4.2.3.2 Printing parameters optimization

Besides developing and optimizing the rheology and the printability of the paste and calibrating the extrusion flow for a continuous and homogeneous flow, the printing parameters have a major effect on the printing quality and the final material's mechanical performances. Therefore, the effect of road parameters and raster angle on mechanical performance and the effect of infill percentage and printing height on dimensional accuracy was studied.

Effect of Layer and road parameters

To optimize the effect of layer and road parameters as well as studying the independent effect of each of the parameters, bending bars specimens were printed with different layer heights, road width, and extrusion flow. For every different parameter combination of at least 10 specimens were prepared for further mechanical testing according to the method described in section 2.6.4.8 (p.135) of this chapter. The parameters that were held constant during the printing process of this set of specimens are given in Table 2-7.

Table 2-7: Constant parameters for studying the effect of road's parameters.

Parameter	value
Printing speed	900 mm/min
Nozzle diameter	0.72 mm
Formulation	PFA-Cell28-B
Raster angle	45°/-45°
infill	100%
Shells number	2
Overlap	0%
Feeding pressure	3 bar

The studied variable parameters are detailed in Table 2-8. The layer height (H%) ranged from 50% to 90% and the width (W) was varied from 100% to 120% of the nozzle's diameter. The last parameter to be studied is the extrusion flow (E%) which was varied by increasing the extrusion multiplier by 10 to 30% to have an over-extrusion.

Table 2-8: Set of variable rod parameters.

Code	H (%)	W (%)	E (%)
H0.6	90	100	100
H0.5	80	100	100
H0.4	65	100	100
H0.3	50	100	100
W0.8	65	120	100
W1	65	150	100
E1.1	65	100	110
E1.2	65	100	120
E1.3	65	100	130

Effect of raster angle

The raster orientation is another printing parameter. The effects of 3 raster angles on flexural properties were chosen to be studied. At least 10 specimens were printed (3D sliced models are presented in Figure 2-11) for each raster angle while maintaining several printing parameters constant (listed in Table 2-9).

Table 2-9: Constant parameters for studying the effect of raster angle.

Parameter	value
Printing speed	900 mm/min
Nozzle diameter	0.72 mm
Formulation	PFA-Cell28-B
Shells number	0
Infill	100%
Feeding pressure	3 bar

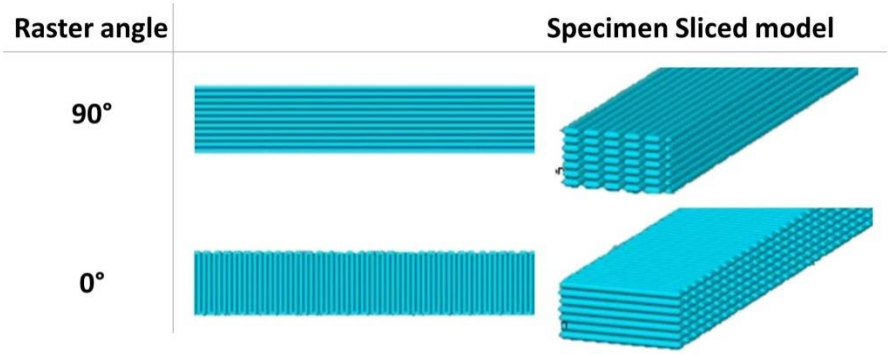

Figure 2-11: 3D sliced model of tensile specimens with different raster angles.

Effect of Infill percentage on dimensional accuracy

DIW is a challenging technique when it comes to unsupported areas and high object printing as the object is not yet solidified and is only supported by viscous forces. To assess the dimensional accuracy, a rectangular cuboid with a 2.00 cm square cross-section with a height from 2.5 to 7 cm was printed with a varied infill from 25% to 75% as shown in Figure 2-12. The shape fidelity to the 3D model is evaluated and the quality and horizontality of the solid top layer are assessed.

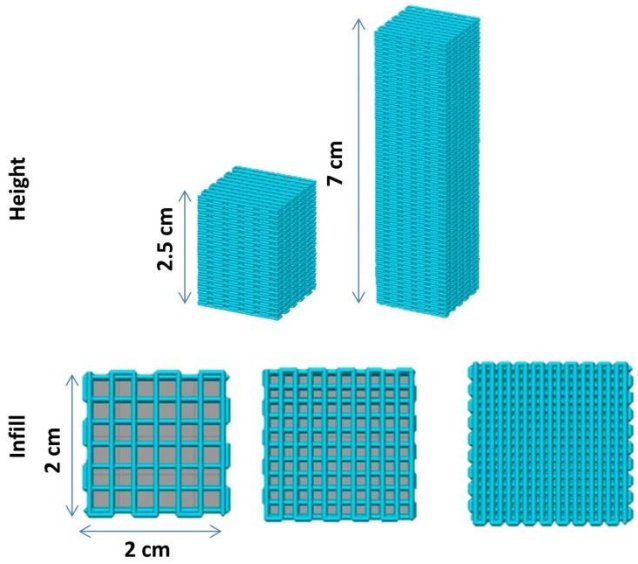

Figure 2-12: 3D model of a sliced cuboid with low infill and important height (on right) and with high infill and low height (on left).

2.4.3 Curing process

The crosslinking step is done by a thermal treatment in an open-air lab oven. The thermal treatment starts at a temperature inferior to 90°C overnight followed by a step post-curing for 3 hours at 130°C.

2.5 Pyrolysis step

After formulating inks, the resulting cured composites can be carbonized thanks to the use of poly(furfuryl alcohol) polymers which have a char residue of at least 50 wt% as discussed in chapter 1. The pyrolysis step is performed to yield a carbon/carbon composite which increases the EC of both conductive and structural materials.

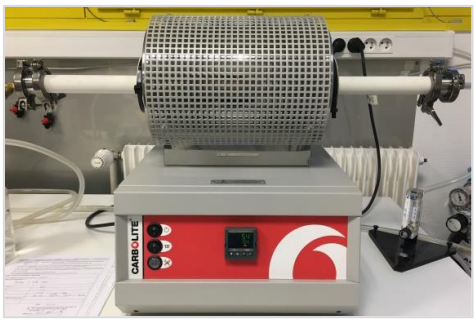

Figure 2-13: Carbonization oven Carbolite® Type 3216.

The pyrolysis of cured composites was done in a tubular oven (*Carbolite®, type 3216*) under nitrogen flux (Figure 2-13). The heating program is determined based on the TGA test results. This heating

schedule, listed in Table 2-10, is slow and meticulous to avoid any deformation or break caused by violent volatiles release.

Table 2-10: Carbonization heat treatment program.

T range (°C)	Heating rate (°C/min)	Dwell time at final temperature (min)
Tamb-150	5.0	15
150-300	10.0	30
300-450	0.1	60
450-800	0.1	60
800-950	0.2	15

2.6 Characterization methods

In every step of the research and development, process characterization and assessment is the key to a better understanding and a wiser progress. In the next paragraph, the different techniques used for analysis and characterization will be described.

2.6.1 Raw materials characterization

2.6.1.1 Nuclear magnetic resonance spectroscopy (NMR)

To analyze the structure and composition of the commercial PFA and cellulose powder, ^{13}C and ^{1}H NMR investigations were done on both liquid and solid polymers. Spectroscopic measurements were recorded on a Bruker AVANCE400 spectrometer *(Billerica, MA, USA)* equipped with a 5 mm BB/19F-1H/d Z-GRD probe operating at 100.612 MHz for ^{13}C, and 400.130 MHz for ^{1}H. For solid-state RMN the sample was compacted in 4 mm ZrO_2 rotors while the liquid NMR measurements were performed on PFA samples dissolved in DMSO-d6 and placed in a 10 mm tube.

2.6.1.2 Fourier transform infrared spectroscopy (FTIR)

Chemical structure characterization is conducted with a *PerkinElmer* FT-IR spectrometer *(Perkin Elmer, USA)*. For solid samples analysis, each sample was grounded and then mixed with KBr powder with a ratio of 1:125 for pellets preparation. The spectra were acquired in a frequency range of 4,000-500 cm^{-1} with a resolution of 4 cm^{-1} and then corrected with the environmental spectrum. For liquid resin analysis, the sample was placed between two NaCl plates after removing the water.

2.6.1.3 Polymerization degree determination

For the characterization of molecular weight and polymerization degree (DP) of PFA, the matrix-assisted laser desorption/ionization mass spectrometry (MALDI-TOF-MS) was used. It is an ionization technique applied for the analysis of large organic molecules. This technique produces ions from large molecules using a laser energy-absorbing matrix. The ions are then accelerated and the time of flight is analyzed which is directly related to their molecular weight (heavier molecular longer time of flight). In this work, the PFA sample was analyzed by Autoflex Speed *(Brüker Daltonics, USA)* and the scan is realized between 50 to 2,000 m/z.

The DP of cellulose was measured according to ISO 5351:2010 standard. Intrinsic viscosity (η_{int}) of cellulose dissolved in copper (II) ethylenediamine was measured and then the DP was deduced using the Mark– Houwink–Sakurada equation. Two measurements were made.

2.6.1.4 Crystallinity index

Wide-angle X-ray diffraction diagrams (XRD) spectra were used to determine the crystallinity index (CI) of cellulose. The powder sample is placed above a zero background holder and a *X'Pert PRO MPD* diffractometer was used to make the measurements at room temperature with a monochromatic CuKα radiation source (radiation λ = 1.5419 Å) in step-scan mode with a 2θ angle ranging from 5° to 56° with a scanning time of 10 min.

The cellulose CI (%) was determined according to the peak height method as described in eq 1:

$$\mathrm{CI} = \frac{(\mathrm{I}_{002} - \mathrm{I}_{\mathrm{am}}) \cdot 100}{\mathrm{I}_{002}} \qquad \textit{eq 1}$$

where I_{002} represents the diffraction intensity of the main crystalline peak at 2θ ~ 22.5˚ and I_{am} the intensity at 2θ ~ 18.7˚.

2.6.1.5 Fibers morphology and size distribution

The fiber length and width distributions were measured using the *Morfi®* approach (*Techpap®, Grenoble, France*) (Passas et al., 2001). Furthermore, the size distribution of the particles was measured using a granulometer (*Cilas particle size analyzer 1190*) based on the Fraunhofer method.

2.6.2 Paste characterization

2.6.2.1 Density

To measure the density of the paste, a 5 cm long filament was first extruded using a 1 mm diameter nozzle. The filament was then weighed and its real diameter was further measured using a binocular microscope. The density was measured as the ratio between the weight and the volume of the extruded filament. The test was done on 5 filaments.

2.6.2.2 Rheology

To assess the rheological behavior of the pastes and the resin, a parallel plate of 25 mm in diameter was used on an *MCR 301* rheometer *(Anton Paar, Austria).* The gap between the plate and the platform was set to 1 mm and the temperature was fixed at 25°C. Before any rheological measurements, the fluids were sheared at a shear rate of 100 1/s for 200 seconds, followed by a rest of 200 seconds to remove any previous shear history. The samples were covered during the tests to avoid any solvent evaporation.

To perform the flow curve experiments, the shear rate was increased from 0.1 to 100 1/s or 1000 1/s depending on the paste nature during which the viscosity was recorded.

To assess the thixotropic behavior of the pastes, the shear rate was fixed at 100 1/s for 60 s before a sudden drop to 0.1 1/s. The rheological behavior in terms of viscosity trends as well as stress response was evaluated as a function of time.

Oscillatory tests were also conducted to evaluate the viscoelastic properties of the prepared pastes. To do so, amplitude sweep tests were performed at the frequency of 1 Hz and strain ranging from 0.001 to 100%. The evolution of the storage modulus (G') and loss modulus (G"), as a function of strain, or stress was analyzed.

To check the reproducibility of the rheological measurements especially when using concentrated slurry the tests were duplicated at least 3 times.

2.6.3 Curing characterization

2.6.3.1 Differential Scanning Calorimetry

The thermal analysis of the thermosetting PFA resin and the paste was performed by Differential Scanning Calorimetry (DSC) using *TA DSC Q-100* apparatus *(TA Instruments, USA)*, equipped with a liquid nitrogen cooling system unit. An average of 10 mg of each sample was ppplaced in a closed

aluminum crucible and heated from 40°C to 200°C at 5 °C/min under airflow. The enthalpy values were calculated based on the effective PFA weight in the sample without considering the water and catalyst weight ratios.

2.6.3.2 Soxhlet extraction

To better understand the curing kinetics and behavior of the PFA resin, samples of PFA cured with different crosslinking degrees were prepared. The crosslinking degree was varied mainly via the crosslinking time while keeping the curing temperature and the composition constant. Later, the crosslinked polymer ratio (gel content) was determined by soxhlet extraction. Approximately 6 g of the liquid resin with 5 wt% catalysts were introduced in an aluminum pan to form a thin disc. After precisely weighing the sample, the pan was introduced in a previously heated oven where the temperature is controlled thanks to a thermocouple device. After curing for a variable time, the sample is weighed to conclude the water evaporated.

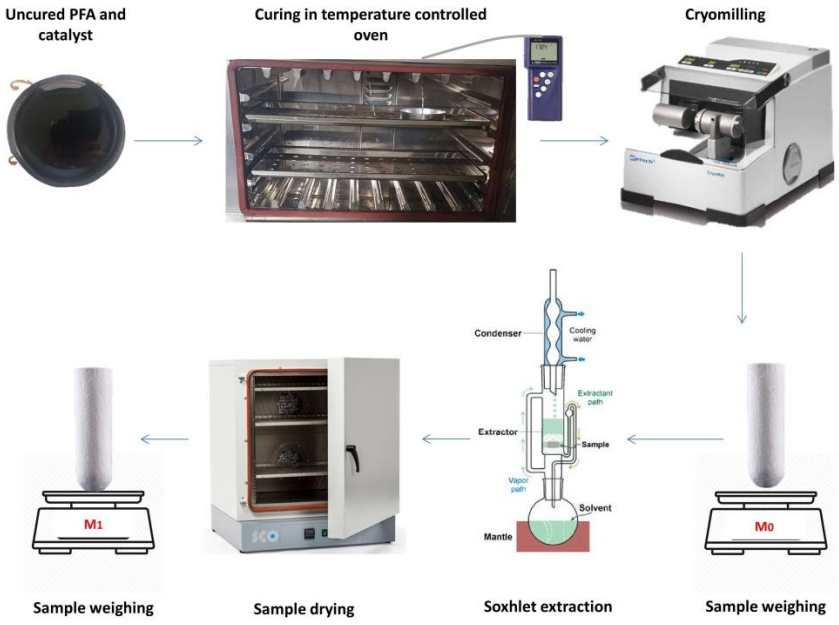

Figure 2-14: Soxhlet extraction experiment steps illustration.

This procedure is repeated for different temperatures and different duration (from few minutes to few hours depending on the curing temperature). The cured or semi-cured samples are then milled using a cryomiller (*Retsh*) for 4 min at 30 Hz frequency to obtain a fine powder. Then, about 500 mg of the powder are introduced into cellulosic soxhlet thimble; the sample was weighed to within ±0.0001 g (M_0). The sample was then loaded in a 100 ml soxhlet using acetone as a solvent heated using a heating mantle. The extraction lasted 8 hours per extraction for every sample. Then the

sample was dried in an oven heated at 60°C for few hours to evaporate the remaining solvent. The insolubilized sample fraction was then weighed to within ±0.0001 g (M_1). The gel fraction G% (unsolubilized) was then calculated as in equation eq 2 which is directly related to the crosslinking rate (Hirschl et al., 2013). The soxhlet extraction steps are illustrated in Figure 2-14.

$$G\% = \frac{M0-M1}{M0} \cdot 100 \qquad \textit{eq 2}$$

2.6.3.3 DMA shear mode

To study the viscoelastic properties of the paste during crosslinking, a shear specimen holder for pasty materials *PEC1013000* was used on a DMA apparatus *Metravib50 (METRAVIB-ACOEM, France)*. The measurements were conducted in an isothermal mode at temperatures between 70 and 120°C. The paste was placed in a hollow aluminum cup fixed to the bottom part of the DMA apparatus and a plunger was fixed on the top part as showed in Figure 2-15. The reactive paste was placed in the air gap of the cup-piston system. The DMA applies uniaxial stress from top to bottom, so the reaction mixture is sheared. On a temperature level, we can therefore follow the progress of the polymerization as a function of time by analyzing the evolution of the modulus G', and G''.

In the present work, the hollow part of the cup has a height of 5 mm and a diameter of 10 mm whereas the plunger has an 8 mm diameter. Therefore the gap volume (paste volume) between the two parts is 142 mm^3. The dynamic vertical displacement (D dyn) was fixed at 1 µm with a 1 Hz frequency.

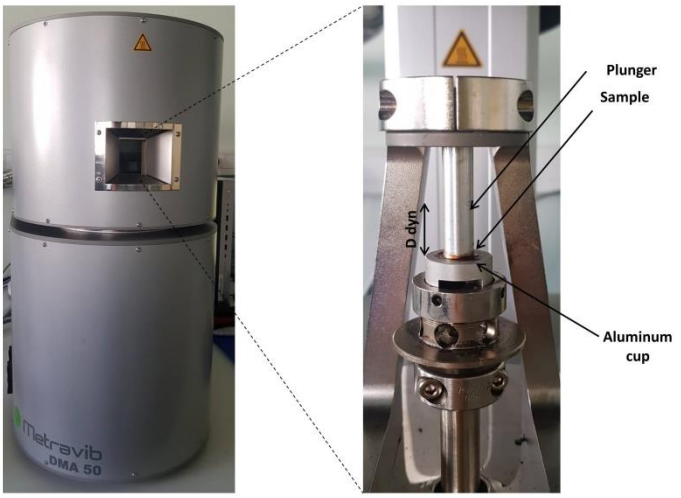

Figure 2-15: DMA Metravib50 and paste shearing specimen holder.

2.6.4 Cured composite characterization

2.6.4.1 Dimension measurement

To evaluate the shrinkage upon crosslinking of the neat PFA and the biocomposites, the French standard NF 51-401 was followed. 5 specimens of 80 mm × 10 mm × 4 mm were prepared for each sample according to the protocol described in section 2.4.1 (p.120). The samples were then placed in a normalized atmosphere for 24 hours before measuring their length L' after curing, using a digital caliper (±0.01 mm). The measurement was repeated at least 5 times on every specimen for a total of 5 specimens per sample. The shrinkage upon curing R% was calculated according to equation eq 3.

$$R\,(\%) = \frac{L'}{L} \cdot 100 \qquad \textit{eq 3}$$

2.6.4.2 Porosity and density measurement

To measure the closed porosity in the composite and the Neat cured PFA, 2.5 cm square specimens with 2 mm thickness were cured overnight at 90°C and 130°C. The Buoyancy method was used (ASTM D792) to measure the experimental density (D_{ex}) with a surfactant aqueous solution as test liquid (Figure 2-16). The theoretical density (D_{th}) was calculated by considering that the cured PFA was perfectly compact using the rule of mixtures and D_{PFA}= 1.36 g/cm^3 (Domínguez and Madsen, 2015) and D_{cell}= 1.5 g/cm^3 as the respective densities of the cured PFA and cellulose. The porosity percentage in the composites was calculated based on the equation eq 4:

$$P\,(\%) = \frac{(D_{th} - D_{ex}) \cdot 100}{D_{th}} \qquad \textit{eq 4}$$

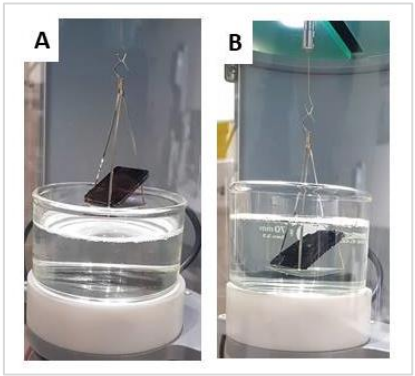

Figure 2-16: Density measurement with Buoyancy method. (A) measuring the dry weight (B) measuring the wet weight.

2.6.4.3 Humidity and water sensitivity

To assess the composite sensitivity to humidity, samples of the cured composite and neat PFA along with cellulose powder were placed in a *Varimass®* apparatus developed in the LGP2. The relative humidity (RH) was controlled and the mass variation was recorded during the entire test via an integrated precision balance. The humidity program consisted of 3 cycles. In the first cycle, the humidity was fixed at 50% for 2 hours. The second cycle started with two hours at low humidity (20%) followed by two hours at 50%. The third cycle started with two hours at a high humidity level (90%) followed by stabilization at 50% for two extra hours.

2.6.4.4 Microscopic observations

The morphology of both fillers and the composite surface and cross-section were investigated by scanning electron microscopy (SEM). The specimens were gold coated and examined using a *QuantaFEG250* instrument. The accelerating voltage was fixed at 2.50 kV and the magnitude between 60 and 2000.

The morphology of the cellulose fibers and powder was further investigated via optical microscopy. The homogeneity of different CNT suspensions (in ethanol with and without PFA) was assessed using *Zeiss Axio Imager M1* optical microscope.

2.6.4.5 Thermogravimetric analysis

Thermogravimetric analysis (TGA) of the different composites and raw materials were performed on *TGA-DSC3+ Mettler Toledo*. Samples of about 13 mg were placed in an open 70 µL ceramic crucible and then heated from room temperature to 1000°C at a heating rate of 10 °C/min. The thermo-oxidative degradation of the composites and the neat PFA were studied under a 40 mL/min oxygen flow and further tests were performed under nitrogen flow of 40 mL/min.

2.6.4.6 Electrical conductivity measurements

The conductivity of dried extruded filament or bulk composites was measured using an ohmmeter (*HP 34401A multimeter*). Hook-type probes were used for an optimized contact with the filament. The electrical resistance between the two ends of the 2 to 5 cm long filament is then measured. The Electrical Conductivity (EC), was calculated following eq 5; with L (m), the length between the two probes, R (ohm), the electrical resistance and S (m^2) the cross-section area of the filament. At least triplicate was performed for every composite.

$$EC = \frac{L}{R \cdot S} \qquad \textit{eq 5}$$

2.6.4.7 Dynamic mechanical analysis: bending mode

The thermo-mechanical dynamic properties, such as storage modulus G', were studied with a Dynamic Mechanical Analyzer (DMA) *Metravib50 (METRAVIB-ACOEM, France)*. Tests were realized using 3 points bending mode with a temperature scan ranging from 25°C to 300°C at a 2°C/min heating rate with 1 Hz frequency. The static force had an average value of 25 N and the dynamic deformation was ±15 µm. The specimen's dimensions were 40×10×4mm (length, width, and thickness) and were measured precisely for every sample before the scan. Tests in the isothermal mode were also performed to evaluate the thermal stability of composite for prolonged exposure at high temperatures in isothermal mode. At least 3 specimens per sample were analyzed.

2.6.4.8 Mechanical characterization

Before any mechanical testing, most of the composites were conditioned at 23°C and 50% relative humidity for at least 16 h. The mechanical properties were tested with an *Instron Universal* testing machine *(Instron, USA),* and the data analyzed with the help of the *Blue Hill* software. The tensile test was inspired by the ISO 527 standard using the 5A specimen dimension and a crosshead speed of 2 mm/min. The flexural properties were measured according to ISO 178 at a crosshead speed of 2 mm/min.

The obtained data were the average of 10 to 15 measurements. The specimens were prepared by open-air casting molding or by 3D printing, as described above. The surfaces of the samples were polished by sandblasting and the exact dimensions were measured before every test.

2.7 Chapter conclusions

In this chapter, a detailed description of the used materials and methods was provided and the general approach was exposed.

In the second part of this manuscript, the obtained results will be presented and described. Therefore, the next part contains 4 chapters:

Chapter 3: Investigation and characterization of the used commercial raw materials.

Chapter 4: Development and characterization of new bio-based materials for 3D printing by cold extrusion.

Chapter 5: Dealing with process study and composed of two parts:

- Part 1: Understanding the curing process toward a defect-free cured composite.
- Part 2: Optimization of printing parameters for improved additively manufactured composites.

2.8 References

Arnold, E.L., Weager, B.M., Park, A.B.B., Hoydonckx, H.E., Madsen, B., 2011. Next generation sustainable composites: development and processing of furan-flax biocomposites. Int. Comm. Compos. Mater.

Behzadfar, A., Imani, M., Farahmandghavi, F., 2019. Shelf-life of polyfurfuryl alcohol resin: an accelerated rheokinetics study. Polym. Bull. https://doi.org/10.1007/s00289-019-02692-4

Domínguez, J., Madsen, B., 2015. Development of new biomass-based furan/glass composites manufactured by the double-vacuum-bag technique. J. Compos. Mater. 49, 2993–3003. https://doi.org/10.1177/0021998314559060

Domínguez, J.C., Madsen, B., 2014. Development of new biomass-based furan/glass composites manufactured by the double-vacuum-bag technique. J. Compos. Mater. 49. https://doi.org/10.1177/0021998314559060

Flahaut, E., Bacsa, R., Peigney, A., Laurent, C., 2003. Gram-scale CCVD synthesis of double-walled carbon nanotubes. Chem. Commun. 0, 1442–1443. https://doi.org/10.1039/B301514A

Ghimbeu, C., Decaux, C., Brender, P., Dahbi, M., Lemordant, D., Raymundo-Piñero, E., Anouti, M., Beguin, F., Vix-Guterl, C., 2013. Influence of Graphite Characteristics on the Electrochemical Performance in Alkylcarbonate LiTFSI Electrolyte for Li-Ion Capacitors and Li-Ion Batteries. J. Electrochem. Soc. 160, A1907-1915. https://doi.org/10.1149/2.101310jes

Hirschl, Ch., Biebl–Rydlo, M., DeBiasio, M., Mühleisen, W., Neumaier, L., Scherf, W., Oreski, G., Eder, G., Chernev, B., Schwab, W., Kraft, M., 2013. Determining the degree of crosslinking of ethylene vinyl acetate photovoltaic module encapsulants—A comparative study. Sol. Energy Mater. Sol. Cells 116, 203–218. https://doi.org/10.1016/j.solmat.2013.04.022

LG Hemija, 2017. CFF [WWW Document]. http://www.lghemija.co.rs/pages/partners.phphttp://www.lghemija.co.rs. URL http://www.lghemija.co.rs/pages/partners.php (accessed 6.8.21).

Nanoamor, 2021. NanoAmor, Amorphous Products | Nanoscale Products | Nanopowder | Nanoparticles - multi-walled carbon nanotube, Single-Walled Carbon Nanotubes, Carbon Nanotubes, double wall carbon [WWW Document]. URL https://www.nanoamor.com/inc/pdetail?v=1&pid=4017 (accessed 6.9.21).

Passas, R., Voillot, C., Tarrajat, G., Caucal, G., Khelifi, B., Tourtollet, G., 2001. Morfi as a novel technology for morphological analysis of fibers. Recents Progres En Genie Procedes 15, 259–264.

PubChem, 2021. PubChem [WWW Document]. URL https://pubchem.ncbi.nlm.nih.gov/ (accessed 6.9.21).

STREM, 2021. Graphene nanoplatelets (6-8 nm thick x 25 microns wide) | CAS # 1034343-98-0 | Strem Chemicals [WWW Document]. www.strem.com. URL https://www.strem.com/catalog/v/06-0220/12/carbon_1034343-98-0 (accessed 6.8.21).

Thibaut, C., 2020. Développement de matériaux fibreux cellulosiques pour la production d'objets bio-sourcés imprimés en 3D par extrusion (These de doctorat). Université Grenoble Alpes.

Thygesen, A., Madsen, B., Thomsen, A.B., Lilholt, H., 2007. Effect of acidic conditions on interface and strength of cellulose fibres. Interface Des. Polym. Matrix Compos. - Mech. Chem. Model. Manuf. 289–296.

3 Characterization of commercial polymers

Chapter content

3.1 Chapter introduction

Developing a new material requires the utilization of several raw materials or components. These materials can either be synthesized in the laboratory or acquired from a commercial supplier. In this work, the materials are commercially available and were provided by different suppliers around the world as mentioned before. As the main focus of this project is the development and the optimization of a bio-based composite, the use of commercial materials readily available and produced by experts was privileged. This choice comes with several limitations such as poor information and data provided by the supplier about the origin, the structure and the production process of these materials.

In research, knowing the materials which are the building blocks of our composite is primordial. Thus, a complete characterization of these materials is fundamental to identify their main characteristics. This step is primal for a potential material replacement and also to identify the chemical reactivity between the composite components. Therefore, in this chapter, we will provide a thorough chemical and morphological structure and characteristics of the used PFA polymer and cellulose using several analytical techniques. The first part is focusing on characterizing the cellulose powder, while the second part deals with the PFA oligomer.

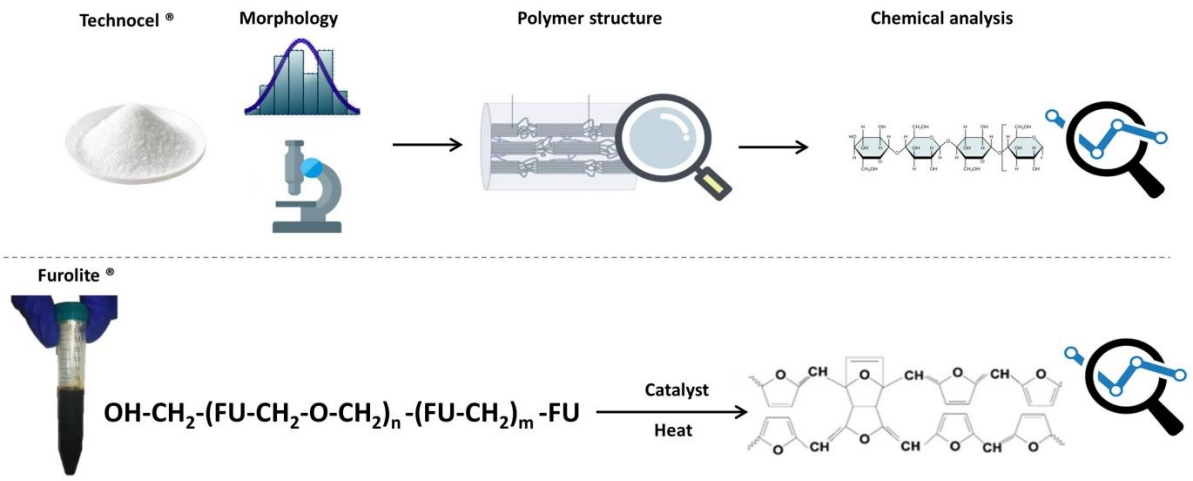

Figure 3-1: Chapter 2 graphic abstract.

3.2 Cellulose fibers and powder

3.2.1 Size distribution

A correct evaluation of the size distribution of the cellulose powder (Cell8) is challenging; although it is considered as a powder, the particles have different morphology with an aspect ratio superior to 1. They can neither be considered as fibers because of their low aspect ratio. The evaluation of their size distribution was done according to two techniques; first, the *Morfi* apparatus was used to evaluate the content of long fibers and their size distribution and that of the 'fines' which are the fibers with a length <80 µm. The Morfi only considers the particles with fiber morphology in its analysis. Therefore, the powder was further evaluated by a granulometer which is mainly used for the estimation of the size of spherically shaped powders to estimate the overall size distribution of the powder.

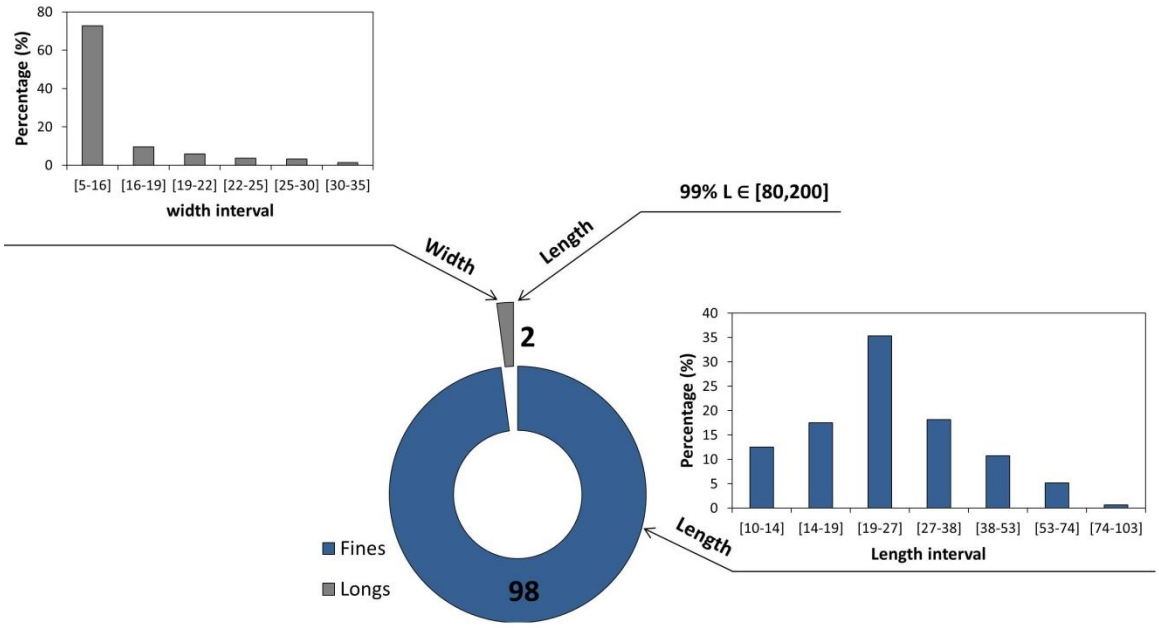

Figure 3-2: Morfi analysis of length distribution of Cell8.

Unsurprisingly, according to *Morfi* analysis data, Cell8 is composed of mainly 'fines' (98%) with 2% of long fibers which are the non-milled fibers in the powder, with an average length of 117 µm and an average width of 14 µm. On the other hand, the short fibers in Cell8 have a length distribution ranging from 10 to 74 µm with an average of 27 µm. Morfi does not provide data regarding the width of the 'fines' elements but it can be considered similar to the width of the long fibers as these long fibers are nothing but the non-milled fibers. The size distributions are displayed in Figure 3-2.

According to these results, we can conclude that the aspect ratio of cell8 is superior to 1 but is still low to be considered as fibers.

In Figure 3-3, one can see the overall size distribution of cellulose powder Cell8 ranging from 1 to 50 µm which is in alignment with *Morfi* data. 90% of these particles have a size below 20 µm and 50% below 10 µm making it one of the finest commercial MCC powders. The non-spherical shape and low size of these particles would lead to a better surface area for bonding during powder compression and eventually improve their liquid bonding (Khan and Pilpel, 1986; Levis and Deasy, 2001).

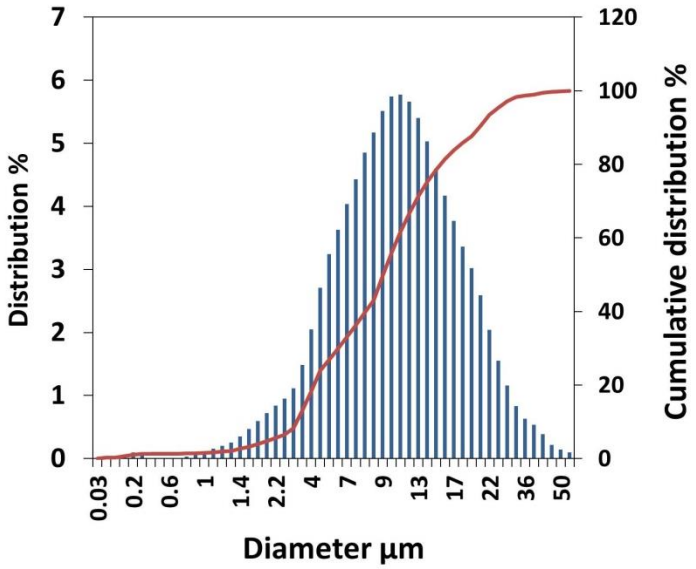

Figure 3-3: Granulometer analysis of size distribution of Cell8.

3.2.2 Morphology

For further characterization of the cellulose particles morphology, the cellulose fibers Cell200 and the powder Cell8 were dispersed in water and observed under an optical microscope as shown in Figure 3-4. The long fibers (0.2 mm long) morphology revealed most likely hardwood-like fibers while the Cell8 particles exhibited the shape of short sticks, retaining the morphological characteristics of plant fibers with good dispersion in water. The dry Cell8 was further observed with a SEM, as one can notice on the bottom images of Figure 3-4, the observation with the optical microscope is confirmed since the powder contains rod-shaped particles along with some fine particles. The powder is well dispersed and contains limited agglomerates with an aspect ratio (L/d) ranging from 1 to 5.

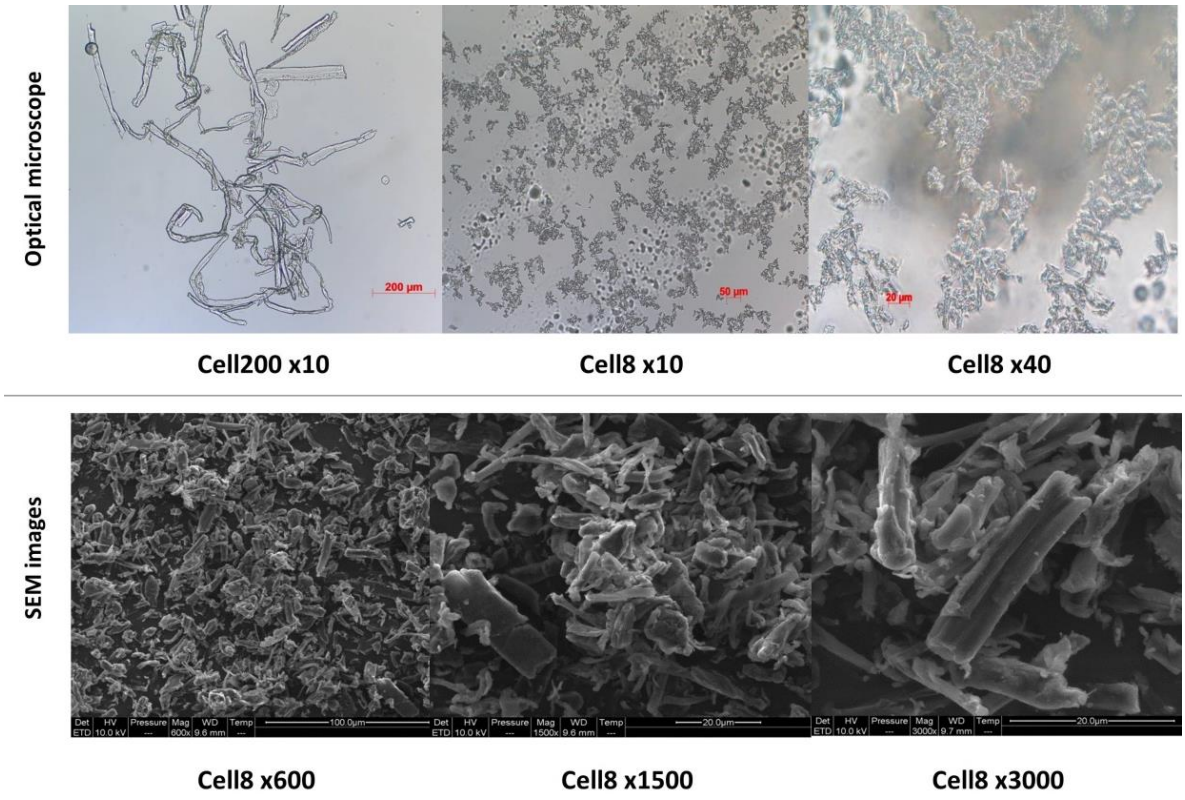

Figure 3-4: Microscopic observations of the used celluloses under different magnitudes.

3.2.3 Crystallinity index and DP

According to the information provided by the supplier, Cell8 is MicroCrystalline Cellulose (MCC) which is a purified partly depolymerized cellulose prepared by treating cellulose pulp with a mineral acid. In this process, the amorphous region is preferentially hydrolyzed so that cellulosic crystals are released. The acid hydrolysis causes dramatic depolymerization of the cellulose until reaching a constant level of DP (Battista and Smith, 1962). To confirm the supplier's information and obtain precise information about the cellulose form and crystallinity level, an XRD test was conducted.

On the XRD pattern in Figure 3-5, we can first confirm that the cellulose is well crystallized and that the different planes' peaks of crystalline polymorph cellulose are visible (Park et al., 2010). Moreover, we can notice the well-known diffraction peaks at 2θ around 14.5°, 16.5°, and 22.5° which are in agreement with the characteristic diffraction peaks of cellulose I-β (French, 2014). Thus the manufacturing process of this fine MCC powder was mild enough to maintain the cellulose in its native form.

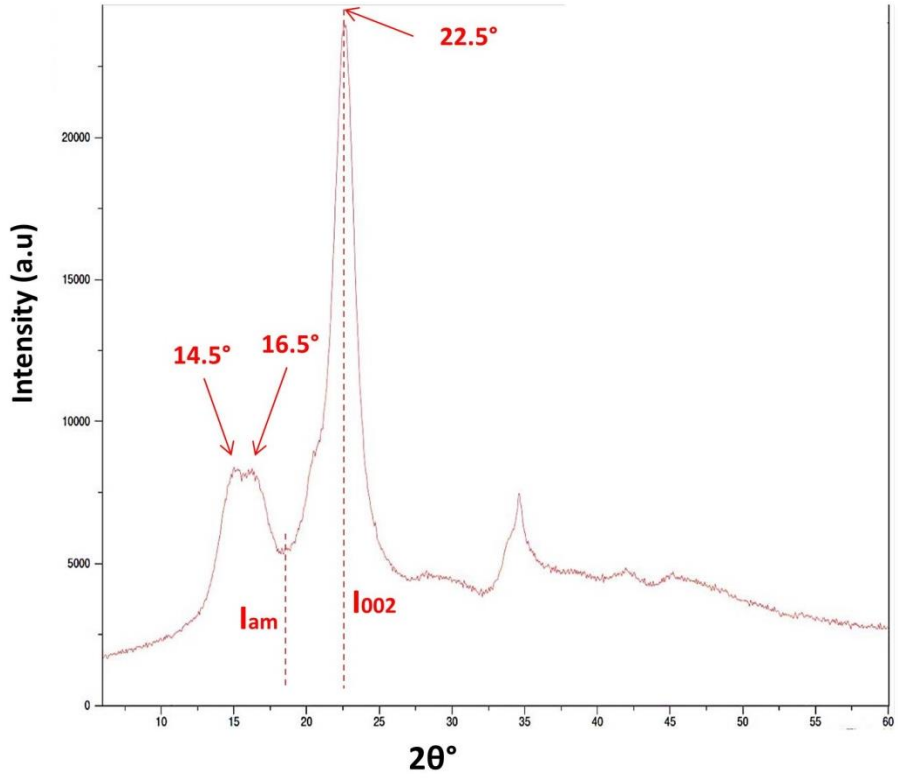

Figure 3-5: X-ray diffraction pattern of cellulose Cell8.

Crystallinity has an important effect on the physical, mechanical, and chemical properties of cellulose. For instance, with increasing crystallinity, tensile strength, dimensional stability, and density increase, while chemical reactivity and swelling decrease. The CI was calculated using the peak height method (Segal et al., 1959) and gave a value of 76.6%. Although the CI is high, it is still lower than that of commercially available MCC such as *Avicel PH-101* which has a CI higher than 88% (calculated with the same technique) (Terinte et al., 2011). The latter MCC has coarser particles so the CI drop in cell8 could be caused by longer mechanical milling which deteriorated the crystals (Zheng et al., 2018). Furthermore, the DP_v was measured by the intrinsic viscosity method which gave a low value of 102 ±3. Thus, the biopolymer was either severely depolymerized during the different industrial processes or the used hardwood fibers had a very limited starting DP. The DP drop can be caused by chemical treatments of the fibers such as a harsh pulping process to obtain pure cellulose and a stiff bleaching process, but can also be related to severe mechanical treatment in the milling step to obtain such fine particles. These results are consistent with some previous findings that mechanical ball milling of microcrystalline cellulose decreases particle size, reduces the DP of cellulose, and increases the amorphous content of cellulose (Paakkari et al., 1989; Zhao et al., 2006; Zheng et al., 2018).

3.2.4 Composition and chemical structure

Solid-state ^{13}C NMR was performed on the Cell8 cellulose powder to study the purity and its chemical structure. The ensuing spectrum is displayed in Figure 3-6.

First of all, we can notice that the carbon contributions of the cellulose backbone are clearly identified on the spectrum. The intense peak between 100 and 110 ppm is attributed to the carbon C1 (as shown on the cellulose structure), the two peaks between 80-90 ppm come from the amorphous (86-92 ppm) and crystalline (79-86 ppm) C4. The intense peaks around 70-80 ppm are given by carbon C2, C3, and C5, and the last peaks around 60 ppm were attributed to the C6 (Atalla and VanderHart, 1999).

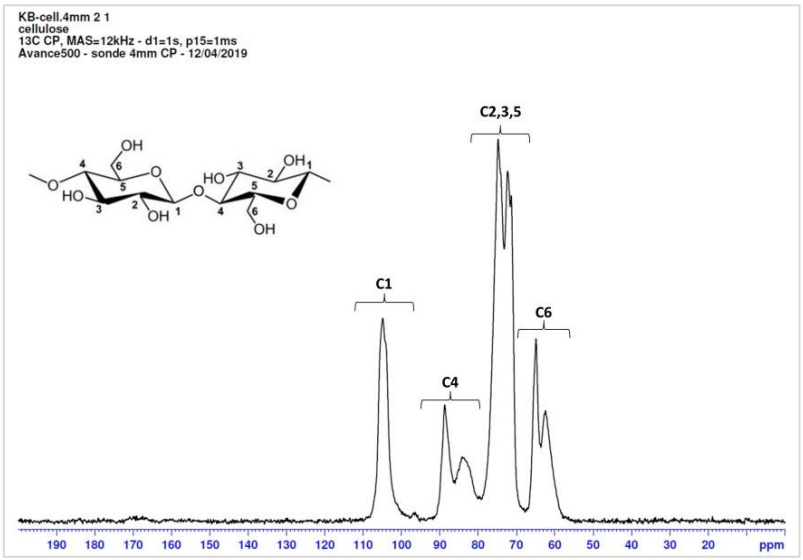

Figure 3-6: Solid-state ^{13}C NMR spectrum of Cell8.

In order to further analyze the chemical composition of the MCC Cell8, it was characterized by FT-IR analysis. The results are shown in Figure 3-7. First, a broad band can be observed in the region of 3600–3000 cm^{-1}, attributed to stretching of the hydroxyl (OH) groups, and 3000–2800 cm^{-1}, attributed to CH and CH_2 stretching. According to the Infrared band assignments for cellulosic materials found in the literature, the bands at 1429, 1369, 1338, and 1319 cm^{-1} are attributed to CH_2, in-plane CH deformation, in-plane OH bending, and CH_2 wagging, respectively. In the fingerprint region of the spectrum, the bands at 1160, 1113, 1061, 1033, 896, and 668 cm^{-1} are associated with the asymmetric C–O–C bridge stretching, the anhydroglucose ring, C-OR stretching, C–O–C pyranose ring skeletal vibration, CH deformation and out-of-plane OH bending, respectively (Poletto et al., 2011; Tserki et al., 2005; Viera et al., 2007). The infrared spectrum shows that the MCC Cell8 sample has the characteristic absorption peaks of cellulose I.

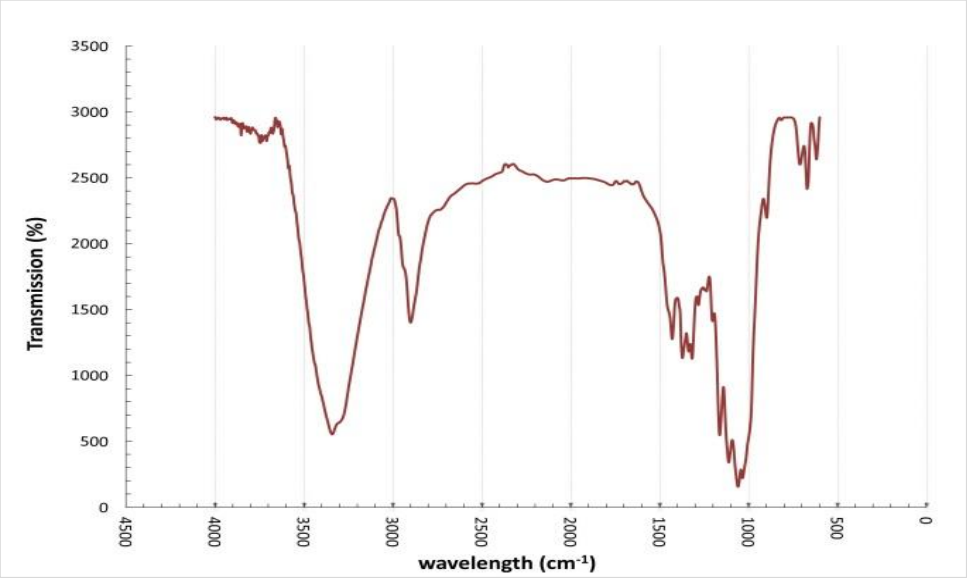

Figure 3-7: FT-IR spectra of MCC Cell8.

To conclude, the used Cell8 cellulose is microcrystalline cellulose with rod-shaped particles 90% of which have a size below 20 µm. According to XRD this MCC has a CI of about 77% and still conserving its native form. These results are further confirmed with ^{13}C NMR and FT-IR spectra which revealed a typical signature of rather pure cellulose I without evidence of neither chemical transformation nor functional groups grafting. Cell8 powder can be considered as an inert cellulosic micro-sized particle filler.

3.3 Furan oligomer: Furolite

The commercial oligomeric furfuryl resin was characterized with different techniques such as NMR, MALDI-ToF, and FT-IR.

We start first by defining the following abbreviations:

- Furan ring is symbolized by FU (Figure 3-8-A)
- 2-Monosubstituted furan rings will be symbolized by FU- (Figure 3-8-B)
- 2,5-Disubstituted furanic rings will be symbolized by -FU- (Figure 3-8-C)

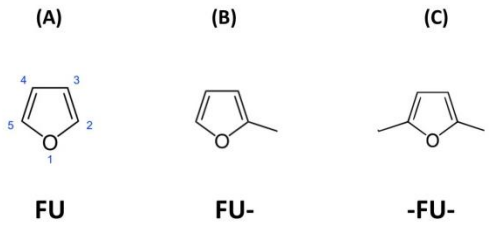

Figure 3-8: Different representations of furanic ring.

3.3.1 Polymer structure

3.3.1.1 Oligomer

The ^{1}H NMR spectrum of the commercial OFR in Figure 3-9 shows a clear peak around 6.2 ppm, which reflects the resonance of the H3 and H4 protons of the furan ring. The peak of the H5 proton around 7.5 ppm is surprisingly very weak because, in the case of the oligomerization of exclusively FA monomers, those protons will be present at least at one of the extremities of the formed oligomers (Choura et al., 1996).

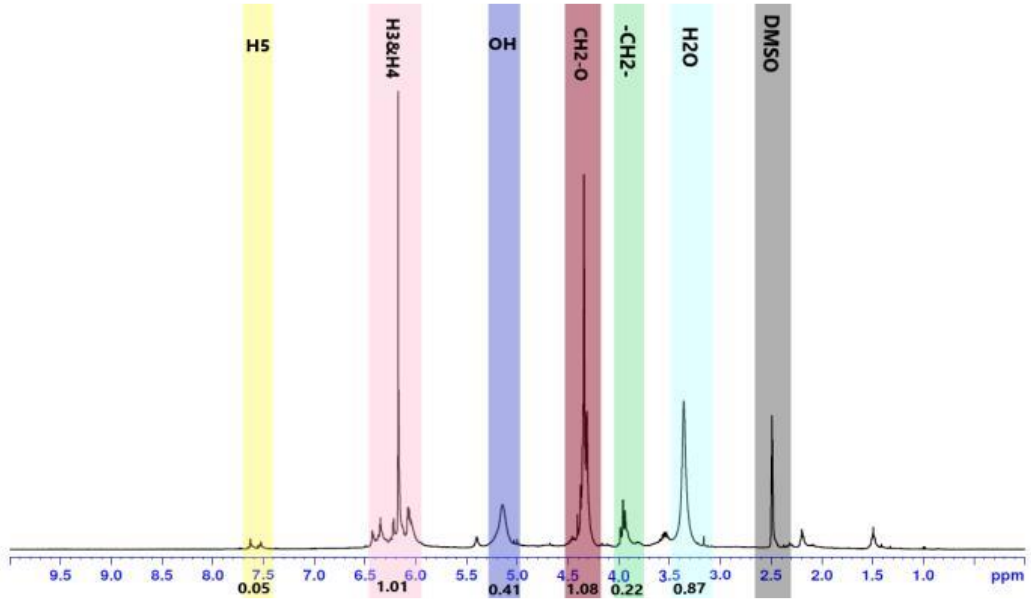

Figure 3-9: ^{1}H NMR spectrum of the commercial PFA oligomers in DMSO-d6.

On the other hand, if one compares the signal of the -CH_2- methylene bridge protons between two furan rings around 3.8 ppm and the signal of CH_2-O protons, which can be either those derived from the terminal CH_2OH groups or those in the ether bridge formed after the condensation according to reaction [2], shown and detailed in section 1.3.1.2 (p.65) of the first chapter, one can notice that the latter is uncommonly more important (Choura et al., 1996; Deka et al., 2013; Principe et al., 1999).

Around 5.3 ppm is the signal of the CH_2OH hydroxyl protons which is a much more important peak than that of the free H5 protons. The strong peak at 3.3 ppm is related to the water protons, assigned to the remaining moisture in the commercial product.

On the ^{13}C NMR spectrum of the commercial oligomers, shown in Figure 3-10, the signals between 156 ppm and 149 ppm match the C3 and C4 carbons, and those of the C2 and C5 are found between 110 and 113 ppm, which reveal the presence of furan rings. Comparing the methylene bridge and the ether bridge signals, at respectively 27 ppm and 56 ppm, one can see again a stronger presence of the latter. Around 175 ppm, one can also detect a modest signal of carbonyl groups which is due to the furan ring-opening posterior the acid hydrolysis of the furan ring during the oligomerization (Chuang et al., 1984). The NMR spectra are in agreement with a recent investigation of the same commercial resin (Lopez de Vergara et al., 2014).

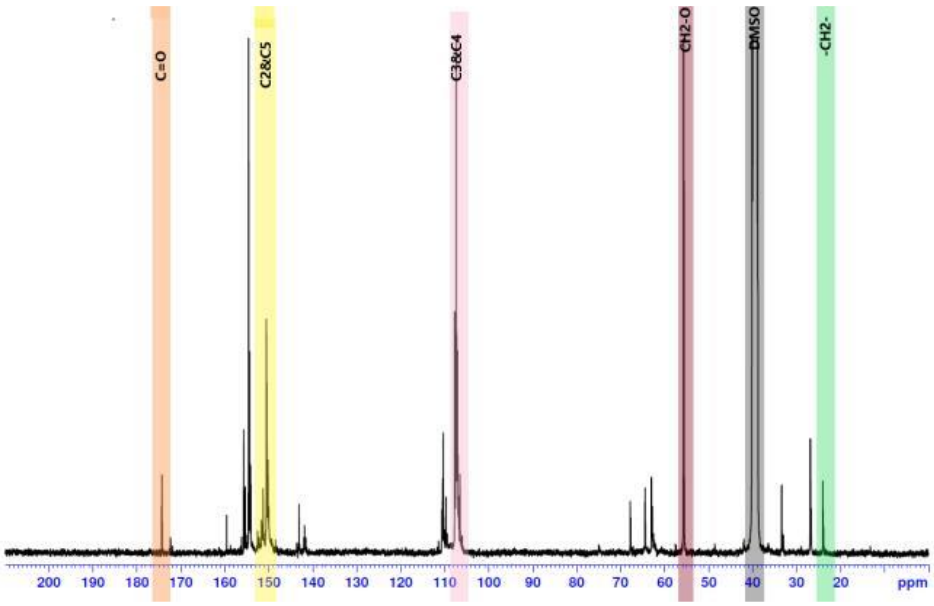

Figure 3-10: ^{13}C NMR spectrum of the commercial PFA oligomers in DMSO.

Examining the FT-IR spectra in Figure 3-11, the first observation relates to the important signal around 3400 cm^{-1} of the OH groups of the "dry" product which we have verified on the ^{1}H NMR spectrum, probably partially arising from the residual moisture in the resin. However, these hydroxyls are mainly due to the terminal groups of the oligomers, which are the reason behind the partial solubility in water of the commercial resin thanks to the polarity of its molecules. The presence of the furan ring is proven by the two signals around 1000 and 800 cm^{-1}. One can also distinguish the typical double peak around 2900 cm^{-1} of the CH_2 groups. The peak around 1200 cm^{-1} is indicative of ether bonds (CH_2-O-CH_2). Around 1720 cm^{-1} a peak of the carbonyl groups is due to

the furan ring opening during the oligomerization, as discussed above (Choura et al., 1996; González et al., 2002).

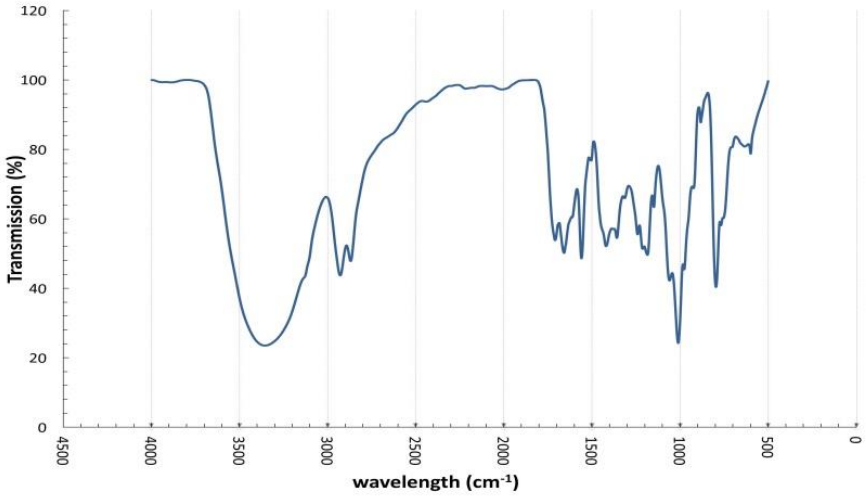

Figure 3-11: FT-IR spectrum of the commercial OFR.

According to the NMR data of the commercial oligomer, the ether bridges are more frequent than the methylene ones, and terminal CH_2OH groups are much more frequent than unsubstituted H5 end groups, both facts being entirely uncommon for typical FA oligomers, in view of the established mechanism shown in the first chapter. Indeed, in the case of the predominance of reaction [2] without loss of formaldehyde, and hence the important presence of ether bridges, the condensation would be soon blocked for lack of CH_2OH moieties, i.e. one would only be faced with oligomers ending with 2 unreacted protons at the C5 positions, which is clearly not the present situation. Conversely, the strong presence of hydroxyl groups on the NMR and FTIR spectra versus a very limited sign of the proton at the C5 position, suggests that these oligomers are ending predominantly with hydroxymethyl groups rather than a furan ring with an unreacted H5 proton.

Interestingly, a MALDI-ToF spectrum of the PFA oligomer, confirmed these conclusions, showing the same pattern of moieties within a mixture of oligomers bearing two-to-four monomer units. Indeed on the spectrum in Figure 3-12, we can first notice that the molecular mass (m/z in Dalton) distribution is around the average of 350 Dalton corresponding to an average DP_n of 4 units per oligomer. After the electrons shelling the fragmentation of the oligomer took place with a sequence of 80 Dalton, which corresponds to the molecular weight of the repetition unit of the oligomer (FA (98) – H_2O (18) = 80). According to this data, the pre-polymers in the commercial product are short and hence the frequency of the terminal hydroxyl groups detected in the RMN and FTIR spectrums.

We can as well detect some fragments of 110 Dalton corresponding to the fraction of the furan ring attached to an ether bridge, viz. FU-CH_2-O-CH_2. The average distribution of the fragment is around 351, which corresponds to about 3 units of a furan attached to the ether bridge. The DP_n of this pre-polymer ranges between 2 and 5.

It seems logical to suggest therefore that the synthesis of the commercial PFA required the concomitant use of FA and another furan monomer capable of generating a high frequency of ether bridges and terminal CH_2-OH groups, most likely 2,5-hydroxymethylfuran.

This structural investigation showed that the interest of the product developed by *Transfurans* in that it allows water compatibility (hence a reduced viscosity and therefore better processability) while maintaining the potential to polymerize and crosslink following essentially the same mechanisms discussed in Chapter 1 for FA alone, using a temperature activation catalyst which allows the process to occur upon heating the system, as will be discussed in Chapter 5.

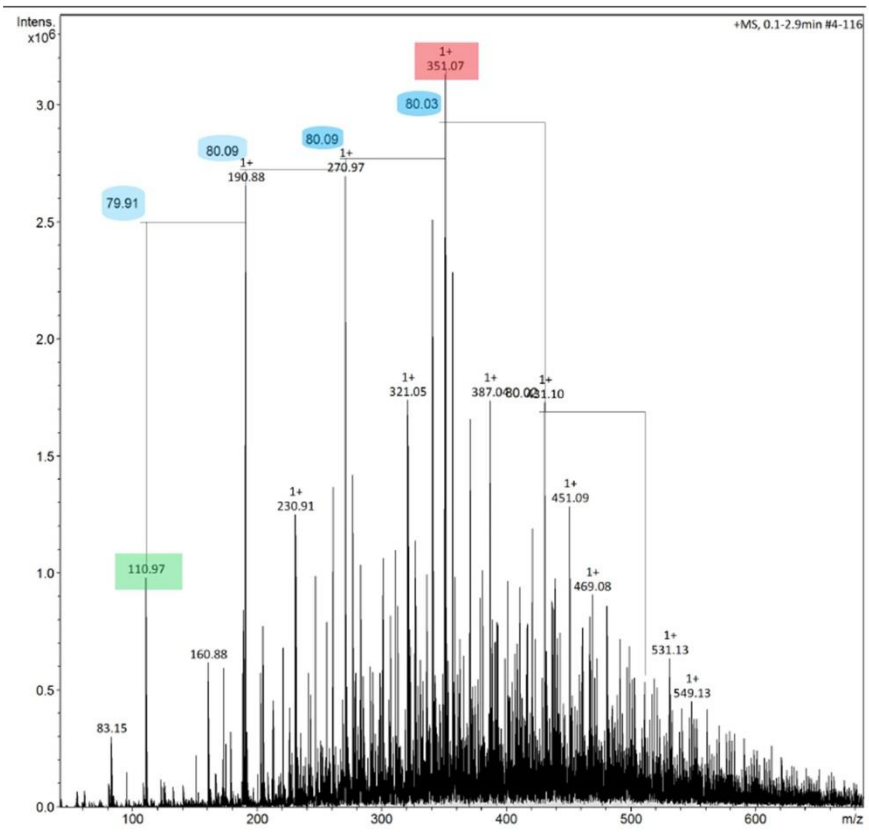

Figure 3-12: Maldi-TOF spectrum of the PFA oligomers.

3.3.1.2 Cured polymer

According to the data provided by the RMN ^{13}C of the product after crosslinking in Figure 3-13, we can recognize the structure of the PFA. For instance, the peaks around 150-160 ppm and 110 ppm prove the presence of furan rings. Moreover, the peaks at around 27 and 65 ppm prove the presence of the methylene and ether bridges after the curing of the resin. At around 205 ppm we can also notice the presence of the carbonyl groups after the furan ring opening. As we can notice in Figure 3-13, the majority of suggested structures of the crosslinked PFA in the literature, detailed earlier in section 1.3 of Chapter 1 (p.63), could be detected which also demonstrates how complex the structure of the crosslinked product is.

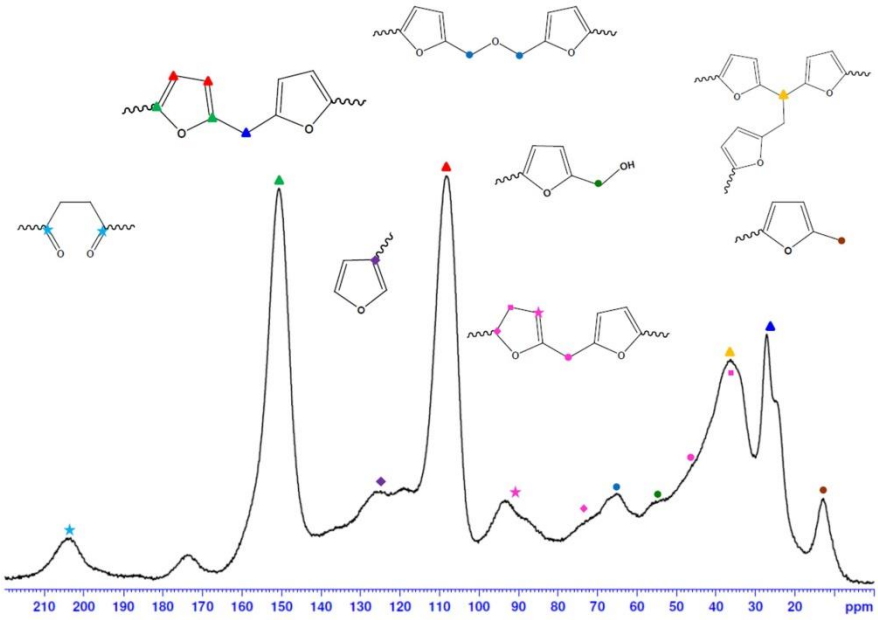

Figure 3-13: Solid-state RMN of the cured Furolite.

3.3.2 Conclusions

According to the data provided by NMR and FTIR spectra, it was obvious that not only furfuryl alcohol (FA) monomers were involved in the pre-polymerization of the PFA oligomer. The most probable co-monomer used was the 2,5-hydroxymethylfuran (BHMF).

During the polymerization step, 3 polymerization reactions are possible FA-FA, FA-BHMF, or BHMF-BHMF but the oligomer produced is always the poly(furfuryl alcohol). As for the proportions of the two monomers in the initial mixer, we suggest that the BHMF is in excess because of the quasi absence of the non-substituted protons H5 and the domination of the ether bridges.

According to the data of the MALDI TOF, the average polymerization degree is around 3 with a maximum of 5. In conclusion, we can suggest a basic structure of the commercial *Furolite* used in this work as:

$$OH\text{-}CH_2\text{-}(FU\text{-}CH_2\text{-}O\text{-}CH_2)_n\text{-}(FU\text{-}CH_2)_m\text{-}FU$$

with n>m because the ether bridges are more frequently present in the polymer than the methylene bridges.

3.4 Chapter conclusions

In a conclusion, on one hand, we can consider that the used cellulosic fillers are micro-sized rod-shaped chemically inert particles. On the other hand, we can propose that the commercial Furolite oligomer is a sequence of an average of 2 to 5 furan rings connected predominantly by ether bridges and ending with hydroxyl groups making it rather soluble in water. In the light of these assignments, the combination of these two components should yield a mechanical reinforcement of the furanic matrix without any chemical interaction between the two components (Lems et al., 2019).

3.5 References

Atalla, R. H, et D. L VanderHart. 1999. « The Role of Solid State 13C NMR Spectroscopy in Studies of the Nature of Native Celluloses ». *Solid State Nuclear Magnetic Resonance* 15 (1): 1-19. https://doi.org/10.1016/S0926-2040(99)00042-9.

Battista, O A, et P A Smith. 1962. « Microcrystalline cellulose », industrial and engineering chemistry, 9 (septembre): 10.

Choura, Mekki, Naceur M. Belgacem, et Alessandro Gandini. 1996. « Acid-Catalyzed Polycondensation of Furfuryl Alcohol: Mechanisms of Chromophore Formation and Cross-Linking ». *Macromolecules* 29 (11): 3839-50. https://doi.org/10.1021/ma951522f.

Chuang, I Ssuer, Gary E. Maciel, et George E. Myers. 1984. « Carbon-13 NMR Study of Curing in Furfuryl Alcohol Resins ». *Macromolecules* 17 (5): 1087-90. https://doi.org/10.1021/ma00135a019.

Deka, Harekrishna, Manjusri Misra, et Amar Mohanty. 2013. « Renewable Resource Based "All Green Composites" from Kenaf Biofiber and Poly(Furfuryl Alcohol) Bioresin ». *Industrial Crops and Products* 41 (janvier): 94-101. https://doi.org/10.1016/j.indcrop.2012.03.037.

French, Alfred D. 2014. « Idealized Powder Diffraction Patterns for Cellulose Polymorphs ». *Cellulose* 21 (2): 885-96. https://doi.org/10.1007/s10570-013-0030-4.

González, Regino, Juan M. Figueroa, et Hilda González. 2002. « Furfuryl Alcohol Polymerisation by Iodine in Methylene Chloride ». *European Polymer Journal* 38 (2): 287-97. https://doi.org/10.1016/S0014-3057(01)00090-8.

Khan, F, et N Pilpel. 1986. « The Effect of Particle Size and Moisture on the Tensile Strength of Microcrystalline Cellulose Powder ». *Powder Technology* 48 (2): 145-50. https://doi.org/10.1016/0032-5910(86)80073-0.

Lems, Eva-Marieke, Stefan Winklehner, Christian Hansmann, Wolfgang Gindl-Altmutter, et Stefan Veigel. 2019. « Reinforcing Effect of Poly(Furfuryl Alcohol) in Cellulose-Based Porous Materials ». *Cellulose* 26 (7): 4431-44. https://doi.org/10.1007/s10570-019-02348-6.

Levis, S. R, et P. B Deasy. 2001. « Production and Evaluation of Size Reduced Grades of Microcrystalline Cellulose ». *International Journal of Pharmaceutics* 213 (1): 13-24. https://doi.org/10.1016/S0378-5173(00)00652-9.

Lopez de Vergara, Unai, Mariasun Sarrionandia, Koldo Gondra, et Jon Aurrekoetxea. 2014. « Polymerization and Curing Kinetics of Furan Resins under Conventional and Microwave Heating ». *Thermochimica Acta* 581 (avril): 92-99. https://doi.org/10.1016/j.tca.2014.02.017.

Paakkari, T., R. Serimaa, et H.-P. Fink. 1989. « Structure of Amorphous Cellulose ». *Acta Polymerica* 40 (12): 731-34. https://doi.org/10.1002/actp.1989.010401205.

Park, Sunkyu, John O. Baker, Michael E. Himmel, Philip A. Parilla, et David K. Johnson. 2010. « Cellulose crystallinity index: measurement techniques and their impact on interpreting cellulase performance ». *Biotechnology for Biofuels* 3 (1): 10. https://doi.org/10.1186/1754-6834-3-10.

Poletto, Matheus, Vinícios Pistor, Mara Zeni, et Ademir J. Zattera. 2011. « Crystalline Properties and Decomposition Kinetics of Cellulose Fibers in Wood Pulp Obtained by Two Pulping Processes ». *Polymer Degradation and Stability* 96 (4): 679-85. https://doi.org/10.1016/j.polymdegradstab.2010.12.007.

Principe, Martha, Pedro Ortiz, et Ricardo Martínez. 1999. « An NMR Study of Poly(Furfuryl Alcohol) Prepared with p-Toluenesulphonic Acid ». *Polymer International* 48 (8): 637-41. https://doi.org/10.1002/(SICI)1097-0126(199908)48:8<637::AID-PI206>3.0.CO;2-C.

Segal, L., J.J. Creely, A.E. Martin, et C.M. Conrad. 1959. « An Empirical Method for Estimating the Degree of Crystallinity of Native Cellulose Using the X-Ray Diffractometer ». *Textile Research Journal* 29 (10): 786-94. https://doi.org/10.1177/004051755902901003.

Terinte, Nicoleta, Roger Ibbett, et Kurt Schuster. 2011. « Overview on native cellulose and microcrystalline cellulose I structure studied by X-ray diffraction (WAXD): Comparison between measurement techniques ». *Lenzinger Berichte* 89 (janvier).

Tserki, V., P. Matzinos, S. Kokkou, et C. Panayiotou. 2005. « Novel Biodegradable Composites Based on Treated Lignocellulosic Waste Flour as Filler. Part I. Surface Chemical Modification and Characterization of Waste Flour ». *Composites Part A: Applied Science and Manufacturing* 36 (7): 965-74. https://doi.org/10.1016/j.compositesa.2004.11.010.

Viera, Rose G. P., Guimes Rodrigues Filho, Rosana M. N. de Assunção, Carla da S. Meireles, Júlia G. Vieira, et Grasielle S. de Oliveira. 2007. « Synthesis and Characterization of Methylcellulose from Sugar Cane Bagasse Cellulose ». *Carbohydrate Polymers* 67 (2): 182-89. https://doi.org/10.1016/j.carbpol.2006.05.007.

Zhao, Haibo, Ja Hun Kwak, Yong Wang, James A. Franz, John M. White, et Johnathan E. Holladay. 2006. « Effects of Crystallinity on Dilute Acid Hydrolysis of Cellulose by Cellulose Ball-Milling Study ». *Energy & Fuels* 20 (2): 807-11. https://doi.org/10.1021/ef050319a.

Zheng, Yu, Zongqiang Fu, Dong Li, et Min Wu. 2018. « Effects of Ball Milling Processes on the Microstructure and Rheological Properties of Microcrystalline Cellulose as a Sustainable Polymer Additive ». *Materials* 11 (7): 1057. https://doi.org/10.3390/ma11071057.

4 Development and characterization of new bio-based materials for 3D printing by cold extrusion

Chapter content

4.1 Chapter introduction

Recently, 3D printing is getting more and more popular in many fields and for many applications that require different materials. In AM by material extrusion one can notice the dominance of thermoplastics which are for the most part petroleum-based. Under the upraising environmental concerns, as already stated in chapter 1, many research works have been conducted to find a substitute to the use of thermoplastics and among the suggested materials one can notice cellulose and, more generally, lignocellulosic materials. The latter bio-based material is particularly interesting for 3D printing as it is available, renewable, cost-effective, and lightweight. However, these advantages come with a major limitation: cellulose cannot be melted and hence cannot be used as a matrix for AM by melt extrusion. Therefore, researchers suggested several formulations using different forms of cellulose for printing by cold extrusion in particular aerogels of NFC, MFC, and CNC which were compatible with this AM technique. Nonetheless, the use of these cellulose-based aerogels, and in some cases suspensions and solutions, raised additional challenges and limitations to its printability such as an important shrinkage upon drying due to a limited solid content in the formulation or a complicated and expensive freeze-drying process.

From a more technical point of view, thermoplastics have limited thermal stability making the use of the 3D printed parts limited to low-temperature environments. Despite the existence of technical thermally stable printable filaments such as PEEK and PEI, they are still expensive (upto 790 $/kg) and rather complicated to print. To overcome these thermal performances limitation when using thermoplastics, several articles have been published about formulations compatible with AM by extrusion of composites with the use of thermosetting resin with better thermal and mechanical performances. Nonetheless, the majority of the suggested composites (chapter 1) are still fossil-based. To overcome these limitations the intention of the present work is to develop a 3D printable material by AM by cold extrusion using cellulose fibers as bio-based and cost-effective filler along with a bio-based thermosetting resin which will play the role of binder with excellent thermal performances. This mixture would yield a fully bio-based printable composite with performances over-stepping currently existing materials. However, an optimization step should be done to define the appropriate proportions to obtain a printable ‘ink’ and optimal performance of the cured composite which is the main goal of this chapter. As mentioned in chapter 2, two different ‘inks’ are developed in this work:

- A structural ink based on cellulose fibers and PFA oligomers and eventually a solvent.
- An electrically conductive ink based on conductive particles, cellulose, and PFA oligomers.

The different formulations and their optimization for both inks will be detailed in this chapter along with a rheological study and an investigation of the most relevant properties for the resulting cured composites. Figure 4-1 is an illustration of the chapter's content and layout highlighting the main conducted studies and short conclusions which will be detailed in the present chapter.

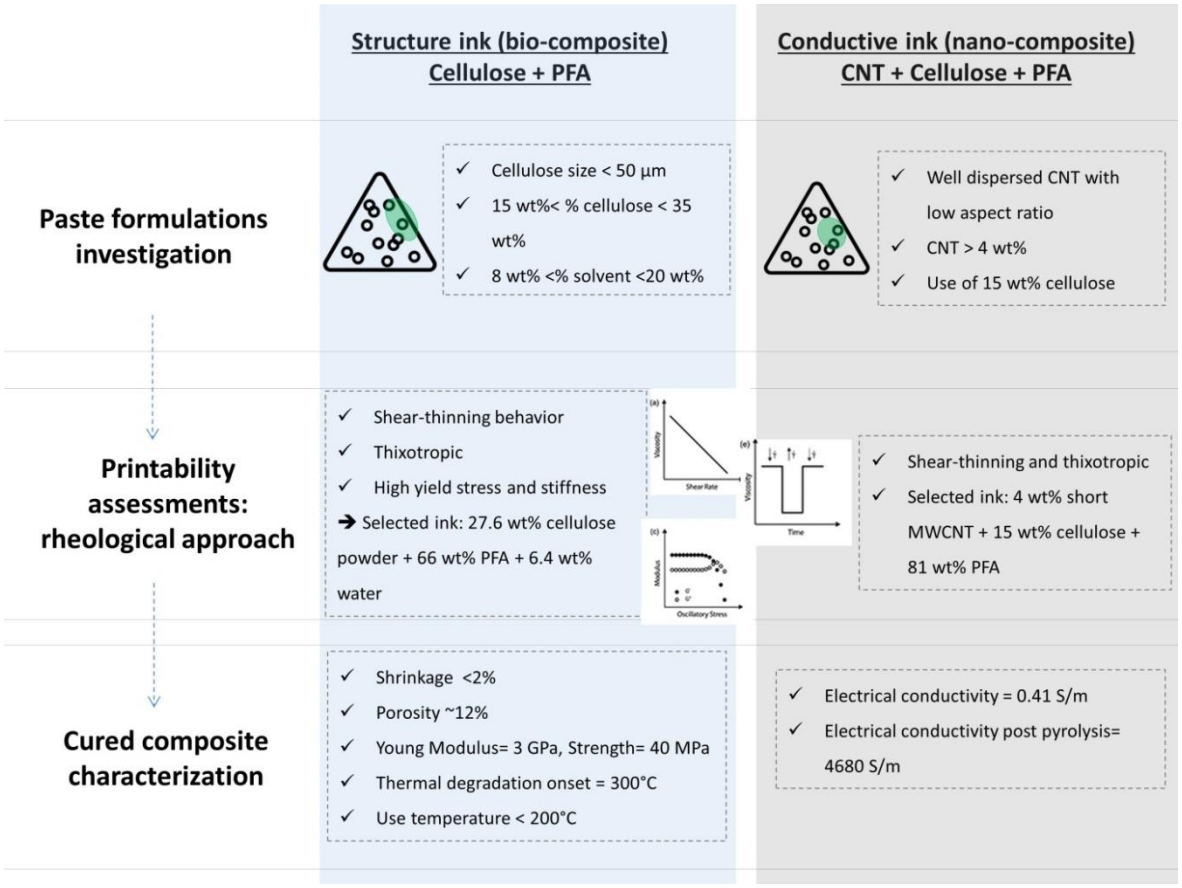

Figure 4-1: Graphic abstract of chapter 4.

4.2 Development and characterization of a fully bio-based paste for additive manufacturing by cold material extrusion

4.2.1 Introduction

In no uncertain terms, direct ink writing is inseparable from rheology. One cannot begin DIW without first questioning the rheological properties of the formulation. Indeed, these properties determine the range of structures that can be printed, the optimal printing parameters, and ultimately the quality of the printed part. Despite this, the manner in which rheology ties in with these considerations has to date not been specified well in the literature. Some work has been done to identify some of the important rheological requirements of the ink formulation and suggested a range of values these properties should take for a successful print. This chapter aims to advance the understanding of how each key rheological property affects different aspects of the printing process and to begin to refine the quantitative requirements of these properties.

4.2.2 Formulation optimization

The 'ink' formulation is a very important step towards successful additive manufacturing by material extrusion. A simple suspension containing cellulose particles as the solid phase and PFA oligomers as the liquid phase is aimed to be prepared. The ink suspension will thus contain 3 main components, cellulose particles as fillers, PFA oligomers as the binder, and water or ethanol as resin diluents. To define an optimal ink that is extrudable, printable and with a defect-free solidification, several formulations with different liquid and solid contents were prepared. An early estimation of the liquid content required for an extrudable suspension is advantageous. Theoretically, the maximum liquid content in a powder to obtain a paste-like highly filled suspension can be estimated by predicting the free space in a body of powder but even doing so the yielding paste can present deagglomeration. The simpler way is to perform a subsidiary experience by adding gradually the liquid phase until obtaining a smooth workable paste. Regulating the liquid content in the suspension is crucial to have the optimum amount of liquid filling the space between the filler particles (depends on the packing properties of the powder) and lubricating the relative particle movement along the wall of the die which will enable the extrusion of the paste. There is a narrow range of liquid content with which extrusion is possible, as too much liquid content will lead to a drop in the pressure needed to extrude and no shape maintenance in the extrudate, whilst an exaggerated increase in solid content would lead to the formation of a wet powder causing the die's clogging. To restrict the solid content range in the 'ink', a preliminary testing step was carried out.

The preliminary formulations were prepared with fibrous and powdery cellulose and by varying the cellulosic content, the binder content, and the solvent ratio. The assessment of these formulations was done in two steps, the first by assessing its extrudability (through 2 mm and then 1 mm nozzles) and the second step by a visual assessment of the drying and curing quality of the formulations. The formulation that can be both extrudable and crosslinked without any visible major flaws and instabilities can be qualified as possibly printable. In chapter 2 (p.115) an exhaustive list of the tested formulations was presented which are also presented on the ternary diagrams in Figure 4-3 and Figure 4-4.

In Table 4-1, the aspect of the extrudates and the crosslinked disks of the most important formulations are presented. The formulations IF-01-L and IF-01 contain the same weight fractions of the 3 components, but the former was prepared with cellulose long fibers (Cell200) and the latter with cellulose powder (Cell8). As we can see in Table 4-1, despite a defect-free crosslinking for both forms of cellulose, the extrusion of the long fibers suspension was not possible through a 2 mm nozzle. We can notice a phase migration phenomenon due to a phase separation in the nozzle. This phase separation mechanism during extrusion can occur by filtration in the die, where the pressure exerted on the liquid phase causes it to flow along the die more quickly than the solids. This phenomenon is exacerbated by the formation of solid mats which causes an ultimate clogging of the nozzle (Yaras et al., 1994; Yilmazer et al., 1989). Indeed, under high shear stress, the slip velocity (V_s) that occurs on the walls of the die becomes significant and starts to be comparable to the overall velocity of the suspension (V) and in the case of high filled suspensions, the extrusion flow takes place only by slip as it flows as a plug ($V=V_s$). However, the pressure drop across the suspension does not only move the suspension as a plug, but also generates a driving force for the suspending liquid to filter through the particles leading to a velocity of the liquid with respect to the fillers (V_m) which should be minimized to avoid the liquid filtration to occur (Yilmazer et al., 1989). Moreover, a study on the effect of the formulation parameters on the extrusion flow was done and it was found that in order to avoid any phase migration, the matrix viscosity should be maximized and the particle size should be minimized in order to maximize the V_s and minimize V_m. Thus, the use of cellulose powder with limited particle size was more advantageous to avoid the phase migration phenomenon. Furthermore, limiting the particle size allows reaching better printing resolution by using small nozzle sizes as the absolute maximum dimension of the particles must be a tenth of the smallest die diameter to prevent particles bridging during flow (Benbow and Bridgwater, 1993).

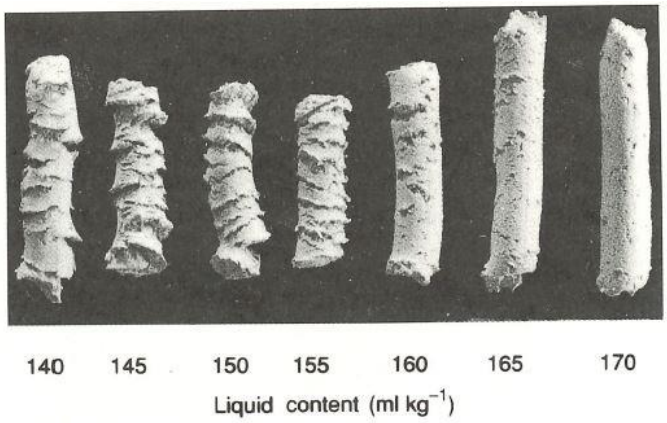

Figure 4-2: Surface fracture phenomenon influenced by the composition (Benbow and Bridgwater, 1993).

As the experimental solid content limit of the cellulose powder was quickly reached, the viscous binder was further diluted with water in IF-04 and with ethanol in IF-04-E to reach a total cellulose weight fraction of 31 wt%. These highly concentrated suspensions were hardly extruded through a 2mm nozzle and their extrusion flow was not stable with a noticeable surface fracture phenomenon. Surface fracture, as the name suggests, is when the extrudate shows a rough and uneven surface as we can see on the photograph of the extrudate of IF-04. This phenomenon can be influenced by the limited liquid phase content in paste formulation as shown in Figure 4-2 (Benbow and Bridgwater, 1993). Moreover, we can notice cracking upon crosslinking of these composites whether using water or ethanol as solvent. These cracks can be due to a very limited polymeric binder (45 wt%) and an important added solvent. The added solvent volume has to be removed and leaves interparticle pores which lead to the cracking of the composite (Benbow and Bridgwater, 1993). Not only is the quantity of the liquid phase, but also its viscosity are critical to obtain an extrudable paste. The matrix should have a high viscosity to generate stresses during mixing to produce consolidation of the paste and for shape retention of the extrudate, but should not be too high to limit extrusion pressure and to ensure homogeneous mixing. Furthermore, the evaporable liquid volume should be limited to avoid cracking upon drying and crosslinking (Benbow and Bridgwater, 1993).

The formulations IF-01 and IF-03 are the only pastes exhibiting a stable extrudate flow, through 2 and 0.7mm nozzles. The formulation containing 25.5% cellulose weight fraction is the most filled suspension being extrudable through narrow nozzles. 79 wt% is then the approximate liquid phase weight fraction that can be added in the suspension to have a stable extrusion to fill the voids in the cellulose powder to insure enough lubrication between the particle and the wall of the die for a steady and easy extrusion.

In the light of the preliminarily tested formulations, plotted on the ternary diagram in Figure 4-3, we can limit the testing area of the fraction of the 3 different components of the printable ink. As

highlighted on the diagram, the total solvent content in the formulation should not exceed 20% (32% of the polymeric matrix) to avoid any cracking and defect in the composite upon crosslinking. On the other hand, the cellulose weight fraction cannot exceed a maximum of 30%, which leads to a powdery crumbly aspect of the mixture. Moreover, it was found that less than 10 wt% of cellulose powder yields a diluted suspension with a law bulk yield stress which is needed in the formulation so that the ink maintains the shape of the die after extrusion, which is very important for 3D printing. Finally, the use of fine cellulose particles is privileged to avoid any extrusion defects and to make possible the use of small nozzles without clogging. These conclusions leave us with a better-targeted formulation composition range highlighted in blue in Figure 4-3.

Table 4-1: Example of the assessed preliminary tested formulations

	Solid content	Liquid content	Extrudable		Drying and crosslinking	
IF-01-L	21.0 wt% Cellulose fibers	79.0 wt% (32.5 wt% water)	Phase migration		yes	
IF-01	21.0 wt% Cellulose powder	79.0 wt% (32.5 wt% water)	yes		yes	
IF-03	25.5 wt% Cellulose powder	74.5 wt% (32.5 wt% water)	yes		yes	

	Solid content	Liquid content	Extrudable		Drying and crosslinking	
IF-04	31.6 wt% Cellulose powder	68.4 wt% (52.0 wt% water)	Surface fracture	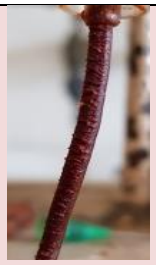	no	
IF-04-E	31.6 wt% Cellulose powder	68.4 wt% (7.5 wt% water and 44.5 ethanol)	Surface fracture		no	

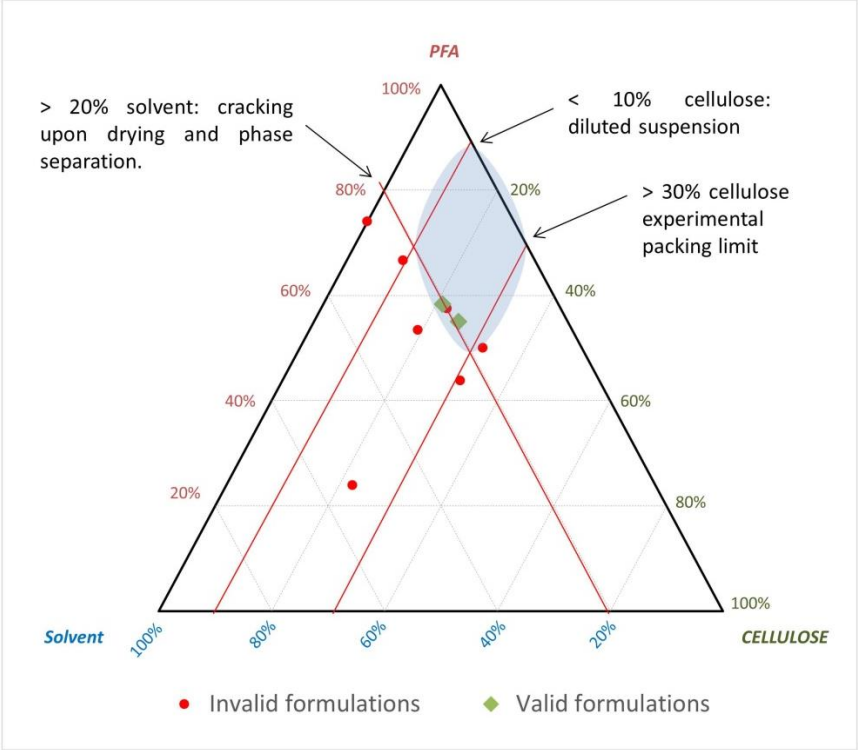

Figure 4-3: Ternary diagram indicating the weight fractions of PFA, cellulose fibers, and water for the preliminarily tested formulations.

The next step is the optimization of the formulation. As discussed before, the solid content is a very important parameter in the formulation of a suspension compatible with AM by material extrusion. The target is to define the optimal cellulose content for an extrudable, printable, and shape-maintaining ink. To do so, 6 formulations were prepared with cellulose weight fractions ranging from

16 to 29 wt%. No extra solvent was added to the PFA oligomers in order to avoid any defects during crosslinking. As explained in chapter 1, water can generate many defects during the exothermic crosslinking reaction such as high porosity and possible foaming. However, as mentioned in chapter 2, the oligomeric product and the added solution of the catalyst contain 7.5 wt% and 40 wt% water, respectively, which sums up to be upto 7.5 wt% of total free water in these formulations.

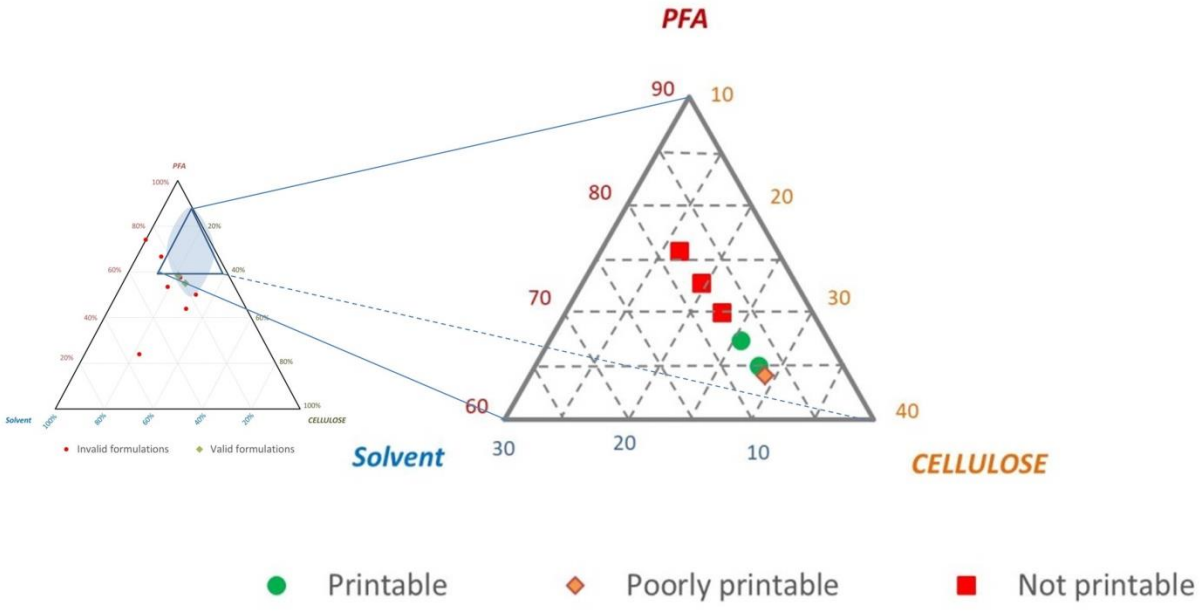

Figure 4-4: Ternary diagram of the optimized printable formulation.

These 6 tested formulations are placed on the ternary diagram in Figure 4-4. In Figure 4-5, photographs of the suspensions with varying cellulose content are displayed and a change of the rheological behavior and aspect can be be noticed, ranging from a diluted consistency with a limited bulk stress suspension (Figure 4-5-A) to a highly filled paste-like suspension with starting of deagglomeration (Figure 4-5-F). This progressive change can be explained by the bridging of viscous PFA oligomers between the cellulosic particles formed by a diffusion process or by the formation of particle network via a contact sticking thanks to the matrix layer around fillers particles.

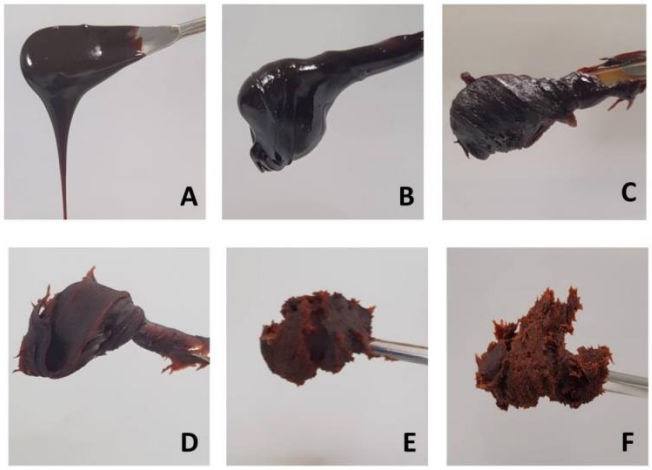

Figure 4-5: Photographs of different suspensions aspect.

In the next section, the ink formulation will be further optimized by assessing the printability. The printability assessment is carried out through the characterization of the different formulations according to a rheological approach.

4.2.3 Effect of cellulose concentration on the rheological behavior and the printability of the suspensions

4.2.3.1 Basic Rheological Properties and printability concept

In most of AM techniques, the used material undergoes an instant phase transition such as solidification in the case of fused melt deposition which insures the shape maintenance of the part during printing. In contrast, in the case of cold extrusion, the material does not undergo any phase transition so the printed part is only held by the properties of the extrudate. Thus, the rheological behavior of the ink plays a crucial role in the printability and the quality of the printed object.

In the following subsection, general rheology principles, as well as printability concept definition according to the state of art, will be briefly presented.

Dynamic rheology

The most used parameter to describe how a material flows is its viscosity which can be defined as the resistance of the fluid to flow. The dynamic viscosity (η) can be measured according to eq 6 where τ (Pa) is the shear stress and $\dot{\gamma}$ (1/s) is the shear strain rate.

$$\eta = \frac{\tau}{\dot{\gamma}} \qquad \textit{eq 6}$$

The sheared material can undergo different flow types as a function of the shear rate and their flow curves can be summarized as illustrated in Figure 4-6. The flow can be either with or without yield stress and we can distinguish three different flow possibilities:

- Newtonian: shear stress evolves linearly with the shear rate and the viscosity is insensitive to the shear rate.
- Shear-thickening (Dilatant): viscosity increases with increasing shear rate.
- Shear-thinning (Pseudoplastic): viscosity decreases with increasing shear rate.

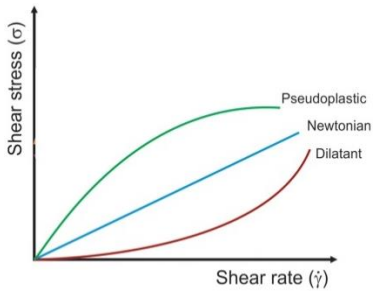

Figure 4-6: Classification of fluids according to their shear stress/shear rate relationship (Kubo et al., 2019).

The rheological behavior of non-newtonian fluids can be described by the simple power-law relating the shear rate and the shear stress presented in eq 7.

$$\tau = K\,\dot{\gamma}^{n} \qquad \textit{eq 7}$$

Where τ is the shear stress (Pa), $\dot{\gamma}$ is the shear rate (1/s), K is the consistency coefficient (Pa·s^n) and n is the flow behavior index (dimensionless). By arranging eq 6 and eq 7, the shear rate can be related to the apparent viscosity according to eq 8.

$$\mu = K\,\dot{\gamma}^{1-n} \qquad \textit{eq 8}$$

The flow behavior index (n) assesses the relation between the shear stress and the shear rate.

- n> 1, the flow is shear thickening.
- 0 <n< 1, the flow is shear thinning.
- n= 1 Newtonian or Bingham flow.

Oscillatory rheology

In addition to the viscosity measurement and flow ramp measurements, an assessment of the viscoelastic behavior of the material is also important. The viscoelastic properties of the flowing material can be characterized with oscillatory tests which can be performed on a rheometer by subjecting the fluid to sinusoidal oscillatory stress and measuring the elastic and the viscous response. The shear complex modulus (G*) is the most important parameter provided, which is the resistance of the ink against the subjected deformation with its two components, viz. the storage modulus G' (or elastic) and the loss modulus G" (or plastic) (McKenna, 2003).

The storage modulus G' represents the elastic behavior of the material. This modulus, given by eq 9, expresses the ability of the material to return to its original shape after stress removal. In the case of a pure viscous behavior, G' is zero because the deformation is out of phase with the shear stress. The loss modulus G" represents the viscous behavior and energy dissipation when the material starts to flow. The loss modulus G" is given by eq 10. Another important parameter is the loss factor (eq 11) which helps to understand if the material is behaving more as a solid or as a liquid. When the material is solid-like, the loss factor approaches zero and when the material is behaving liquid-like, the loss factor approaches infinity (Barnes et al., 1989; Wildemuth and Williams, 1984).

$$G' = G^* \cos(\delta) \qquad \textit{eq 9}$$

$$G'' = G^* \sin(\delta) \qquad \textit{eq 10}$$

$$\tan \delta = \frac{G''}{G'} \qquad \textit{eq 11}$$

To study the viscoelasticity of a material, one of the used tests is the amplitude sweep where the deformation increases whilst G' and G" are being measured. The modulus is constant in the linear viscoelastic region (LVER) and G' starts to decrease when the material structure breaks down, this point being nothing else than an estimation of the yield stress, which can be approximated as the crossover of G" over G' (Steffe, 1996).

The importance of the ink formulation

These rheology changes induced by the flow generate different macroscopic behaviors. The interaction between solid particles at rest affects the flow of these suspensions. In fact, when a shear force is applied to a complex fluid, energy is supplied to the elements and this energy varies from one element to another since the forces are distributed in a complex way through the network of disordered elements. Thus, this fraction of displaced elements allows the fluid to flow macroscopically (Coussot and Ancey, 1999). The interaction between the solid particles would be influenced by the arrangement of the particles relative to each other, by their size, their shape, and possibly by the chemical potential of the suspending fluid. As discussed before, and confirmed by the primary tested formulation, these parameters should be taken into consideration when preparing ink suspension for AM by cold extrusion. As one can see in Figure 4-7, the ink suspension can be in three different regimes, depending on the filler volume fraction. The first is a diluted regime, where the solid particles have no interaction. This regime is not interesting for the formulation of printable and extrudable inks. The second is a concentrated regime, where the particles can still move in the suspension, but particle-particle contacts are frequent. The latter regime is limited by a critical volume fraction when the suspension starts to be too brittle and crumbly. The final regime is the solid regime when the maximum possible packing of the filler is attained (Coussot and Ancey, 1999).

In this work, the selected suspensions are in the concentrated regime recognizable in Figure 4-5.

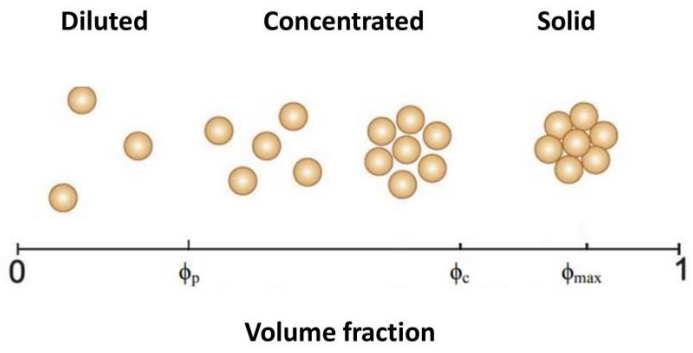

Figure 4-7: Illustration of different dispersion regimes as a function of particles concentration.

The Printability concept

Up to this point , the term ‘printability’ or ‘printable’ have been used multiple times without defining exactly what is printability, and what qualifies material as printable.

In a general manner, printability is a measure of how suitable a suspension's properties are for AM by a certain technique, which in our case is cold material extrusion. As much as this printability concept can seem to be almost innate, especially for researchers that have been working on AM by material extrusion (called also direct ink writing or robocasting in the literature), up to now there is not a clear and standardized method to define this emergent concept. However, in the literature, we can find few attempts to define some criteria and figures of merit.

In 2002, a first attempt simply considers the minimum G' required for printing a spanning structure (James E. Smay et al., 2002). The minimum G', given by eq 12, was determined by setting a maximum spanning rod deflection to be 0.05×D, where D is the rod's diameter.

$$G'_{min} = 1.4 \cdot \rho \cdot g \cdot D \cdot s^4 \qquad \textit{eq 12}$$

Where ρ is the density of the fresh paste, g the gravitational constant, and with (s=d/D) is the normalized span distance between rods. The stiffness of the paste (expressed by the storage modulus G') is a very important rheological parameter to print spanning structure, but is not the only crucial parameter to establish a general printability understanding.

In another work, a printability criterion was set, based on the yield stress required to withstand both forces of gravity and surface tension (M'Barki et al., 2017). The printability criterion Ξ is given by eq 13, where τ_y is the paste's yield stress, ρ the density of the paste, Υ_s the surface tension, h the height of the part, g gravitational acceleration, and R the radius of curvature of the smallest printed feature. This criterion takes into account not only the intrinsic properties of the ink, but also includes the printing part properties.

$$\Xi = \frac{\tau y}{\rho g h + \gamma s \, R^{-1}} \qquad \textit{eq 13}$$

That is why in 2017 a new figure of merit was suggested by (Feilden, 2017) which is only based on the rheological properties of the paste formulations, thus allowing a rapid selection of a promising formulation for AM by material extrusion. This figure of merit was developed based on the rheological properties required, experimental work and the state of art, for a successful printing, such as:

- Maximizing G' to minimize the elastic deformation during printing, hence shape maintainance.
- Minimizing the flow index n, the consistency coefficient K and the yield stress τ_y to reduce the force required to bend the extruded filament, to deposit it gently without deforming the printed layers.
- Nonetheless, τ_y should not drop from a minimum value in order to resist the surface forces and gravity.
- Minimizing the yield shear rate γ_y to reduce the paste compressibility during extrusion for an instant break of extrusion, when needed.

Accordingly, a paste-specific figure of merit (Φ) was suggested and a minimum value of 20 was found to be required for a successful robocasting (eq 14).

$$\Phi = \frac{G'}{\tau_y} \qquad \textit{eq 14}$$

In the most recent work (Duty et al., 2018), a more general viscoelastic model was proposed based on the rheological and thermophysical properties of the ink and the processing parameters. This model establishes a methodical approach to characterize printability by providing different equations serving printing criteria for a series of conditions that must be satisfied in order to successfully print a part. These equations depend not only on the material properties, but also on the used hardware and time-depending printing parameters. In the literature, we also come across other attempts to define the concept of printability for AM by material extrusion, but they focus more on assessing the printing quality, with no clear definition of a figure of merit for the ink itself (Gillispie et al., 2020; Naghieh and Chen, 2021).

In the present work, the figure of merit (Φ), coupled with maximization of paste stiffness G', were considered as criteria to optimize the ink formulation as this approach is paste-based without compassing printing parameters, which will be assessed more in detail in chapter 5.

4.2.3.2 Rheological study and optimization of the ink formulation - figure of merit

In the absence of a clear definition of printability with material extrusion, if we rely on the different criteria leading to a successful printing in the recent literature (Beach et al., 2021; Chu et al., 2021; Duty et al., 2018; Fahmy et al., 2020; Gillispie et al., 2020; Montoya et al., 2021; Naghieh and Chen,

2021; Panda et al., 2019, 2018, 2017; Rieger et al., 2021; Zhang et al., 2019), we can define 3 main rheological properties:

- Shear-thinning behavior to facilitate the extrusion of the ink through different nozzles.
- Optimized yield stress and stiffness of the ink formulation to ensure maximum shape fidelity and minimum structure slumping without affecting the extrudability.
- Thixotropic behavior for a good viscosity recovery upon extrusion to avoid layer slump.

These properties will be assessed in the next 3 subsections.

4.2.3.2.1 Shear-thinning behavior

The evolution of the slurries' apparent viscosity with increasing cellulose volume fraction is given in Figure 4-8. The viscosity of each slurry was measured at low shear rates (0.1 1/s) over at least 150 s. Figure 4-8 shows that the addition of cellulose powder increases very considerably the apparent viscosity of the neat PFA. For instance, the apparent viscosity increases to about 500 Pa·s for 13 vol% cellulose and exceeds 6.5 10^4 Pa·s when filling 24% of the slurry volume with cellulose particles. This exponential viscosity increase can be explained by an increase in the interaction energy between the particles which increases the fluid resistance to flow, hence an increase in the viscosity under the same shear strain.

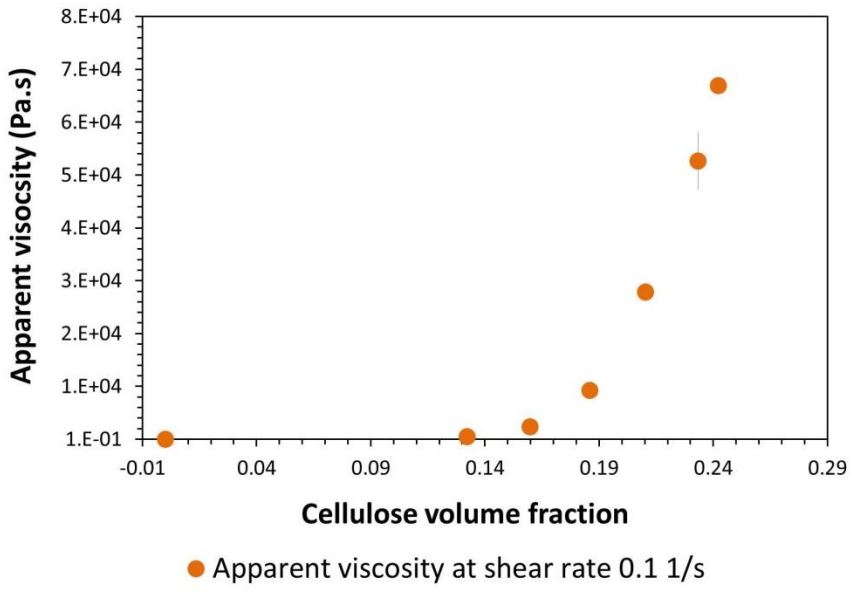

Figure 4-8: Slurry apparent viscosity as a function of cellulose volume fraction.

To assess the slurries flow under different shear rates, rotational rheological measurements were performed. Figure 4-9 shows that the neat PFA resin (red curve) has a Newtonian flow where the viscosity is independent of the applied shear rate, whilst the addition of cellulose powder led to a shear-thinning flow. This shear-thinning behavior is more or less marked for each formulation. Thus, in order to quantify the shear-thinning degree, a fitting of the apparent viscosity versus shear rate curves with the power-law (eq 8) was done. To do so, a log-log plot of the apparent viscosity vs. shear rate was used to compute the values of n and K by linear regression over the linear portions. The values of n and K of different formulations are given in Figure 4-9-B. One can notice a clear interdependency between the cellulose fraction in the different suspensions and their consistency index K which increases from barely 155 $Pa{\cdot}s^n$ when adding only 16 wt% of cellulose to over 2.5 10^3 $Pa{\cdot}s^n$ with 28 wt% cellulose.

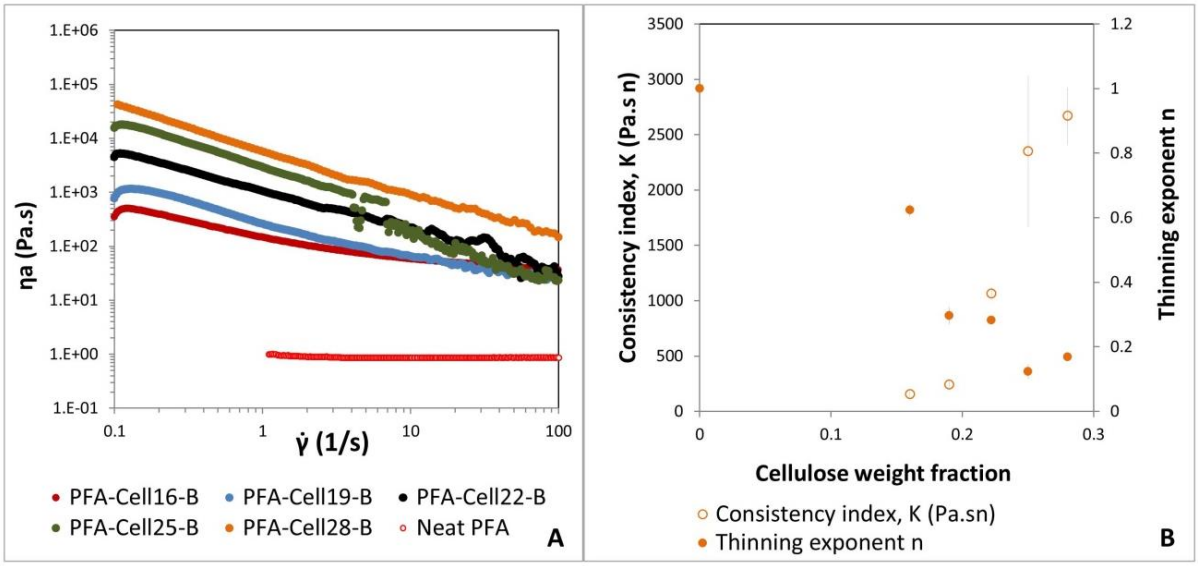

Figure 4-9: Rotational rheology of different slurries. (A) Flow curves and (B) values of the consistency index K and thinning exponent n.

On the other hand, the thinning exponent n decreases with increasing filler fraction, dropping from 0.65 for the formulation containing 16 wt% cellulose, to 0.1-0.3 when exceeding 19 wt% of cellulose. Over a certain filler fraction, no clear correlation can be concluded between the shear-thinning ability and the content of the filler. This can be explained by the fact that, adding only 16 wt% of particle, the network is not strong enough to resist shearing forces and could easily be broken and flow, thus leading to a negligible dependence between the viscosity and the shear stress. However, when reaching a critical fraction of the fillers, the network starts to be stronger and the inter-particle interactions becom dominant, thus making the structure flow more dependent on the shear stress applied. After this critical point, the shear-thinning mechanism does not change, thus making the

thinning exponent insensitive to the filler content. The values of n are in agreement with those of other printable mixtures of viscoelastic materials (Feilden et al., 2016; H. Li et al., 2016; M'Barki et al., 2017; Thibaut et al., 2019).

4.2.3.2.2 Oscillatory rheology tests

In order to assess the viscoelastic properties of the different formulations, an amplitude sweep between 1% and 100% was performed at a 1 Hz frequency. Figure 4-10 shows the storage and loss moduli (G' and G", respectively) of different slurries. As one can notice, in the Linear ViscoElastic Region (LVER), the G' value is more or less stable, which defines the stiffness of the formulation (G' LVER) which is, as discussed before, rucial to printability assessment. Then, as stress increases, the storage modulus drops until below the loss modulus. The crossover point, associated with the breakdown of the particle network within the slurry, can serve as an approximation of the yield stress τ_y. The stiffness expressed by the G' (LVER) and the yield stress values of the tested slurries are plotted in Figure 4-11-A. One can notice that with the addition of cellulose particles, there is an important increase of several orders of magnitude in the stiffness and yield stress.

Therefore, to select the most printable formulations, the merit figure (eq 14) suggested by (Feilden, 2017) was used. It was recommended that the value of Φ be superior to 20, based on the analysis of different printable formulations in the literature that were declared printable by material extrusion. A plot of stiffness (G' LVER) against the yield stress (τ_y) of each formulation is presented in Figure 4-11-B. The first criterion to classify printable and unprintable formulation is the absolute value of Φ, the line delimiting the value Φ= 20 is highlighted, but all the tested formulations were above this minimum value and the highest value is that of the formulation PFA-Cell28-B.

The second criterion is the minimum yield stress necessary to bear the gravitational forces for a certain build height. By neglecting the effect of the surface tension and considering only the effect of gravitational forces, the criterion suggested by (M'Barki et al., 2017) (eq 13) can be simplified and the yield stress can be expressed in terms of the building height according to eq 15. If we consider a minimum build height of h= 10 mm the yield stress value should be above 146 Pa. The upper limit of the yield stress can be determined by the extruder force.

Respecting these criteria, the formulations with the most printability potential are those containing over 25 wt% of cellulose (highlighted in green on Figure 4-11-B). Furthermore, by applying printability criteria (J. E. Smay et al., 2002), which consist of maximizing the stiffness of the

suspension for better-spanning structures (eq 12), the formulations containing 28 wt% and 29 wt% are more advantaged.

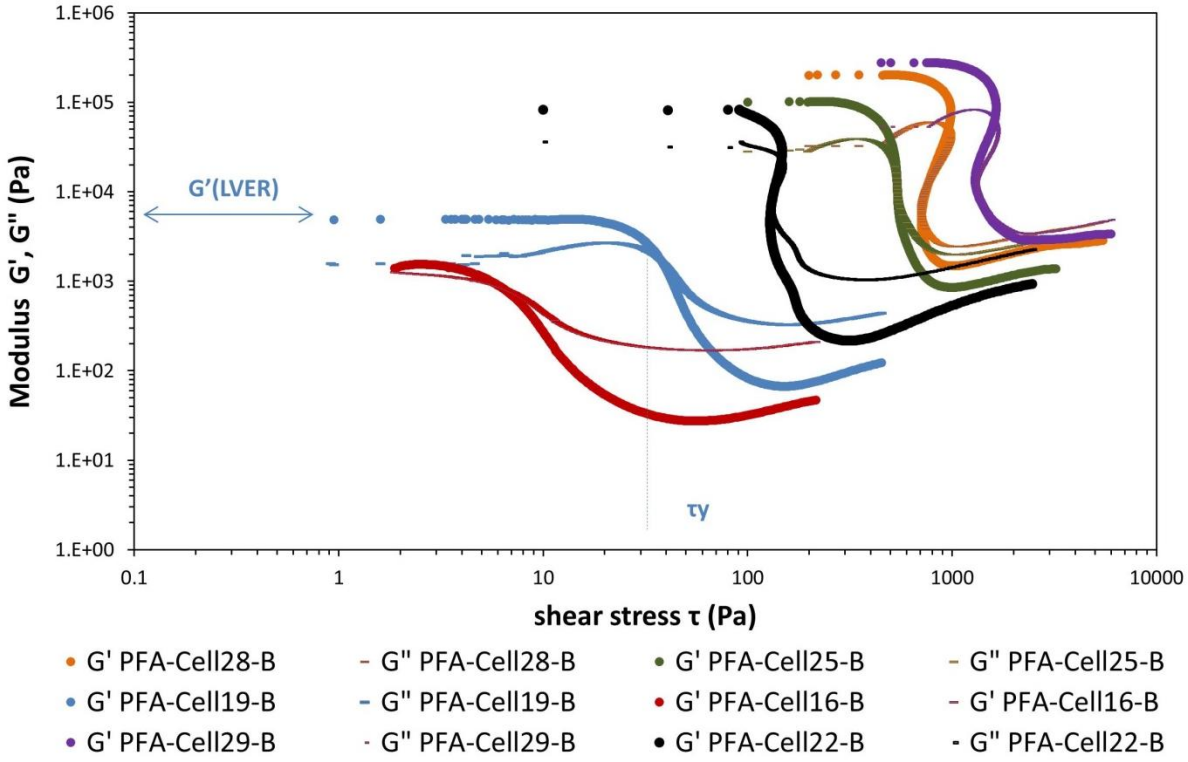

Figure 4-10: Storage and loss moduli vs. shear stress obtained by amplitude sweep at 1 Hz for different suspensions.

eq 15

$$\tau_y = h \cdot \rho \cdot g$$

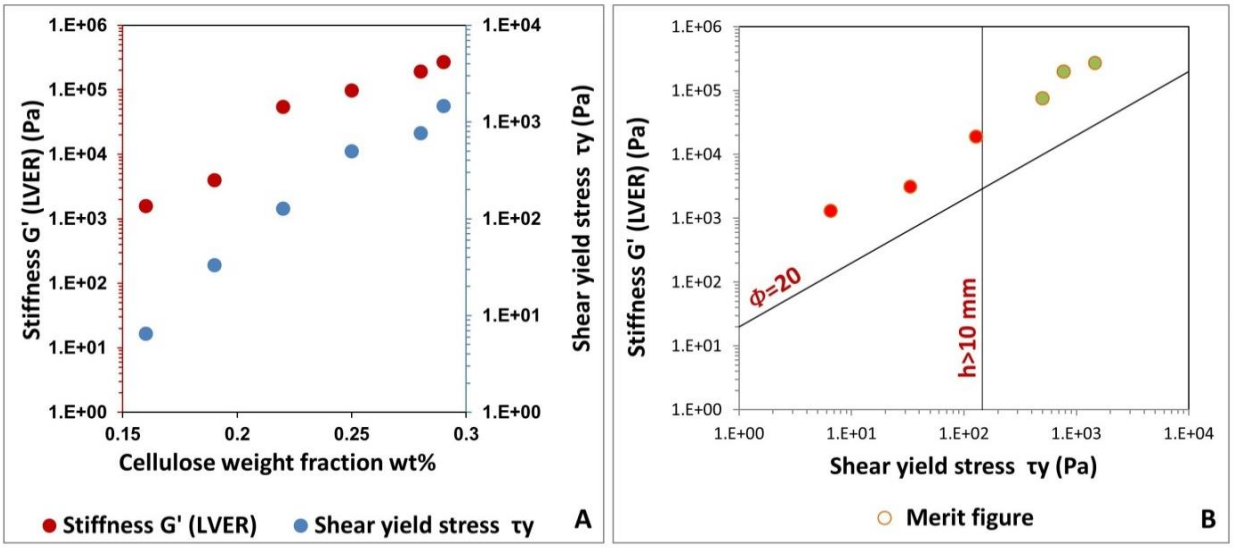

Figure 4-11: (A) Evolution of the yield stress and stiffness as a function of cellulose weight fraction and (B) formulation selection map showing a minimum merit figure and minimum printable object without collapsing.

4.2.3.2.3 Shear recovery behavior

During 3D printing with material extrusion, the inks experience shear forces and undergo physical changes, especially for complex fluid. The thixotropic rheological component of the different suspensions should be examined because it has crucial importance in the extrusion-deposition process. Indeed, ideally, the viscosity of the developed ink should decrease at high shear rates to facilitate the extrusion process (shear-thinning) and increase immediately after a total recovery at the outlet of the nozzle (Kraut et al., 2017; Lille et al., 2018). To investigate the thixotropy of formulations, a 5-step experiment was applied to model the high shear deposition process by alternating high shear rates and low shear rates at 60 s intervals. An estimation of the shear rate in the nozzle was first realized using the Rabinowitsch–Mooney equation, according to which a shear rate ($\dot{\Upsilon}$) through a circular orifice of radius (R) for shear-thinning materials can be expressed according to eq 16 (Dealy and Wissbrun, 2012).

$$\dot{\gamma} = \frac{4Q}{\pi R^3}\left(\frac{3n+1}{4n}\right) \qquad \textit{eq 16}$$

Where Q is the volume flow rate and n the flow behavior index of the shear-thinning material. To determine the maximum shear rate which could be reached in our work, we can consider the formulation PFA-Cell28-B (n=0.16) printed using a nozzle with a minimum diameter of 0.5 mm (10

times larger than the largest particle of the powder) with a flow rate of 4.5 mm^3/min (corresponding to a printing speed of 1800 mm/min). In these conditions, the shear rate would be 848 1/s.

Unfortunately, shearing such complex suspensions at this value of rate on the rotational rheometer was not possible because of edge fracture phenomenon. This kind of sample instability is characterized by a deformation of the sample's surface at the free edges between the upper and lower part of the geometry, as shown in Figure 4-12. Indeed, a 3-step thixotropic behavior test was performed on the formulation PFA-Cell28-B by shearing the slurry at 1000 1/s and the recorded viscosity change was unstable at high shear rate, as one can see in Figure 4-12-A. In Figure 4-12-B, a flow curve from 0.1 to 1000 1/s displayed the same phenomenon at around 200 1/s, i.e. a sudden drop in the viscosity values and a change in the flow behavior. This rheological characterization limitation is caused by a deformation of the surface and a secondary flow propagating radially as a function of both time and applied deformation which increases measuring errors at high shear rates (Hemingway et al., 2017; Meyer and Crawford, 2018). For a relevant thixotropic characterization, the formulations were sheared at 100 1/s and 0.1 1/s rates.

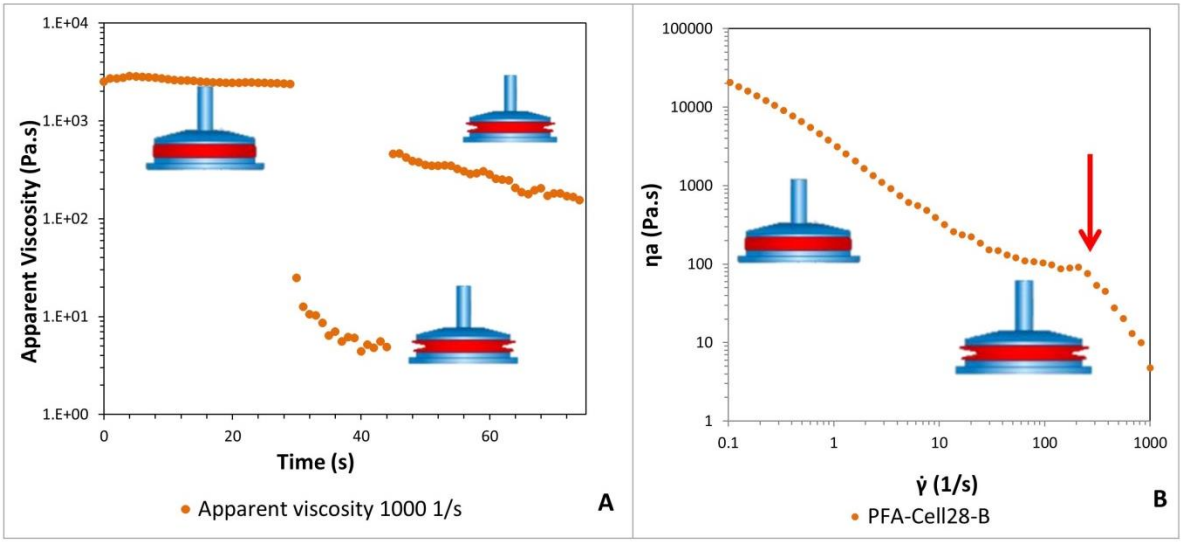

Figure 4-12: Edge fraction problem at a high shearing rate of highly filled formulations.

The results of the thixotropic shear recovery behavior are illustrated in Figure 4-13. All formulations' viscosity decreased significantly at high shear rate and recovered more or less rapidly at low shear rate until reaching stabilized values at the end of the shearing interval. When adding from 16 to 22 wt% of cellulose powder one can notice a drop in viscosity of 2 orders of magnitude reaching up to 3 orders of magnitude when adding more than 25 wt% of particles. When shifting to a low shear rate after 60 s of high rate shearing, the viscosity starts to build up again. In the viscosity build-up phase,

a difference between the formulations occurs. The formulation containing the least cellulose builds up more quickly than those containing over 19 wt% cellulose, which can be explained by the difficulty of the highly filled structures to build up again after an important decrease in viscosity and breakage of the particles network. This might also be related to an increase in the temperature of the suspension due to particles friction, which decreases the resin viscosity. To quantify the overall recovery of the viscosity, a recovery percentage R(%) is calculated according to eq 17 where η_{in} is the average viscosity during the last 10 s of step 3 and η_{fin} the average of the viscosity during the last 10 s of step 5.

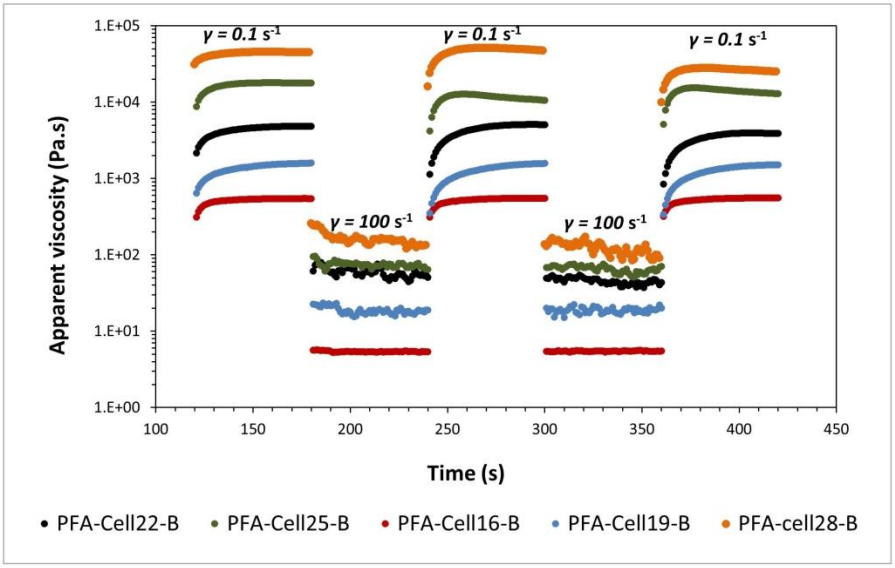

Figure 4-13: A 5-step thixotropic behavior study of different suspensions.

$$R(\%) = \frac{\eta_{fin} \cdot 100}{\eta_{in}} \qquad \textit{eq 17}$$

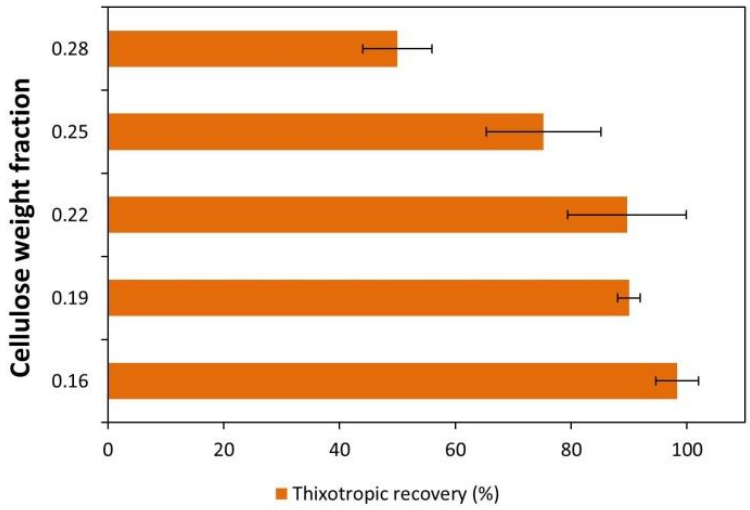

Figure 4-14: Thixotropic recovery rate as a function of cellulose weight fraction in different slurries.

Figure 4-14 shows the recovery percentage of the inks within 60 s after the removal of the high shear rate (100 1/s) as a function of cellulose powder content. The recovery percentage is dependent of the cellulose weight fraction, which is inversely proportional. This tendency might be due to a permanent disruption of the more entangled network. The viscosity recovery is between 65 and 100%, which is an acceptable value, but for an optimized shape fidelity, this value should be maximized for a total recovery of the structure during layer deposit.

4.2.4 Effect of cellulose particles incorporation on physical and mechanical properties of bulk composite

4.2.4.1 Water absorption under controlled relative humidity

The capacity of water absorption and desorption of the neat cured PFA, cellulose powder, and the composite was assessed with the *Varimass* device. Mass gain and loss during the different relative humidity levels are gathered in Figure 4-15.

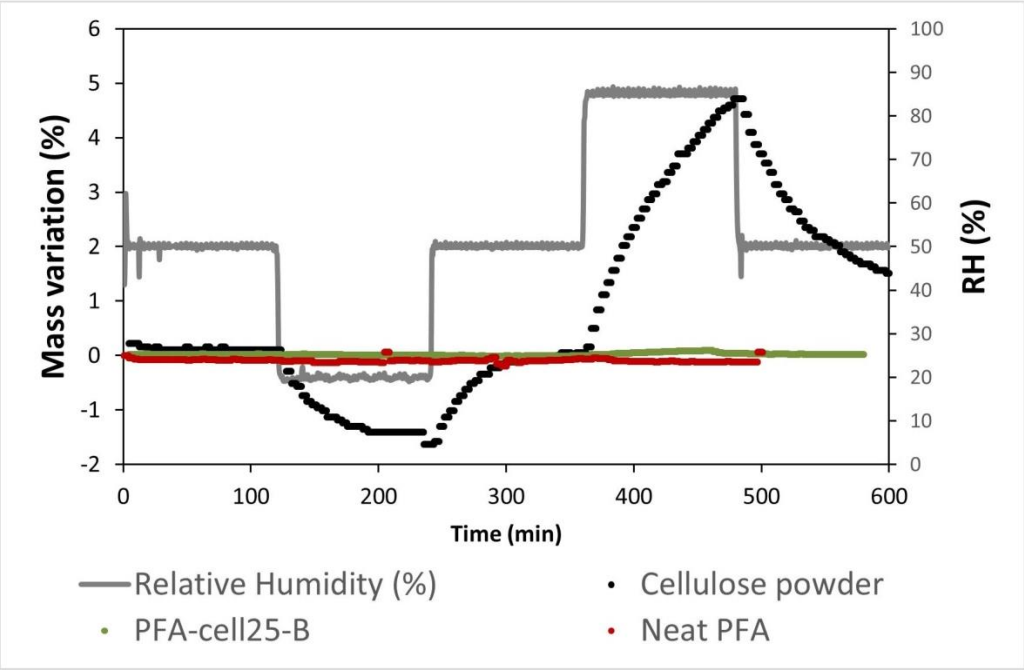

Figure 4-15: Water absorption of composites, neat PFA, and cellulose under controlled relative humidity.

Cellulose contains hydroxyl groups that can interact with water molecules which makes this biopolymer highly sensitive to humidity. As one can notice in Figure 4-15, after mass stabilization at 50% of relative humidity, the cellulose lost up to 1.5% of its weight upon desorption at low humidity levels. At a high humidity level (90%), cellulose gained weight rapidly to reach 5% in two hours. On the other hand, cured PFA is a hydrophobic matrix insensitive to water. Therefore, it is expected that the number of OH groups in FA, available for hydrogen bonding with water molecules, was reduced during PFA polymerization, resulting in a non-polar polymer. As shown in Figure 4-15, the weight of the specimen was stable with virtually no mass variation. The composite with up to 27 wt% of cellulose remained very little sensitive to water with a mass variation that does not exceed 0.1%, even at high humidity levels. The composite nevertheless is slightly more sensitive to humidity compared with that of the neat matrix. These curves suggest that the ensuing composite is quasi-hydrophobic despite the high cellulose fraction, a fact that can be explained by the encapsulation of cellulose particles in the hydrophobic polymer matrix.

These findings are in agreement with a previous work (Mokhothu and John, 2017) where the coating performances of PFA for a flax/phenolic composite were assessed. Coated samples with different polymers were tested for water absorption properties according to ASTM D570 for 7 days and the moisture content was evaluated after aging for 3 days according to ASTM D5229. It was found that the PFA coated laminate had the best performance, as highlighted in Figure 4-16, with a reduction of

75% in water absorption and of 70% in moisture content after aging with respect to the uncoated laminates which also agrees with other works in the literature (Dong et al., 2014; Kumar et al., 2012). The PFA coating showed also preservation in mechanical properties and prevention of thermal degradation (Deka and Karak, 2009; Dong et al., 2014).

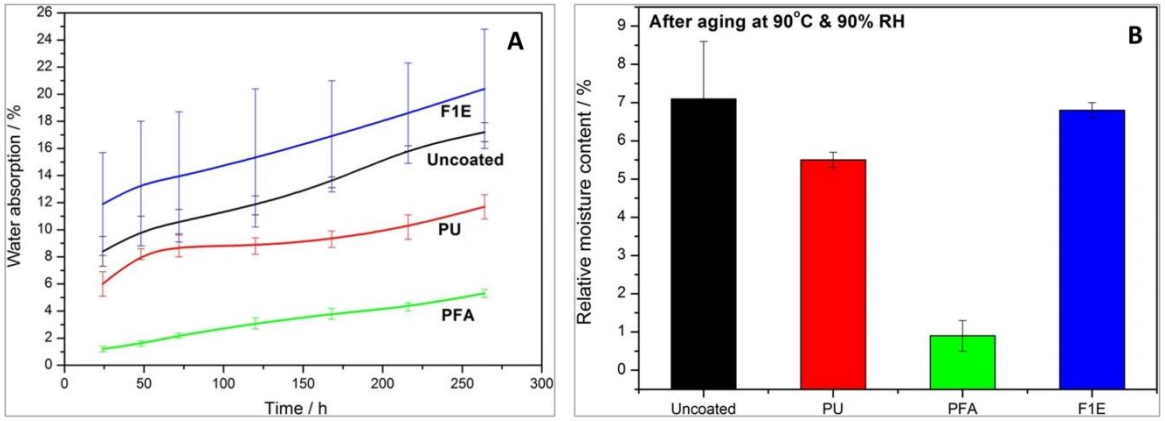

Figure 4-16: (A) water absorption and (B) moisture content after aging, of composite with a different polymeric coating (PFA in green) (Mokhothu and John, 2017).

Hence, the important cellulose content in the composites developed in the present work should not disrupt the outstanding performance of PFA polymers such as insensitivity to moisture and aging, thermal stability, and water resistance.

4.2.4.2 Effect of cellulose on porosity and dimensional stability

One of PFA major issues is the high water content in the resin and the water generated by the condensation reactions during curing. This issue is particularly noticeable in composite manufacturing because it leads to high porosity and low dimensional stability. Other parameters can trigger pores formation in the furanic resin, but moisture content and viscosity are the dominant factors (Oishi et al., 2013).

The used commercial PFA contains 7.5 wt% of water and generates over 2 wt% during curing (Domínguez and Madsen, 2015), added to over 1.75 wt% of water brought by the catalyst. Therefore, at least 11 wt% of the resin's weight should be eliminated during the curing phase, which promotes porosity when the gas release is blocked. This important water content can lead to foaming caused by the boiling of the water inside the curing process especially for samples with thick walls which blocks the evacuation of gases through the structure. The foaming is particularly noticeable when the curing kinetic is fast, leading to a low gel time which interferes with gas elimination and hence the bubbles can be trapped inside the rubbery polymer matrix.

To further investigate the effect of cellulose on the porosity caused by the water evaporation during curing, the prepared formulations were cured in the oven, but at a higher temperature (around the exothermic peak of the curing reaction) to favor resin foaming and to assess the effect of cellulose on this phenomenon. Some samples fluffed up and the porosity could not be accurately measured. However, the effect of cellulose is clearly shown in Figure 4-17. One can notice that when curing at 90°C, below the water boiling temperature, the composite with or without cellulose did not foam, but still displayed micro and macro-porosity.

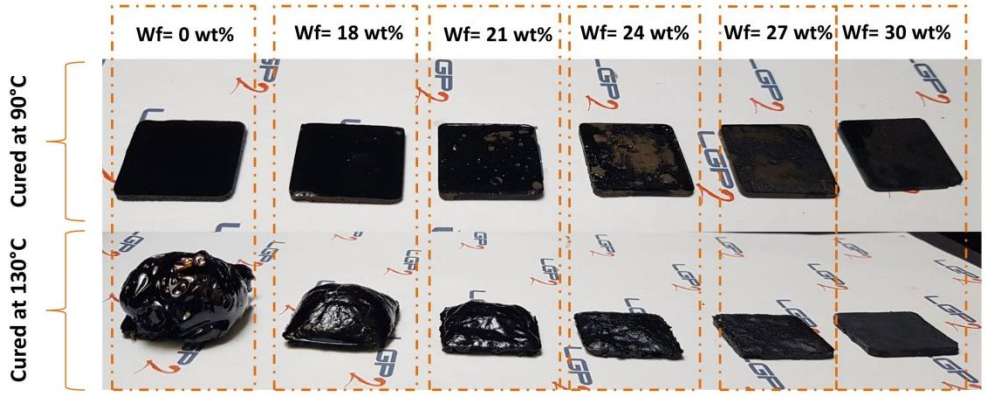

Figure 4-17: Photographs of different composites aspect cured overnight at 90°C and 130°C.

When curing at 130°C, above the water boiling point, and with a lower gel time, the resin foamed because of the internal pressure caused by the generated gases and blocked by the external rubbery resin layer which is illustrated in Figure 4-18-B. This foaming was mitigated by the addition of cellulose, particularly in the PFA-Cell25-B composite. This effect can be related to the percolation of highly hydrophilic cellulose fibers which helped steam diffusion through the fibrous network without causing any noticeable deformation in the composite showed in Figure 4-17-B and explained in Figure 4-18-B.

As shown in Figure 4-19, and in line with the above explanations, the neat cured PFA displayed almost no internal pores, but one can distinctly see macro-pores with perfect circular shapes all over the surface (Figure 4-19-B), showing the presence of air bubbles leaving the resin after water evaporation. These pores were more visible on the surface in contact with the mold, which obstructed bubbles degassing, as illustrated in Figure 4-18-A. On the other hand, for the PFA-Cell25-B composite, one can notice on Figure 4-19-C numerous internal pores with different sizes and shapes, but mostly oval and recumbent along the casting direction. The surface of the specimen is smooth and presents no bubble marks Figure 4-19-C.

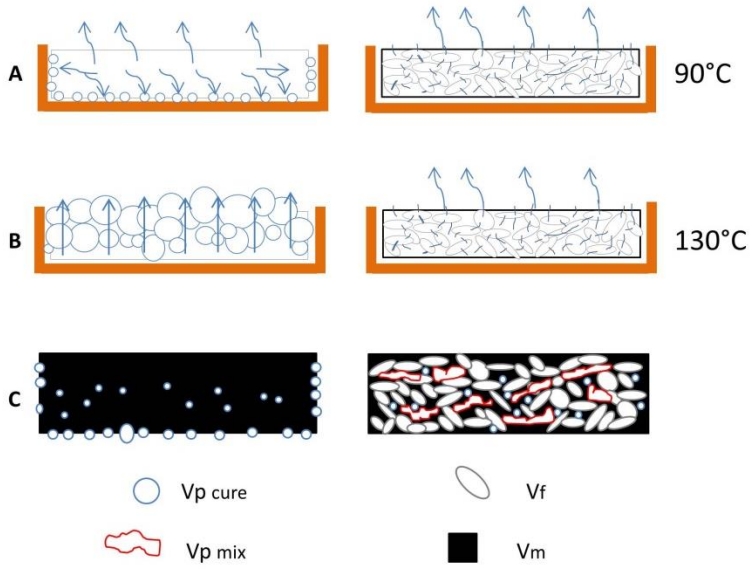

Figure 4-18: Illustration of the foaming and porosity formation phenomenon under different conditions. (A) Representation of the water evaporation and porosity formation in the mold at 90°C of the neat PFA resin and the cellulose-based slurry. (B) Water evaporation at 130°C through neat PFA with foam formation under the evaporation forces and through cellulose-based slurry. (C) a representation of the different types of forms porosity in molded cured neat PFA and in the biocomposite.

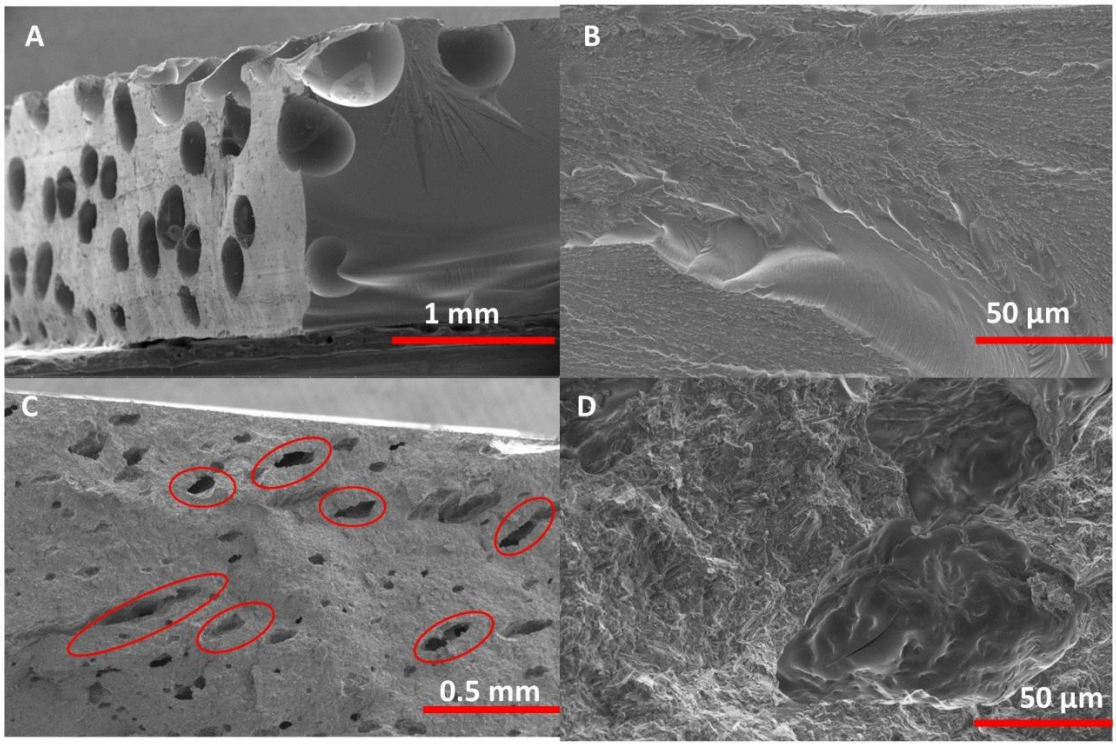

Figure 4-19: SEM images of several cured (90°C) PFA surface: (A) surface of the cured specimen of neat PFA,(B) fractured surface of neat PFA, (C) PFA-Cell25-B composite fractured surface, (D) zoom on the pores in PFA-Cell25-B composite.

This porosity might be mainly due to manual molding and mixing and not to vapor bubbles which were probably, as discussed above, drained through the fibrous network. On the micrograph in Figure 4-19-D one can visualize the fibers network. However, pores formation by vapor generation can still be possible and we suppose that they partially coalesced with the pre-existing air bubbles in the composite.

The porosity content of different composites is displayed in Figure 4-20-A. The pure PFA resin cured at 90°C had 8.8% porosity which is in agreement with the porosity found in a previous work for the same commercial PFA resin using the double-vacuum-bag technique (Domínguez and Madsen, 2015). The porosity percentage doubled after the addition of 18 wt% of cellulose. Above 18 wt% of cellulose, the porosity decreased steadily when increasing the cellulose weight fraction. Owing to the particularly viscous and sticky nature of the PFA-Cell16-B slurry, the sudden increase in porosity when adding 18 wt% cellulose might be ascribed to air inclusion during the mixing and casting step and not only to water vapor generation during the thermal curing. In fact, this specific slurry was not as fluid as the pure PFA, which flowed easily in the molds. The stickiness of this particular slurry against the spatula further complicated the molding process leading to porosity embedding. For this reason, when the formulation started to be less sticky, casting was easier and voids inclusion was avoided. However, the porosity percentage of all the composites containing cellulose is higher than the neat PFA sample which is inconsistent with water content 30% lower than that of the bare resin. Therefore, the porosity volume (V_p) in the composites was mainly associated with the mixing and casting process ($V_{p\ mix}$). For a better understanding, the hypothesized internal composite structure is illustrated in Figure 4-18-C where red circles represent the porosity creating during the mixing and molding and those represented with blue circles present the porosity created later during curing. Accordingly, to estimate the porosity created during paste mixing and molding step ($V_{p\ mix)}$, few assumptions should be made, namely:

- The porosity volume created in the neat resin in the curing step ($V_{p\ cure}$) is not affected by the cellulose addition (neglecting the draining effect of fibers).
- Any porosity in the fibers is neglected.

In this case, the $V_{p\ cure}$ can be estimated based on the porosity of the neat PFA, which was found to be 8.9% using eq 18:

$$V_{p\ cure}\ (vol\%) = V_{p\ neat\ PFA} \cdot Vm \qquad \textit{eq 18}$$

Where V_m is the volume fraction without considering any eventual porosity in the composite calculated using eq 19.

$$\mathrm{Vm\ (Vol\%)} = \frac{\mathrm{V_{PFA}\ (cm^3)} \cdot 100}{\mathrm{V_{PFA}\ (cm^3)} + \mathrm{V_{cellulose}\ (cm^3)}} \qquad \textit{eq 19}$$

Where $V_{PFA}\ (cm^3) = \frac{W_{PFA}\ (g)}{\rho_{PFA}}$ is the added oligomers volume inside the formulation, and $V_{Cellulose}\ (cm^3) = \frac{W_{cellulose}\ (g)}{\rho_{cellulose}}$ the added cellulose powder volume inside the formulation.

The porosity volume caused by the mixing can be therefore estimated as the difference between the total porosity and the porosity created in the resin phase during curing as:

$$\mathrm{V_{p\ mix}\ (vol\%)} = \mathrm{V_p} - \mathrm{V_{p\ cure}} \qquad \textit{eq 20}$$

The effective volume fractions in the composite considering the pores volume can therefore be recalculated and the results are given in Table 4-2.

Table 4-2: Summary of the weight and volume fractions of different components and their respective shrinkage rates.

	Without porosity				With porosity			Porosity origin		Shrinkage	
Reference	Wm (wt%)	Wf (wt%)	Vf (vol%)	Vm (vol%)	Vm_{eff} (vol%)	Vf_{eff} (vol%)	Vp (vol%)	Vp_{cure} (vol%)	Vp_{mix} (vol%)	$Shrinkage_{exp}$	$Shrinkage_{theo}$
Neat PFA	100.0	0.0	0.0	100.0	91.2	0.0	8.8	8.8	0.0	2.9	2.9
PFA-Cell16-B	82.2	17.8	14.9	85.2	67.7	11.8	20.5	7.5	13.0	2.3	1.9
PFA- Cell19-B	78.7	21.3	17.9	82.1	67.0	14.6	18.4	7.2	11.2	1.3	1.9
PFA- Cell22-B	75.5	24.5	20.7	79.3	69.6	18.2	12.2	6.9	5.2	1.8	2.0
PFA- Cell25-B	72.6	27.5	23.4	76.6	68.4	20.9	10.8	6.7	4.0	1.9	1.9

	Without porosity				With porosity			Porosity origin		Shrinkage	
Reference	Wm (wt%)	Wf (wt%)	Vf (vol%)	Vm (vol%)	Vm_{eff} (vol%)	Vf_{eff} (vol%)	Vp (vol%)	Vp_{cure} (vol%)	Vp_{mix} (vol%)	$Shrinkage_{exp}$	$Shrinkage_{theo}$
PFA- Cell28-B	69.8	30.2	25.8	74.1	65.3	22.8	11.9	6.5	5.4	1.8	1.9

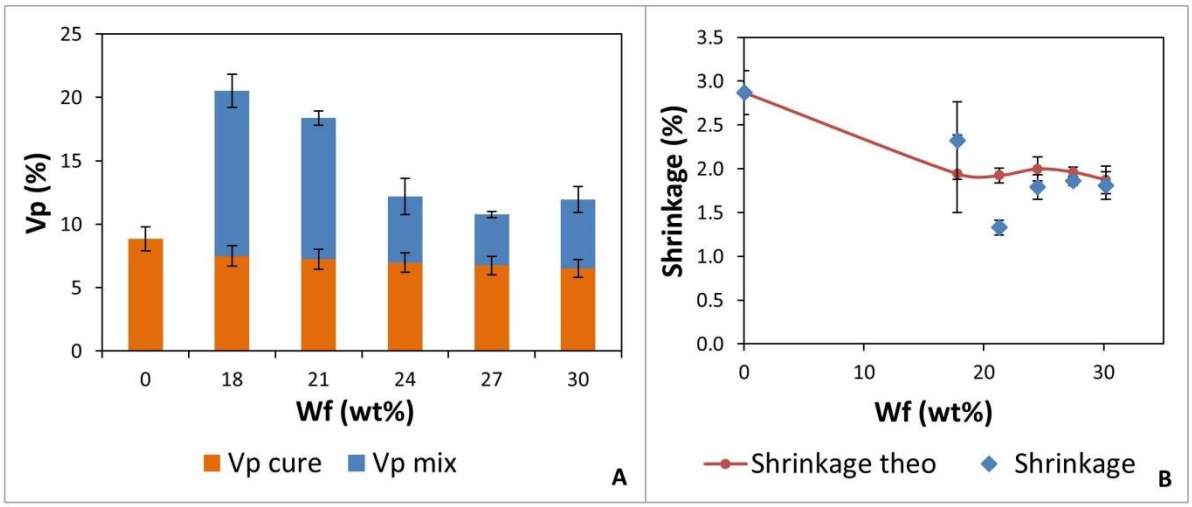

Figure 4-20: (A) Porosity percentage in composites with different cellulose contents, cured at 90°C in the oven, (B) Shrinkage percentage of composites with different cellulose contents cured at 90°C in the oven.

PFA, like the majority of thermosetting polymers, shrinks during curing, which, according to the supplier data, can reach 7%. The dimensional stability is important for composite production and 3D printing and it is, therefore, essential to minimize it. As shown in Figure 4-20-B, the shrinkage decreased when increasing the volume fraction of cellulose. Shrinkage upon curing of the PFA went from 2.9% for neat PFA to 1.8% when adding at least 24 wt% of cellulose fibers. The shrinkage of the resin is due the densification of the network and the evaporation of water and other volatiles during the curing process. However, the cured composites have up to 35% of their volume occupied by dimensionally stable components (cellulose and pores), which could explain the shrinkage decrease. A theoretical shrinkage percentage was estimated by considering the shrinkage to be strictly related to the matrix phase shrinkage (which is estimated to be 2.9 %) using eq 21 and the resulting values are plotted in Figure 4-20-B.

$$\text{Shrinkage composite (\%)} = \frac{\text{Vm (vol\%)}}{100} \cdot \text{Shrinkage PFA (\%)} \qquad \textit{eq 21}$$

As one can see in Figure 4-20-B, the calculated theoretical shrinkage estimates well the experimental data except for the composite containing 21 wt% of fibers which might be related to an experimental issue (like incomplete curing of the specimens inside the oven).

Overall, cellulose addition has a major role in improving the composite dimensional stability during the curing process as shown by the fact that, under the tested conditions, cellulose decreased by 35% the shrinkage of the neat PFA down to 1.8% for the formulation PFA-Cell28-B (i.e. 3 times the usual shrinkage of ABS and PLA but less than the shrinkage of PP and PA which is over 2%). Cellulose addition can also prevent the foaming of the resin minimizing the curing porosity. It follows that, when avoiding air bubbles inclusion during the processing of the pasty formulation, the composite porosity can be decreased to less than 6%.

4.2.4.3 Thermal stability

The thermal stability of the crosslinked PFA, cellulose and the composites was assessed by thermogravimetric analysis (TGA). The TGA curves given in Figure 4-21, show that in an oxidative atmosphere, cellulose loses 3% of its weight between 90 and 200°C, which is considered to be the residual moisture, followed by a classical abrupt degradation starting at 300°C, before a total degradation of the material when the temperature reaches 530°C. In the case of PFA, one notices a three-step degradation process. The first ramp starts at 200°C with only 10% weight loss, which could be explained by a further curing and consequent water evaporation (Ma et al., 1995). The second step starts when the decomposition rate increases around 400°C to reach a 50% weight loss at 600°C, which is attributed to the decomposition of the furan polymer (Guigo et al., 2009). The final degradation step leads to the total burning of the organic polymer at 700°C.

The degradation of the composites with 31 wt% cellulose content goes through the same 3 steps as for the neat PFA, with an increase in the cellulose decomposition temperature when the degradation rate increases, to reach a 25% weight loss at 400°C.

Under inert atmosphere (N_2), the degradation curves (Figure 4-21) show the same degradation steps, but the degradation rate decreases considerably starting from 500°C to reach a plateau at 800°C. After the stabilization of the weight loss, the char residue is about 50 wt%, which is in agreement with values given in the literature (Gandini, 1997). This residue decreases when increasing the thermally unstable cellulose fraction that loses up to 90% of its initial weight. The char residue of the composite with more than 30 wt% of cellulose is around 40 wt%, which therefore does not exclude the possibility of carbonization of the molded composites.

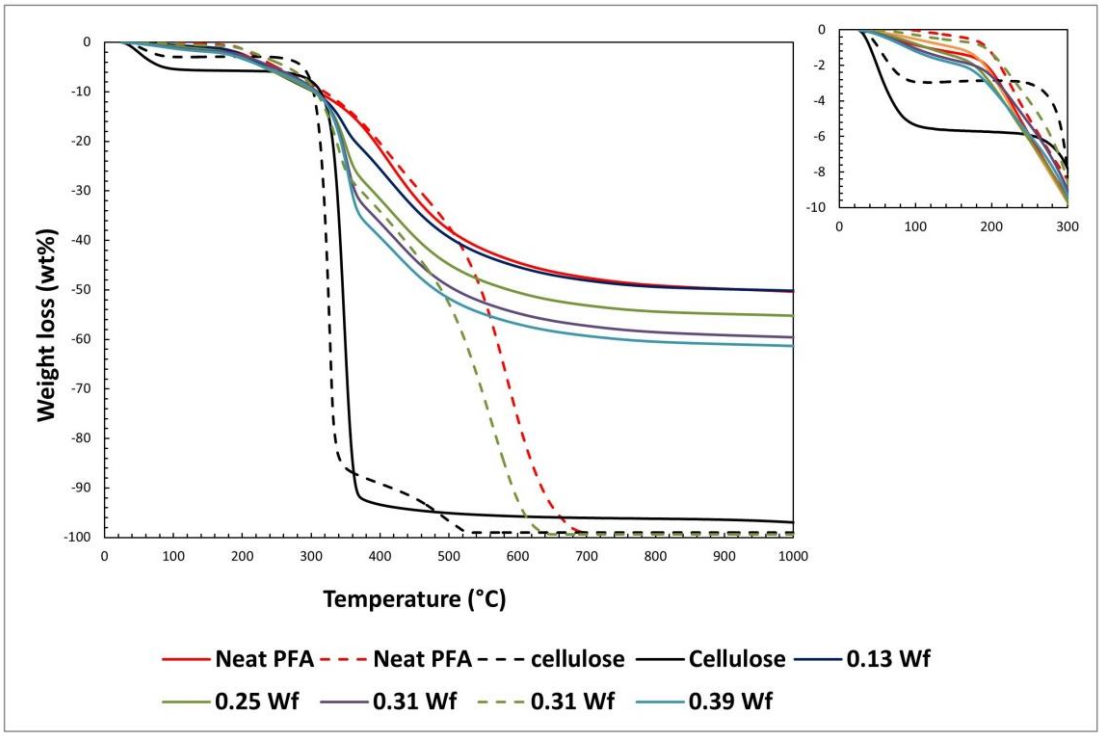

Figure 4-21: TGA scans collected at 10°C/min showing the degradation of cured neat PFA, cellulose powder, and biocomposites with different cellulose weight content under N_2 (continuous curves) and under an oxygen atmosphere (dashed curves).

4.2.4.4 Thermomechanical behavior

The storage modulus E' of composites as a function of temperature is given in Figure 4-22-A. Cellulose addition increased the storage modulus of the composites, which is higher than that of the neat cured PFA over the whole temperature region. This could be ascribed to the tension transfer from the matrix to the high-modulus filler, which enhanced the composite stiffness.

At room temperature, the modulus E' increased when increasing the cellulose fraction, which was maximized for W_f= 30 wt%. Cellulose addition also improved the composite thermomechanical stability by increasing the stiffness at high temperatures, as highlighted in Figure 4-22-B. For instance, with a 30 wt% weight fraction of cellulose, the modulus remained higher than 4 GPa up to 150°C and higher than 2 GPa up to 200°C, whereas, for the neat cured PFA, it dropped below 2 GPa when reaching 150°C. The thermal stability and the rigidity of both the cured neat PFA and the composites were higher than those reported in the literature when incorporating sisal whiskers and lignin in conventional PFA (Ahmad et al., 2013; Guigo et al., 2010). In addition to the typical thermomechanical stability of cellulose fibers, cellulose microparticles are supposed to hinder polymer chains mobility thus further enhancing the composite thermomechanical behavior.

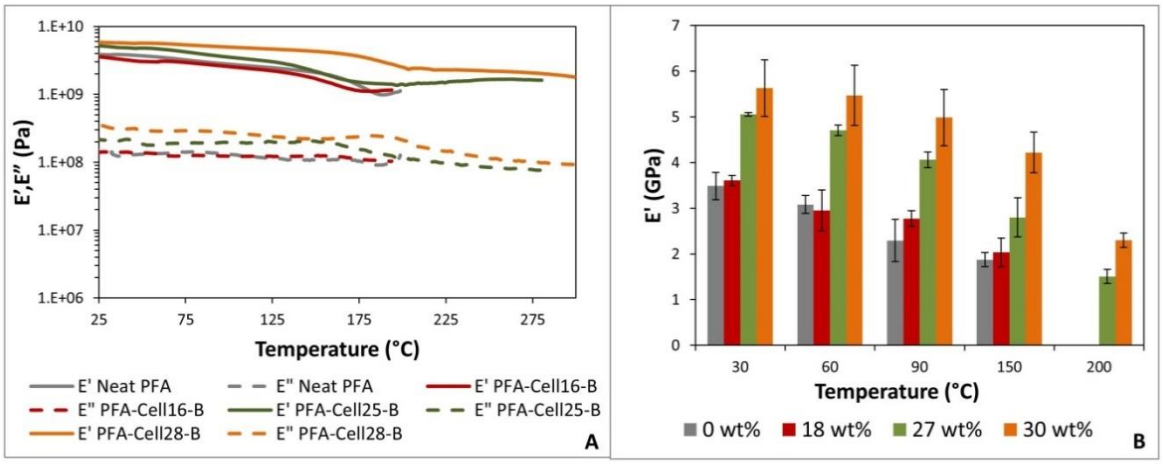

Figure 4-22: Storage (continuous curves) and loss (dashed curves) moduli of composites with different cellulose weight fraction plotted as a function of temperature.

This thermomechanical stability is competitive with those of PEEK and some other technical polymers used in 3D printing (Diez-Pascual et al., 2009; Cao et al., 2015; Qu et al., 2017; Papageorgiou et al., 2019; Niu et al., 2021). Unlike the PFA/cellulose composite, these technical thermoplastics can be extremely expensive and also rather complicated to print, apart from the fact that they are fossil-based materials.

In order to evaluate composite mechanical properties at high temperature and under prolonged solicitations, composite samples were tested during 6 h at 200°C. Figure 4-23 shows the storage modulus of the composite PFA-cell28-B (containing 30 wt% cellulose) under a static force of 10 and 20 N with a dynamic displacement of ±15 µm at a frequence of 1 Hz. As one can see on the figure, under 10 N of static force (dashed red curve) the storage modulus is around 5 GPa at room temperature and, when heating at 200°C, it drops to 1 GPa to raise again until stabilizing at 2.8 GPa. This decrease-increase of the storage modulus when heating at 200°C was related to further crosslinking of the polymeric structure. Accordingly, another sample was heat-treated in an oven for 2 hours at 200°C and the same DMA test was run again. In this case, the storage modulus at room temperature increased by 20% with respect to the untreated sample and when the temperature increased to 200°C the storage modulus dropped to 3 GPa and the increase of the modulus was also remarkably limited comparing the untreated sample. Furthermore, the storage modulus decreased only by 20% when increasing the temperature from 25°C to 200°C and was stable for more than 6 hours. The same test was carried out under 20 N static force and the same behavior was observed with a 30 % decrease in the storage modulus.

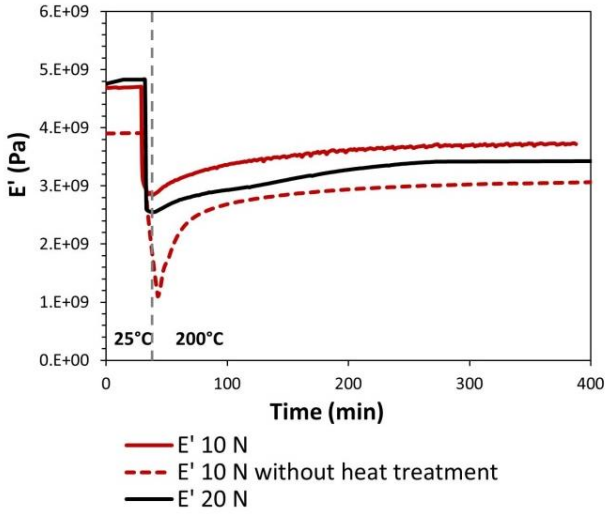

Figure 4-23: Storage modulus evolution at room temperature and at high temperature.

4.2.4.5 Mechanical performances

As can be seen in Figure 4-24, the composite stiffness improved after the addition of cellulose powder. The tensile modulus increased from 2527 to 2880 MPa and the flexural modulus from 3092 to 4309 MPa by adding 30 wt% of cellulose. This modest improvement suggests a good wetting by the resin of the cellulose particles (Ku et al., 2011) and agrees well with the DMA results.

On the other hand, the tensile and flexural strength decreased when adding cellulose with an opposite evolution of porosity. This can be explained by the fact that high porosity content in the composite is deteriorating the strength because pores act as stress concentrators and fracture nucleation sites (Pfister and Larock, 2010). Therefore, when recalculating the specific modulus by normalizing the measured values to their density, one can notice that cellulose is improving the mechanical properties of the composite by increasing the flexural modulus by 40% and tensile modulus by 10%. Therefore, voids generated during the paste preparation and manual casting are supposed to be at the origin of the limited enhancement of the mechanical performance of the tested samples.

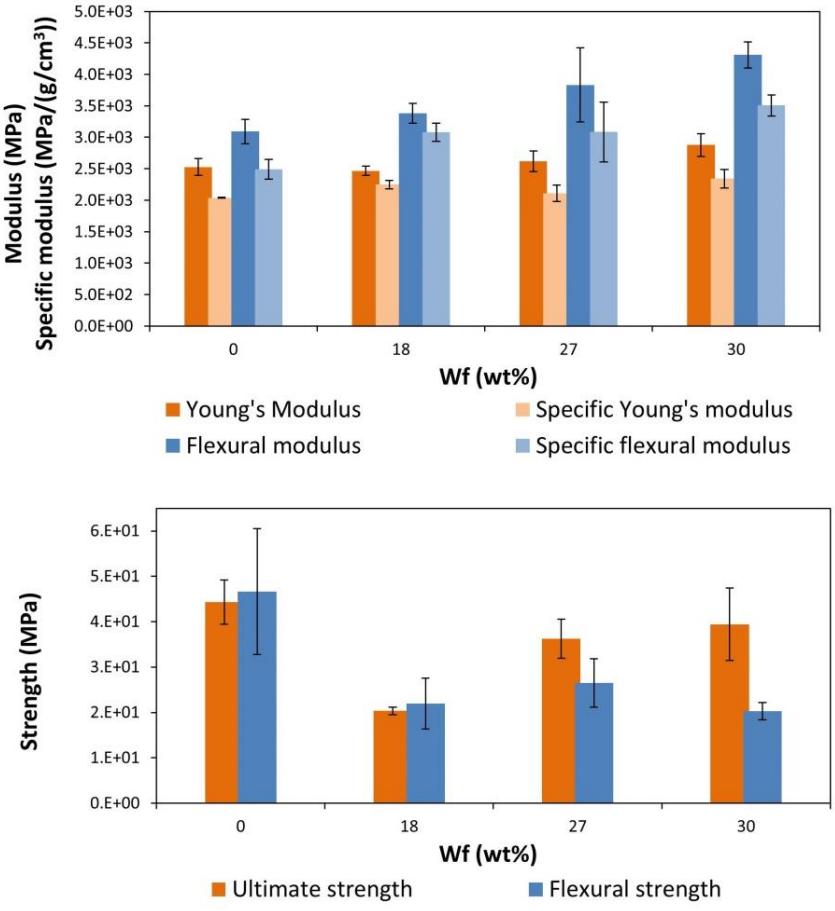

Figure 4-24: Tensile and flexural modulus and strengths of neat cured PFA and different biocomposites.

4.2.5 Conclusions

To sum up this section, the following points can be retained.

i. The conducted preliminary tests showed that:

- The use of microscopic powdery cellulose is preferred for a stable extrusion through narrow nozzles usually used in 3D printing to maximize the printing resolution.
- An addition of at least 10 wt% of cellulosic fillers is needed to convert the fluid PFA oligomers to a more concentrated suspension with a stable extrusion flow whilst the addition of more than 30 wt% cellulose results in highly concentrated solid-like paste, which is hardly extrudable.
- The solvent content in the formulation should be limited as much as possible to prevent cracking of the composite upon curing and pores creation usually caused by the exothermic curing of the PFA oligomers.

ii. The conducted rheology tests revealed that:

- The shear-thinning behavior of all the slurries is maximized with the addition of at least 25 wt% fillers.
- The yield stress and stiffness increased with the increase of fillers content, to reach respectively 1.46 kPa and 270 kPa when adding 29 wt% of cellulose powder.
- The slurries containing cellulose powder exhibited a thixotropic behavior, but the viscosity recovery decreased when increasing the cellulose content and it was limited to 60% when adding 28 wt% of fillers, against 98% when adding only 16% of cellulosic particles.
- According to these rheology features, the ink formulation containing at least 25 wt% of cellulose and less than 6.6 wt% of solvent (imported by the resin and the catalyst) have the highest potential for 3D printing by material extrusion.

iii. Finally, the physical, thermal, and mechanical characterization of the cured composite showed that:

- Cellulose particles thwart the PFA foaming when curing under fast kinetics thanks to steam diffusion through the fibrous network, but, on the other hand, they promote pores creation during mixing and hand-casting because of the sticky nature of the slurries.
- The dimensional shrinkage of the cured composite containing 30 wt% of cellulose (PFA-Cell28-B) decreased by 40% with respect to that of neat PFA.
- The neat PFA and the ensuing composites exhibited good thermal stability until 400°C with a mass loss of less than 10%.
- The thermomechanical performance of PFA enhanced with cellulose addition in order to reach a storage modulus of about 5 GPa at room temperature and more than 2 GPa at 200°C which remained stable for at least 6 hours.
- In agreement with the DMA tests, the flexural and tensile modulus of the composites increased with increasing cellulose content to reach respectively 4.3 and 2.9 GPa for the composite containing 30 wt% cellulose, referred to as PFA-Cell28-B. However, the strength of the composite decreased when adding cellulose which was in line with samples porosity. Thus, the drop of composite strength is believed to be caused by the internal pores which act as stress concentrators.

4.3 Development and characterization of 3D printable material with electrical conductivity

4.3.1 Introduction

To upgrade the printable material, the idea of adding electrically conductive filler was explored. In the literature, various printable conductive inks were developed for 3D printing by adding conductive particles such as graphene, carbon fibers, silver wires, and carbon nanotubes to different kinds of polymers. To successfully formulate this conductive printable ink the formulation should fulfill the printability requirements discussed before but also conduct as many electrons as possible after solidification. In this section, we start with preliminary tests to select the most convenient conductive filler, then a study of the effect of fillers morphology on both the dispersion ability in ethanol and on the rheology is studied, and finally, different formulations were prepared to optimize the rheological behavior and the electrical conductivity.

4.3.2 Fillers effect on rheology and electrical conductivity - preliminary tests

As a first step, different formulations were prepared with three different conductive fillers described in chapter 2; graphene pellets (Gr), graphite powder (G), and double-walled CNT dispersed in water (DWCNT-L). The first attempt was to directly add Gr to the PFA and study the effect on the rheological properties. As we can see in Figure 4-25-A, the suspension with 14 wt% Gr (green curve) has a perfectly Newtonian flow behavior, and the suspension containing 24 wt% Gr (orange curve) start to have a slightly shear-thinning behavior (n=0.85) which can be a proof of the onset of particles percolation.

The limited viscosity and shear-thinning ability of these formulations are probably due to poor dispersion of the Gr particles which was done mechanically and were difficult to disperse in the viscous PFA resin. To overcome the poor rheological performances, formulations with 19 wt% of cellulose powder with the addition of different weight fractions of Gr and G were prepared with a simple mechanical stirring. The flow behavior of these formulations was shear-thinning (n=0.4) with higher apparent viscosity, dominated mainly by the effect of cellulose powder as can be seen in Figure 4-25-A/B. Indeed, the formulation containing cellulose without any added Gr/G (Ref-cell19) has the same flow behavior (dashed red curve) as the other formulations containing the carbon-based particles. The second type of conductive particle widely used in enhancing electrical conductivity are carbon nanotubes (CNT). A suspension of DWCNT-L in water (3 wt%) was tested with

cellulose powder and PFA resin. As we can see in Figure 4-25-C, both of the formulations DWCNT-1 and DWCNT-3 have a highly shear-thinning behavior, appreciated for a 3D-printable ink. The formulation DWCNT-1 contains less CNT and cellulose compared with DWCNT-3, which can explain the smaller shear-thinning behavior compared with that of DWCNT-3. However, the apparent viscosity of the latter is lower, which might be mainly due to the important water content which comes with the addition of CNT (27 wt% vs. 17 wt% water in the formulations).

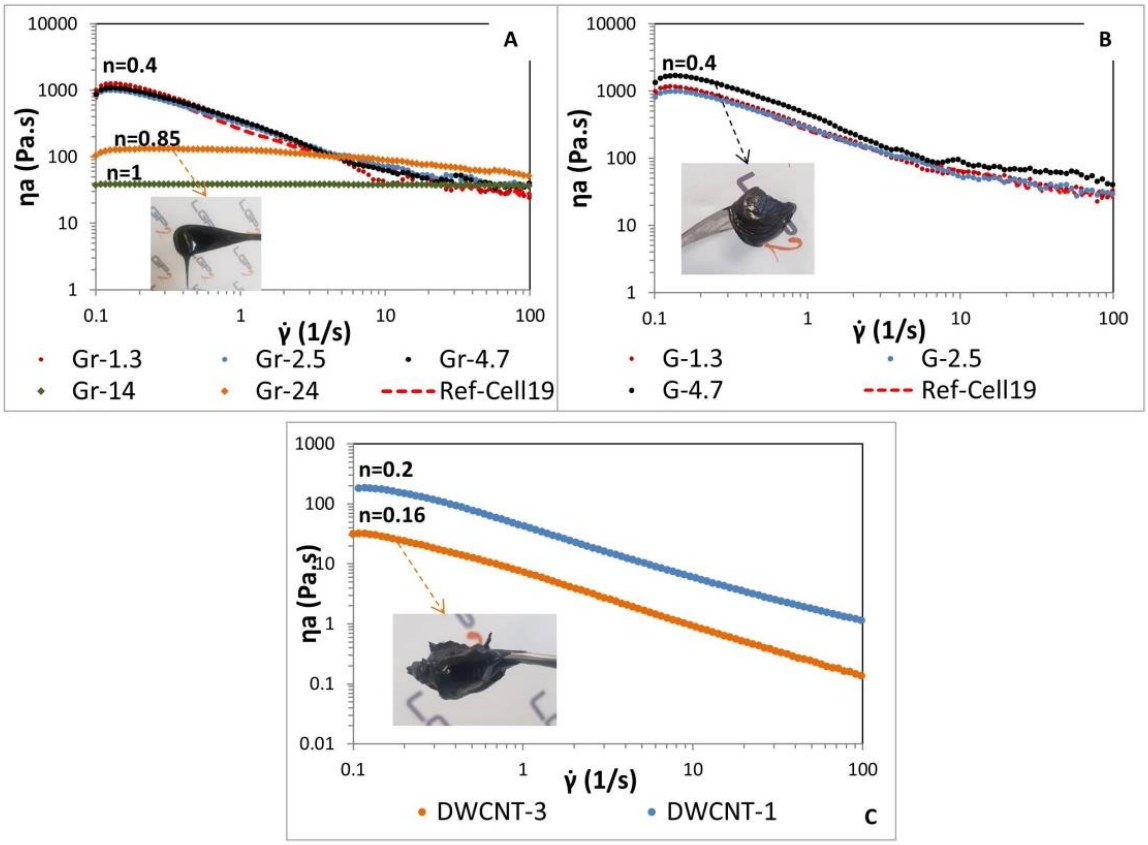

Figure 4-25: Flow curve of PFA-based formulations containing (A) 14 to 24 wt% graphene pellets and 1 to 5 wt% graphene pellets with 19 wt% cellulose powder, (B) 1 to 5 wt% graphite powder with 19 wt% cellulose powder, and (C) from 0.55 to 0.85 wt% DWCNT with 11 to 15 wt% cellulose powder and 17 to 27 wt% water.

Another important parameter to assess is the electrical conductivity of these formulations after curing. The conductivity of the formulations containing graphite and graphene particles along with 19% cellulose was not detected so these materials are considered to be non-conductive.

In Figure 4-26-A, one can see that the electrical conductivity of a casted cylinder of Gr-24 is around 3.4 10^{-2} S/m which exceeds that of the formulation containing 1.23 wt% of DWCNT-L (after water evaporation). However, the electrical conductivity of the formulation containing DWCNT-L increases with the decrease of nozzle diameter. This opposite proportionality is due to the increase of the

shear stress applied during the extrusion when decreasing the nozzle size which favors the alignment of the CNT. The shear-induced alignment of CNT in the nozzle during extrusion is a well-known phenomenon that increases the contact probability among CNT in the extrusion direction, increasing accordingly the electrical conductivity in the same direction (Lanticse et al., 2006; Tang et al., 2012; Zheng et al., 2016). In the case of graphene pellets, the electrical conductivity decreased (Figure 26-A), which can be due to a breakage of the contact between the particles during shearing or the formation of disconnected clogs of the particles due to the high friction between the pellets.

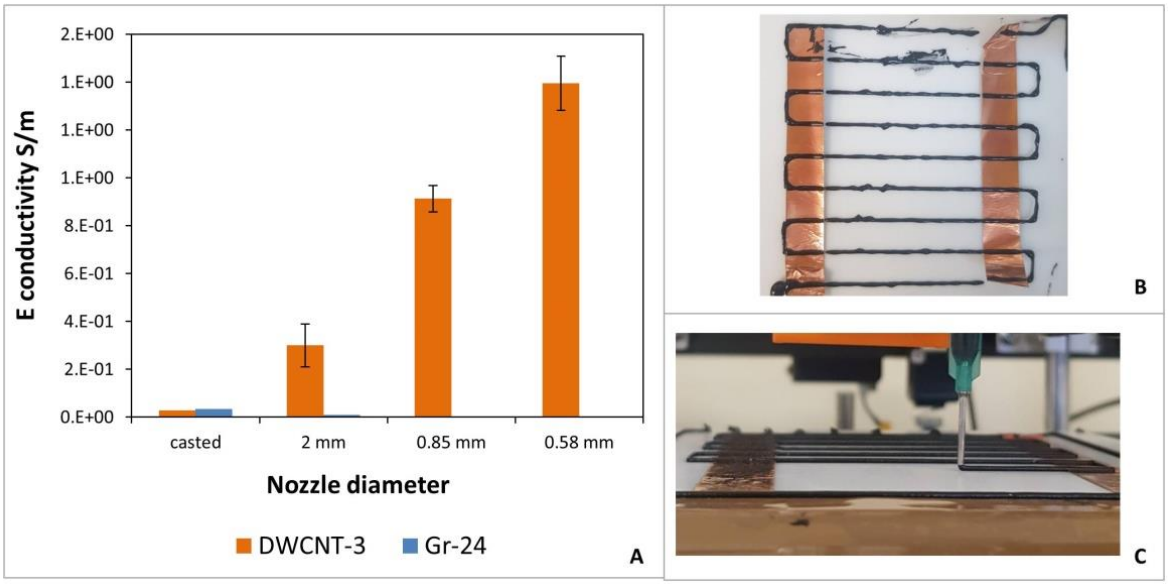

Figure 4-26: (A) Electrical conductivity of extruded filament through different nozzle sizes, (B) printed tracks of Gr-24, and (C) printable tracks of DWCNT-3.

In the photographs presented in Figure 4-26-B/C, one can notice the poor printability of the formulation with the graphene pellets as the printed lines tend to spread on the plastic substrate. On the other hand, the lines printed with ink formulation DWCNT-3, containing 0.9 wt% CNT, 27 wt% water, 14 wt% cellulose, and 58 wt% PFA, tend to retain the shape of the extruded filament with no visible spreading on the substrate.

In light of these first tests, the use of CNT seems to be more convenient because: (i) it confers a shear-thinning flow behavior and a certain shape maintaining compatible with the requirements of 3D printing by extrusion, (ii) it can be aligned with shear applied in the nozzle outlet improving the electrical conductivity, and (iii) it has a low percolation threshold in PFA/cellulose composites.

4.3.3 Development and optimization of a printable electrically conductive ink

4.3.3.1 Suspension of CNT in ethanol

Based on the results of the preliminary formulation tests, carbon nanotubes seem to be the most suitable filler for a functional printable ink formulation. Nonetheless, one of the challenges encountered is the high water content added to the formulation when increasing the CNT fraction in the formulation, which not only affects the rheological behavior of the formulation, but also can lead to phase separation since the PFA resin is only soluble in 24 wt% of water. In addition, defaults can be caused by the high water content during curing. As explained in chapter 1, the exothermal reaction of PFA oligomers can cause high porosity and foam upon curing. To overcome these challenges, it was decided to use CNT powder and disperse it in ethanol (a solvent of PFA resin which can be easily evaporated) using the protocol described in chapter 2. The already tested double-walled nanotubes with a high aspect ratio are known for their good electrical conductivity, but their dispersibility can be tricky (Li et al., 2007). Therefore, a choice of CNT type should be made according to their dispersibility. Thereafter, 6 stock dispersions of 6 different CNT types (whose properties are given in chapter 2 p.111) with different aspect ratios were prepared and their contents are detailed in Table 4-3. As already mentioned in chapter 2, a dispersing agent provided with the CNT was added according to the fraction recommended by the manufacturer.

Table 4-3: Summary of components mass and weight fractions in the prepared CNT dispersions.

Reference	CNT (g)	Dispersant (g) (*Nanoamor*)	Ethanol (g)	Dispersant fraction	CNT (%)
SWCNT	2.0	10.0	188	05:01	1.0
DWCNT	2.0	4.0	188	02:01	1.0
MWCNT 1	2.0	1.5	188	0.75:01	1.0
MWCNT 2	2.0	1.0	188	0.50:01	1.0
MWCNT Gr	2.0	1.0	188	0.50:01	1.0
MWCNT short	2.0	2.0	188	01:01	1.0

As a first assessment, the stability of these dispersions was visually evaluated. As one can see in Figure 4-27-A, after few hours, the majority of the suspensions are visibly stable with no clear sedimentation with the exception of SWCNT, where one can start noticing signs of sedimentation

despite the important amount of added dispersant. After 24 hours, the sedimentation of SWCNT starts to be more noticeable and the same phenomenon was detected for MWCNT1 and DWCNT (these 3 CNT types have a high aspect ratio of 1500-2500). After 10 days, the same dispersion behavior was observed for the high aspect ratio CNT, whilst the suspensions with low aspect ratio CNT (<333) had a stable dispersion.

To further assess the homogeneity of the CNT suspensions, the 1 wt% CNT solutions were then mixed with the PFA resin, which results in an overall 0.3 wt% concentration of CNT. The suspensions were placed on glass supports to form a film to be observed under a fluorescence microscope. These observations are displayed in Figure 4-27-B. One can notice that the dispersion of SWCNT and DWCNT is not uniform and inhomogeneous with the formation of important aggregates and bundles, which is a classic issue when using high aspect ratio nanotubes (Ma et al., 2010). The suspensions with an aspect ratio ranging from 33 (MWCNT-short) to 333 (MWCNT-2 and MWCNT-Gr) were easily dispersed despite the existence of some visible aggregates which could be broken with a longer sonication. Despite the advantage of the use of a high aspect ratio of CNT to decrease the percolation threshold, these long CNT have seriuous dispersion issues which can impair the electrical conductivity and the printability of the composite paste (Huang and Terentjev, 2008; Valentino et al., 2008; McClory et al., 2010).

Accordingly, the flow behavior of the different suspensions in ethanol under a steady shear rate was studied. For every type of CNT, three suspensions with 1, 0.5, and 0.2 wt% concentrations were prepared and their flow curves are shown in Figure 4-28-A, B, and C, respectively. By analyzing the flow curves, one can first notice a shear-thinning behavior explained by an alignment of the CNT in the shear direction which breaks the network interaction resulting in lower viscosity values. This shear-thinning behavior is proportional to the CNT concentration. Similarly, the viscosity measured at a shear rate of 0.1 1/s, summarized in the graph of Figure 4-28-D, increases when increasing CNT concentration with a sharp increase when the concentration exceeds 0.5 wt%, thus suggesting a stronger entanglement. An exception should be made for the MWCNT-1 suspension which exhibits constant viscosity values. This can be explained by the poor dispersion (Figure 4-27) and weak network interactions compared wth the other suspensions. Furthermore, as one can notice in Figure 4-28-C, for low CNT concentration (0.2 wt%) the flow is unstable with noticeable disruptions, especially for the SWCNT, which might be due to the important aggregates and the non-uniform dispersion shown in Figure 4-27. On the other hand, the suspensions that showed fewer aggregates and more uniform dispersion exhibit a more stable flow curve over the whole range of shearing rates. The flow of the suspension gets more stable when increasing the CNT concentration, probably due to a stronger network interaction which diminishes the aggregates effect. The short CNT

(MWCNT-short) and Long DWCNT exhibit the highest viscosity values for the concentration higher than 0.5 wt% triggered in the first case by a good dispersion and in the second by the high aspect ratio.

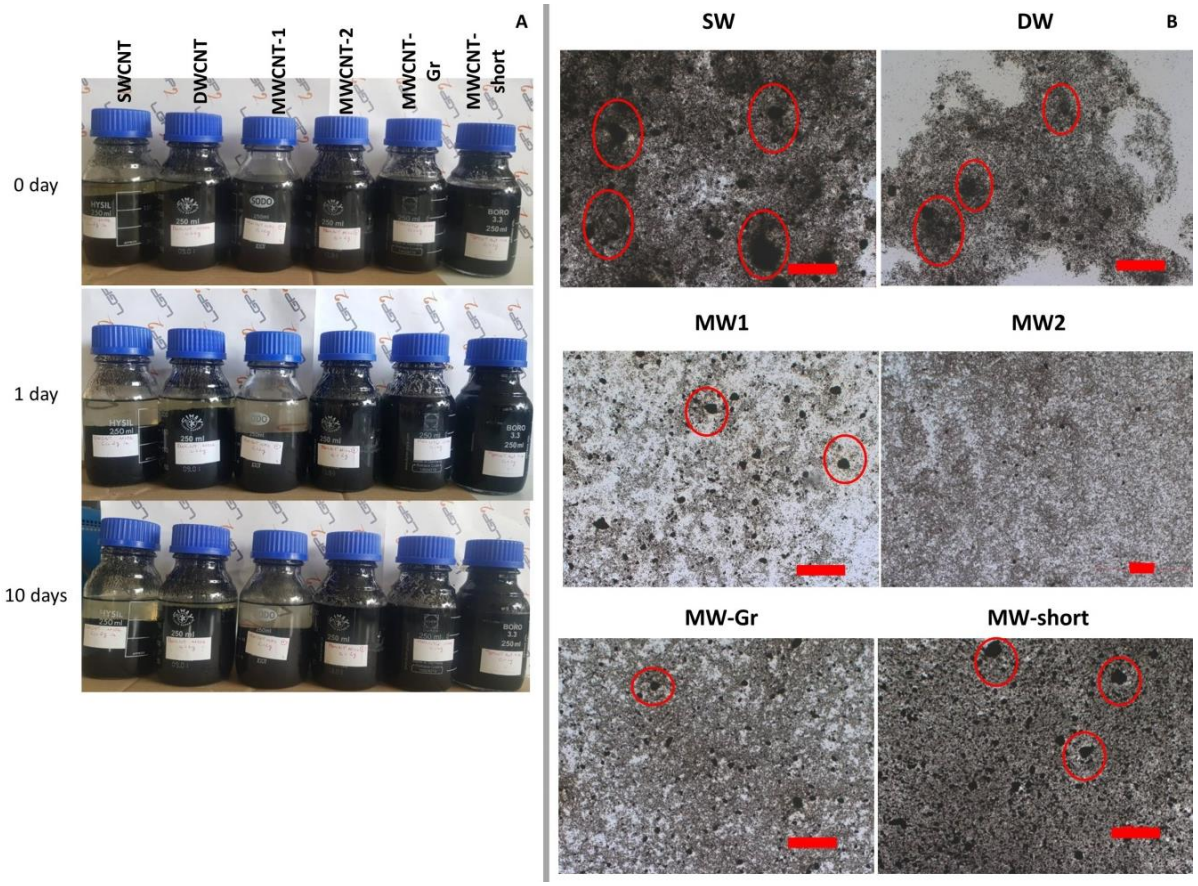

Figure 4-27: (A) photograph of CNT dispersions after sonication and mechanical shearing; (B) Optic microscopy images of 0.3 wt% CNT films in diluted PFA resin under the same magnification. Scale bar: 100 µm.

Given the latter results, the short nanotubes (MWNCT-short) tend to have the best morphology in order to provide good and stable dispersions, resulting in a stable flow, higher viscosity, and a shear-thinning behavior needed for the future 3D printable ink. For the development of the printable formulation, different suspensions were prepared using MWCNT-short and DWCNT with a concentration between 0.5 wt% (concentration from which a clear entanglement is noticed) and 4 wt%.

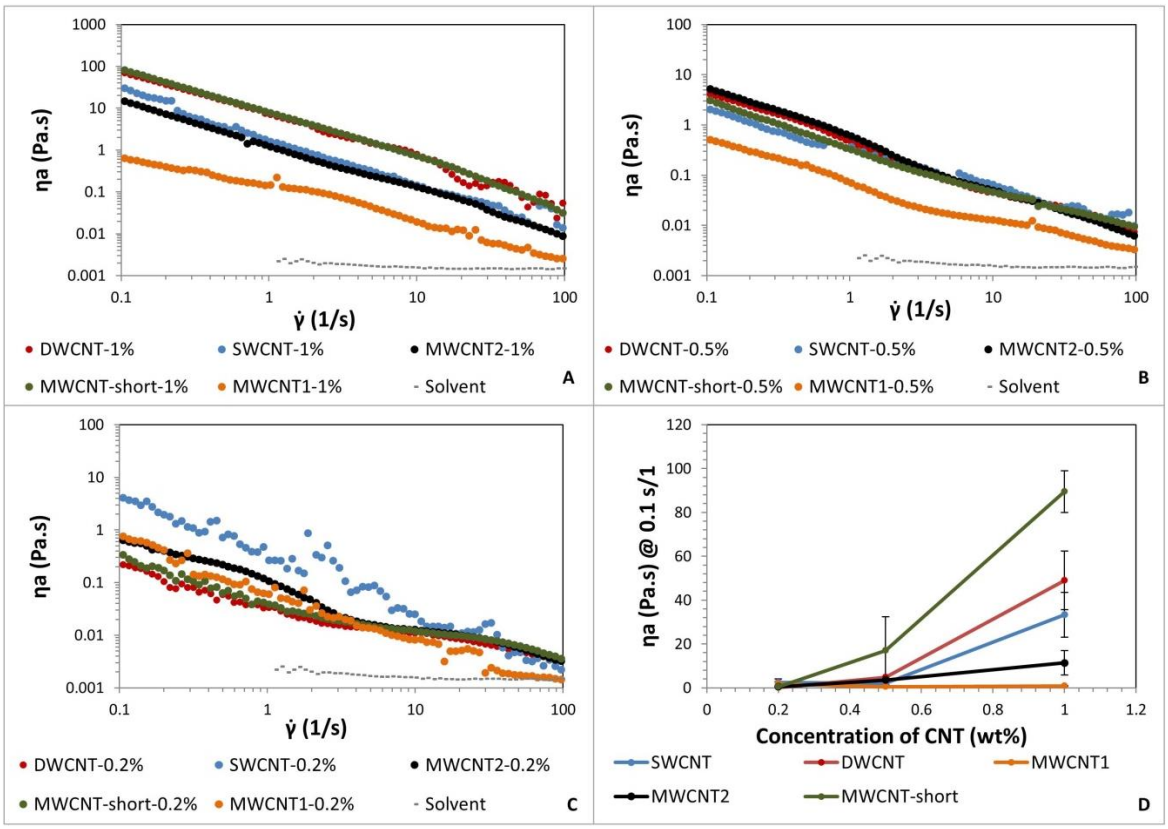

Figure 4-28: Viscosity and flow curves for CNT dispersions in ethanol at different concentrations.

4.3.3.2 Conducive ink formulation

To obtain a conductive and 3D printable ink, different suspensions of DWCNT and MWCNT-short in PFA with or without cellulose powder were prepared using the protocol detailed in chapter 2. These suspensions are referred to as DCNT-x-y for the DWCNT and MCNT-x-y for MWCNT-short with x being the CNT weight fraction and y the cellulose weight fraction in the formulation.

Once again, a rough rheological characterization is necessary to assess the printability and thus to determine the most adapted ink for 3D printing by material extrusion. To this end, the variation of the apparent viscosity with shear rate of the 0.5 wt% and 4 wt% CNT dispersions was measured and shown in Figure 4-29-C. A concentration of 0.5 wt% CNT in PFA results in a Newtonian flow behavior characterized by a constant viscosity. The viscosity of the suspension containing short MWCNT is higher than that with high aspect ratio CNT, which correlates well with the results presented in the former section where the viscosities of the different stock suspensions were compared (Figure 4-28-D). However, the shear-thinning behavior observed in the case of ethanol suspension is not detectable here, which is most likely due to a poorer dispersion in the viscous PFA resin. When increasing the CNT content to 4 wt%, a shear-tinning behavior of the suspension starts to appear with a clear increase in the apparent viscosity, especially for the formulation MCNT-4.

For a better assessment of the printability, an amplitude sweep test was carried out on the formulation MCNT-4 presented in Figure 4-29-D, which shows a dominance of the loss modulus over all the range of the shear amplitude declining the printability of this fluid. Therefore, more formulations were prepared with the addition of cellulose powder to tailor the rheology and enhance printability. The flow behavior of suspension containing 0, 15, and 20 wt% of cellulose at a constant CNT content (4 wt%) for both short and long nanotubes was analyzed and shown in Figure 4-29-A/B. We can notice that in the case of low aspect ratio CNT, the addition of 15 wt% cellulose powder was enough to confer the suspension (MCNT-4-15) flow a pronounced highly shear-thinning behavior. On the other hand, when using high aspect ratio nanotubes, 15 wt% cellulose (DCNT-4-15) only increased the apparent viscosity of the suspension without any noticeable shear-thinning in its flow. The addition of an extra 5 wt% cellulose (DCNT-4-20) was needed to form a more solid cellulose/CNT network to detect a shear-thinning flow triggered by the breakage of the network under shear stress. An amplitude sweep test of DCNT-4-15 and MCNT-4-15 was performed and the corresponding results are shown in Figure 4-29-D. The storage modulus of the two formulations containing 15 wt% of cellulose is slightly higher than the loss modulus before a cross-over point corresponding to yield stresses of 770 ±170 Pa for MCNT-4-15 and 524 ±125 Pa for DCNT-4-15. However, the stiffness of both formulations cannot be easily concluded based on these oscillatory rheology results, as the G' starts to decrease in the tested strain range (from 1 to 100%). Nevertheless, the storage modulus of the formulation containing short nanotubes is higher, which can be explained by their better dispersion.

According to this rheological assessment, the addition of at least 15 wt% of cellulose is needed for yielding a shear-thinning flow needed for a stable extrusion through nozzle without any clogs formation. Morover, the additional cellulose can increase the viscosity and the stiffness of the material in order to resist the printing force and also to obtain a viscoelastic material with high yield stress sufficient to bear the gravitational forces. The use of short nanotubes is also preferred because of their better dispersion.

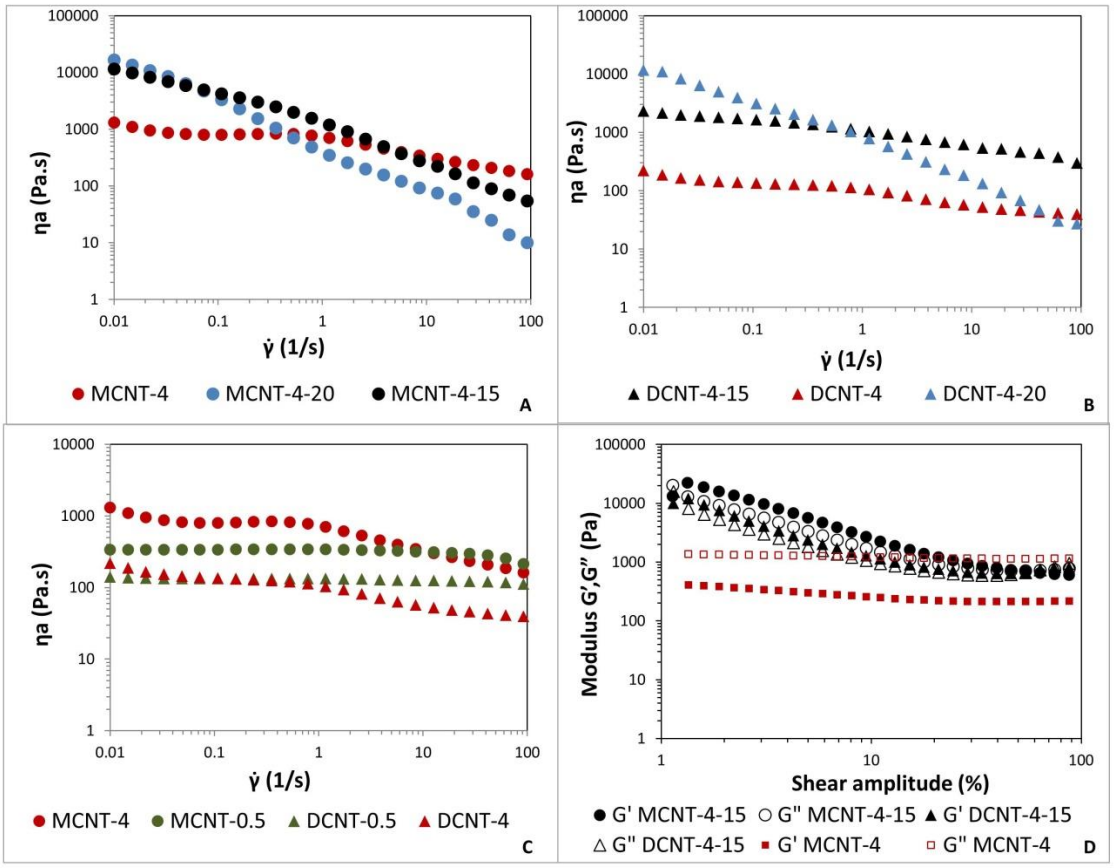

Figure 4-29: A), (B), and (C): Flow curves of conductive ink formulationsand (D): amplitude sweep tests.

To determine the effect of the addition of CNT to the PFA matrix, the volume electrical conductivity (EC) of CNT/PFA nanocomposites was evaluated from resistance measurements performed on nanocomposite filaments extruded from a 2mm diameter nozzle with increasing CNT content (0.5–4 wt%). Each resistivity measurement was done on 3 different filaments.

As shown in Figure 4-30, the resistivity of the nanocomposite with 0.5 wt% CNT was out of the range to be measured with the multimeter and hence the EC was considered to be zero. The EC starts to increase substantially upon the addition of 1.5 wt% CNTs to reach 1.6 10^{-4} S/m for DWCNT and 6.1 10^{-4} S/m for MWCNT-short. Furthermore, an abrupt increase in EC is observed when increasing the MWCNT concentrations to 4 wt%, reaching values of 5 10^{-3} S/m and 4 10^{-2} S/m for, respectively, DWCNT and MWCNT-short. The difference in EC values about an order of magnitude between the two types of CNT is once again mainly due to the dispersion quality which rules the percolation of the conductive particles and hence favors the EC for the better-dispersed nanotubes which are in the present case the short CNT (MCNT-4). Indeed, by examining the cross-section SEM images in Figure 4-31, one can clearly notice the presence of large aggregated DWCNT (highlighted with red circles) suggesting a poor dispersion of the CNT. On the other hand, the short CNT diaplays a good dispersion

in the PFA, with no visible aggregates. The overall EC is higher than that reported by Lanticse et al. which was about 10^{-5} S/m for 5 wt% of MWCNT in the PFA matrix (Lanticse et al., 2006). It is also worth mentioning that the measured electrical conductivity is underestimated, since it does not consider the contact resistance between the probe placed on the filament surface and the material.

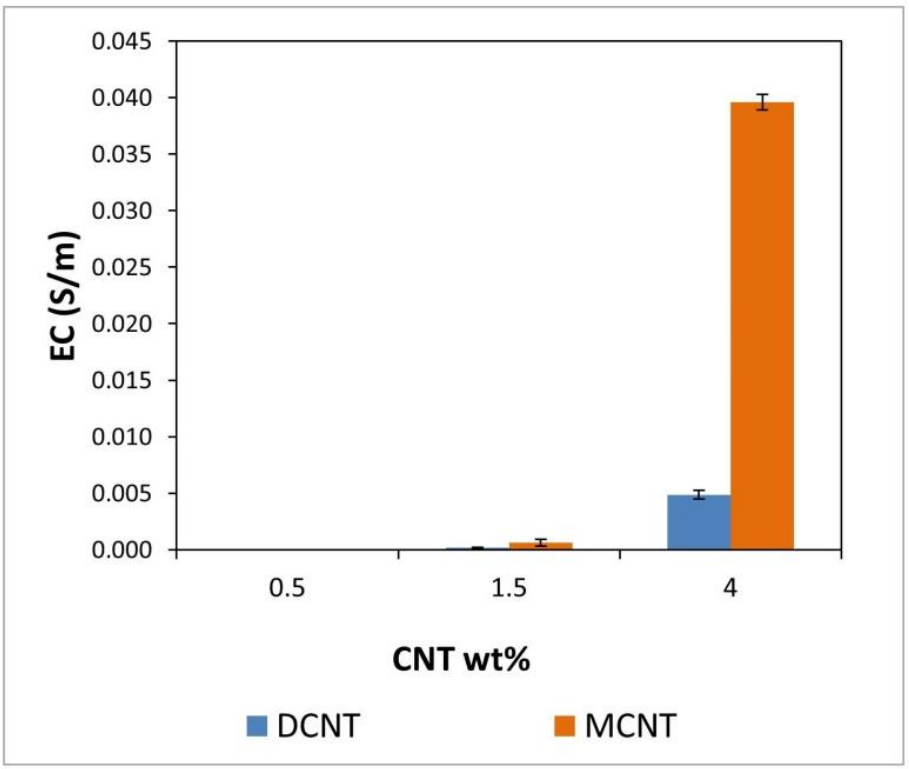

Figure 4-30: Electrical conductivity (EC) of extruded filaments of nanocomposite as a function CNT concentrations and type.

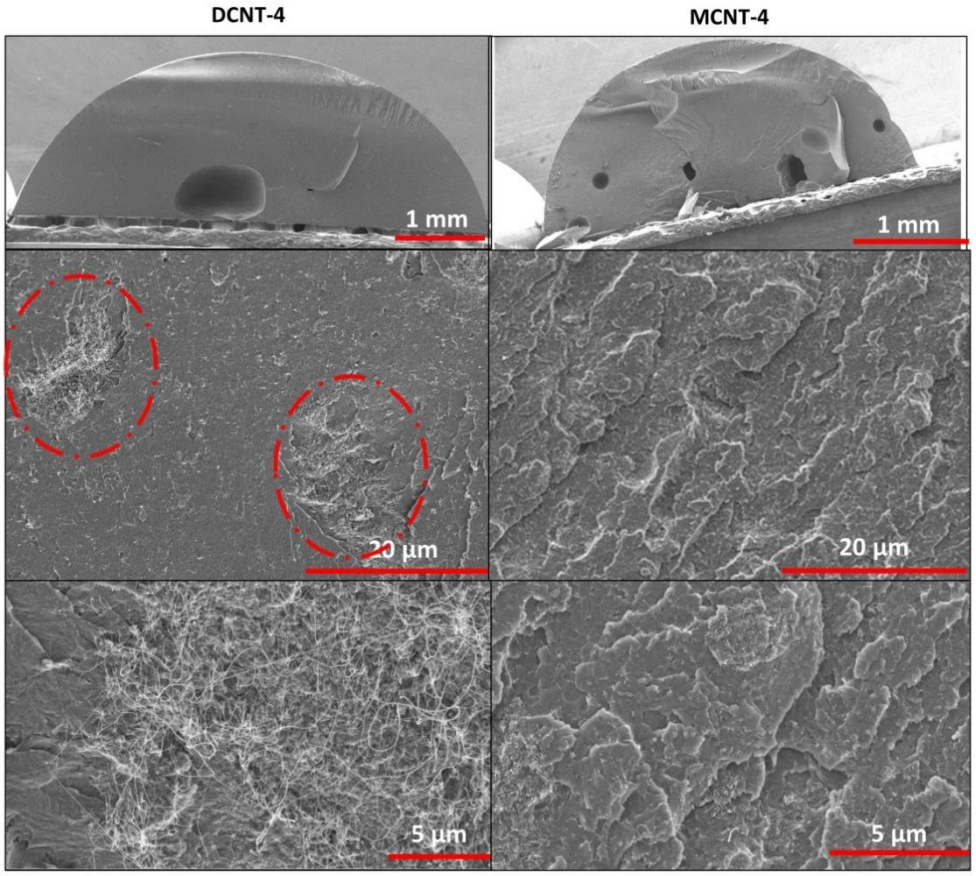

Figure 4-31: SEM images at different magnitudes of the cross-section of a cured filament of nanocomposite containing 4 wt% of MWCNT-short (right) and DWCNT (left).

The electrical conductivity of the composites containing an equal content of CNT (4 wt%) and 15wt% and 20 wt% of cellulose powder was measured and is shown in Figure 4-32. After the incorporation of 15 wt% of cellulose, the electrical conductivity increases by one order of magnitude for both CNT types. The EC increases further when adding 5 wt% more cellulose powder to reach 4.5 10^{-1} S/m. This phenomenon is explained by a decrease in the percolation threshold of the CNT after the incorporation of inert filler. The filler occupies a certain volume in the composite which makes the space occupied by the PFA/CNT dispersion less important. This increases the contact probability among the nanotubes which therefore decreases the percolation threshold with the same overall CNT concentration in the composite and thus increases the electrical conductivity. The CNT arrangement in the composite with and without cellulose powder is illustrated in Figure 4-33 for a better understanding. This phenomenon is also explained by Bao et al., where they introduced the concept of the effective concentration of CNT as the ratio between the CNT volume and the sum of the CNT and the polymer volumes (Bao et al., 2008). The effective concentration in our case is calculated on the weight base according to eq 22 and found to be respectively 0.048 and 0.050, when

adding 15 and 20 wt% cellulose against 0.04 without any inert particles, which explains the increase in EC.

$$CNT_{eff} = \frac{W_{CNT}}{W_{(CNT+PFA)}} \qquad eq\ 22$$

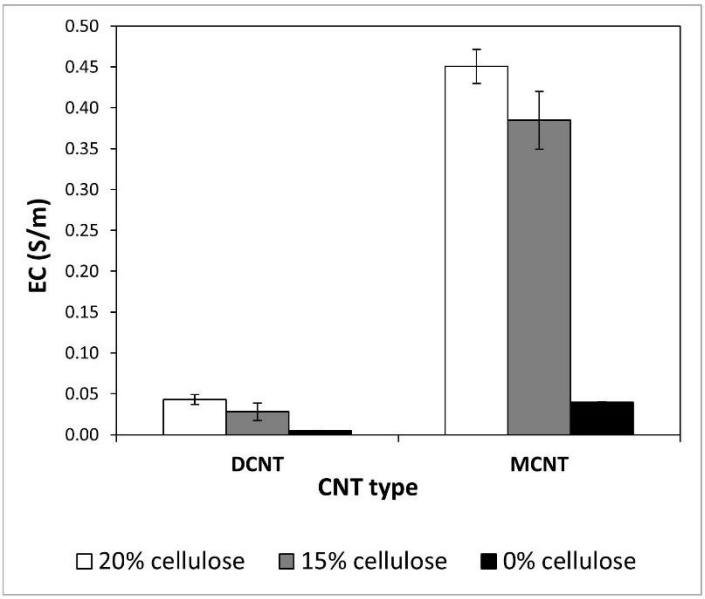

Figure 4-32: Electrical conductivity of composite containing 4 wt% of CNT with different cellulose content.

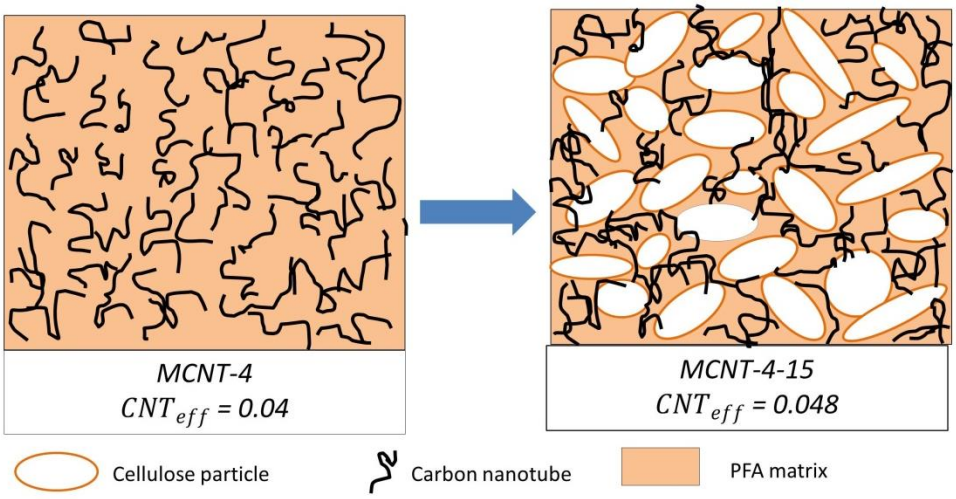

Figure 4-33: Illustration of the influence of cellulose powder on the arrangement of CNT in the composite: (left) PFA/CNT composite without inert particles, (right) PFA/CNT/cellulose powder composite.

SEM cross-section images of a fractured MCNT-4-15 filament are shown in Figure 4-34. First, one can notice a perfect circular shape of the filament in Figure 4-34-A, suggesting a higher stiffness and better resistance to the gravitational forces compared with the cellulose-free nanocomposites shown

in Figure 4-31, where the structure collapsed. These observations are in agreement with the rheological tests. In Figure 4-34-B, a good dispersion of cellulose particles in the nanocomposite can be observed and in Figure 4-34-C one can see how the CNT particles (visible in white on the SEM image) are dispersed in the polymer and arranged in the space between the cellulose particles highlighted with red lines. These observations corroborate the latter conclusions about the effect of the addition of cellulose particles on the percolation of CNT.

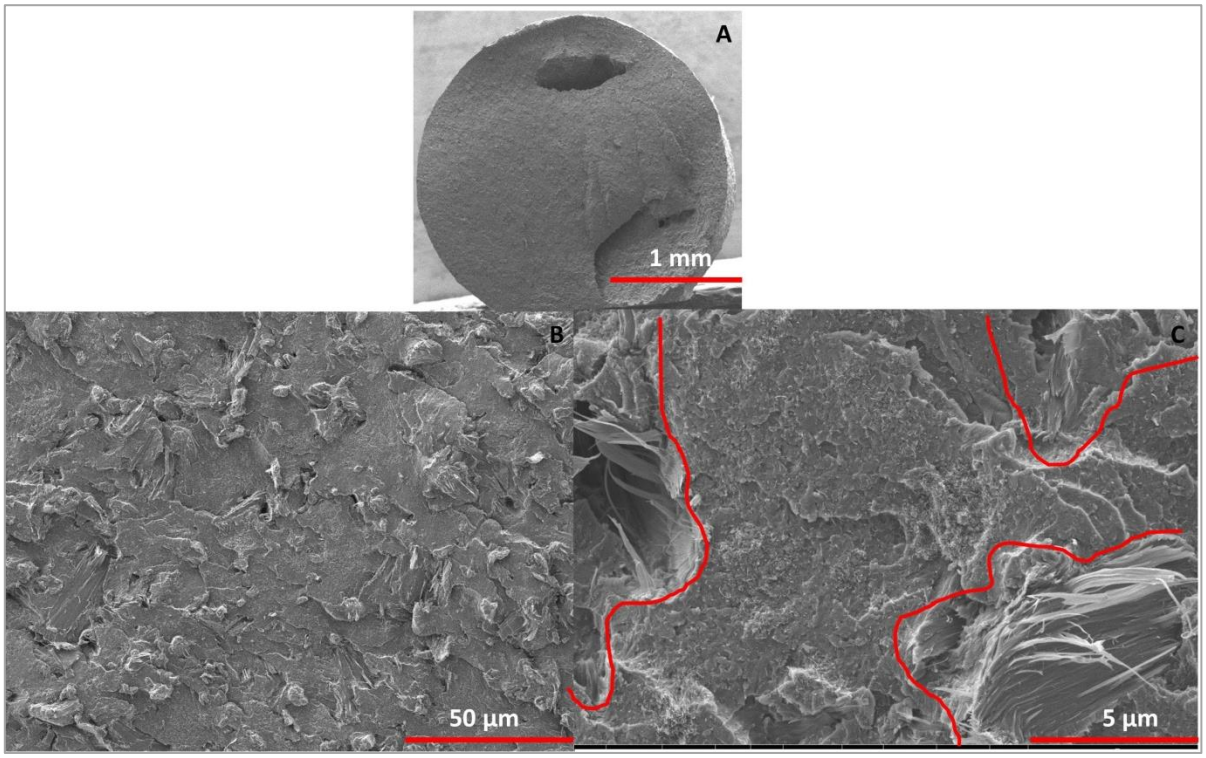

Figure 4-34: SEM images of the cross-section of a cured extruded filament of a nanocomposite containing 4 wt% of MWCNT-short and 15 wt% of cellulose powder at three different magnifications.

Therefore, we can conclude that:

- The CNT addition increases the viscosity of the PFA resin without changing its Newtonian and viscous flow behavior.
- An addition of at least 1.5 wt% of CNT in the PFA matrix is needed to effectively increase the electrical conductivity.
- The dispersion of low aspectratio CNT in PFA is better than that with high aspect ratio, which resulted in higher viscosity, better shear-thinning behavior, and higher electrical conductivity.
- The addition of cellulose enhances the printability of the nanofluid by enhancing the shear-thinning behavior and transforming the viscous flow to a viscoelastic behavior with a yield stress of 770 ±170 Pa.

- The added cellulose increases the electrical conductivity by one order of magnitude at a constant CNT concentration with respect to the cellulose-free nanocomposite. The cellulose addition enables a reduction in the CNT content, thus limiting the material cost and environmental impact.

In the light of these findings, the formulation MCNT-15-4 was selected to be the most relevant to our application as, on the one hand, its rheological properties fulfill 3D printing by extrusion's requirements and, on the other, it exhibits good electrical conductivity values. The addition of 20 wt% cellulose was found to deteriorate the mechanical properties of the extruded filament which was found to be too fragile.

4.3.4 Towards a better electrical conductivity- pyrolysis

Organic polymers with high carbon content and limited oxygen content can usually be carbonized and in the case of some polymers even graphitized. Furan resin fulfills these carbonization requirements and, as shown previously, the used PFA resin can yield up to 50 wt% char residue. Thus, this polymer is largely used as a precursor for a non-graphitizing carbon called glassy carbon (same for cellulose) resulting in a lower electrical conductivity compared to graphite, but in an improved hardness (Manoharan et al., 2010; Rajagopalan et al., 2004; Sharma, 2018). A study of the Raman spectra of PFA pyrolyzed at different temperatures revealed certain critical temperatures. At 400°C carbonization starts, at 550°C graphite nucleation appears, at 700°C crystallite growth is observed, and above that temperature crystallite size increases (Li et al., 2008). These critical temperatures can be also recognized in the TGA and heat flow curves of Figure 4-21. It was also proven that the increase of heat treatment (above 850°C) raised the efficiency of creation of charge carriers by a better degradation of PFA molecules which resulted in an improvement in electrical conductivity (Wang et al., 1997). Based on these findings, and the TGA curves obtained in this work, the PFA-based composites (with and without CNT) were pyrolyzed under inert gas under a low heat rate and until reaching the high temperature of 950°C in order to increase the electrical conductivity of the furanic material.

Filaments of composite MCNT-4-15 and the CNT-free composite (PFA-Cell25-B) were pyrolyzed and their electrical conductivity was measured and displayed in Figure 4-35. As expected, the electrical conductivity increased by 5 orders of magnitude from 4 10^{-2} to 4.7 10^{3} S/m for the composite containing CNT and 2 10^{3} S/m for the composite without CNT. These EC values surpass the value reported by Hawes et al. of laser-induced carbonization of PFA polymer doped with graphene oxide, which was in the range of 9 10^{2} S/m (Hawes et al., 2019). The increase in EC conductivity when

adding CNT can be explained by the higher conductivity of the percolated CNT (> 10^4 S/m) compared with that of the vitreous carbon formed after PFA and cellulose pyrolysis.

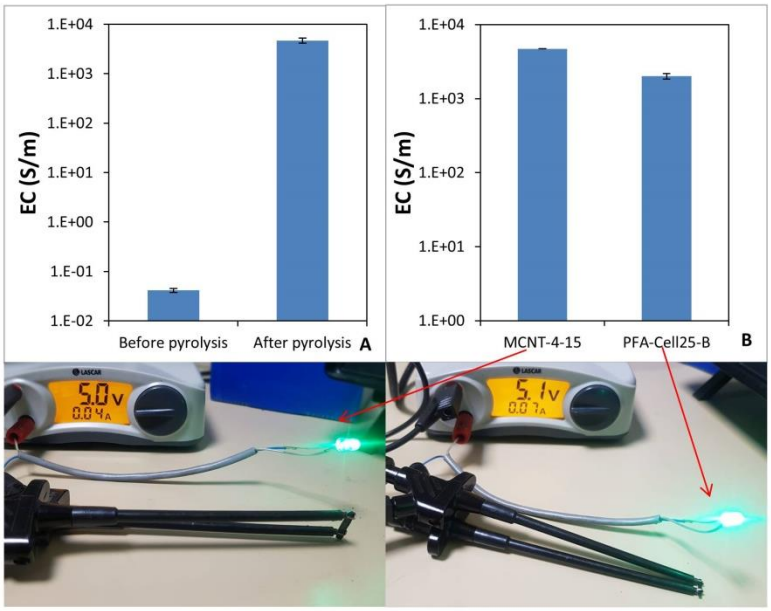

Figure 4-35: (A) Electrical conductivity of the composite MCNT-4-15 before and after pyrolysis and (B) after pyrolysis of composite with and without added CNT.

From a morphological point of view, one can see on the SEM cross-section images of fractured filaments in Figure 4-36 that the PFA-Cell25 composite conserved its main circular form and that the rough cross-section transformed into a smooth glass-like material after pyrolysis. Many macroscopic pores can also be observed before and after pyrolysis, which is most likely caused by volatile evaporation difficulties during the curing step, as we can see on the filament image before pyrolysis which was discussed more in detail in the previous section of this chapter. In addition to the macropores, the formation of open pores was suspected to facilitate the transport of volatiles and tar products formed during the pyrolysis of PFA (Fitzer et al., 1969; Fitzer and Schäfer, 1970). This hypothesis was confirmed later to show the formation of meso and micropores when heating below 400°C and a complete collapse of the mesoporous structure and the exclusive residue of microspore with a size of 4–5 Å (Burket et al., 2006). In the case of the present work, the remaining micropores after the heat treatment at 950°C were out of the limit of the SEM resolution.

For large samples, pure glassy carbon is only obtained using temperatures as high as 2000°C or more to ensure effective annealing of volatiles from the core of the sample (Hancox et al., 1991). However, it was demonstrated that for samples with dimensions <3 mm, which is the case of the used filament in this work, a temperature as low as 900°C was sufficient to yield a glassy carbon with some oxygen

impurities (Maleki et al., 1997). The lower electric conductivity obtained in the present study (2 10^3 S/m), with respect to the electrical conductivity of pure glassy carbon, might be due to the not compensated contact resistance when the EC conductivity was measured.

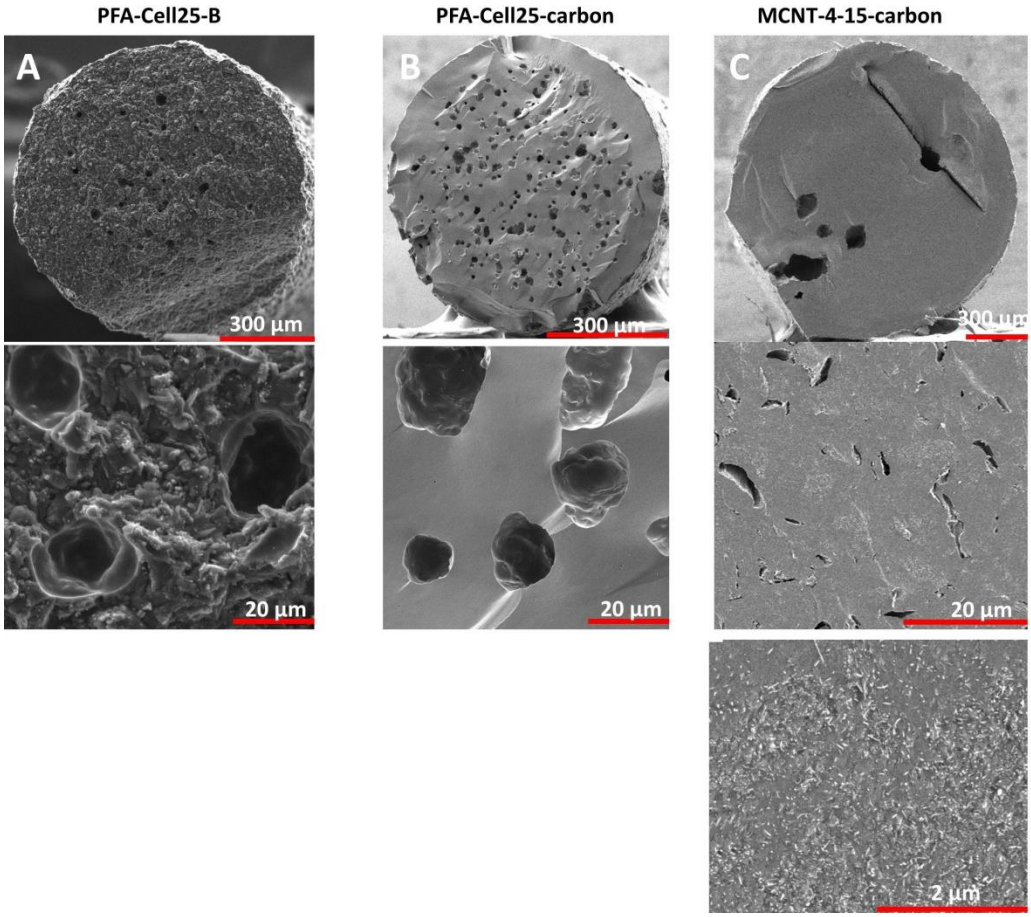

Figure 4-36: SEM images of the cross-section of (A) a cured extruded filament of PFA-Cell25-B composite, (B) a carbonized filament of PFA-Cell25-B composite, and (C) a carbonized filament of nanocomposite (MCNT-4-15) containing 4 wt% of MWCNT-short and 15 wt% of cellulose powder at three different magnifications.

4.3.5 Conclusions

In this section, a printable formulation for the manufacturing of a semi-conductive composite was successfully developed. The formulation containing 4 wt% of MWCNT-short and 15 wt% cellulose, referred to as MCNT-4-15, exhibited the best rheological performances and electrical conductivity values reaching at least 3.85 10^{-1} S/m.

Furthermore, the carbonization of the pristine electrically insulating biocomposite containing 30 wt% cellulose (PFA-cell28-B), yields an increase of its electrical conductivity to attain 2 10^3 S/m. This electrical conductivity doubles when carbonizing the biocomposite containing 4 wt% of carbon

nanotube (MCNT-4-15) to reach 4.7 10^3 S/m. These different printable biocomposites with variant electrical conductivity levels, highlighted in Figure 4-37 by a yellow star, can allow the direct fabrication of conductive structures with tailored 3D objects and enable the integration of electronic functionalities into complex 3D structures.

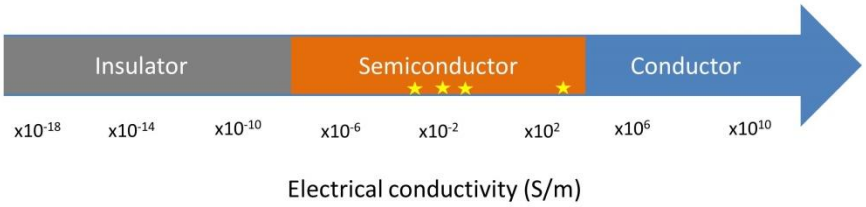

Figure 4-37: Materials classification based on their electrical conductivity levels and the positioning of biocomposite developed in this work.

4.4 Chapter conclusions

In this chapter, two types of printable ink formulation by extrusion were developed and the resulting cured composites were characterized.

For the development of the structural ink, a rheological study of different slurries based on a PFA thermosetting resin and microcrystalline cellulose powder was conducted. Accordingly, the rheological data singled out two ink formulations with potential for 3D printing. These two formulations contain from 25 to 28 wt% cellulose powder, respectively referred to as PFA-cell25-B and PFA-cell28-B. These identified slurries exhibited a shear-thinning behavior, satisfactory yield stress, and a thixotropic behavior, which are crucial parameters for a successful 3D printing by cold extrusion.

The obtained composite materials after the thermal curing of the prepared slurries were characterized for a better understanding of the resulting physical and mechanical properties. The tensile and flexural moduli of the composites increased with increasing cellulose content, to reach 2.9 GPa and 4.3 GPa, respectively. On the other hand, the strengths decreased after the addition of cellulose particles with respect to the pure PFA because of the high porosity caused by air inclusion during the mixing and casting steps of the composites. The tensile and flexural strength of the PFA-cell28-B composite are respectively 40 and 20 MPa.

Shrinkage is another parameter to supervise when 3D printing, especially when using shrinkable amorphous polymers. The neat PFA had a dimensional shrinkage of 2.9 %, which was decreased by almost 40% for PFA-cell28-B (30 wt% cellulose in the cured composite).

Furthermore, cellulose addition enhanced the thermomechanical properties of the composite with a storage modulus of over 5 GPa at room temperature. At high temperature (200°C), the modulus decreased by only 20% and stayed stable for hours. The thermal stability of the composite was also assessed by TGA tests, which showed a limited weight loss (<10%) at temperatures below 300°C.

The development of conductive ink started with a comparison of the dispersion quality and the rheology of suspensions of different types of carbon nanotubes, which revealed a better dispersion and hence a better rheology behavior of the CNT with a low aspect ratio.

The formulation containing 4 wt% of MWNT-short and 15 wt% of cellulose powder showed the best rheological performances for a better printability and an electrical conductivity of at least 2 10^{-2} S/m.

Furthermore, the carbonization of the two different composites (conductive and structural) further increased the electrical conductivity thanks to the formation of a glassy-carbon structure or, in the case of the addition of CNT, a carbon/carbon composite with an electrical conductivity of at least 4.7 10^3 S/m, enough to turn on a LED in a simple electric circuit.

An optimized ink for LDM additive manufacturing is not enough to achieve a defect-free and accurate solidified printed object. The optimization and the comprehension of both the 3D printing process and the curing step of the object, especially when handling an oligomer with a challenging curing process such as the poly(furfuryl alcohol). Optimization of the printing and curing process of the optimized structural ink formulations will be detailed in the following chapter.

4.5 References

Ahmad, E.E.M., Luyt, A.S., Djoković, V., 2013. Thermal and dynamic mechanical properties of bio-based poly(furfuryl alcohol)/sisal whiskers nanocomposites. Polym. Bull. 70, 1265–1276. https://doi.org/10.1007/s00289-012-0847-2

Bao, H.-D., Guo, Z.-X., Yu, J., 2008. Effect of electrically inert particulate filler on electrical resistivity of polymer/multi-walled carbon nanotube composites. Polymer 49, 3826–3831. https://doi.org/10.1016/j.polymer.2008.06.024

Barnes, H.A., Hutton, J.F., Walters, K., 1989. An Introduction to Rheology. Elsevier.

Beach, J., Patterson, S., Zlatanic, A., Messman, J.M., Dvornic, P.R., 2021. New “all-in-one” silicone pastes for additive manufacturing of elastomer parts. MRS Commun. 11, 88–93. https://doi.org/10.1557/s43579-020-00007-7

Benbow, J., Bridgwater, J., 1993. Paste Flow and Extrusion. Clarendon Press.

Burket, C.L., Rajagopalan, R., Marencic, A.P., Dronvajjala, K., Foley, H.C., 2006. Genesis of porosity in polyfurfuryl alcohol derived nanoporous carbon. Carbon 44, 2957–2963. https://doi.org/10.1016/j.carbon.2006.05.029

Cao, Z., Qiu, L., Yang, Y., Chen, Y., Liu, X., 2015. The surface modifications of multi-walled carbon nanotubes for multi-walled carbon nanotube/poly(ether ether ketone) composites. Appl. Surf. Sci. 353, 873–881. https://doi.org/10.1016/j.apsusc.2015.07.025

Chu, S.H., Li, L.G., Kwan, A.K.H., 2021. Development of extrudable high strength fiber reinforced concrete incorporating nano calcium carbonate. Addit. Manuf. 37, 101617. https://doi.org/10.1016/j.addma.2020.101617

Coussot, P., Ancey, C., 1999. Rheophysical classification of concentrated suspensions and granular pastes. Phys. Rev. E 59, 4445–4457. https://doi.org/10.1103/PhysRevE.59.4445

Dealy, J.M., Wissbrun, K.F., 2012. Melt Rheology and Its Role in Plastics Processing: Theory and Applications. Springer Science & Business Media.

Deka, H., Karak, N., 2009. Bio-based hyperbranched polyurethanes for surface coating applications. Prog. Org. Coat. 66, 192–198. https://doi.org/10.1016/j.porgcoat.2009.07.005

Diez-Pascual, A., Naffakh, M., Gómez, M., Marco, C., Ellis, G., González-Domínguez, J., Ansón, A., Martínez, M., Martinez Rubi, Y., Simard, B., Ashrafi, B., 2009. The influence of a compatibilizer on the thermal and dynamic mechanical properties of PEEK/carbon nanotube composites. Nanotechnology 20, 315707. https://doi.org/10.1088/0957-4484/20/31/315707

Domínguez, J., Madsen, B., 2015. Development of new biomass-based furan/glass composites manufactured by the double-vacuum-bag technique. J. Compos. Mater. 49, 2993–3003. https://doi.org/10.1177/0021998314559060

Dong, Y., Yan, Y., Zhang, S., Li, J., 2014. Wood/Polymer Nanocomposites Prepared by Impregnation with Furfuryl Alcohol and Nano-SiO2. BioResources 9, 6028–6040.

Duty, C., Ajinjeru, C., Kishore, V., Compton, B., Hmeidat, N., Chen, X., Liu, P., Hassen, A.A., Lindahl, J., Kunc, V., 2018. What makes a material printable? A viscoelastic model for extrusion-based

3D printing of polymers. J. Manuf. Process. 35, 526–537. https://doi.org/10.1016/j.jmapro.2018.08.008

Fahmy, A.R., Becker, T., Jekle, M., 2020. 3D printing and additive manufacturing of cereal-based materials: Quality analysis of starch-based systems using a camera-based morphological approach. Innov. Food Sci. Emerg. Technol. 63, 102384. https://doi.org/10.1016/j.ifset.2020.102384

Feilden, E., 2017a. Additive manufacturing of ceramics and ceramic composites via robocasting. https://doi.org/10.25560/55940

Feilden, E., 2017b. Additive manufacturing of ceramics and ceramic composites via robocasting. https://doi.org/10.25560/55940

Feilden, E., Blanca, E.G.-T., Giuliani, F., Saiz, E., Vandeperre, L., 2016. Robocasting of structural ceramic parts with hydrogel inks. J. Eur. Ceram. Soc. 36, 2525–2533. https://doi.org/10.1016/j.jeurceramsoc.2016.03.001

Fitzer, E., Schaefer, W., Yamada, S., 1969. The formation of glasslike carbon by pyrolysis of polyfurfuryl alcohol and phenolic resin. Carbon 7, 643–648. https://doi.org/10.1016/0008-6223(69)90518-1

Fitzer, E., Schäfer, W., 1970. The effect of crosslinking on the formation of glasslike carbons from thermosetting resins. Carbon 8, 353–364. https://doi.org/10.1016/0008-6223(70)90075-8

Gandini, A., 1997. Furans in polymer chemistry. Prog. Polym. Sci. 22, 1203–1379. https://doi.org/10.1016/S0079-6700(97)00004-X

Gillispie, G., Prim, P., Copus, J., Fisher, J., Mikos, A.G., Yoo, J.J., Atala, A., Lee, S.J., 2020. Assessment methodologies for extrusion-based bioink printability. Biofabrication 12, 022003. https://doi.org/10.1088/1758-5090/ab6f0d

Guigo, N., Mija, A., Vincent, L., Sbirrazzuoli, N., 2010. Eco-friendly composite resins based on renewable biomass resources: Polyfurfuryl alcohol/lignin thermosets. Eur. Polym. J. 46, 1016–1023. https://doi.org/10.1016/j.eurpolymj.2010.02.010

Guigo, N., Mija, A., Zavaglia, R., Vincent, L., Sbirrazzuoli, N., 2009. New insights on the thermal degradation pathways of neat poly(furfuryl alcohol) and poly(furfuryl alcohol)/SiO2 hybrid materials. Polym. Degrad. Stab. 94, 908–913. https://doi.org/10.1016/j.polymdegradstab.2009.03.008

Hancox, R.N., Lamb, G.D., Lehrle, R.S., 1991. Sample size dependence in pyrolysis: An embarrassment, or a utility? J. Anal. Appl. Pyrolysis, Proceedings of the 9th International Conference on Fundamentals Aspects, Analytical Techniques, Processes and Applications of Pyrolysis 19, 333–347. https://doi.org/10.1016/0165-2370(91)80054-C

Hawes, G.F., Yilman, D., Noremberg, B.S., Pope, M.A., 2019. Supercapacitors Fabricated via Laser-Induced Carbonization of Biomass-Derived Poly(furfuryl alcohol)/Graphene Oxide Composites. ACS Appl. Nano Mater. 2, 6312–6324. https://doi.org/10.1021/acsanm.9b01284

Hemingway, E., Kusumaatmaja, H., Fielding, S., 2017. Edge Fracture in Complex Fluids. Phys. Rev. Lett. 119. https://doi.org/10.1103/PhysRevLett.119.028006

Huang, Y.Y., Terentjev, E.M., 2008. Dispersion and rheology of carbon nanotubes in polymers. Int. J. Mater. Form. 1, 63–74. https://doi.org/10.1007/s12289-008-0376-6

Kraut, G., Yenchesky, L., Prieto, F., Tovar, G.E.M., Southan, A., 2017. Influence of shear thinning and material flow on robotic dispensing of poly(ethylene glycol) diacrylate/poloxamer 407 hydrogels. J. Appl. Polym. Sci. 134, 45083. https://doi.org/10.1002/app.45083

Ku, H., Wang, H., Pattarachaiyakoop, N., Trada, M., 2011. A review on the tensile properties of natural fiber reinforced polymer composites. Compos. Part B Eng. 42, 856–873. https://doi.org/10.1016/j.compositesb.2011.01.010

Kubo, M.T.K., Rojas, M.L., Miano, A.C., Augusto, P.E.D., 2019. Chapter 1 Rheological Properties of Tomato Products 1–25. https://doi.org/10.1039/9781788016247-00001

Kumar, R., Kumar, R., Anandjiwala, R., 2012. Biofilms from soy protein isolate and polyfurfuryl alcohol. Plast. Rubber Compos. 41, 1–7. https://doi.org/10.1179/1743289811Y.0000000002

Lanticse, L.J., Tanabe, Y., Matsui, K., Kaburagi, Y., Suda, K., Hoteida, M., Endo, M., Yasuda, E., 2006. Shear-induced preferential alignment of carbon nanotubes resulted in anisotropic electrical conductivity of polymer composites. Carbon 44, 3078–3086. https://doi.org/10.1016/j.carbon.2006.05.008

Li, H., Liu, S., Lin, L., 2016. Rheological Study on 3D Printability of Alginate Hydrogel and Effect of Graphene Oxide. Int. J. Bioprinting 2. https://doi.org/10.18063/IJB.2016.02.007

Li, J., Ma, P.C., Chow, W.S., To, C.K., Tang, B.Z., Kim, J.-K., 2007. Correlations between Percolation Threshold, Dispersion State, and Aspect Ratio of Carbon Nanotubes. Adv. Funct. Mater. 17, 3207–3215. https://doi.org/10.1002/adfm.200700065

Li, Z., Kandel, H.R., Dervishi, E., Saini, V., Xu, Y., Biris, A.R., Lupu, D., Salamo, G.J., Biris, A.S., 2008. Comparative Study on Different Carbon Nanotube Materials in Terms of Transparent Conductive Coatings. Langmuir 24, 2655–2662. https://doi.org/10.1021/la701880h

Lille, M., Nurmela, A., Nordlund, E., Metsä-Kortelainen, S., Sozer, N., 2018. Applicability of protein and fiber-rich food materials in extrusion-based 3D printing. J. Food Eng., 3D Printed Food – Design and Technology 220, 20–27. https://doi.org/10.1016/j.jfoodeng.2017.04.034

Ma, C.C.M., Yn, M.S., Han, J.L., Chang, C.J., Wu, H.D., 1995. Pultruded fibre-reinforced furfuryl alcohol resin composites: 1. Process feasibility study. Compos. Manuf. 6, 45–52. https://doi.org/10.1016/0956-7143(95)93712-S

Ma, P.-C., Siddiqui, N.A., Marom, G., Kim, J.-K., 2010. Dispersion and functionalization of carbon nanotubes for polymer-based nanocomposites: A review. Compos. Part Appl. Sci. Manuf. 41, 1345–1367. https://doi.org/10.1016/j.compositesa.2010.07.003

Maleki, H., Holland, L.R., Jenkins, G.M., Zimmerman, R.L., 1997. Determining the shortest production time for glassy carbon ware. Carbon 35, 227–234. https://doi.org/10.1016/S0008-6223(96)00144-3

Manoharan, M.P., Lee, H., Rajagopalan, R., Foley, H.C., Haque, M.A., 2010. Elastic Properties of 4–6 nm-thick Glassy Carbon Thin Films. Nanoscale Res. Lett. 5, 14–19. https://doi.org/10.1007/s11671-009-9435-2

M'Barki, A., Bocquet, L., Stevenson, A., 2017. Linking Rheology and Printability for Dense and Strong Ceramics by Direct Ink Writing. Sci. Rep. 7, 6017. https://doi.org/10.1038/s41598-017-06115-0

McClory, C., McNally, T., Baxendale, M., Pötschke, P., Blau, W., Ruether, M., 2010. Electrical and rheological percolation of PMMA/MWCNT nanocomposites as a function of CNT geometry and functionality. Eur. Polym. J. 46, 854–868. https://doi.org/10.1016/j.eurpolymj.2010.02.009

McKenna, B.M., 2003. Texture in Food: Semi-Solid Foods. Elsevier.

Meyer, F., Crawford, N., 2018. Optimizing process conditions and ensuring end product requirements of plastics with rheological analysis 7.

Mokhothu, T.H., John, M.J., 2017. Bio-based coatings for reducing water sorption in natural fibre reinforced composites. Sci. Rep. 7, 13335. https://doi.org/10.1038/s41598-017-13859-2

Montoya, J., Medina, J., Molina, A., Gutiérrez, J., Rodríguez, B., Marín, R., 2021. Impact of viscoelastic and structural properties from starch-mango and starch-arabinoxylans hydrocolloids in 3D food printing. Addit. Manuf. 39, 101891. https://doi.org/10.1016/j.addma.2021.101891

Naghieh, S., Chen, D., 2021. Printability – a Key Issue in Extrusion-based Bioprinting. J. Pharm. Anal. https://doi.org/10.1016/j.jpha.2021.02.001

Niu, Y., Zheng, S., Song, P., Zhang, X., Wang, C., 2021. Mechanical and thermal properties of PEEK composites by incorporating inorganic particles modified phosphates. Compos. Part B Eng. 212, 108715. https://doi.org/10.1016/j.compositesb.2021.108715

Oishi, S.S., Rezende, M.C., Origo, F.D., Damião, A.J., Botelho, E.C., 2013. Viscosity, pH, and moisture effect in the porosity of poly(furfuryl alcohol). J. Appl. Polym. Sci. 128, 1680–1686. https://doi.org/10.1002/app.38332

Panda, B., Paul, S.C., Hui, L.J., Tay, Y.W.D., Tan, M.J., 2017. Additive manufacturing of geopolymer for sustainable built environment. J. Clean. Prod. 167, 281–288. https://doi.org/10.1016/j.jclepro.2017.08.165

Panda, B., Unluer, C., Tan, M.J., 2019. Extrusion and rheology characterization of geopolymer nanocomposites used in 3D printing. Compos. Part B Eng. 176, 107290. https://doi.org/10.1016/j.compositesb.2019.107290

Panda, B., Unluer, C., Tan, M.J., 2018. Investigation of the rheology and strength of geopolymer mixtures for extrusion-based 3D printing. Cem. Concr. Compos. 94, 307–314. https://doi.org/10.1016/j.cemconcomp.2018.10.002

Papageorgiou, D.G., Liu, M., Li, Z., Vallés, C., Young, R.J., Kinloch, I.A., 2019. Hybrid poly(ether ether ketone) composites reinforced with a combination of carbon fibres and graphene nanoplatelets. Compos. Sci. Technol. 175, 60–68. https://doi.org/10.1016/j.compscitech.2019.03.006

Pfister, D.P., Larock, R.C., 2010. Green composites from a conjugated linseed oil-based resin and wheat straw. Compos. Part Appl. Sci. Manuf. 41, 1279–1288. https://doi.org/10.1016/j.compositesa.2010.05.012

Qu, S., Penaranda, J., Wang, S.-S., 2017. Elevated-Temperature Wear and Friction of PTFE/PEEK composite. https://doi.org/10.12783/asc2017/15385

Rajagopalan, R., Ponnaiyan, A., Mankidy, P.J., Brooks, A.W., Yi, B., Foley, H.C., 2004. Molecular sieving platinum nanoparticle catalysts kinetically frozen in nanoporous carbon. Chem. Commun. 2498–2499. https://doi.org/10.1039/B407854C

Rieger, T., Schubert, T., Schurr, J., Butschle, M., Schwenkel, M., Bernthaler, T., Schneider, G., 2021. Slurry development for lithography-based additive manufacturing of cemented carbide components. Powder Technol. 383, 498–508. https://doi.org/10.1016/j.powtec.2021.01.049

Sharma, S., 2018. Glassy Carbon: A Promising Material for Micro- and Nanomanufacturing. Materials 11, 1857. https://doi.org/10.3390/ma11101857

Smay, James E., Cesarano, J., Lewis, J.A., 2002. Colloidal Inks for Directed Assembly of 3-D Periodic Structures. Langmuir 18, 5429–5437. https://doi.org/10.1021/la0257135

Smay, J. E., Gratson, G.M., Shepherd, R.F., Cesarano, J., Lewis, J.A., 2002. Directed Colloidal Assembly of 3D Periodic Structures. Adv. Mater. 14, 1279–1283. https://doi.org/10.1002/1521-4095(20020916)14:18<1279::AID-ADMA1279>3.0.CO;2-A

Steffe, J.F., 1996. Rheological Methods in Food Process Engineering. Freeman Press.

Tang, H., Chen, J.-B., Wang, Y., Xu, J.-Z., Hsiao, B.S., Zhong, G.-J., Li, Z.-M., 2012. Shear Flow and Carbon Nanotubes Synergistically Induced Nonisothermal Crystallization of Poly(lactic acid) and Its Application in Injection Molding. Biomacromolecules 13, 3858–3867. https://doi.org/10.1021/bm3013617

Thibaut, C., Denneulin, A., Rolland du Roscoat, S., Beneventi, D., Orgéas, L., Chaussy, D., 2019. A fibrous cellulose paste formulation to manufacture structural parts using 3D printing by extrusion. Carbohydr. Polym. 212, 119–128. https://doi.org/10.1016/j.carbpol.2019.01.076

Valentino, O., Sarno, M., Rainone, N.G., Nobile, M.R., Ciambelli, P., Neitzert, H.C., Simon, G.P., 2008. Influence of the polymer structure and nanotube concentration on the conductivity and rheological properties of polyethylene/CNT composites. Phys. E Low-Dimens. Syst. Nanostructures 40, 2440–2445. https://doi.org/10.1016/j.physe.2008.02.001

Wang, Z., Lu, Z., Huang, Y., Xue, R., Huang, X., Chen, L., 1997. Characterizations of crystalline structure and electrical properties of pyrolyzed polyfurfuryl alcohol. J. Appl. Phys. 82, 5705–5710. https://doi.org/10.1063/1.366434

Wildemuth, C.R., Williams, M.C., 1984. Viscosity of suspensions modeled with a shear-dependent maximum packing fraction. Rheol. Acta 23, 627–635. https://doi.org/10.1007/BF01438803

Yaras, P., Kalyon, D.M., Yilmazer, U., 1994. Flow instabilities in capillary flow of concentrated suspensions. Rheol. Acta 33, 48–59. https://doi.org/10.1007/BF00453463

Yilmazer, U., Gogos, C.G., Kalyon, D.M., 1989. Mat formation and unstable flows of highly filled suspensions in capillaries and continuous processors. Polym. Compos. 10, 242–248. https://doi.org/10.1002/pc.750100406

Zhang, Yu, Zhang, Yunsheng, She, W., Yang, L., Liu, G., Yang, Y., 2019. Rheological and harden properties of the high-thixotropy 3D printing concrete. Constr. Build. Mater. 201, 278–285. https://doi.org/10.1016/j.conbuildmat.2018.12.061

Zheng, Z., Wang, Z., Wang, L., Liu, J., Wu, Y., Zhang, L., 2016. Dispersion and shear-induced orientation of anisotropic nanoparticle filled polymer nanocomposites: insights from molecular dynamics simulation. Nanotechnology 27, 265704. https://doi.org/10.1088/0957-4484/27/26/265704

5 Process optimization and study

Chapter content

5.1 Chapter introduction

As described in chapter 1, among other additive manufacturing technologies, material extrusion remains the most widespread in terms of the printed volume. Resultantly, if one looks into the scientific production since the flourishing of the additive manufacturing technology, one will notice that most of the studies on the print quality, the effect of printing parameters are related to FFF and the most commonly used thermoplastics such as PLA and ABS. When it comes to direct ink writing, the effects of these parameters are poorly studied and also can differ from one material to another due to their different properties. Accordingly, when developing a new material it is important to first understand and optimize every step in the printing process.

Subsequently, the objective of this chapter is to study the printing and solidification process of the PFA/cellulose paste with the aim to optimize the process and the ensuing performances of the cured composite. The chapter is divided into two distinct but complementary parts. The first part deals with the understanding of the curing kinetics of the used PFA commercial polymer and the water evaporation step. These insights would permit to better program the solidification step during or after the printing process in order to obtain a defect-free-fully-crosslinked composite. The focus of the second part, is the printing step. In order to master the printing step, several key parameters need to be controlled and understood. Thereafter, the extrusion step was optimized by the calibration of the extrusion head to match with the flow calculation. Then, the effect of the main printing parameters was assessed to better quantify the printability and the limitations of the used material. Finally, a customized printer was developed. The general layout of the present chapter is shown in Figure 5-1. On the same figure, one can see the addressed issue along with the main used characterization techniques.

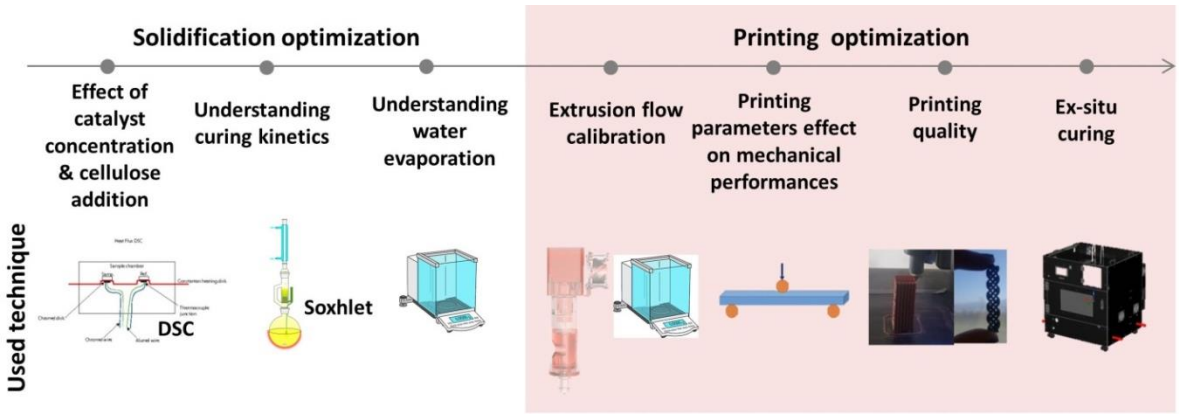

Figure 5-1: Graphic abstract of chapter 5.

5.2 Part 1 - Solidification and crosslinking optimization

5.2.1 Introduction

The crosslinking of PFA is a complex process as explained in chapter 1 which should be optimized to avoid any defects during curing and to ensure a total crosslinking in order to yield high mechanical and thermal properties. The optimization of the curing process of the oligomer can only be achieved when the different events during curing are identified and the crosslinking kinetics are investigated. Accordingly, in this first part of the fifth chapter, DSC scans were first performed to have a close-up of the events occurring during the crosslinking of PFA oligomers, then the kinetics of both curing and water evaporation during crosslinking were studied in order to optimize the solidification step. Finally, shear tests were performed on the PFA/cellulose paste to monitor the changes in the viscoelastic properties during the crosslinking process.

5.2.2 Polymer curing and crosslinking understanding - Differential Scanning Calorimetry

5.2.2.1 Effect of catalyst concentration

Different PFA/catalyst ratios were analyzed by DSC at a 5 °C/min heating rate. The PFA samples were prepared by diluting the commercial product with 15 wt% water and adding the catalyst at 0, 2, 5, and 15 wt%. On the DSC thermograms at different catalyst content, shown in Figure 5-2 and summarized in Table 5-1, the variation of the exothermic network-polymerization peak can be observed. The higher the catalyst concentration, the more pronounced the exothermic peak and the lower the exothermic peak temperature. In the same Figure, one can also see that the addition of the catalyst is essential for curing since, in the absence of catalyst, one cannot observe any exothermic peak, but only the endothermic peak of water evaporation at around 100°C. The increase in catalyst concentration up to 15 wt% induced a more exothermic (the maximum heat flow at the peak increases) and rapid reaction (lower onset temperature) which, in the case of PFA, can lead to the quick evaporation of residual water and foaming/high porosity. When adding 5 wt% of catalyst the curing heat has a similar value as when adding 15 wt% catalyst (292-309 J/g), thus suggesting that 5 wt% of catalyst is enough for a total crosslinking of the polymer in the tested conditions. On the other hand, the use of only 2 wt% of the catalyst seems to be insufficient for rapid curing because the reaction curing heat is around 262 J/g, well below the enthalpy of 300 J/g measured when adding 5-15 wt% of catalyst. This reduction is supposed to be due to the fact that this low amount of catalyst

is not capable of reaching all the reactive sites in the resin network leading to an incomplete crosslinking reaction (Montserrat et al., 1995; Ooi et al., 2000; Domínguez et al., 2012).

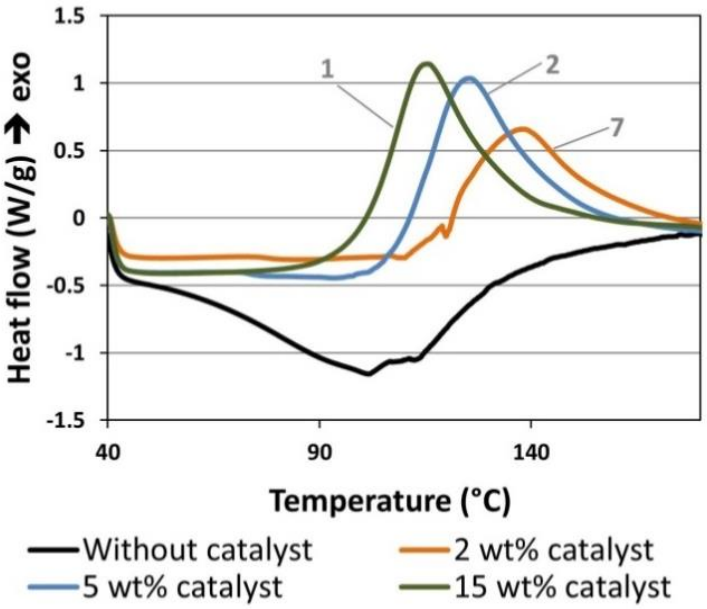

Figure 5-2: Curves of DSC scans of PFA containing different catalyst concentrations at a heating rate of 5°C/min. The given numbers corresponding to different codes of samples detailed in Table 1-5.

It can be concluded that 5 wt% seems to be the best catalyst concentration to minimize the lower water content (the catalyst is water-based) while keeping a rapid curing rate with high conversion and a limited exothermic reaction peak.

5.2.2.2 Effect of heating rate

To assess the effect of the heating rate on the curing of the polymer when adding 5 wt% catalyst DSC tests with 2, 5, and 10 °C/min heating rates were realized and their respective thermograms are displayed in Figure 5-3. As one can observe in Figure 5-3, the faster the heating rate, the more pronounced the exothermic peak, and the peak shifts to higher temperatures as highlighted in Table 5-1. This behavior is described in the literature for the curing of PFA/FA (Domínguez et al., 2012; Guigo et al., 2007b; Lopez de Vergara et al., 2014) and similar thermosetting polymers systems (Gaisford et al., 2019; Montserrat et al., 1995). In terms of curing heat, at 2°C/min and 5°C/min the heat was in the range of 282-294 J/g whilst at 10°C/min the curing heat was limited to 230 J/g which suggests an under-curing of the resin because of the lower curing time caused by a decrease in the reactivity of the system which can be overcome by the addition of more catalyst if needed. However, a fast curing rate is not wanted when using this kind of polymers because this might suppress water degassing and induce resin foaming, as explained in chapter 4.

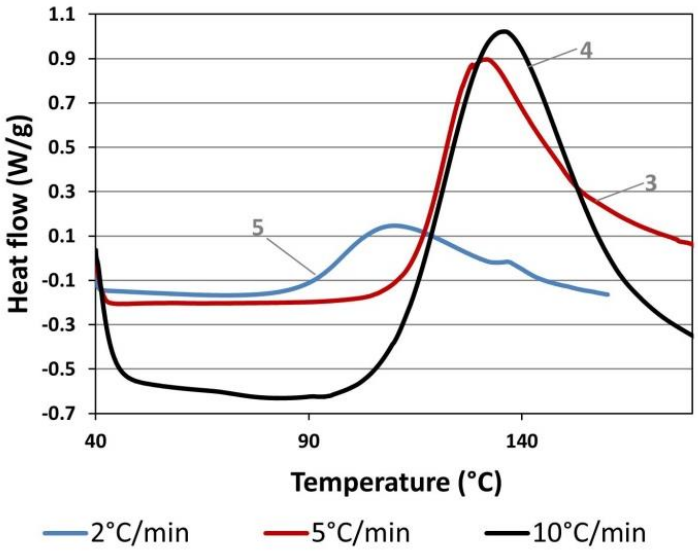

Figure 5-3: Curves of DSC scans of PFA containing 5 wt% catalyst at different heating rates. The given numbers corresponding to different codes of samples detailed in Table 1-5.

5.2.2.3 Effect of cellulose addition

The latter DSC scans have all been conducted on a sample of PFA polymer with catalyst and eventually added water. However, the developed formulation for 3D printing (Chapter 4) contained from 15 to 30 wt% cellulose powder. Despite that, the analysis of the cellulose powder showed neither transformation nor functionalization which might provide to cellulosic particles a catalytic effect on the polymerization of PFA (Pranger and Tannenbaum, 2008). Therefore, a scan with the addition of 10 wt% cellulose and 5 wt% catalyst with a heating rate of 2°C/min was done to deny or confirm any eventual catalytic effect of the cellulose on the system. The scan (red curve on Figure 5-4) shows a similar thermogram to that without any cellulose and the occurrence of the exothermic peak around the same temperature, indicating that the used cellulose does not interfere with the catalyst activity. However, the total heat of the reaction decreased by 10%. An explanation for this slight decrease of the reaction total heat was suggested by (Harsch et al., 2007); these fillers adsorb the reacting monomers at the surface which can affect the stoichiometry and thus create sterical hindrance to the forming network.

Furthermore, a second run was performed on the same cured sample with a 5 wt% catalyst and without any cellulose. The thermogram is displayed in Figure 5-4 and shows no heat flow variation, which indicates that complete curing had occurred in the first reaction.

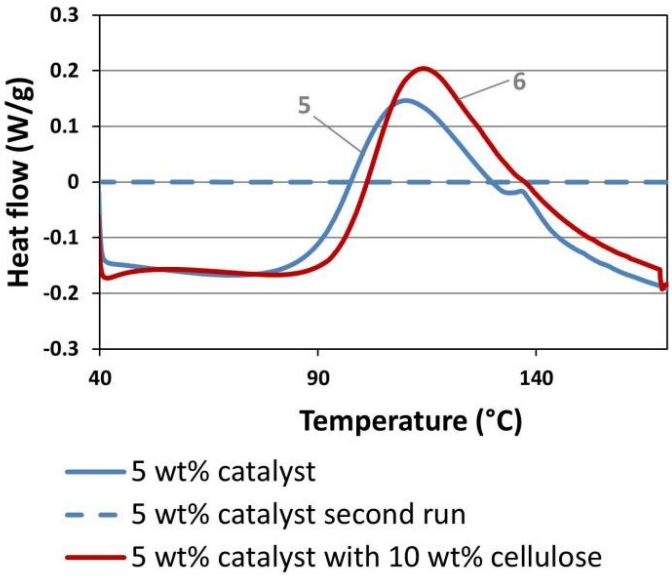

Figure 5-4: Curves of DSC scans of neat PFA with 5 wt% catalyst with and without cellulose at a heating rate of 2°C/min. The given numbers corresponding to different codes of samples detailed in Table 1-5.

Table 5-1: Summary of DSC scans data

Sample	Catalyst content (wt%)	Cellulose content (wt%)	Heat ramp (°C/min)	Total water content (wt%)	Onset Temperature (°C)	Peak temperature (°C)	Reaction enthalpy (J/g)
1	2	0	5	21.75	119	137	262
2	5	0	5	24.75	109	124	309
3	5	0	5	9.75	115	128	282
4	5	0	10	9.75	112	134	231
5	5	0	2	9.75	91	110	294
6	5	10	2	9.75	95	113	262
7	15	0	5	29.25	100	114	292

According to the previous data 5 wt% of added catalyst seems to be enough to increase the reactivity of the system while avoiding extra water brought by the catalyst solution. The onset reaction temperature is in the range of 90-115°C. It was also found that the addition of inert cellulose particles has no catalytic effect on the curing of the resin and might even act as inhibitors but this effect can be neglected because the onset reaction temperature remains unchanged.

5.2.3 Curing and water evaporation kinetics investigation for a defect-free curing

5.2.3.1 Curing kinetics of the resin - soxhlet extraction

The curing kinetics of PFA has been studied in the literature with different techniques such as DSC, DMA, and rheology using different types and concentrations of catalyst and curing methods (Domínguez et al., 2012; Guigo et al., 1386; Iroegbu and Hlangothi, 2018; Ooi et al., 2000; Sadler et al., 2018; Seyedlar et al., 2016). In this work, our focus is to monitor the evolution of the curing of the commercial oligomers using a fixed amount of latent catalyst (5 wt%) under variable curing temperatures. The degree of crosslinking (α) can be directly correlated with the gel fraction (G%) which was experimentally measured with the soxhlet extraction method described in chapter 2.

5.2.3.1.1 Extraction time

Although soxhlet extraction method of the uncrosslinked fraction of the polymer is a well-known method for a direct and accurate assessment of the crosslinking degree, it can be time-consuming and can resort to the use of hazardous solvents. In our work acetone was used as a proven appropriate solvent for uncured PFA resin (Seyedlar et al., 2016). Furthermore, to optimize the extraction time (the number of cycles) a poorly crosslinked sample was left in the soxhlet from 5 to 16 hours, and the dissolved fraction was carefully determined after every extraction.

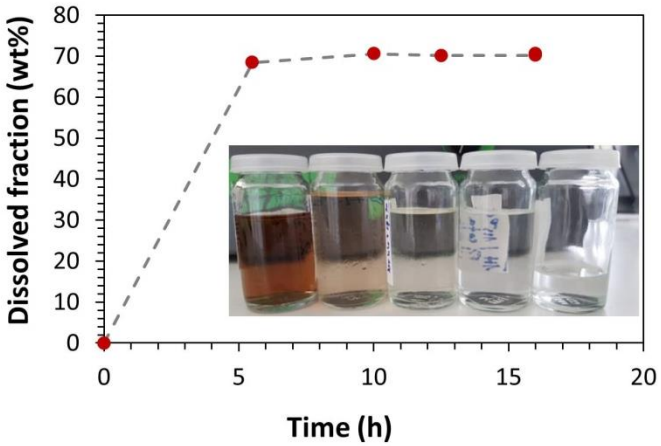

Figure 5-5: Evolution of dissolved oligomer fraction as a function of soxhlet extraction time

As one can see in Figure 5-5, after only 5.5 hours of extraction time (corresponding to 24 cycles) 68 wt% of the oligomer has been dissolved, and then after 10 hours the total extracted fraction stabilized at 70 wt%. The extraction time was then fixed at 8 hours (35 cycles) for optimum extraction. Another more crosslinked sample was extracted for 8 hours and then 14 hours which

revealed no further oligomer extraction which confirms an adequate extraction time of 8 hours. Furthermore, a visual assessment of the extraction solvent, presented as well in Figure 5-5, is in agreement with what was discussed previously. It is also worth mentioning that the samples were later further extracted for 8 hours in ethanol and no further dissolution was observed.

5.2.3.1.2 Crosslinking of oligomers- kinetics

The experimentally measured values of the crosslinking degree (α) of the PFA resin crosslinked at temperatures ranging from 80°C (around the onset temperature of reaction) to 120°C (around the peak temperature) for a time ranging from 0 to 500 min are plotted in Figure 5-6. The curing of resin especially at higher temperatures follows a logarithmic evolution form typical for such crosslinking reactions.

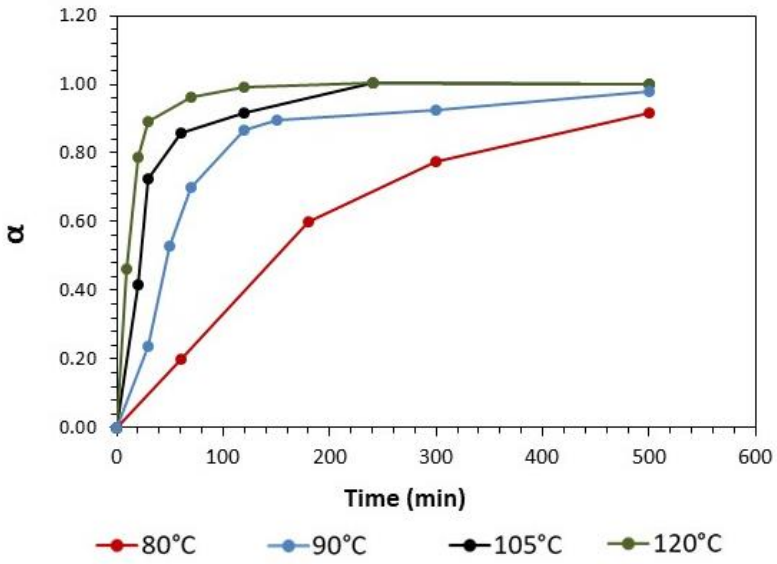

Figure 5-6: The evolution of the experimental degree of crosslinking (α) of PFA resin with 5 wt% catalyst under different temperatures over time.

The curing process of a thermosetting polymer is commonly described by a single-step kinetic equation (eq 23).

$$\frac{d\alpha}{dt} = k(T)f(\alpha) \qquad \textit{eq 23}$$

Where α represents the curing degree of the polymer, t is the time, k(T) is the rate constant, which depends on temperature, and f(α) is the process mechanism function.

In thermosets curing, we can simply consider n^{th} order equation as a kinetic model which is shown below in eq 24.

$$\frac{d\alpha}{dt} = k(T)(1-\alpha)^n \qquad \textit{eq 24}$$

Here (1- α) represents the concentration of reactants which varies from 1 at the start of the reaction to zero at the completion of the reaction. In our case, the reaction of polymerization by condensation of poly(furfuryl alcohol) oligomers follows second order kinetics (n=2) (Sadler et al., 2018), so eq 24 can be finally written as:

$$\frac{d\alpha}{dt} = k(T)(1-\alpha)^2 \qquad \textit{eq 25}$$

To determine the rate constant k(T), dα/dt was plotted in Figure 5-7 versus the square concentration of the remaining reactant $(1-\alpha)^2$ using the equation eq 25.

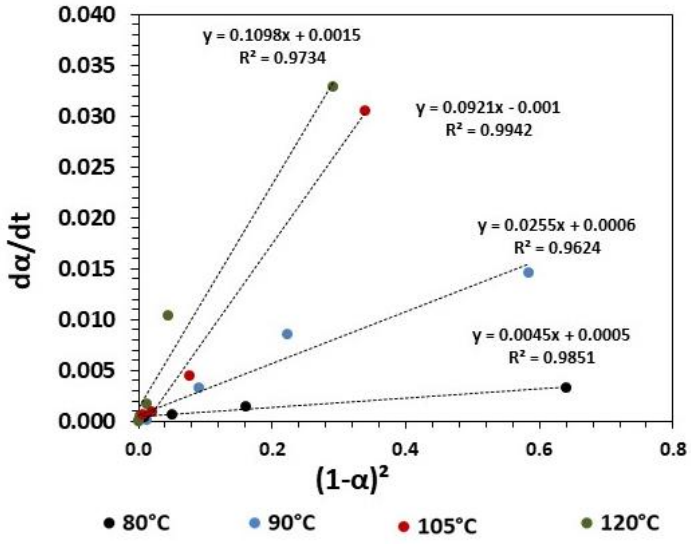

Figure 5-7: The differential rate law plot for PFA crosslinking under different cure temperatures using 5 wt% catalyst.

The constant rate for every temperature can be determined as the slope of the best fit line in Figure 5-7. The constant rate is, as expected, proportional to the curing temperature and increases from 4.5 10^{-3} 1/min to 1.1 10^{-1} 1/min when curing at 80°C and 120°C respectively.

It is possible to calculate the activation energy considering that the rate constant (k) follows the Arrhenius law shown in eq 26 where R is the universal gas constant, T is the absolute temperature, E_a is the energy of activation, and A_0 is the pre-exponential function.

$$k(T) = A_0 e^{(-E_a/RT)} \qquad \textit{eq 26}$$

The log of the different rate constant (k) was plotted versus the inverse of the curing temperature T as shown in Figure 5-8. The slope of the fit line was used to determine the energy of activation (E_a) and the pre-exponential factor A_0 by fitting it to equation eq 26. The calculated energy of activation (E_a) for 5 wt% added catalyst is 93.6 kJ/mol which is similar to the 55-80 kJ/mol found in the literature calculated with model-free kinetics model and stronger acid catalysts (Domínguez et al., 2012; Lopez de Vergara et al., 2014; Sadler et al., 2018).

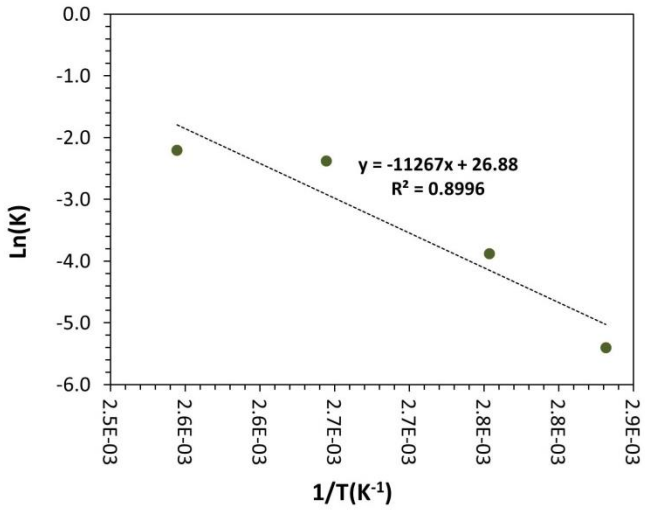

Figure 5-8: Arrhenius Law plot of experimental results with the best fit line (dashed line).

The degree of crosslinking α *versus* time for both experimental and estimated values calculated with the general integrated kinetic second-order law equation (eq 27) are plotted in Figure 5-9. The performance of this general model start to decline at low temperatures as highlighted in Table 5-2. Indeed the calculated Mean Absolute Error (MAE) exceed a value of 0.1 for α values predicted when crosslinking at 80°C.

$$\frac{1}{(1-\alpha)} = 1 + kt \qquad \textit{eq 27}$$

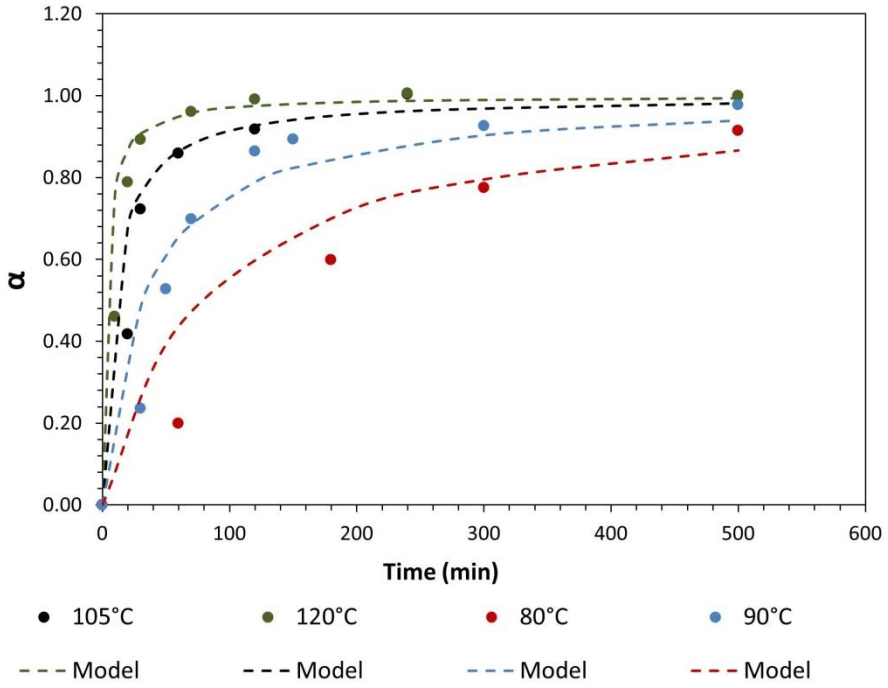

Figure 5-9: Evolution of the degree of crosslinking (α) of PFA resin experimentally measured (points) and estimated with second-order kinetic law (dashed lines) under different temperatures over time.

Table 5-2: MAE values for the predicted crosslinking degrees at different temperatures.

T (°C)	MAE
120	0.055
105	0.053
90	0.066
80	0.101

5.2.3.2 Water evaporation during curing

Water and volatile evaporation rate during curing is also another important event conditioning the solidification quality of the objects. In Figure 5-10, one can clearly notice the effect of water evaporation kinetics on the porosity and the overall dimensional stability of the cured PFA. When curing at 120°C, both curing and water evaporation rates are high which results in foam formation whilst when curing under 100°C water evaporation seem to be less sudden especially since the water boiling point was not reached.

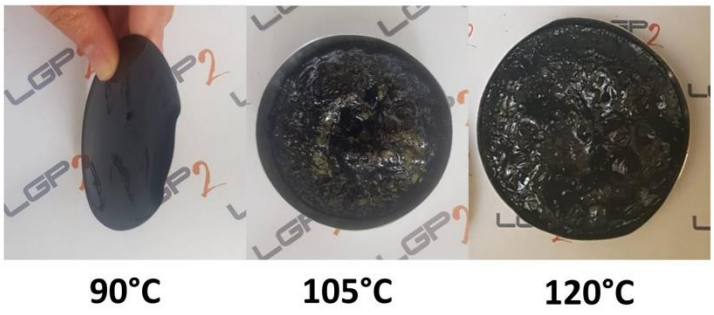

Figure 5-10: Effect of the curing temperature on the dimensional stability and aspect of cured neat resin with 5 wt% catalyst.

In order to better understand the kinetics of water evaporation through the cured sample, about 5 g of PFA/catalyst were weighed within ±0.0001 g before curing (M_0) and after curing (M_1) for a certain time, and the mass loss was calculated according to the following equation eq 28.

$$W\% = \frac{M_0 - M_1}{M_0} \cdot 100 \qquad \textit{eq 28}$$

To follow the evolution of water evaporation during curing, the total water originally in the system PFA/catalyst should be calculated. This total water in the uncured mixture resin/catalyst can be divided into 3 sources:

i. Physical water brought by the PFA resin can be estimated with equation eq 29 elaborated by (Domínguez and Madsen, 2015).

$$W_{PFA}(\%) = CW_{PFA} \cdot (1 - C_{catalyst}) \qquad \textit{eq 29}$$

i. Physical water brought by the catalyst is alike estimated with the equation eq 30.

$$W_{catalyst}(\%) = CW_{catalyst} \cdot C_{catalyst} \qquad \textit{eq 30}$$

Where $C_{catalyst}$ is the concentration of the catalyst (5 wt%), CW_{PFA} is the concentration of water in the resin (7.5 wt%) and $CW_{catalyst}$ is the water content in the catalyst (45 wt%).

ii. Chemical water from the condensation reaction between two PFA oligomers can be estimated with eq 31.

$$W_{cond}(\%) = \frac{a \cdot M_{H_2O}}{M_{PFA}}(1 - W_{catalyst}) \cdot (1 - W_{PFA}) \qquad eq\ 31$$

Where M_{H2O} is the molecular mass of water, M_{PFA} the average molecular mass of PFA oligomer and *a* is the number of water molecular released for every PFA macromolecule during the condensation reaction.

Accordingly, the physical water yields a value of 9.37 wt%. The chemical water on the other hand cannot be precisely calculated because the exact molecular mass of the oligomer is not exactly known as discussed in chapter 2. However, as the maximum water evaporation experimentally measured was 17.4 wt% the chemical water should be at least 7 wt%. To achieve this value the molecular mass should not exceed an average value of 230 g/mol which is hardly achievable if we consider only the structure suggested in chapter 3 (structure I bellowed) with values of n>2. It is then believed that there is another type of macromolecule as result of homo-condensation of two BHMF (structure II) which allows the release of two water molecules (*a*=2).

$$OH\text{-}CH_2\text{-}(FU\text{-}CH_2\text{-}O\text{-}CH_2)_n\text{-}(FU\text{-}CH_2)_m\text{–}FU \quad (I)$$

$$OH\text{-}CH_2\text{-}FU\text{-}CH_2\text{-}O\text{-}CH_2\text{-}CH_2\text{-}OH \quad (II)$$

However, no conclusions can be made as to the average molecular weight of the oligomers, but it is believed that the chemical water released during curing is more than that calculated by (Domínguez and Madsen, 2015) which did not exceed 4 wt%. The mass loss during the condensation measured experimentally exceeded 8 wt% and known that free furfuryl alcohol monomers in the resin are lower than 1 wt%, the possibility of the release of other volatile at this range of temperature can be neglected and hence we can suppose that the total water in the resin/catalyst system to be 17.4 wt%.

The water evaporation extent can be therefore be calculated according to eq 32 and the respective experimental values are plotted in

Figure 5-11 as a function of time for temperature ranging from 80°C to 120°C.

$$\alpha'(t) = \frac{W\%(t)}{17.4} \qquad \textit{eq 32}$$

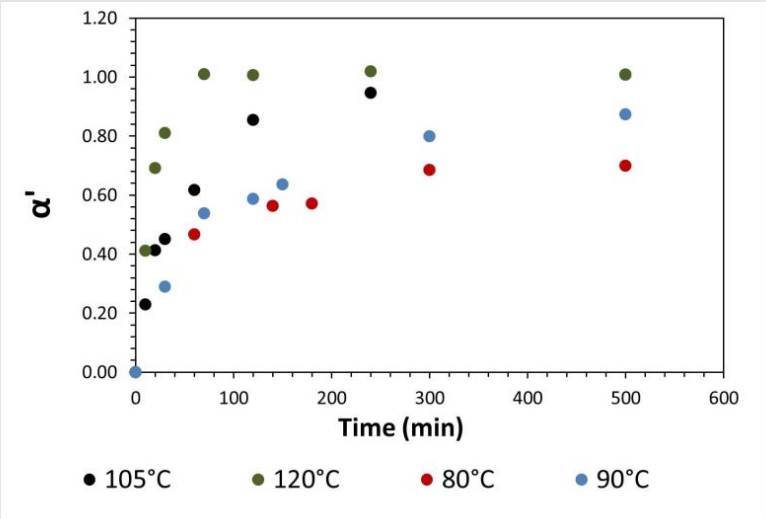

Figure 5-11: Water evaporation extent (α') over time under different temperatures.

As one can see the evolution of the evaporation extent follows nearly a logarithmic tendency especially when curing at high temperature and the evaporation kinetics can be fitted with a first-order kinetic law. To verify this, in Figure 5-12-A, the natural log of (1-α') was plotted virus time and the best fit line was plotted. By fitting the Arrhenius law (eq 26), to the equation of the best fit line of ln(K) versus the inverse of temperature the activation energy can be calculated which yields a value of 72 kJ/mol, as expected, is higher than that of evaporation of bulk water (44 kJ/mol) (Prado and Vyazovkin, 2011).

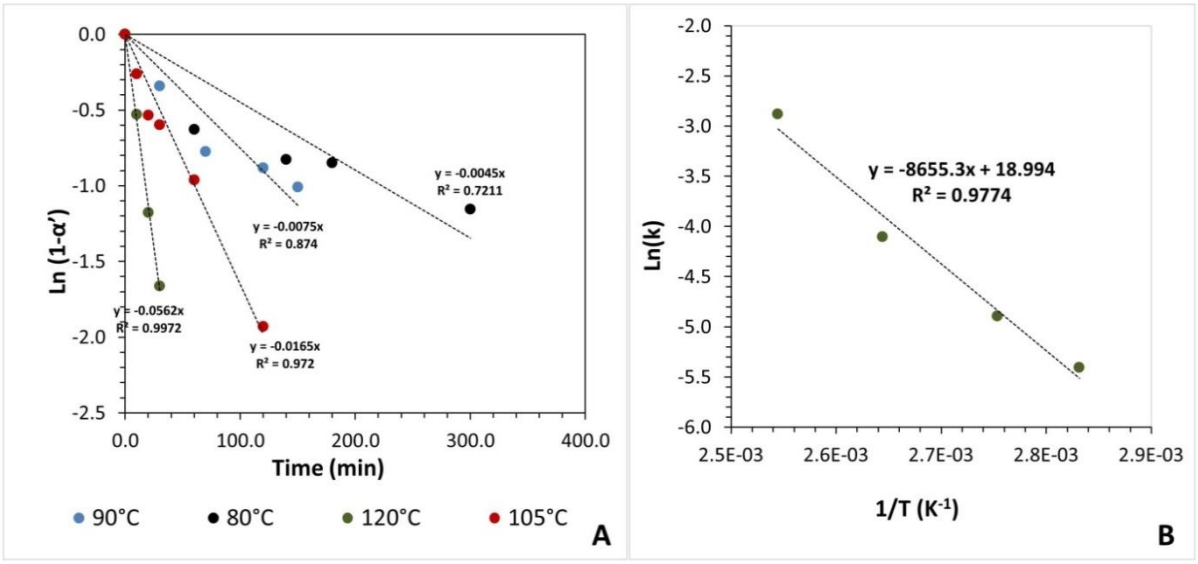

Figure 5-12: Natural logarithmic of the integrated first-order rate law plot for water evaporation during crosslinking (A) and Arrhenius Law plot (B).

Finally, by comparing the first-order kinetic model to the experimentally determined data we can see in Figure 5-13 that water evaporation follows the model when heating at a temperature higher than 90°C but when heating at lower temperatures the model seems to be no longer valid as it is visible in Figure 5-13. This is highlighted by the MAE values calculated and displayed in Table 5-3 where the error of α' reaches 0.125 when crosslinking at 80°C. One can also notice that, when curing at temperature below 100°C the evaporation rate decrease significantly when the curing gel time is reached (α=0.5-0.7) so around 150 min at 80°C and 80 min at 90°C until reaching a plateau when only 60% of water is evaporated. This can be due to water molecules entrapping in the compact polymer structure which hinders the water evaporation. On the other hand, when curing at a higher temperature, the water evaporation continues even after the gel time which can be explained by the gel deformation and foaming induced by the higher vapor pressure which results in a faster and complete vapor release. As was shown in chapter 4, the cellulose addition can help to solve this issue by promoting the water vapor migration through the gelled structure which can help to eliminate the totality of water at a temperature under 100°C and hinder foaming and shape deformations when curing at higher temperatures by decreasing the vapor pressure in the structure.

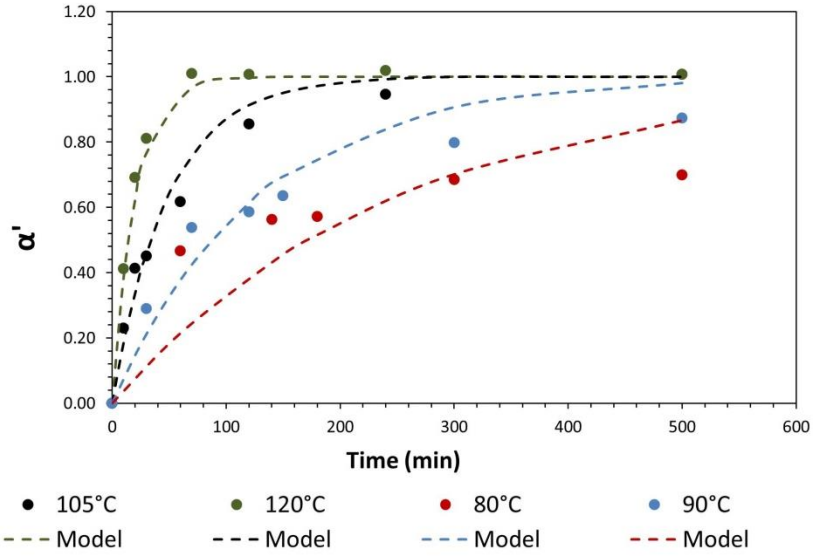

Figure 5-13: Water evaporation experimental normalized amount (α') plotted over time under different temperatures and the theoretical values estimated by the first-order kinetic model.

Table 5-3: MAE values for the predicted normalized amount of evaporated water at different temperatures.

T (°C)	MAE
120	0.028
105	0.046
90	0.071
80	0.125

5.2.3.3 Survey of rheology behavior during paste curing

To simulate and better understand the viscoelastic behavior during printing of the developed paste PFA-Cell25-B, it was sheared according to the protocol explained in chapter 2 in the linear viscoelastic region at different temperatures while the evolution of storage and loss modulus was tracked. In Figure 5-14, the evolution of G', and G" over 8 hours is plotted under isothermal curing at 90°C. As one can see, when 5 wt% of catalyst was added, the storage modulus start to increase after 70 min which suggests an increase in the stiffness of the paste caused by the beginning of the gelation of the resin. This gel time is in agreement with the curing kinetics shown in Figure 5-9. On the other hand without the addition of catalyst the modulus remains stable for 8 hours with a slight increase after 120 min which can be related to solvent loss. These results prove that the changes in the viscoelastic properties, and more precisely the storage modulus G,' can be directly correlated with the curing of PFA oligomers and can be used to determine experimentally the gel time for the developed paste containing 25 wt% cellulose.

The G' and G" evolution over time at temperature ranging from 70°C to 80°C is shown in Figure 5-15. One can notice that both moduli start to increase when the condensation reaction advances and the onset time of this increase is proportional to the curing temperature. When curing at high temperature, the increase rate of G' is high and quickly reaches a plateau whilst when curing at low temperature this increase is gradual and the plateau was not yet reached when curing at 80°C. These observations are directly related to the curing kinetics of the resin/catalyst discussed previously. Moreover, as one can see in Figure 5-15, under the different temperatures G' slightly decreases before starting to increase; this drop is believed to be caused by the decrease in the viscosity of the resin when heating before the polymerization takes place.

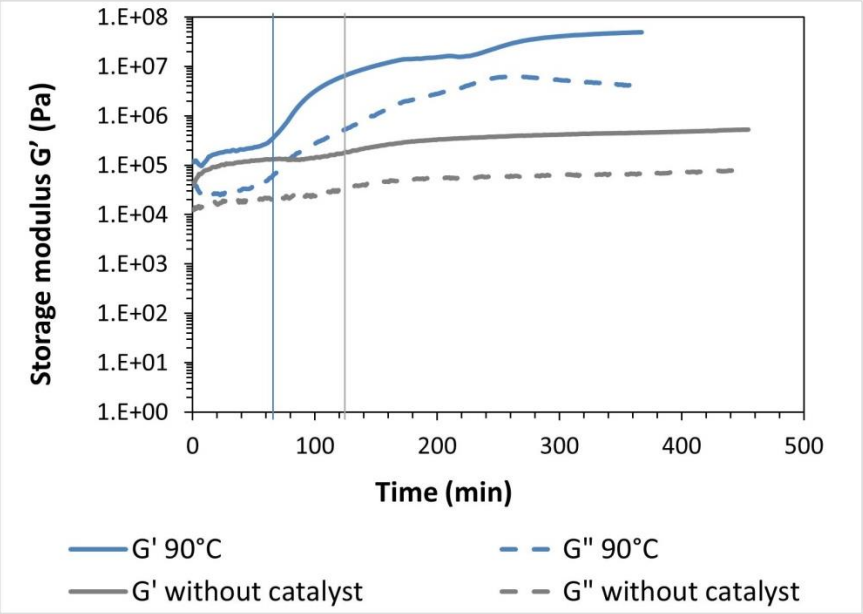

Figure 5-14: Evolution of G' and G" during curing of PFA/cellulose paste at 90°C with and without catalyst addition.

The time around which the modulus starts to increase can be considered as a gelation time (t_{gel}), when the network of polymeric chains densifies and chain ramification decreases their flexibility thus inducing the increase of G'. The influence of the curing temperature on $t_{gel,}$ ie. the onset time of G' exponential increase, is clearly shown in Figure 5-15-B and summarized in Table 5-4. On the same table, the correspondent crosslinking degree (α_{gel}) was calculated based on the second-order kinetic model (eq 25) as well as the theoretical time needed to cure 90% of the resin ($t_{0.9}$). Therefore, according to the data in Table 5-4, the extent of the reaction should be around 0.68 ±0.012 to reach the gelation state of the paste. Furthermore, the $t_{0.9}$ correlates well with the evolution of the G' as we can see in Figure 5-15 (dashed lines) after this time the G' starts to reach plateau.

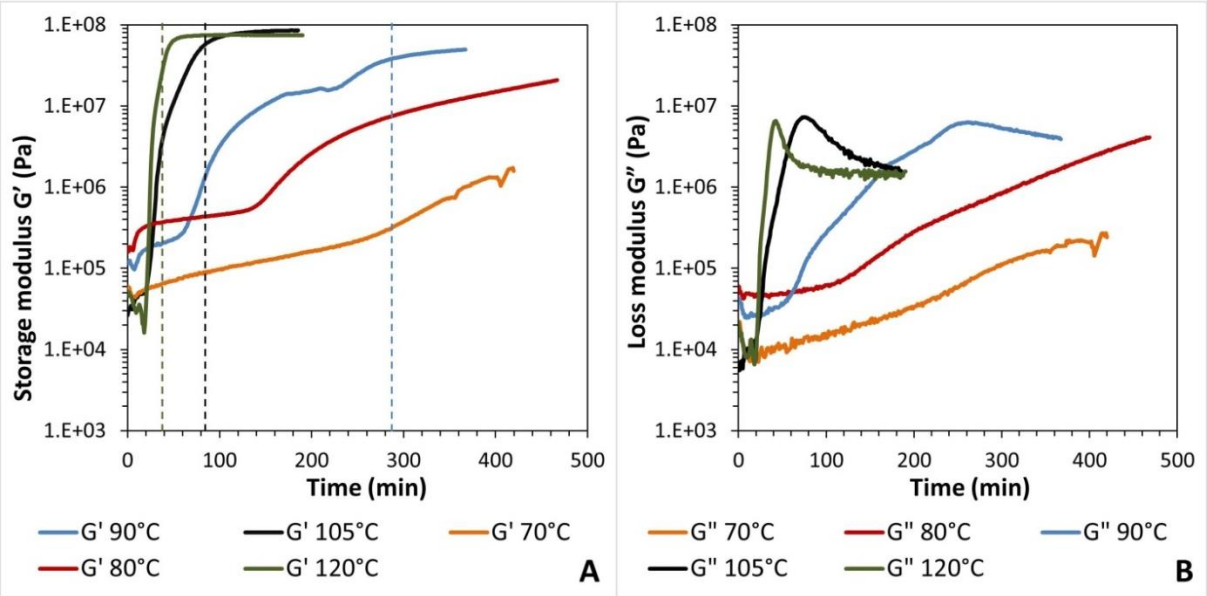

Figure 5-15: Evolution of G' (A) and G'' (B) during curing of PFA/cellulose paste under different temperatures.

Table 5-4: Summary of different gelation times and correspondent crosslinking degrees when curing under different temperatures

T (°C)	t_{gel} (min)	α_{gel}	$t_{0.9}$ (min)
70	>346	0.664	1600
80	142.5	0.668	650
90	72	0.709	280
105	18	0.674	80
120	6	0.680	30

5.2.4 Conclusions

The results of this first section of chapter 5 can allow us to optimize the catalyst type, concentration, and the curing thermal program. The main conclusions are listed below:

- The use of latent catalyst is preferred to expand the pot life of the developed pasty 'ink' and to avoid any eventual unwanted curing in the printing head.
- According to DSC findings, 5 wt% of latent catalyst seem to be enough for effective curing of the resin at intermediate temperature (80°C–120°C) while avoiding increasing the water content in the final paste.
- According to the curing kinetics of the resin at a temperature higher than 100°C, the curing rate is higher but the foaming of the resin takes place. Whilst when curing under lower

temperature the foaming can be avoided but the curing kinetics slows down remarkably and the water evaporation cannot be completed.

- The cellulose addition can facilitate the total water evaporation and hinder the dimensional deformation of the eventually solidified composite.
- The gelation of the paste occurs when reaching ca. 68% of resin crosslinking extent which varies from over 2 hours when curing at 80°C to only 6 min when curing at 120°C.

Accordingly, a 3-steps crosslinking strategy to solidify the printed object with good shape fidelity, low porosity, and optimized thermomechanical properties can be proposed;

1. Pre-curing stage to gently evaporate the water from the 'fresh' composite until reaching the gelation. This stage is conducted under 70-90°C;
2. Curing stage to favor the crosslinking of the printed object under a temperature ranging from 90-100°C to avoid any porosity caused by the remaining water;
3. Post curing stage under high temperature 150°C-200°C to guarantee a total crosslinking and densification of the structure as it was demonstrated previously in chapter 4.

The temperature in the first stage should be as low as possible for a massive compacted structure as the water evaporation can be more difficult. However, when curing a thin-walled structure or with low infill water evaporation is easier and the temperature can be increased to minimize the curing time.

5.3 Part 2 - 3D printing process optimization

5.3.1 Introduction

In the first part of the present chapter, some insights were provided concerning the solidification step for the sake of obtaining a defect-free printed object. In the second part, the optimization and the understanding of the printability of the developed paste will be discussed. To do so, a calibration of the extrusion head was first carried out as it is one of the key steps for accurate printing. Afterwards, the effect of the main printing parameters on the mechanical properties is investigated. Finally, the printability of different forms is assessed.

5.3.2 Calibration of extrusion flow

As described in the material and method chapter, the paste is provided through an air pressurized cartridge to the inlet cavity of the extruder which permits the adjustment of the feed flow rate. The rotation of the screw conveys the paste at a set rotation velocity until the nozzle. The paste is extruded through the nozzle at a certain extrusion flow, which is a key parameter for accurate printing.

5.3.2.1 Calculation method of the extrusion multiplier

Screw pump calibration

In the printer firmware, the screw extruder has a nominal calibration factor e_{cal} = 400 µstep/mm. This value is valid for a « virtual » filament with a diameter of 1.75 mm, a stepper motor with 200 steps/round and a stepper driver with 16 µstep/step. In the case of volumetric/screw pumps, the filament diameter must be provided in couple with the calibration factor 'e' just to allow the slicer to correlate the volume flow of extruded material with the pump angular speed.

Calibration of the screw pump (extruder)

The typical flow vs. rotation speed of a screw pump can be obtained by converting the G-Code command Ex (where x is the length of extruded filament) and Fy (where y is the extrusion speed in mm/min) into the corresponding number of revolutions and rotation speed.

An extrusion G-Code command G1 Ex Fy can be therefore converted into the corresponding pump rotation parameters, like the number of revolutions (E_R) which can be calculated according to eq 33.

$$E_R = \frac{x \cdot e_{cal}}{N_{rev}} \qquad \textit{eq 33}$$

Where x is the length of the 1.75 mm "virtual" filament to extrude, e_{cal} is the extruder calibration factor (i.e. 400 µstep/mm) and N_{rev} is the number of µsteps for a complete revolution (i.e. 3200 for a stepper with 200 steps/rev and a 16-µstep driver).

Similarly, the rotation speed can be calculated according to eq 34 where y is the extrusion speed of the "virtual" filament.

$$F_R = \frac{y \cdot e_{cal}}{N_{rev}} \qquad \textit{eq 34}$$

Using the machine control panel, or by directly coding an extrusion command (G1 Ex Fy), and eq 33, it is, therefore, possible to fix the number of revolutions and the rotation speed of the screw pump to obtain its characteristic flow curve by weighing the mass of extruded material when varying the rotation speed F_R with constant number of revolutions E_R and fluid feed pressure (therefore the feed flow rate). The mass flow $(\dot{M})$ can be therefore calculated using eq 35 where M is the weighed mass of extruded material, and E_R/F_R is the extrusion time.

$$\dot{M} = M \cdot \frac{F_R}{E_R} \qquad \textit{eq 35}$$

Since all calculations performed by the slicer to synchronize the extrusion and tool-head moving speed, in the XY-plane, are based on a volume balance, the mass flow obtained by weighing needs to be converted into the corresponding volume flow $(\dot{V}_e)$ using eq 36, where $\dot{M}$ is the mass flow and ρ the material's density.

$$\dot{V}_e = \frac{\dot{M}}{\rho} \qquad \textit{eq 36}$$

The objectives of extracting the pump characteristic are:

i) to precisely calibrate the extrusion flow in order to avoid any under-extrusion or over-extrusion which would generate printing defect and shape fidelity issues.

ii) to identify a linear region where the extrusion flow proportionally varies with the pump rotation speed in order to identify an operational window for the printing speed.

The pump characteristic curve volume flow vs. rotation speed can be correlated to the virtual filament volume flow which can be calculated according to eq 37 where S_f is the section of the "virtual" filament.

$$\dot{V}_f = S_f \cdot y \qquad \textit{eq 37}$$

By using eq 34, the filament volume flow can be plotted as a function of the stepper motor rotation speed and directly compared to the screw pump characteristic curve (eq 38).

$$\dot{V}_f = S_f \cdot \frac{F_R \cdot N_{rev}}{e_{cal}} \qquad \textit{eq 38}$$

The comparison (ratio) between the slope of the linear region in the flow vs. rotation speed of the screw pump and the linear increase of the "virtual" filament flow given by eq 37, is used to extract a multiplicative factor α in order to superpose the pump flow linear region to the virtual flow. This extrusion multiplier (α) can be obtained using the slope of the parity plot $\dot{V}_e$ vs. $\dot{V}_f$ (plotted for similar rotation speeds) in a linear region (eq 39).

$$\alpha = \frac{\dot{V}_e}{\dot{V}_f} \qquad \textit{eq 39}$$

It is important to mention that the calibration protocol (pump characteristic volume flow vs. rotation speed) is specific for a given material formulation; pump inlet pressure and nozzle type (i.e. diameter and geometry). Variation of one of these parameters requires pump re-calibration.

Correlation between the pump flow and the printing speed

Printing parameters such as the layer thickness (H), the deposed filament width (w), and the printing speed (z) are used to calculate the material volume flow necessary to print lines with the desired dimensions according to eq 40.

$$\dot{V}_f = H \cdot w \cdot z \qquad \textit{eq 40}$$

The slicer then calculates the corresponding "virtual" filament extrusion speed (y) using eq 37 and eq 40 according to eq 41.

$$y = \frac{h \cdot w \cdot z}{S_f} \qquad \textit{eq 41}$$

The rotation speed of the extruder stepper motor to obtain the required flow of "virtual" filament can be therefore calculated using eq 34 and eq 41 thanks to eq 42.

$$F_R = \frac{h \cdot w \cdot z}{S_f} \cdot \frac{e_{cal}}{N_{rev}} \qquad \textit{eq 42}$$

Whereas, the rotation speed of the screw pump to obtain the required flow of fluid can be calculated using eq 39 and eq 42 with the following equation.

$$F_R = \alpha \cdot \frac{h \cdot w \cdot z}{S_f} \cdot \frac{e_{cal}}{N_{rev}} \qquad \textit{eq 43}$$

5.3.2.2 Influence of the rotation speed

As explained previously, the printing speed window using the screw pump extruder with the optimized ink formulation PFA-Cell28-B has to be determined. To do so the evolution of the experimental extrusion flow ($\dot{V}_e$) was plotted vs. the rotation speed of the extruder stepper motor (F_R) as shown in Figure 5-16. The extrusion flow was measured for rotation speed ranging from 25 to 275 rpm using a nozzle of 0.72 mm and under a feed pressure of 3 bars. The higher limit of F_R was constrained by a maximum extrusion speed in the firmware of the used 3D printer. As one can notice

in Figure 5-16, the extrusion flow increases linearly with the extrusion speed until the maximum speed without leveling in this wide range of extrusion speed. This means that the optimized paste can be printed at a large printing speed window under 3 bar pressure which minimizes the pressure loss in the nozzle. However, the evolution of this extrusion flow can vary when changing the feed pressure and the used nozzle which is the main interest of the next two sections.

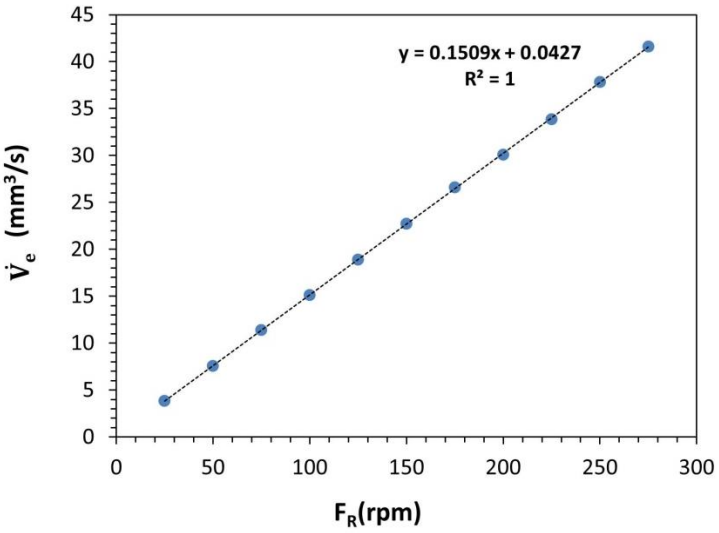

Figure 5-16: Influence of the rotation velocity (FR) on the extrusion flow through a nozzle of 0.72 mm and under a feed pressure of 3 bars.

5.4 Influence of the feed pressure

The influence of the feed pressure at the outlet of the cartridge on the measured extrusion flow ($\dot{V}_e$) through a nozzle with a diameter of 0.72 mm was evaluated for pressure varying from 1.5 to 3 bar. The minimum pressure corresponds to the minimum pressure allowing the extrusion of the paste through the nozzle and 3 bars were set as a maximum pressure to avoid any leakage in the extruder. The plot of the values of $\dot{V}_e$ as a function of the extrusion speed for different feed pressures, is shown in Figure 5-17. As one can notice, for the three applied pressures, ($\dot{V}_e$) increases linearly with the extrusion speed with no levelling which is thanks to the important supply rate from the outlet of the cartridge. However, the proportionality coefficient between $\dot{V}_e$ and F_R increases by increasing the feed pressure. For instance, this proportionality coefficient triples when doubling the feed pressure to pass from 0.05 under 1.5 bars to 1.5 under 3 bars. This increase in the proportionality can be explained by a lower pressure loss in the nozzle allowing a higher extrusion flow. Therefore, it is more interesting to maximize the feed pressure to widen the printing speed window.

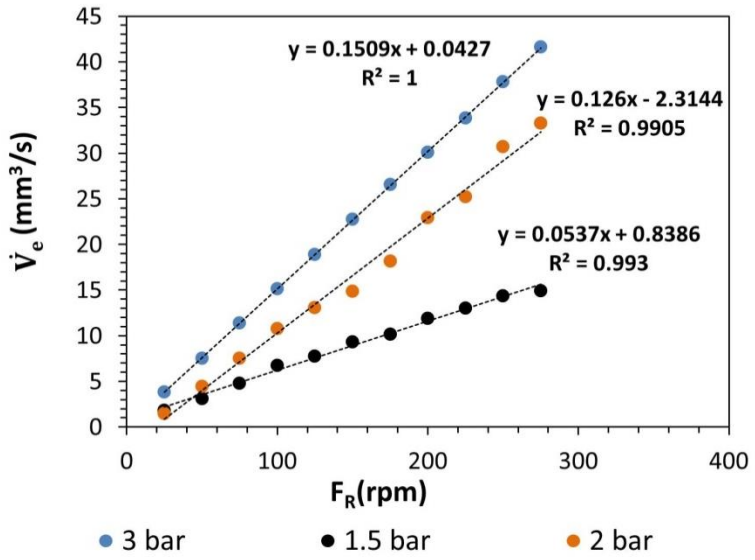

Figure 5-17: Influence of the feed pressure for different rotation speeds on the extrusion flow through a nozzle of 0.72 mm.

5.4.1.1 Influence of the nozzle

The extrusion efficiency was evaluated for three different nozzle diameters ranging from 0.72 to 1.2 mm with extrusion velocity (F_R) ranging from 25 to 275 rpm (Figure 5-18). As one can notice in Figure 5-18-A, the extrusion flow was larger for larger nozzles and it displayed a linear evolution over all the range of extrusion velocity of the 3 nozzles. Nevertheless, the proportionality coefficient increased when increasing the nozzle diameter. Accordingly, and as explained in section 5.3.2.1 (p.248), the extrusion multiplier (α) can be obtained using the slope of the parity plot $\dot{V}_e$ vs. $\dot{V}_f$ shown in Figure 5-18-B for the three nozzles. The extrusion multiplier has the value of the slope of the best fit line which is 2.12, 1.71, and 1.35 for nozzles size 0.72, 1, and 1.2 mm, respectively. These values of α can be used in the G-code as an extrusion multiplier which will allow regulating the extrusion flow for different printing speeds and printing parameters for accurate printing. When printing the paste PFA-Cell28-B, with 3 bars pressure, with a layer height of 0.6 mm and road width of 0.72 mm the theoretical printing speed (calculated from the extrusion flow) can reach 100 mm/s.

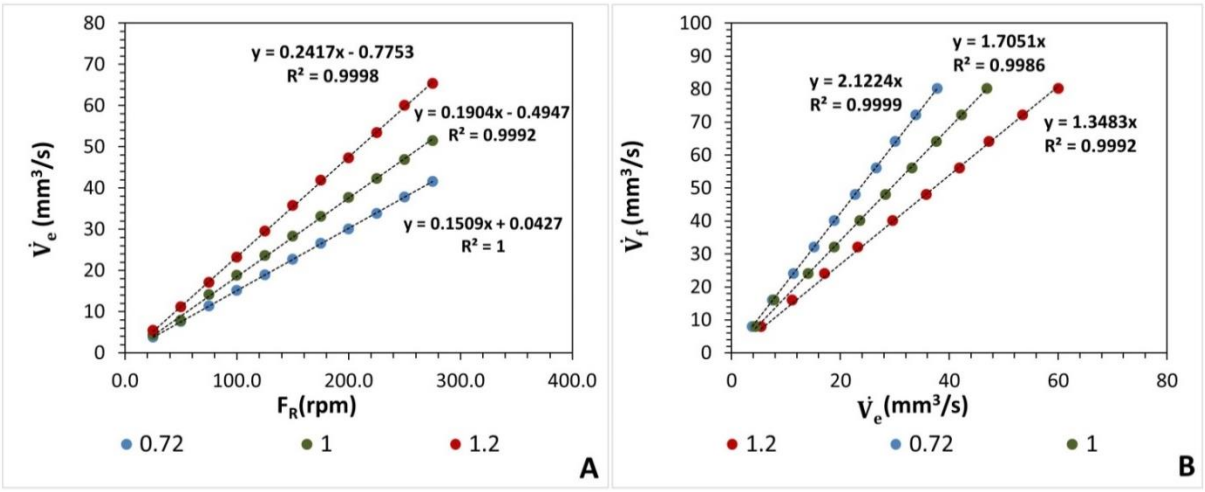

Figure 5-18: Influence of the nozzle size for different rotation speeds on the extrusion flow under 3 bars feed pressure. (A) A plot of extrusion measured extrusion flow as a function of the rotation velocity (B) Plot of the extrusion flow of a virtual thermoplastic filament calculated by the slicer vs. the experimental extrusion flow $\dot{V}_e$.

Finally, to assess the calibration of the extrusion flow and the efficiency of the extrusion multiplier α in the regulation of the extrusion flow, samples with different printing parameters were carefully weighed to evaluate the accuracy of the extrusion calibration. As one can see in Figure 5-19-A, the overall weight is similar for the different samples (detailed parameters corresponding to the codes are provided in chapter 2 p.124). When changing printing parameters, the slicer automatically manages the layers number and the exact volume of material to be deposited which might explain the slight difference in the weights.

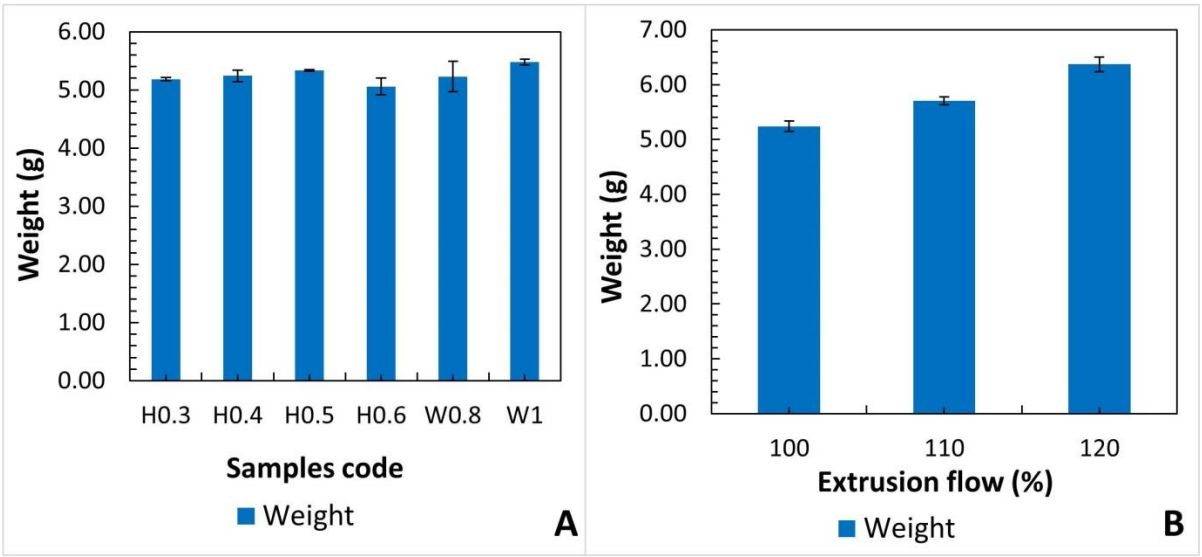

Figure 5-19: Weight changes of printed samples when changing (A) printing parameters and (B) extrusion flow.

On the other hand, when fixing the printing parameter and increasing the extrusion flow by 10% and 20%, we can notice that the extruded weight per sample increased accordingly by 9% and 21% which proves the accuracy of the calibration of the extrusion head.

5.4.2 Effect of 3D printing parameters on mechanical performances

The influence of the main extrusion settings on the mechanical performances and the morphology of the fractured sample was assessed. To do so, as detailed in chapter 2, different flexural bars were printed by varying the layer height, the road width, the extrusion flow, and the raster angle while keeping the rest of the parameters fixed such as the nozzle size and the printing speed. The layer height, the road width, and the extrusion flow ranged from 0.36 to 0.65 mm, 0.72 to 1 mm, and 100 to 120%, respectively. Meaning that the layer height values vary from 50% to 90% of the nozzle diameter (H%) and the road width values vary from 100% to 150% of the nozzle diameter (W%).

5.4.2.1 Layer height effect

In the literature, the effect of layer height is not clearly understood and contradictory results can be found of whether the layer height has an effect on mechanical performances and which proportionality there between these values. Many studies were conducted with different printing techniques and parameters and some authors found that an increase in layer height increases the mechanical properties and some others found the contrary. Moreover, it was stated that the layer height can have a different effect on flexural and tensile performances (Vaezi and Chua, 2011) and might change by changing the printing parameters such as raster angle, the building orientation or even the flow rate (Chacón et al., 2017). These different results are caused by the absence of a common methodology to assess printed parts strength when modifying printing parameters (Kuznetsov et al., 2019).

In the case of our study, as one can notice in Figure 5-20, the variation of the ultimate bending strength and flexural modulus in the range of layer thickness H% = {50, 65, 80, 90} % were negligible. Nevertheless, one can notice a slight increase in the flexural performance when decreasing the layer height which might be due to a better binding of layers due to filament squeezing. This slight increase of the flexural strength can also be due to a more oval filament (less circular) as we can see on the SEM images in Figure 5-21 which limits the 'triangular' inter filament porosity. The difference in the porosity cannot be quantified because of a high intrinsic porosity generated by the water evaporation during the curing process and the presence of air bubbles embedded in the fresh paste. The layer height is directly related to the number of printed layers for a given object and hence to the

printing time which should be minimized. Therefore, from a mechanical point of view, the effect of layer height can be neglected and a larger layer can be preferred for the printing of this material. Moreover, when decreasing the printing layer height the squeezing of the layer against each other can increase the printing force on the already-printed fresh object which might cause the deformation of the object especially when printing objects with a high form factor. However, one should keep in mind that the decrease in layer height is recommended to print objects with overhangs in order to increase the section of the filament supported by the previous layer (Thibaut et al., 2019).

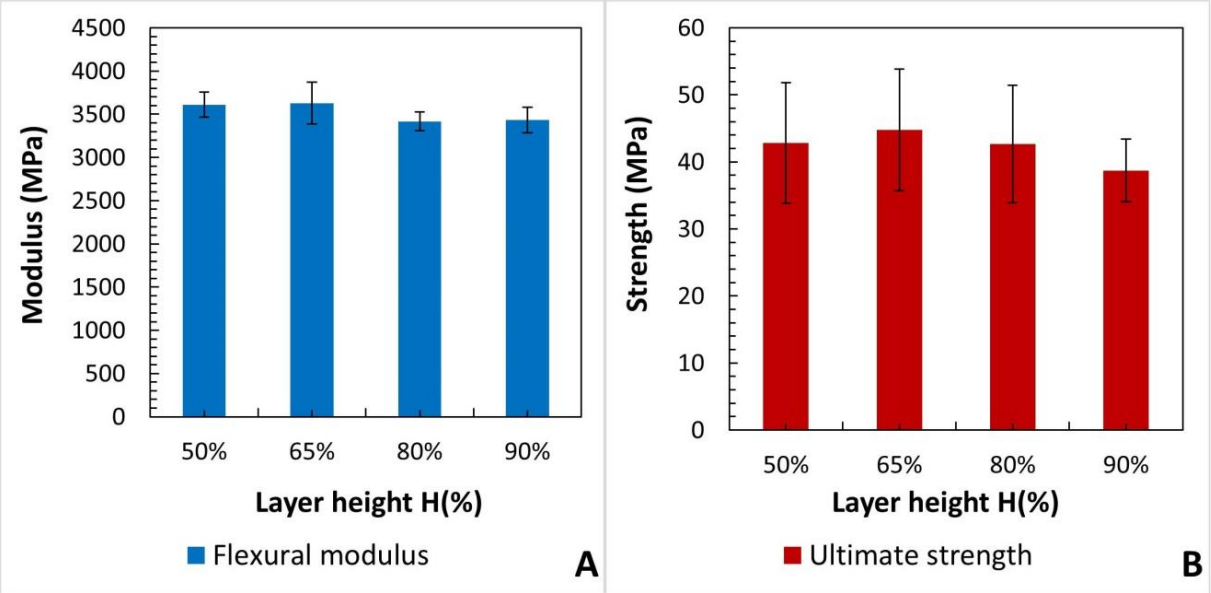

Figure 5-20: Effect of layer height on the mechanical performances of printed bars. (A) Evolution of flexural modulus as function of layer height. (B) Evolution of the ultimate flexural strength as function of the layer height.

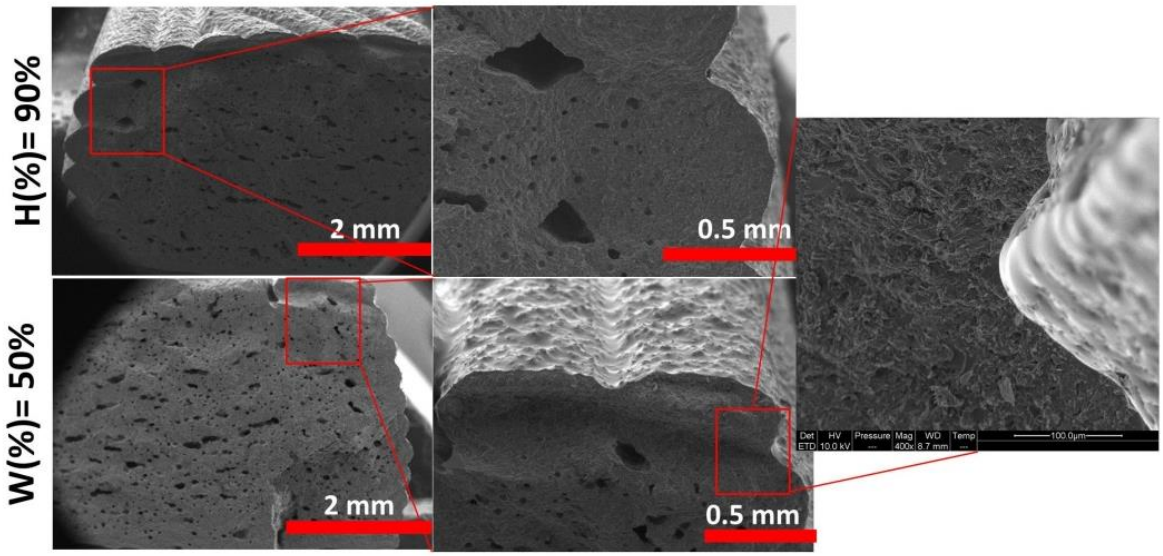

Figure 5-21: SEM images of a fracture surface of bending specimens with a layer height of 0.65 mm (top) and 0.36 mm (below) printed with road width of 0.72 mm and 100% extrusion flow and with 45° infill raster angle.

5.4.2.2 Road width effect

Road width is another parameter that interested many researchers. Similarly to the layer height, the effect of this parameter on mechanical performances of a printed specimen can be different from one study to another and its effect can be related to many other printing parameters such as raster angle and air gap between roads. When printing with thermoplastics by FFF technique, it is usually advised to increase the printing width by at least 10% because of the die-swallow phenomenon of the thermoplastic at the outlet of the nozzle. But this phenomenon is not applied to the extrusion of the developed paste where the extruded filament has the exact diameter of the used nozzle. However, when increasing the road width, the slicer will automatically increase the extrusion flow rate to fulfill the programmed road dimensions which might decrease the printing time. However, the effect of this parameter on the mechanical performance is unknown when fixing the other printing parameters (H%=65%, raster angle=45°, extrusion flow=100%).

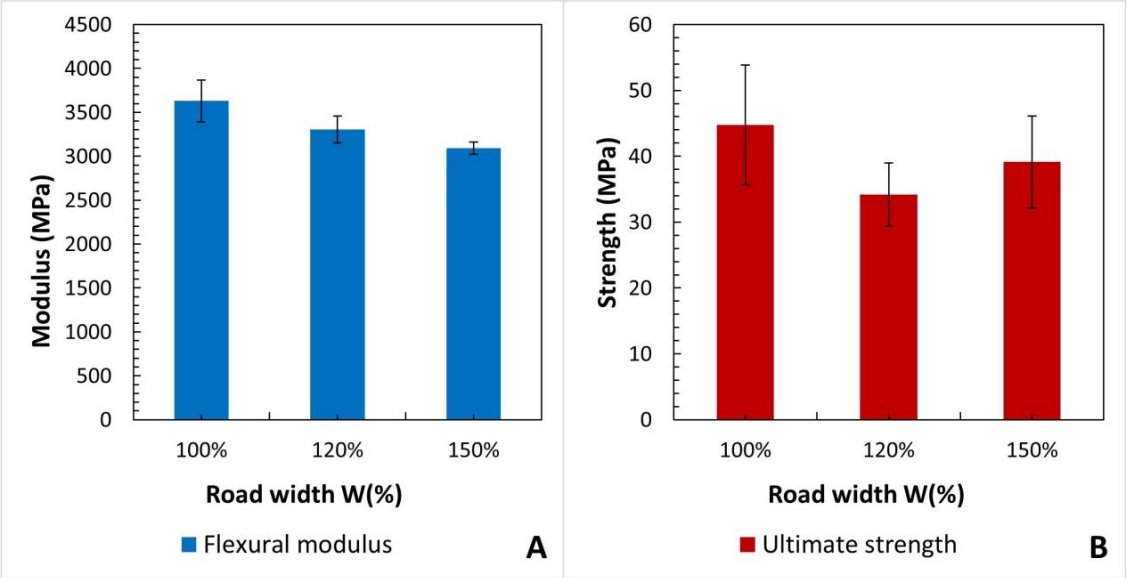

Figure 5-22: Effect of layer height on the mechanical performances of printed bars. (A) Evolution of flexural modulus as a function of layer height. (B) Evolution of the ultimate flexural strength as a function of the layer height.

In Figure 5-22, one can notice that the Flexural modulus decreases when increasing the road width, whereas the ultimate strength decreases when W% increases to 120% and then increases again when W% reaches 150%. However, this difference is marginal considering the errors of the values. The eventual increase in the flexural performances of the specimens can be explained by a higher inter-filamentary and intra-filamentary porosity for the samples with high road width compared to the lowest road width, as we can see on SEM images in Figure 5-23. This increase of porosity might be due to a more difficult water evaporation in thicker filaments or also to the fact that the extrusion flow was not enough to reach the programmed road width which is 50% larger than the nozzle size. Overall, when printing the developed paste is preferred to use a road width equal to the nozzle size.

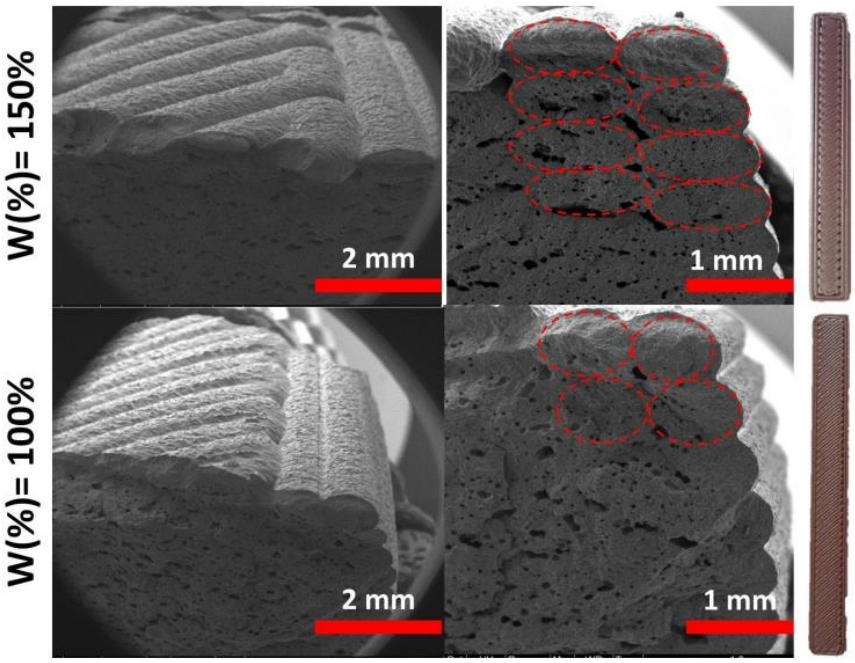

Figure 5-23: SEM images of a fracture surface of bending specimens with a road width of 1 mm (top) and 0.72 mm (below) printed with a layer height of 0.47 mm and 100% extrusion flow and with 45° infill raster angle.

5.4.2.3 Extrusion flow effect

The extrusion flow is calculated and regulated by the slicer for a set of given printing parameters (layer height, road width, and printing speed) thanks to the extrusion multiplier α to match with the real flow supplied by the screw extruder. An extrusion flow of 100% corresponds then to an extrusion multiplier equal to α value previously calculated, which is 2.13 for the used printing parameters. The extrusion flow was increased to 110% and 120% (extrusion multiplier, in this case, is respectively 1.1α and 1.2α) in order to assess its impact on the mechanical performances. As shown in Figure 5-24, there are no significant changes in the stiffness of the printed sample when increasing the extrusion flow. However, the ultimate strength slightly increases by 14% when increasing the extrusion flow from 100% to over 110%. This minor increase is believed to be due to the decrease of the inter-filamentary porosity which was filled with the 10% excess of extruded paste. However, when the extrusion reaches 120% we notice signs of over-filling of the sample and a 'swallowing' of the printed bar as one can notice in Figure 5-26. The calibration of the extrusion is then accurate and permits a proper filling of the prints. In order to optimize the mechanical performances of 100% filled prints it is possible to increase the extrusion to 10%, however to maintain the shape fidelity of the object the extrusion flow should not exceed 110%.

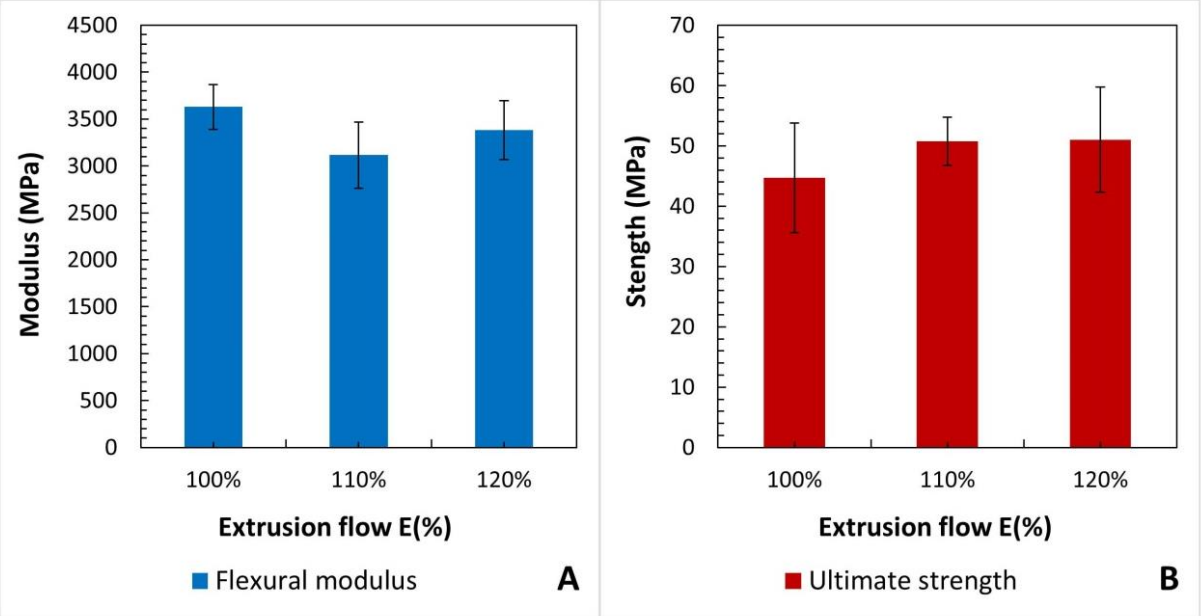

Figure 5-24: Effect of the extrusion flow on the mechanical performances of printed bars. (A) Evolution of flexural modulus as function of extrusion flow. (B) Evolution of the ultimate flexural strength as function of the extrusion flow

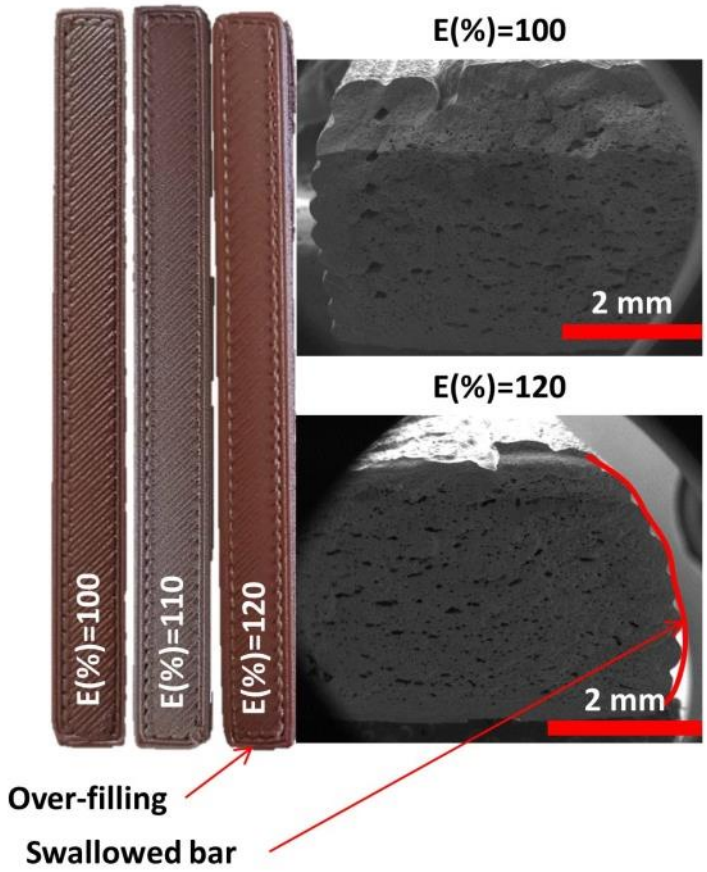

Figure 5-25: Photos of printed bending bars with extrusion flow ranging from 100% to 120%.

5.4.2.4 Raster angle effect

Raster angle is one of the most important parameters of 3D printing which makes the printed object highly anisotropic. Most of the work in the literature agreed that a raster angle of 90° (in the load direction) provided the best mechanical performances as the printed filaments are in the direction of the load. Moreover, when printing composites with high-aspect-ratio fillers, the anisotropy of the material is even magnified. To assess the anisotropy of the printed composites in the present work, the flexural performances of bars printed with a raster angle of 90° and 0° are compared. It is worth highlighting that in bars printed with a raster angle of 0°, the load is perpendicular to the oriented filaments and parallel to the inter-filamentary interface. As one can observe in Figure 5-26, the flexural modulus along the printing direction is slightly higher than the modulus measured on samples with raster printed at 0°, which can probably be due to the effect of the shear-induced cellulose particles or to an imperfect inter-filamentary adhesion in the bars printed at angles 0°. However, in terms of flexural ultimate strength, no significate difference can be detected between the bars printed in both directions except for a higher dispersion in the values of the strength obtained when the load is in along the printing direction. The ultimate strength in the printing direction could reach 50 MPa with an average of 41 MPa.

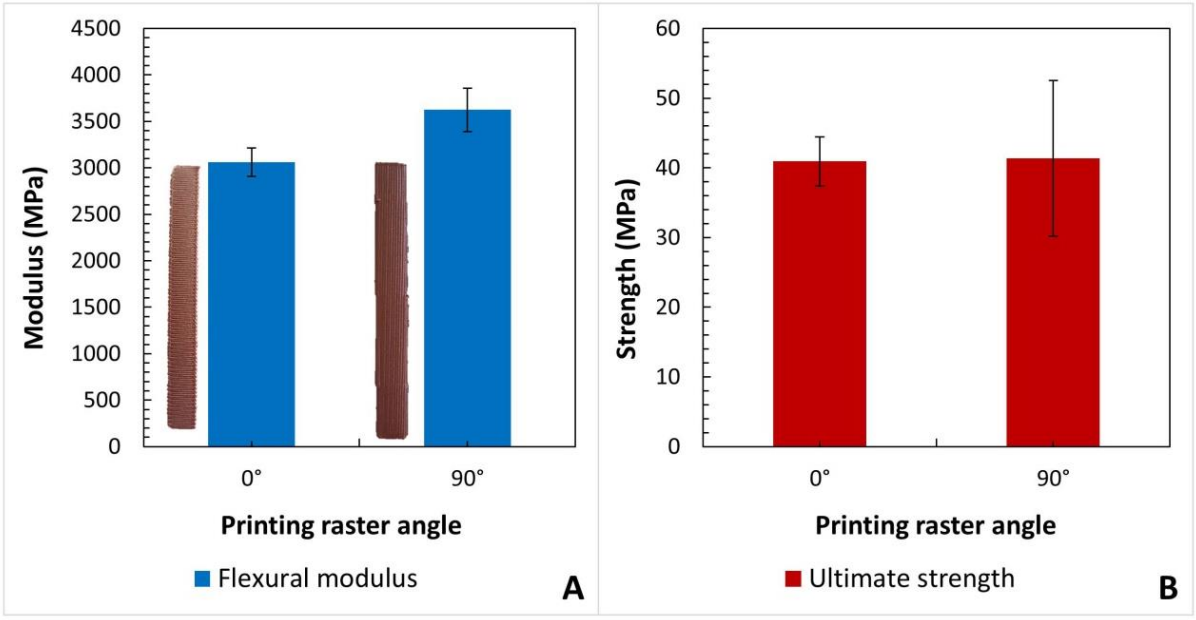

Figure 5-26: Effect of raster angle on the flexural modulus (A) and the ultimate strength (B).

On SEM images of the fractured cross-section in Figure 5-27, no significant difference can be detected between the two specimens except for a slightly more important pore size which seems to be propagated across the surface which might be a sign of a poor layer adhesion in the core of the

specimen. However, when zooming on the edge of both specimens, the inter-layer adhesion seems to be adequate with no signs of delamination. The water evaporation during curing is therefore the main responsible for the cracks embedded between the layers which might be the reason behind the slight decrease in stiffness.

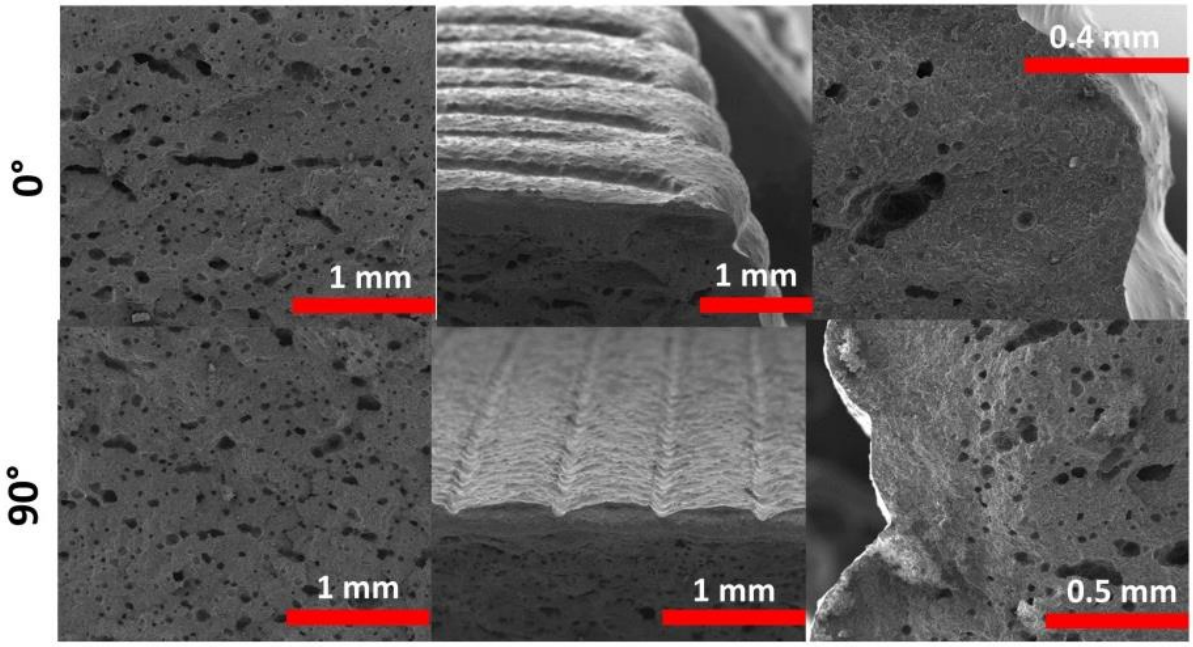

Figure 5-27: SEM images of a fracture surface of bending specimens with a raster angle of 0° (top) and 90° (bottom).

The equality in the strength of both types of specimens suggests also that there is no effect of particles alignment along the raster direction. Usually, the alignment of the particles is proportional to the shear rate ($\dot{\Upsilon}$) applied on the extrudate which also depends on the nozzle size (R) and type, and the extrusion rate as suggested by Rabinowitsch–Mooney in equation (eq 44) where Q is the volume flow rate and n is the thinning exponent of the shear-thinning material. A filament was extruded using a large nozzle of 1 mm and a more restrictive nozzle with 0.5 mm diameter with a low and high extrusion rotation speed of respectively 25 and 275 rpm (which is directly correlated with extrusion flow rate).

$$\dot{\gamma} = \frac{4Q}{\pi R^3}\left(\frac{3n+1}{4n}\right) \qquad \textit{eq 44}$$

When extruding with the large nozzle, Figure 5-28 shows the presence of pores in the core of the filament, whereas nearly no pores are observed in the first 150-200 µm below the filament surface.

This pores distribution was associated to an effective vapor degassing close to the filament surface and vapor segregation in the filament core. Particles seem to be randomly oriented with no clear orientation in the extrusion direction as we can see on the surface of the filament in the zoomed image on the cross-section where one can notice that some of the cellulose fibers are parallel to the surface of the fractured region and some of them are even broken transversally which can explain the isotropy of the resulting material. No difference was noticed when increasing the extrusion flow rate except of a slight decrease in the porosity but this difference is marginal.

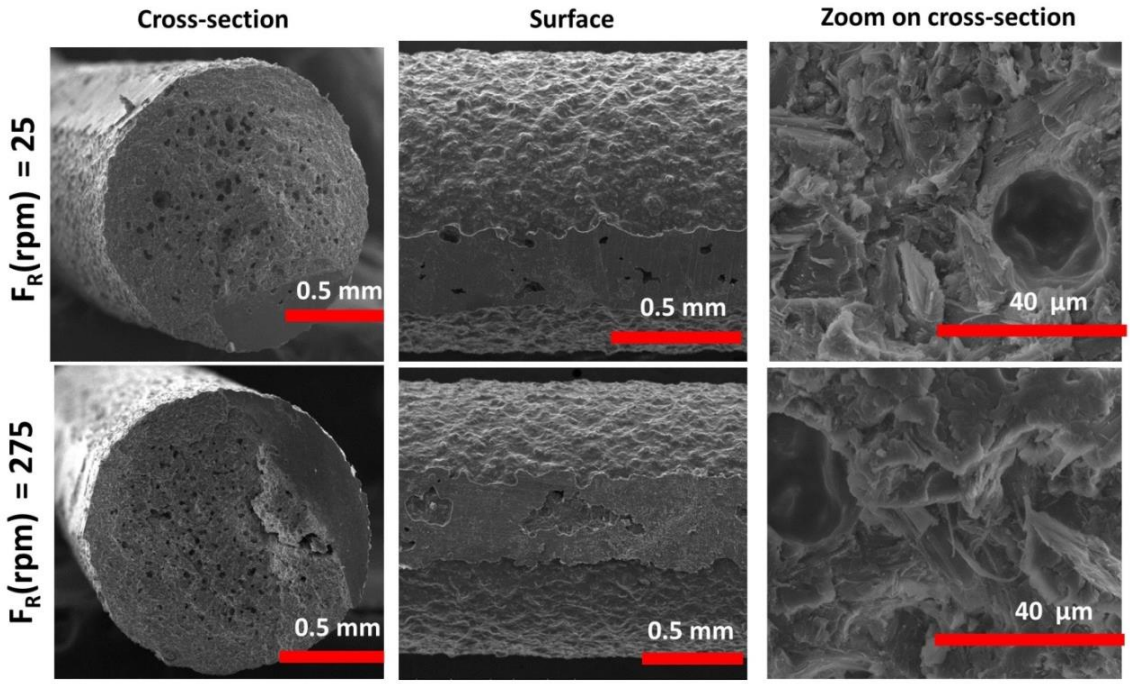

Figure 5-28: SEM images of an extruded filament through 1 mm nozzle with two different levels of extrusion flow rate.

Whilst for the filament extruded with a 0.5 mm nozzle, the first change one can notice is the decrease in the porosity of the filament, which is due to the decrease in the thickness of the filament which facilitates the water evaporation and degassing during the curing phase. In terms of particles alignment, no effect could be noticed as one can see in Figure 5-29, when further increasing the shear rate, the surface of the filament displays the same roughness with no visible alignment, as confirmed by the zoomed observation on the cross-section. This non-alignment of cellulose particles is not surprising as the aspect ratio of the used particle is limited. However, in the case of the addition of a larger fraction of longer fiber, the anisotropy of the printed object should be taken into consideration.

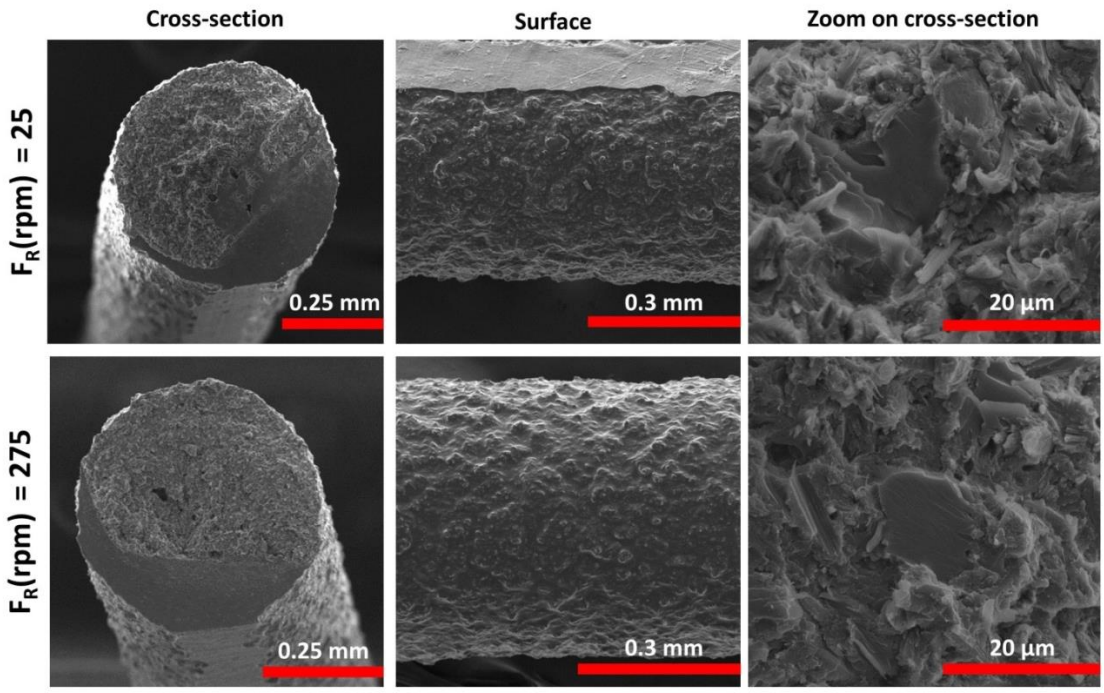

Figure 5-29: SEM images of an extruded filament through 0.5 mm nozzle with two different levels of extrusion flow rate.

5.4.3 3D printing quality and limitations

Printing with DIW, as highlighted before, can be very restrictive and limiting as for the printable forms, the infill level, the maximum height, and the resolution. Therefore, the printability of the spanning structure with a low infill was inspected using the optimized paste formulation (PFA-Cell28-B). Moreover, the maximum printing height was also evaluated using the current printing process.

5.4.3.1 Spanning structure and infill

As already explained in chapter 4, the printability of the spanning structure was assessed (James E. Smay et al., 2002) by determining the minimum G' required for printing a spanning structure with a filament deflection inferior to 0.05D, where D is the filament diameter. Therefore, the normalized maximum span distance(s) can be calculated for a known value of G' by rearranging eq 12 (eq 45) with (s=d/D). For printing the paste with a storage modulus of 0.2 MPa, the density of 1.46 g/cm^3 and nozzle diameter of 0.72 mm, the maximum span distance with a deflection inferior to 5% is ~1.45 mm. Nevertheless, it is possible to print span distance up to 10 mm if deflection is accepted until 25%. As one can see in Figure 5-30-A, the freshly printed filament was only slightly deflected between the edges of the support when reaching a span distance of 10 mm.

$$s^4 = \frac{G'}{1.4 \cdot \rho \cdot g} \qquad \text{eq 45}$$

Furthermore, to assess the performance of the spanned structure, a two-layer circular grid was printed with different infill levels ranging from 10% to 80% which corresponds to a span distance ranging from <0.1 mm to 6 mm. In line with the theoretically calculated span distance, the best-spanned structure with the best quality was obtained when the span distance was inferior to 2 mm which corresponds in our case to 40% rectilinear infill. Moreover, to investigate the effect of the extrusion flow on the quality of the spanned structure, the extrusion flow was decreased by 10% in order to possibly enhance the spanned structure. As one can see in Figure 5-30-B, this caused either a break of the extruded filament because of the under-extrusion or a very thin deposited filament that does not correspond to the nozzle diameter. Therefore, when printing spanned structure, it is preferred to not exceed a spanning distance with a deflection percentage that does not exceed a maximum of 5% of the nozzle's diameter which can be estimated using eq 45. It is important to highlight that this distance is proper to every printing parameter, and printed paste.

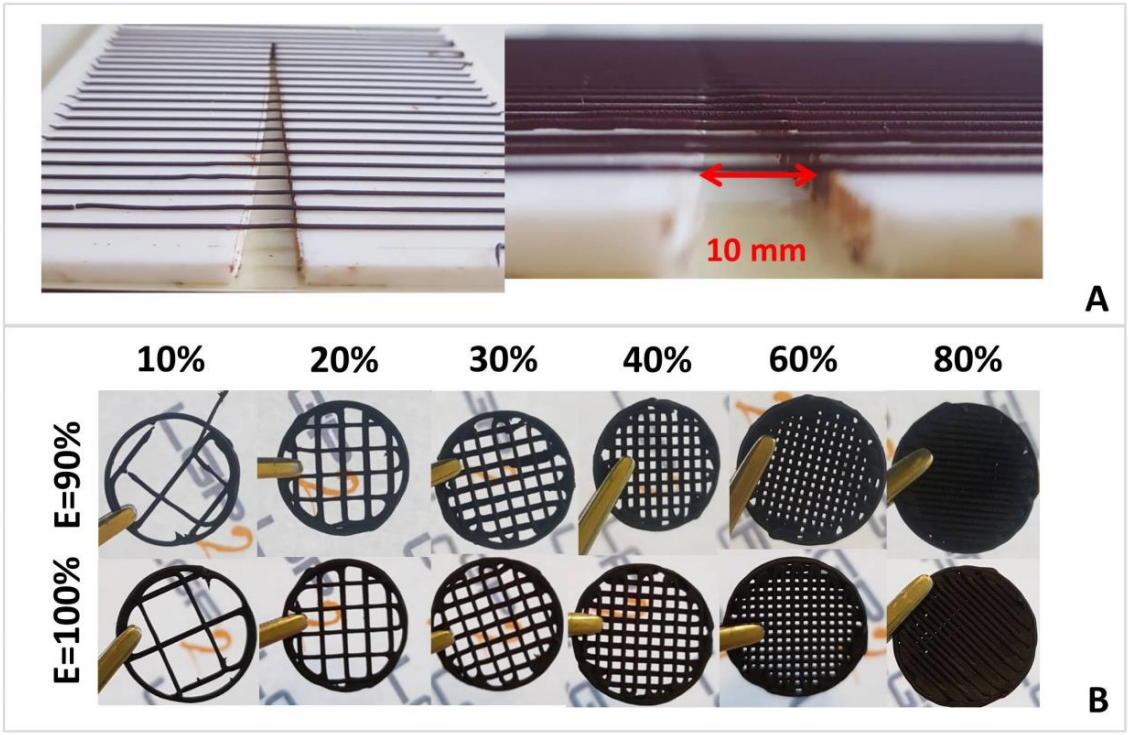

Figure 5-30: Visual assessment of the spanning structure quality (A) printed filament on plastic support with triangular-shaped hollow part (B) circular spanning structure with different infill percentages.

By the same token, the printability of these spanning structures was evaluated on 3D objects by stacking multiple layers and assessing the shape fidelity and the overall stability of the printed part.

To do so, towers with a base of 20 mm² and height ranging from 25 mm to 60 mm were printed with 40% infill and with no surrounding contour. As one can notice in Figure 5-31 when reaching a height of 25 mm the printed structure was neat and stable with no noticeable defects. When reaching 50 mm the structure was still dimensionally stable and the span structure was also neat as we can see on the top view. But we can notice that the tower is slightly tilted because of the stress exerted on the freshly printed part during the transfert to the oven. When reaching 60 mm, the structure collapsed during the travel as well, nevertheless, the tower was not stable and was continuously moving during the printing because of the force applied by the moving nozzle which created many printing defects. As explained in chapter 4, the maximum height, which can be supported by the fresh paste without collapsing under its weight, can be estimated using eq 46. The maximum height (H_{max}) is estimated to be around 55 mm when printing with the optimized ink. These results are in agreement with the observations done previously.

When the form factor of the printed part exceeds 2, destabilization can take place because of the printing forces and also the displacement at the end of the printing process. When curing ex-situ, is preferred to not exceed a form factor of 2 and to let the object dry in the open air at room temperature to increase its stiffness before displacing it.

$$H_{max} = \frac{\tau_y}{\rho \cdot g} \qquad \textit{eq 46}$$

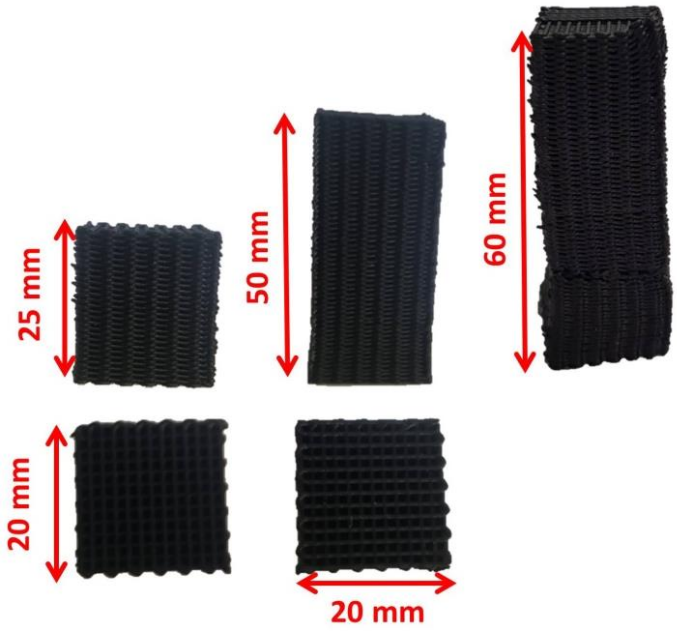

Figure 5-31: Printed tower of spanned structure with 40% infill with no supporting shell with height ranging from 25 mm to 60 mm.

5.4.3.2 Complex structures and printing limitations

Printing by direct ink writing or also referred as to DIW presents different challenges than printing thermoplastics by fused filament fabrication. These challenges are mostly related to the latent solidification when printing thermosets as in our case. Indeed, deposing an N^{th} layer on top of a soggy N-1 layer can cause many issues and limits the possible printing forms and features. For instance, bridging and overhangs can be particularly challenging with the current rheological performances of the paste which is commonly reported by other authors when printing thermoset-based inks where we can rarely see any printed complex structures. However, the printability of more complex parts as shown in Figure 5-32 was possible and successful such as the ring with a low overhang angle, a thin-walled vase (2 shells) with detailed textures. Nevertheless, several printing defects can be detected. Indeed, a distinct mark of z-seam when the nozzle starts a new layer can be observed in Figure 5-32 (photo on the left). This defect is not particular to the printed paste and is a classic issue that can be faced when printing thermoplastics as well, but this issue can be widened when the sticky filament sticks to the nozzle tip when changing positions especially at higher acceleration values. This same phenomenon affected also the quality of corners when printing rectangular objects where the corner get round which is a common challenge when printing with the DIW technique (Feilden, 2017a; Thibaut et al., 2019). Furthermore, the air bubbles embedded during the mixing and the loading in the cartridge caused the filament (road) to break as one can notice in Figure 5-32 (photo on right).

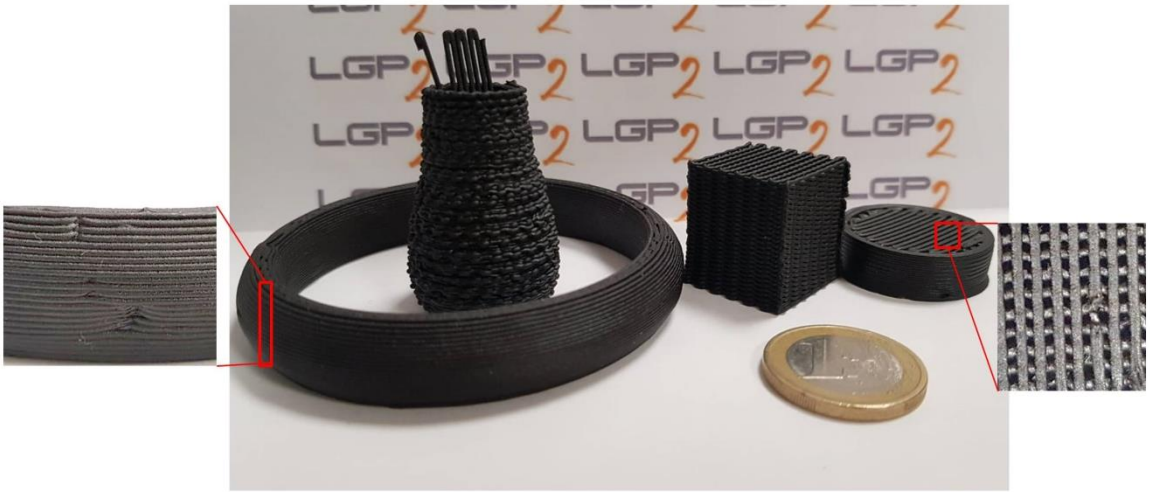

Figure 5-32: A selection of printed objects with a zoom of broken filament on the right and visible z-seam of the left.

Interestingly, the delamination issue classically faced when printing with thermoplastic polymers and especially technical filaments such as PEEK, was not noticed when printing with the developed paste. Indeed the layers are perfectly merged as highlighted before in SEM observations and as we can

notice on the printed object. This good adhesion is particularly interesting for the first-layer adhesion on the printing bed and also for good adhesion with an eventual bi-material support printing.

Warping is another issue when printing with thermoplastics with high Tg, which is caused by an uneven crystallization of the different layers caused by a fast solidification of the first layers compared to the subsequent ones. Favorably, printing by DIW technique and curing ex-situ prevents this phenomenon despite an overall shrinkage of about 2% after curing. When curing in-situ, the curing kinetics should be slowed to prevent a fast shrinkage of the printed layers and by the same token prevent bubbles formation, as explained in the first part of this chapter. However, an arching effect can take place when curing ex-situ due to very fast solidification as one can notice in Figure 5-33. Indeed, when curing at a high temperature around 120°C for 2 hours and then at 200°C for 2 hours (cycle I) the fast curing causes warping of the extremities of the bar upwards whilst when curing at 70°C for 8 h then at 100°C for 2 hours to finally post-cure at 200°C for 2 hours (cycle II) no deformation was noticed on the bar which was straight as highlighted in Figure 5-33. This arching is believed to be due to the slower curing of the first layers which were in contact with the printing film support. Cycle II is therefore advised to avoid this distortion.

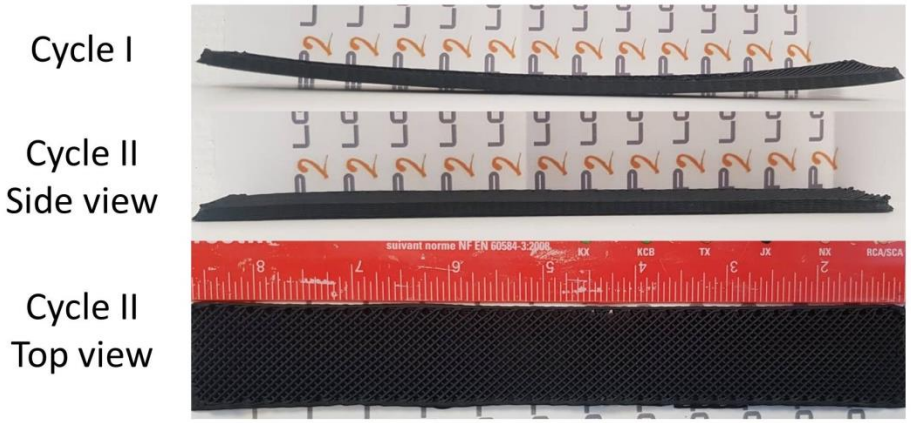

Figure 5-33: Arching of a printed thin bar when changing the thermal curing cycle.

5.4.4 Towards curing in-situ and more complex objects

Until present, the described 3D printer all along this work is a commercial FFF printer with a modified printing head which composition is detailed in chapter 2. This approach only allows an ex-situ curing of the printed object as the printer is not upgraded with a heating chamber. Moreover, the use of a commercially available high-temperature 3D-printing machine is not possible as there is a risk to solidify the paste in the nozzle. It was decided to develop a customized machine by collaborating with a 3D-printer fabricator *Qualup* (France) allowing a better printing quality of thermoset-based pastes revealed in Figure 5-34. This 130-kg-machine is made up of:

i. a heated chamber that can reach 270°C isolated with a hood.
ii. A moving printing head unit.
iii. a case to stock thermoplastic filament feedstock.
iv. an integrated computer serving as a control panel. The machine can be as well controlled with computer thanks to an installed rooter.
v. A fix printing bed of PEEK fixed with vacuum thanks to the action of an integrated vacuum pump.

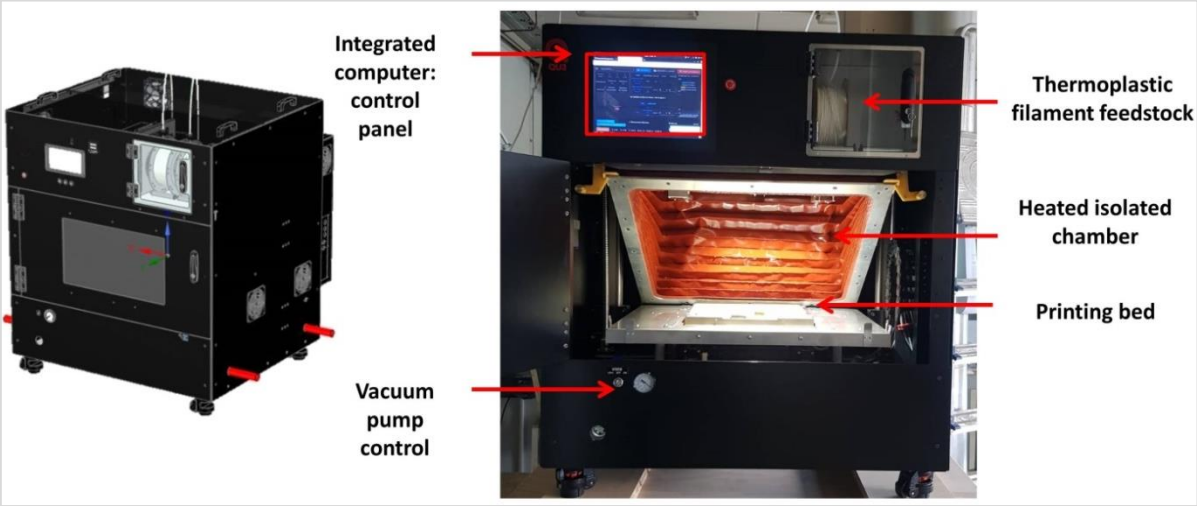

Figure 5-34: Developed personalized 3D printer for thermoset printing and curing in-situ fabricated by Qualup.

The printing unit is presented in Figure 5-35, which contains:

i. Wiping brushes to clean the nozzle before and after every printing and when needed after printing several layers to minimize the printing defects related to the filament drugged with the sticky nozzle.
ii. A video camera to inspect the printing process, especially of the first layer, since the printing chamber is isolated.
iii. A double extrusion head containing a FFF extrusion head and LDM extrusion can be switched thanks to a motion-balance system. The LDM extrusion head is similar to that used in this work and detailed in chapter 2 with minor changes in the connector shape between the cartridge and the extruder chamber for space management reasons. During the curing phase, the printing nozzle retracts towards a ventilated upper compartment to stay isolated thanks to a silicon sheath highlighted in Figure 5-34.

This 3D printer helps to overcome some of the printing issues discussed before such as structure collapsing during transport when curing ex-situ. Furthermore, the printing of higher objects can be improved by increasing the stiffness of the printed layers by initiating a partial-curing and evaporating the solvent in the fresh paste during printing. After printing a few layers the object can also be cured until its gel time by retracting the nozzle to the cold 'safe' zone to avoid any unwanted curing in the nozzle before continuing the printing. When adapting the second strategy it is important to only prime the curing to enhance the rheological properties of the paste without completing the curing to avoid any uneven shrinkage in the object. Furthermore, to print more complex features such as bridges and overhangs it is possible to use the FFF printing head to print support which will be eliminated at the end of the curing but the support should resist a curing temperature of at least 80°C.

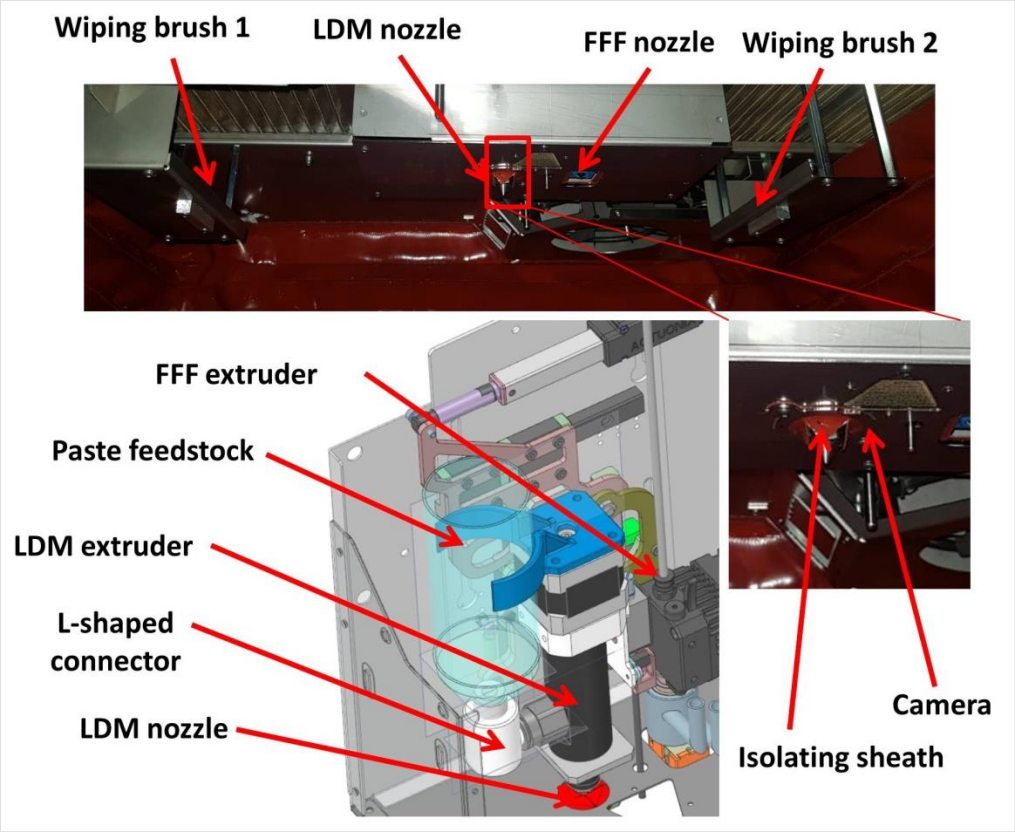

Figure 5-35: Composition of the printing unit and detailed composition of the LDM extrusion head.

The printability of the paste using the developed printer was tested after a recalibration of the extrusion flow because of the changes brought to the extrusion parameters. In Figure 5-36, one can see the results on a printed tube using a 1mm nozzle which demonstrates a good calibration of the extrusion flow and the printing parameters. The curing was done in-situ after the printing step.

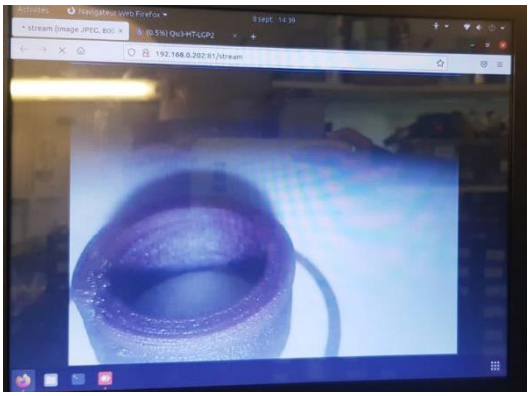

Figure 5-36: Freshly printed tube observed on the control panel screen thanks to the installed camera.

5.4.5 Conclusions

In this part of the chapter, the printing process was optimized and closely studied to obtain accurate 3D printing. Successful printing of the object can only be obtained when mastering first the extrusion flow which has to be carefully calibrated and then the printing parameters have to be adapted to the object form, required performances and the used material. Accordingly, the extrusion flow was first calibrated by determining an extrusion multiplier which we called α. This calibration factor changes when changing extrusion parameters such as the nozzle's size and shape, the extrudate rheology, and the extrusion head settings. This calibration factor permitted accurate printing with a good calibration of the extrusion flow when changing printing parameters. By the same token, the effect of printing parameters such as layer height, road width, extrusion flow, and raster angle on mechanical performances was evaluated and we concluded that:

i. A thick printing layer might slightly decrease the composite strength because of an increase in the inter-filamentary porosity.
ii. Wide printing roads might deteriorate the mechanical performance which is believed to be caused by an insufficient extrusion flow.
iii. Extrusion flow has little effect on mechanical performances but for more compact bulk objects it is possible to increase by 10%. An increase of more than 10% will cause an over-filling effect which should be avoided.
iv. The raster angle had the most effect on the mechanical performances by enhancing the stiffness when the load was applied along the printing direction. However, the effect remains limited compared to other printed materials which suggest a good inter-filamentary cohesion.

Overall, the effect of all printing parameters was little on mechanical performances, thus these parameters should be optimized according to the object morphology and requirements. The average flexural modulus of the tested printed specimen ranged from 3 to 3.5 GPa and its ultimate strength was between 40 and 50 MPa.

Furthermore, the printing of different objects with relatively simple form was possible with some defects caused by the sticky nature of the paste, and the instability of the fresh prints during the curing step. To overcome these challenges, a customized printing machine was designed for ex-situ curing and bi-material printing, allowing thusly the printing of more complex objects.

5.5 Chapter Conclusions

At the outcome of this last chapter, the printing and curing process of the developed ink formulation are more understood which allowed a better optimization of the printing quality and material performances. First, 5 wt% of latent catalyst was fixed for an adequate crosslinking reaction of the resin and it was found that cellulose has little to no effect on the crosslinking reaction. Based on these findings, an understanding of crosslinking evolution was attempted when adding 5 wt% catalysts under different temperatures. It was found that the curing rate was proportional to the curing temperature. On the other hand, it was demonstrated that curing at high temperatures causes foaming and bubble formation in the material which should be avoided. Hence, curing at lower temperatures is privileged. Accordingly, the following curing program was recommended:

1. Pre-curing stage: evaporate water at a temperature lower than 90°C until reaching gel point;
2. Curing stage: reach high crosslinking degree under 90°-100°C allowing the manipulation of the printed object;
3. Post curing stage: maximize the crosslinking of the polymer under 150°C-200°C.

The pre-curing temperature can be increased for a faster solidification for an object with low infill as they dispose of a thin wall facilitates the water evaporation and hence limiting the foaming risk.

The extrusion step was optimized by calibrating the printing head to match the extrusion flow calculated by the slicer. This calibration was done by defining an extruding multiplier which is specific for every extrudate, nozzle shape, nozzle size, and feeding rate. The optimized extrusion flow guaranteed an accurate road deposit and neat printing quality.

Furthermore, the effect of layer height, road width, raster angle, and extrusion flow on mechanical performances was addressed. It was found that these parameters have no significant effect on the mechanical properties of the tested specimens. However, it is recommended to limit the layer thickness, not exceed the nozzle size for the road's width, and to increase by a maximum of 10% the extrusion flow to guarantee an optimized printing quality and mechanical performance. The inter-layer and inter-filamentary adhesion were shown to be optimum which discarded the delamination issues. The printed specimens exhibited a flexural modulus ranging from 3 to 3.5 GPa and ultimate strength between 40 and 50 MPa.

Finally, the printing quality of the developed material was demonstrated to be adequate for the fabrication of simple and relatively more complex objects. Nevertheless, several defects and limitations in the printing of this material were relieved what motivated the idea to develop a customized printer for thermoset-based materials.

5.6 References

Chacón, J.M., Caminero, M.A., García-Plaza, E., Núñez, P.J., 2017. Additive manufacturing of PLA structures using fused deposition modelling: Effect of process parameters on mechanical properties and their optimal selection. Mater. Des. 124, 143–157. https://doi.org/10.1016/j.matdes.2017.03.065

Domínguez, J., Madsen, B., 2015. Development of new biomass-based furan/glass composites manufactured by the double-vacuum-bag technique. J. Compos. Mater. 49, 2993–3003. https://doi.org/10.1177/0021998314559060

Domínguez, J.C., Grivel, J.C., Madsen, B., 2012. Study on the non-isothermal curing kinetics of a polyfurfuryl alcohol bioresin by DSC using different amounts of catalyst. Thermochim. Acta 529, 29–35. https://doi.org/10.1016/j.tca.2011.11.018

Feilden, E., 2017. Additive Manufacturing of Ceramics and Ceramic Composites via Robocasting. https://doi.org/10.13140/RG.2.2.29343.25765

Gaisford, S., Kett, V., Haines, P., 2019. Principles of Thermal Analysis and Calorimetry. Royal Society of Chemistry.

Guigo, N., Mija, A., Vincent, L., Sbirrazzuoli, N., 2007. Chemorheological analysis and model-free kinetics of acid catalysed furfuryl alcohol polymerization. Phys. Chem. Chem. Phys. 9, 5359–5366. https://doi.org/10.1039/B707950H

Guigo, N., Mija, A., Vincent, L., Sbirrazzuoli, N., 1386. Chemorheological analysis and model-free kinetics of acid catalysed furfuryl alcohol polymerization. Phys. Chem. Chem. Phys. 9, 5359–5366. https://doi.org/10.1039/B707950H

Harsch, M., Karger-Kocsis, J., Holst, M., 2007. Influence of fillers and additives on the cure kinetics of an epoxy/anhydride resin. Eur. Polym. J. 43, 1168–1178. https://doi.org/10.1016/j.eurpolymj.2007.01.025

Iroegbu, A.O., Hlangothi, S.P., 2018. Effects of the Type of Catalyst on the Polymerisation Mechanism of Furfuryl Alcohol and its Resultant Properties. Chem. Afr. 1, 187–197. https://doi.org/10.1007/s42250-018-0017-5

Kuznetsov, V.E., Tavitov, A.G., Urzhumtcev, O.D., 2019. Hardware Factors Influencing Interlayer Bonding Strength of Parts Obtained by Fused Filament Fabrication. https://doi.org/10.20944/preprints201905.0108.v1

Lopez de Vergara, U., Sarrionandia, M., Gondra, K., Aurrekoetxea, J., 2014. Polymerization and curing kinetics of furan resins under conventional and microwave heating. Thermochim. Acta 581, 92–99. https://doi.org/10.1016/j.tca.2014.02.017

Montserrat, S., Flaqué, C., Calafell, M., Andreu, G., Málek, J., 1995. Influence of the accelerator concentration on the curing reaction of an epoxy-anhydride system. Thermochim. Acta, Recent Advances in Thermal Analysis and Calorimetry 269–270, 213–229. https://doi.org/10.1016/0040-6031(95)02362-3

Ooi, S.K., Cook, W.D., Simon, G.P., Such, C.H., 2000. DSC studies of the curing mechanisms and kinetics of DGEBA using imidazole curing agents. Polymer 41, 3639–3649. https://doi.org/10.1016/S0032-3861(99)00600-X

Prado, J.R., Vyazovkin, S., 2011. Activation energies of water vaporization from the bulk and from laponite, montmorillonite, and chitosan powders. Thermochim. Acta 524, 197–201. https://doi.org/10.1016/j.tca.2011.06.005

Pranger, L., Tannenbaum, R., 2008. Biobased Nanocomposites Prepared by In Situ Polymerization of Furfuryl Alcohol with Cellulose Whiskers or Montmorillonite Clay. Macromolecules 41, 8682–8687. https://doi.org/10.1021/ma8020213

Sadler, J.M., Yeh, I.-C., Toulan, F.R., McAninch, I.M., Rinderspacher, B.C., La Scala, J.J., 2018. Kinetics studies and characterization of poly(furfuryl alcohol) for use as bio-based furan novolacs. J. Appl. Polym. Sci. 135, 46608. https://doi.org/10.1002/app.46608

Seyedlar, R.M., Imani, M., Mirabedini, S.M., 2016. Curing of poly(furfuryl alcohol) resin catalyzed by a homologous series of dicarboxylic acid catalysts: Kinetics and pot life. J. Appl. Polym. Sci. 133. https://doi.org/10.1002/app.44009

Smay, J.E., Cesarano, J., Lewis, J.A., 2002. Colloidal Inks for Directed Assembly of 3-D Periodic Structures. Langmuir 18, 5429–5437. https://doi.org/10.1021/la0257135

Thibaut, C., Denneulin, A., Rolland du Roscoat, S., Beneventi, D., Orgéas, L., Chaussy, D., 2019. A fibrous cellulose paste formulation to manufacture structural parts using 3D printing by extrusion. Carbohydr. Polym. 212, 119–128. https://doi.org/10.1016/j.carbpol.2019.01.076

Vaezi, M., Chua, C.K., 2011. Effects of layer thickness and binder saturation level parameters on 3D printing process. Int. J. Adv. Manuf. Technol. 53, 275–284. https://doi.org/10.1007/s00170-010-2821-1

General conclusions

The introduction section of this thesis highlighted a research gap in the development of thermoset biocomposites for additive manufacturing. Accordingly, the overarching goal of this thesis was to fill this gap by developing a new biomass-based thermoset composite that can be processed by Direct Ink Writing (DIW).

DIW of thermoset-based composite is a rather new 3D printing approach that can yield new materials with interesting properties and performances permitting to diversify the material panels for additive manufacturing. This approach was and still to this date underexplored. We also demonstrated a more thorough analysis of interests and approaches to printability when it comes to the use of bio-based sustainable thermosets in 3D printing than previous research in the field. What is more, this dissertation focused on understanding the effect of ink's formulation on its rheology and subsequently its printability. Later, the effect of different process parameters (curing and printing parameters) on the printing quality and the material overall performances were studied. The findings of this work can be divided in two major sections whose main conclusions will be sumed-up below.

Overall conclusions

Biocomposite formulation and characterization

At the outset, the characterization of the commercial PFA resin and cellulose powder used in the thesis project was carried out. The characterization revealed that the used cellulosic fillers are micro-sized rod-shaped chemically inert particles. As for the thermosetting polymer, it was proposed that the oligomer is a sequence of an average of 2 to 5 furan rings connected predominantly by ether bridges and ending with hydroxyl groups.

Once the main characteristics of raw material were known, the next step was the formulation of a printable ink for additive manufacturing which was detailed in *Chapter 4*. This chapter was divided into two main parts, the first dealing with the development and characterization of structural material and the second addressing the possibility to develop a conductive ink. The optimized structural ink formulation contains 25 to 28 wt% cellulose powder with PFA matrix which exhibited shear-thinning behavior, high yield stress, and thixotropic behavior thus making it compatible with DIW. By the same token, the ensuing cured composite was characterized. The stiffness of the composite increases when increasing cellulose load whilst the strength decreases, which is correlated with the porosity content in the casted specimens and is believed to be the reason behind the deterioration of the strength. Likewise, cellulose addition enhanced the thermomechanical properties with a 60% increase in storage modulus and enhanced stability at 200°C with less than 10% decrease in storage modulus. Cellulose additionally allowed a 40% decrease in the mold

shrinkage of the thermosetting resin. The physical and mechanical properties of this material are detailed in the datasheet provided below (p.282). As for the second part of the chapter, a formulation containing 4 wt% of short ultiwalled Carbon NanoTubes (CNT) and 15 wt% of cellulose powder was selected for an eventual printing of conductive material with electrical conductivity of at least 2 10^{-2} S/m. To further enhance the electrical conductivity, the carbonization of the two developed materials was tested which yielded an electrical conductivity of at least 4.7 10^{3} S/m when adding CNT.

Biocomposite 3D printing

The setup and optimization of the printing process was explained in *Chapter 5*. In the first part of this last chapter, the curing process of the used resin was investigated when adding 5 wt% of a latent catalyst using different analysis techniques such as DSC, DMA, and soxhlet extraction. It was determined that the curing rate was proportional to the curing temperature and so is the water evaporation rate. However, when curing at a high temperature (>100°C) the foaming and porosity risk is high whilst curing at a lower temperature (<100°C) hinders total evaporation of the solvent. Accordingly, a step-by-step curing process was suggested; starting with a pre-curing stage at a low temperature (<90°C) followed by a curing step at a temperature ranging from 90-100°C and ending with a post-curing stage carried out at a temperature between 150 and 200°C.

The second section of the same chapter was dedicated to a comprehensive study of the printing process of the optimized ink formulation. To do so, the extrusion step was optimized for accurate printing by identifying an extrusion multiplier specific for extrusion parameters (nozzle, material, extruder, feed rate, etc.). Once the extrusion step was successfully completed, the printing parameters' effect on printing quality and mechanical performances was analyzed. It was found that layer height, road width, and extrusion flow have little to no effect on the mechanical performances of the printed specimens. However, the stiffness in the printing direction was slightly higher than that measured perpendicular to the filament direction. Even so, the difference is marginal which showed a good inter-filamentary adhesion of the prints. This adequate adhesion was also visible on different printed objects. Nevertheless, several issues were pointed out in the printability of the developed material such as limited object printing height and aspect ratio because of the forces which may be applied during printing and transport on the fresh print. Furthermore, some of the complex features cannot yet be printed because of the delayed solidification step. To overcome these challenges, a customized 3D printer was developed for an in-situ-curing with the possibility of support printing.

Material performances- Datasheet

PROPERTIES

Designation	Units	Value
Commercial Trade Name	TBD	
Color	Brown - Black	
Maximum Use Temperature	°C	250
Temperature of Start of Degradation	°C	360 (TGA) 250 (DMA)
Flexural Modulus at 23°C	MPa	Bulk >4000 Printed > 3000
Modulus of Elasticity at 23°C	MPa	Bulk >2500 Printed TBM
Storage Modulus (DMA) at 23°C (In 3-Point Bending)	MPa	Bulk >4000
Storage Modulus (DMA) at 150°C (In 3-Point Bending)		Bulk >4000
Storage Modulus (DMA) at 200°C (In 3-Point Bending)	MPa	Bulk >3000
Density	g/cm^3	1,20-1,24 (bulk)
Max Porosity	%	11 (bulk)
Shrinkage	%	<2% (bulk)
Mass Loss at 100°C	%	5
Mass Loss at 200°C	%	5
Mass Loss at 300°C	%	6
Mass Loss at 400°C	%	30
Hygroscopic Behaviour	%	<1
Miscellaneous: The resin offers several interesting properties such as high stiffness, fire resistance, and chemical resistance to organic and inorganic acids. For material with high acid/base resistance, consideration should be given to replacing the organic filler with inorganic/inert filler.		TBM
Dielectric constant: variable, depending on water content and organic/inorganic filler		2-3

TBD: To Be Defined, TBM: To Be Measured

Printing recommendation

3D PRINTING PROPERTIES

3D Printing Technology	LDM (FDM-FFF adapted)	
3D Printing Capability	Medium (TBD)	
3D Printing Layer Adhesion	Good	
3D Printing Chamber Temperature	°C	23-100
3D Printing Crosslinking	°C	~130-160
Extrusion flow	%	100-110
Layer height	% of the nozzle's diameter	50-90
Road width	% of the nozzle's diameter	100
Harmful vapours released during 3D Print	Possible release of different alcohols traces *	
Harmful vapours released during cross-linking	Water vapor, traces of different alcohols *	

* Recommended extraction and filtration system.

Suggested curing thermal program

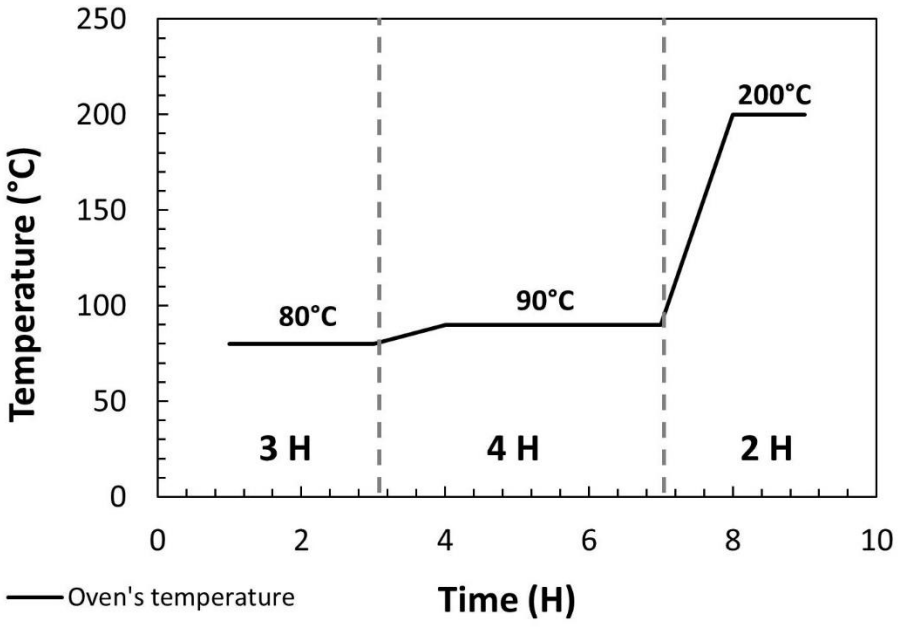

Perspectives and future work

Despite the progress attained in 3 years by transforming brainstormed concepts into a concrete product, many other ideas and approaches have been developed through a better understanding of the process and the material. A perspective of future work is given below.

1. Raw material

A decision has been made to use readily available commercial products as raw material during this project to focus more on formulation and process development. However, this choice limited the understanding of basic crosslinking mechanisms and the tuning of the product and formulations. Accordingly, it is recommended to:

- Use water-free PFA oligomers to reduce the issues caused by water evaporation.
- Use different types of catalysts with less water content.
- Use of cellulose fibers with a higher aspect ratio with better reinforcing-ability.

2. Ink formulation

<u>Structural ink</u>

The choice of a simple 3-component formulation was sought for as a base formulation. Now, one can envision the addition of additives to enhance this printable paste such as:

- Adding nanoparticles of clay or fumed silica to boost the rheological performances and thus the printability.
- Adding carbon nanofibers to increase the mechanical performances of the composite.
- Adding flame retardant agents to complement the low flammability and low smoke release of PFA matrix.

It is also possible to replace the used cellulose powder with cellulose micro/nanofiber which was already tested in the frame of an internship work in this project. The printability and extrudability of the developed paste were limited because of an insufficient dispersion of the nanofibers in the furanic resin. Therefore, in-situ mixing is conceivable in a twin-screw mixer. An overview of these findings is annexed to the present report.

Conductive ink

An increase in the CNT content to further increase the electrical conductivity of the ink can be tested without limiting its printability in restrictive nozzles. The replacement of cellulose fillers with higher carbon char material can be also conceived for a lower shrinkage upon carbonization.

Furthermore, the printability of the developed ink was not fully addressed. Accordingly, in future work, the printability of these inks should be further studied and the printing process should be optimized.

3. Process

The future work will be more focused on the optimization and the set-up of a reliable and stable printing process on the customized 3D printer.

Short term

A thermal camera will be installed for real-time monitoring of the temperature in the heated chamber, the printed layers, and the nozzle. This information will permit a better optimization of the in-situ curing to first avoid curing in-nozzle, to prime the crosslinking of the first layers while avoiding fast curing to ensure an adequate interlayer adhesion.

Moreover a larger 'ink cartridge' will be installed on top of the printer to enable the printing of bigger parts. A 'purge cartridge' will also be installed for a faster and more efficient extruder cleaning to avoid the paste crosslinking inside the system in the long run. The feeding system can be visualized in Figure C-0-1.

Long term

The manual loading of the cartridge should be optimized to avoid the embedding of air bubbles in the paste.

Printing of more complex parts should be tested with the use of a supporting printing material which can be eliminated after curing. This can be achieved thanks to the already installed FFF printing head.

The carbonization step should be more studied especially the carbonization of larger printed geometries. Characterization of the carbonized parts should be conducted especially to assess the mechanical performances of the carbonized material.

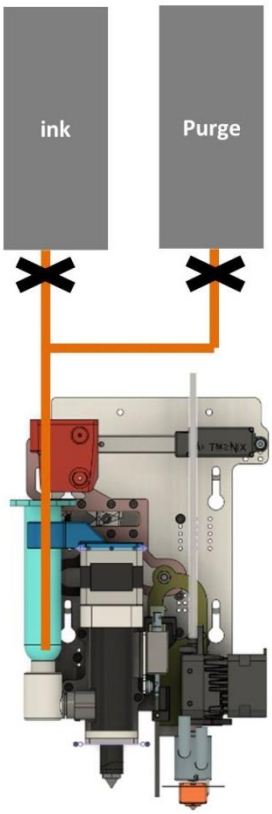

Figure C-0-1: Diagram of the Ink feedstock and purge system on the extruder head of the customized printer.

<u>To go further</u>

- Assessment of the composites' fire and chemical resistance can provide a better idea of their possible use and application.
- A deeper study of composite's thermal stability under different types of solicitation and different levels of load.
- Bi-material printing of both the PFA-based conductive ink and the PFA/cellulose paste can be done to yield a functional object.
- One cannot talk about a bio-based renewable material without thinking about its end of life. It is no secret that the crosslinking of thermosetting polymers is an irreversible reaction limiting its recyclability which was pointed out in the first chapter. The grinding of the

composite might be one solution to obtain a powder useful as filler in future formulations. Another conceivable solution is the synthesis of a furan-based copolymer with the use of bismaleimides to achieve a reversible crosslinking reaction at higher temperatures. The latter solution is currently being investigated in the frame of another Ph.D. project conducted with cooperation between the University of Grenoble and the University of Torino.

Scientific out-puts of the thesis

- *Patent*: Beneventi, D., Chaussy, D., Bouzidi, K., Gandini, A., 2021. Thermosetting Composite Material and Associated Printing Process.

- *Oral presentation in an international conference*: Bouzidi, K., Chaussy, D., Gandini, A., Beneventi, D. "3D printable fully biomass-based composite", EPNOE 2021, Nantes, France.

- *Oral presentation in an international conference*: Bouzidi, K., Chaussy, D., Gandini, A., Beneventi, D. "3D printing of biocomposite by cold material extrusion", addfabcomp 2021, Online.

- *Publication submitted to ASC Applied Polymer Materials*: Bouzidi, K., Chaussy, D., Gandini, A., Beneventi, D. "Development of biomass-based slurry for the manufacture of furan/cellulose composite by open air cast molding".

- *Publication submitted to carbohydrate polymers*: Bouzidi, K., Chaussy, D., Gandini, A., Bongiovanni, R., Beneventi, D. "3D printable fully biomass-based composite using poly(furfuryl alcohol) as binder and cellulose as a filler"

- *Publication in preparation*: Bouzidi, K., Chaussy, D., Gandini, A., Bongiovanni, R., Flahaut, E., Beneventi, D. "Bio-based formulation of an electrically conductive ink with high potential for additive manufacturing by direct ink writing ".

- *A Review paper in preparation*: Mohammed, Z., Shaqour, B., Bouzidi, K., Barnett, P., Hmeidat, N. "Progress in use of Sustainable Materials for Polymeric 3D Printing: Challenges and Future Perspectives".

List of figures

List of tables

Annex

This work was conducted in the frame of collaboration between Politecnico di Torino and Institut Polytechnique de Grenoble INP-Grenoble. The experimental part was entirely conducted in the laboratories of Grenoble INP (LGP2) during an internship gently founded by the host institution.

Objective: Evaluation of the possibility to produce a bio-composite using PFA resin along with in-lab produced Hemp MFC.

Hemp MFC production

Hemp bleached and pre-refined pulp was used to prepare to produce a highly concentrated MFC (>30 wt%). These micro-fibrillated cellulosic fibers were successfully produced with the use of the low energy consuming method Twin-Screw Extrusion. The followed process of MFC production is given in Figure A-0-1. The use of hemp as starting pulp is interesting in terms of the possible mechanical properties of the resulting MFC as well as in terms of sustainability and costs of the plant cultivation. Moreover, the high solid content of these fibers enables the possibility of using them as fillers in the PFA.

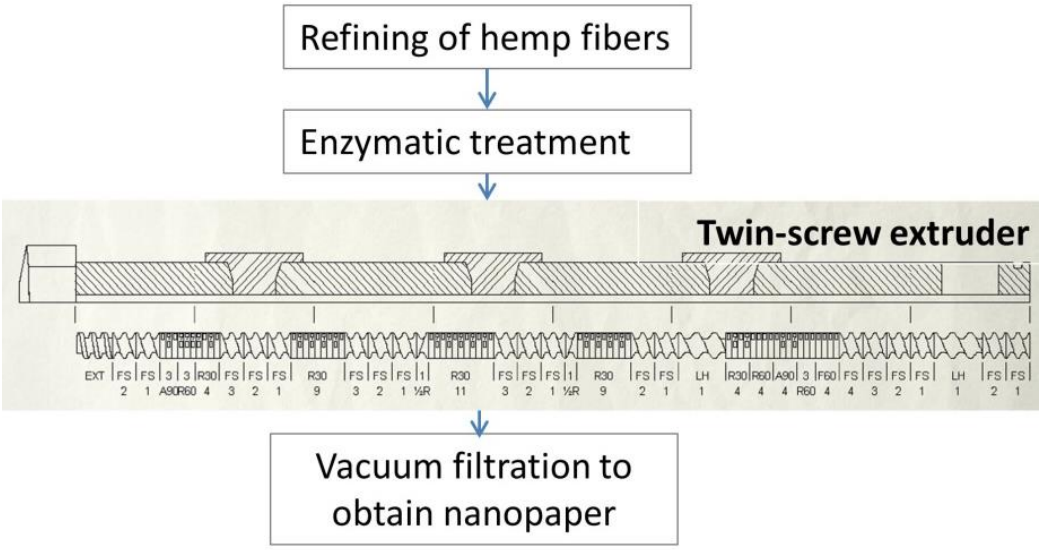

Figure A-0-1: Hemp MFC production process.

Later, paper sheets were prepared using the produced Hemp MFC (Figure A-0-2). The mechanical properties of these papers were characterized with a tensile test and yielded Young's modulus of 6.65 ±0.25 GPa and ultimate strength of 15.6 ±2.94 MPa.

Figure A-0-2: Photo of the produced sheets and the conducted mechanical test.

Printable formulation

The produced Hemp MFC were later mixed with the same afore-described PFA resin at different concentrations ranging from 5 to 35 wt% as detailed in Table 0-1.

Table 0-1: Main composition of the tested paste formulations.

	1	2	3	4	5
MFC (wt%)	5	10	20	25	35
PFA (wt%)	95	90	80	75	65

As suspected, the dispersion of these mico/ nanofibers in the viscous oligomer was not efficient using only Ultra-Turrax high-speed mixer. Therefore, a three-roll milling machine was used to break the fibrous agglomerates formed in the paste and thusly enhance the homogeneity of the paste as one can see in *Figure A-0-3*. Indeed, the homogeneity of the paste was enhanced which yielded a smoother and homogenous paste visible to the naked eye. It is also worth mentioning that the paste viscosity increased when enhancing the paste homogeneity however this was not quantified.

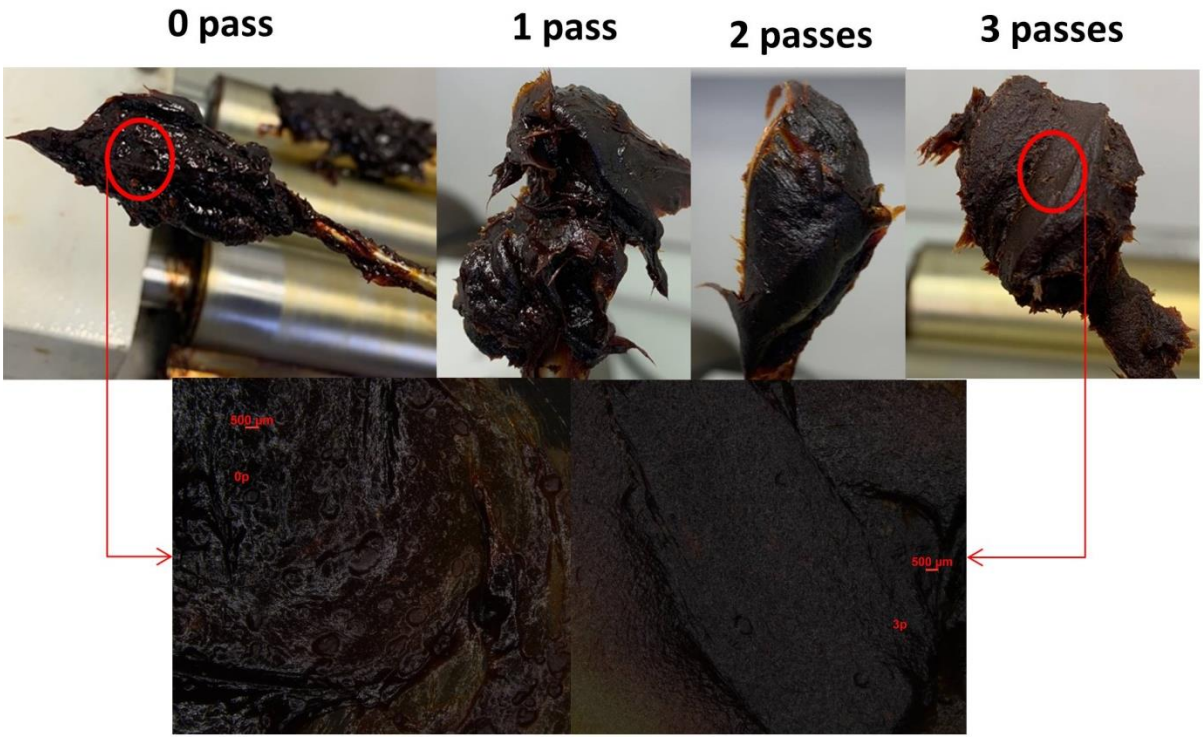

Figure A-0-3: The aspect of the concentrated paste after a 0 to 3 passes through the three-roll milling machine.

The rheological properties of the pastes were characterized with rotational rheometer under shear rate ranging from 0.1 to 1000 1/s. The resulted flow curves are plotted in Figure A-0-4. By applying the power low the shear-thinning exponent 'n' and the consistency K of different formulations could be computed and are presented in Table 0-2. The addition of the produced MfC increased the overall viscosity of the resin and yielded shear-thinning behavior the paste which is more pronounced when adding more than 10% fibers. These rheological performances aligns with additive manufacturing with DIW.

Table 0-2: Computed shear-thinning exponent and constancy of the different formulations.

	0% MFC	5% MFC	10% MFC	20% MFC
K	7,05	21,18	81,61	204,02
n	0,979	0,694	0,473	0,318
R^2	0,361	0,966	0,974	0,988

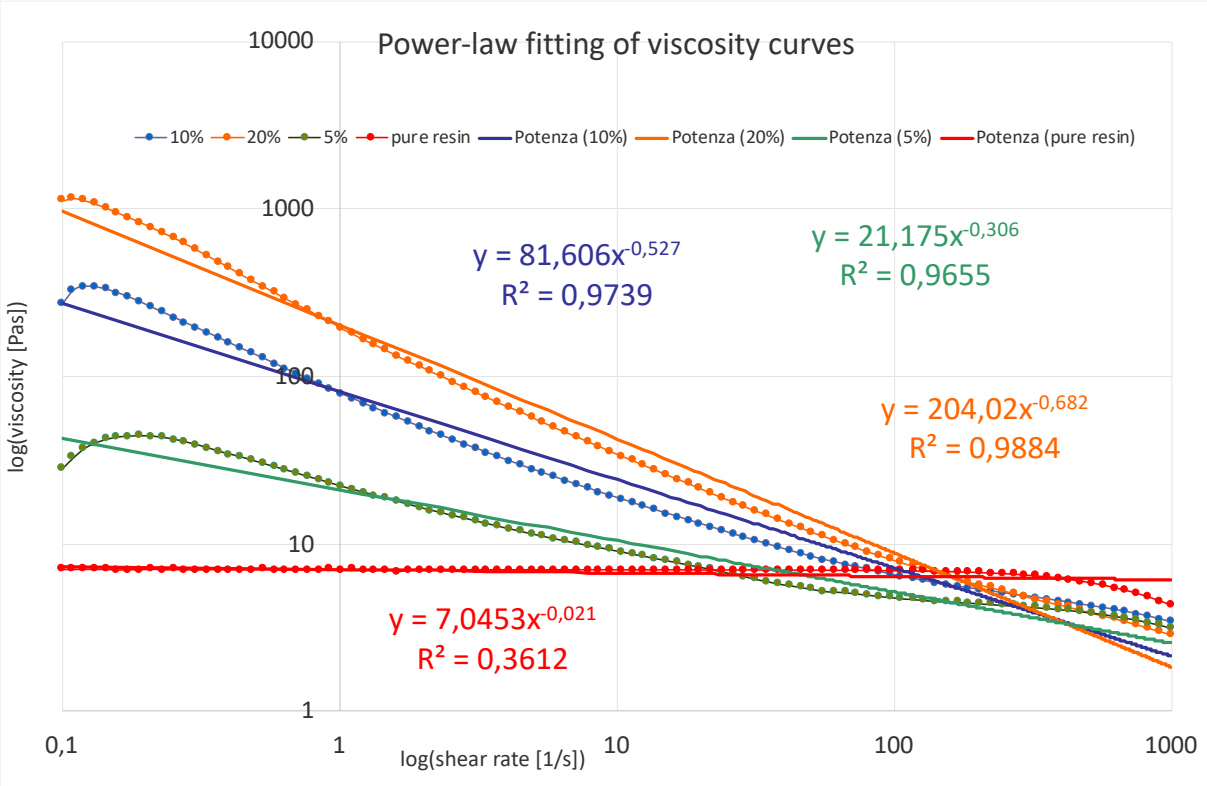

Figure A-0-4: Rheogram curves of different formulations (points) with the respective fitting to the use power law (continuous line).

Accordingly, the extrudability of the formulation (5) was evaluated through a 1mm nozzle which was possible as one can see in Figure A-0-5. The printability of the paste was as well evaluated as shown on the Figure A-0-5 which showed a good potential of the developed formulation. However, occasional clogging of the nozzle occurred because of the remained fiber agglomerates.

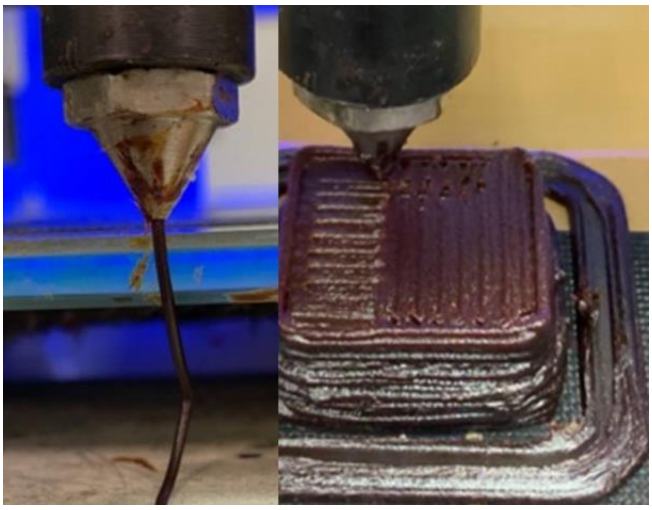

Figure A-0-5: Photos of the extruded paste formulation containing 35 wt% of hemp MFC (on the left) and a printed cube (on the right).

Overall, both the produced hemp MFC and the developed ink have a high potential to produce bio-nano-composite for 3D printing or composite manufacturing in general and need to be more investigated.

Extended French abstract

Résumé en Français

Introduction générale et contexte

La fabrication additive, également appelée impression 3D, est une technologie de fabrication révolutionnaire qui suscite un intérêt considérable ces dernières années. Elle est également évolutive, incitant les fabricants à reconceptualiser l'approche employée pour développer, produire et concevoir de nouveaux objets. Par son adaptabilité et la contrôlabilité de ses paramètres, elle permet une multitude d'applications. De plus, à une époque où les préoccupations environnementales augmentent, ce procédé nécessite peu de consommables et offre une géométrie d'objet personnalisable tout en utilisant une seule machine (Yang et al., 2020).

Plus récemment, le recours croissant à l'impression 3D a été favorisé dans une multitude de projets de recherche réalisés ces dernières décennies. Comme on peut le voir sur la figure R-0-1, le nombre de publications sur la fabrication additive s'est accru depuis 2000, atteignant plus de 45 000 publications en 2020. De plus, la plupart des références fournies par la base de données scientifique Scifinder sont des brevets, ce qui met en évidence la capacité d'innovation de ce nouveau procédé de fabrication. La fabrication additive de composites figure parmi les domaines d'innovation car elle permet, entre autres, le développement de matériaux à hautes performances en dehors des matériaux monophasés conventionnels. Sur le même graphique de la figure R-0-1, l'évolution du nombre de publications sur l'impression 3D de composites suit la même tendance que celle de la fabrication additive avec près de 30% du total de ces publications mentionnant des composites. Toutefois, la fabrication additive de biocomposite n'a pas encore été pleinement explorée, comptant pour moins de 0,5 % des articles publiés.

Par conséquent, certains chercheurs se sont concentrés sur le développement et l'étude de nouveaux biocomposites (Kariz et al., 2016; Kucherov et al., 2017; Li et al., 2017; Montalvo Navarrete et al., 2018). Dans le cadre de cette recherche, des thermoplastiques biosourcés ont été couplés à des charges naturelles et à des fibres naturelles (Nguyen et al., 2018; Tao et al., 2017). De plus, les polymères issus de la biomasse végétale sont l'une des ressources les plus abondantes dans la nature ce qui les rendent des candidats intéressants pour le développement de nouvelles « encres » d'impression par écriture directe à l'encre (DW) (Liu et al., 2019). En particulier, l'utilisation de la cellulose a été étudiée par plusieurs chercheurs pour l'impression de matériaux à haute valeur dans de nombreuses applications biomédicales. Cependant, plusieurs défis ont émergé, comme une fidélité à la forme faible/inexistante et un coût de fabrication élevé (Wang et al., 2018).

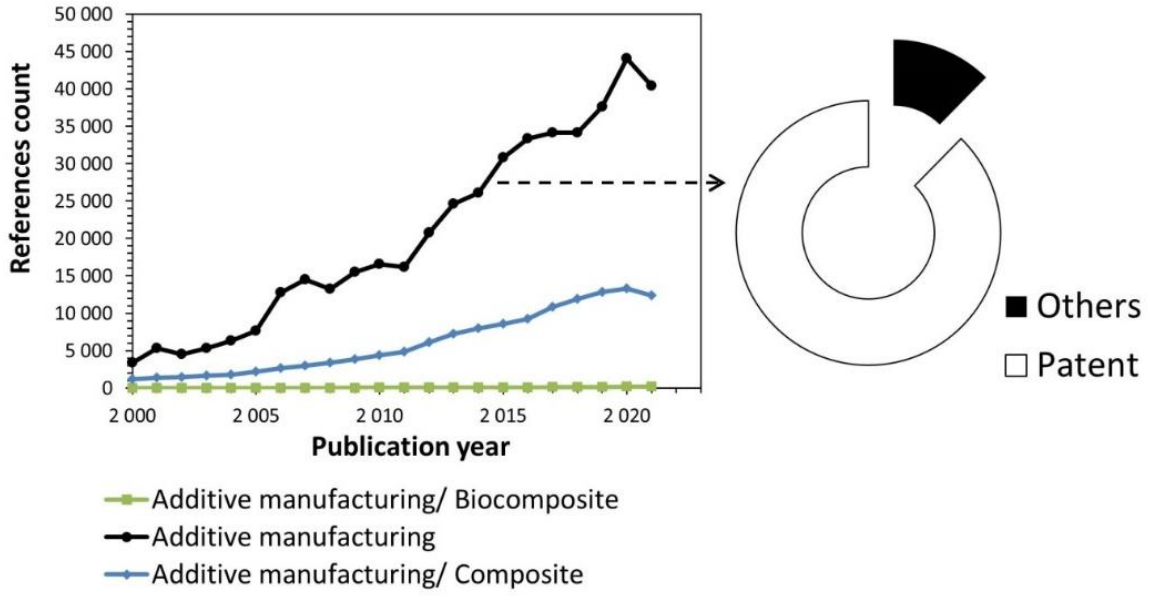

Figure R-0 -1 : L'évolution du nombre de publications concernant la fabrication additive, composite dans la fabrication additive et biocomposite dans la fabrication additive au cours des 2 dernières. Source : Scifinder, 2021.

Par conséquent, l'utilisation comme matrice de polymères thermodurcissable avec une stabilité thermique améliorée et un rendement mécanique élevé a récemment été considérée comme une option viable. (Peerzada et al., 2020). En dépit de la haute performance de ces composites, les matériaux les plus couramment utilisés sont pétro-sourcés et l'utilisation de résine thermodurcissable biosourcée et de charges naturelles demeure assez inexplorée.

Les travaux menés dans ce projet de thèse proposent donc le développement d'un biocomposite ayant pour matrice une résine biosourcée thermodurcissable et pour renfort une poudre de cellulose. Cela permettrait le développement d'un composite entièrement à base de biomasse ayant une stabilité thermique élevée conférée par la matrice et une stabilité dimensionnelle adéquate. La démarche expérimentale et les principaux résultats obtenus au cours de ce projet de thèse sont présentés en 5 chapitres.

Le présent manuscrit de thèse débute par une revue de la littérature exposée dans le **chapitre 1**, qui évalue l'état de l'art actuel de la fabrication additive par extrusion de matière et plus particulièrement la fabrication de matériaux composites et leurs performances. Ce chapitre s'achève par une explication portant sur la production et sur la polymérisation de la résine thermodurcissable utilisée dans ce travail, à savoir l'alcool polyfurfurylique (PFA), et son utilisation dans la production de composites.

Les matériaux et méthodes utilisés le long des travaux de thèse sont détaillés dans **chapitre 2**. Une description détaillée des produits commerciaux est présentée, de même que les techniques de caractérisation utilisées. Par ailleurs, pour mieux comprendre la composition des polymères utilisés, ils ont été analysés et les résultats qui en découlent sont présentés dans le **chapitre 3**. Le **chapitre 4** est consacré au développement, à la caractérisation et à l'optimisation de formulation des composites destinés au procédé d'impression 3D. Le **chapitre 5** porte sur l'étude et l'optimisation du procédé de fabrication et sur la réticulation du biocomposite.

Pour un aperçu clair du contenu du manuscrit de thèse, la disposition générale des chapitres et la structure sont affichées dans la Figure R-0-2.

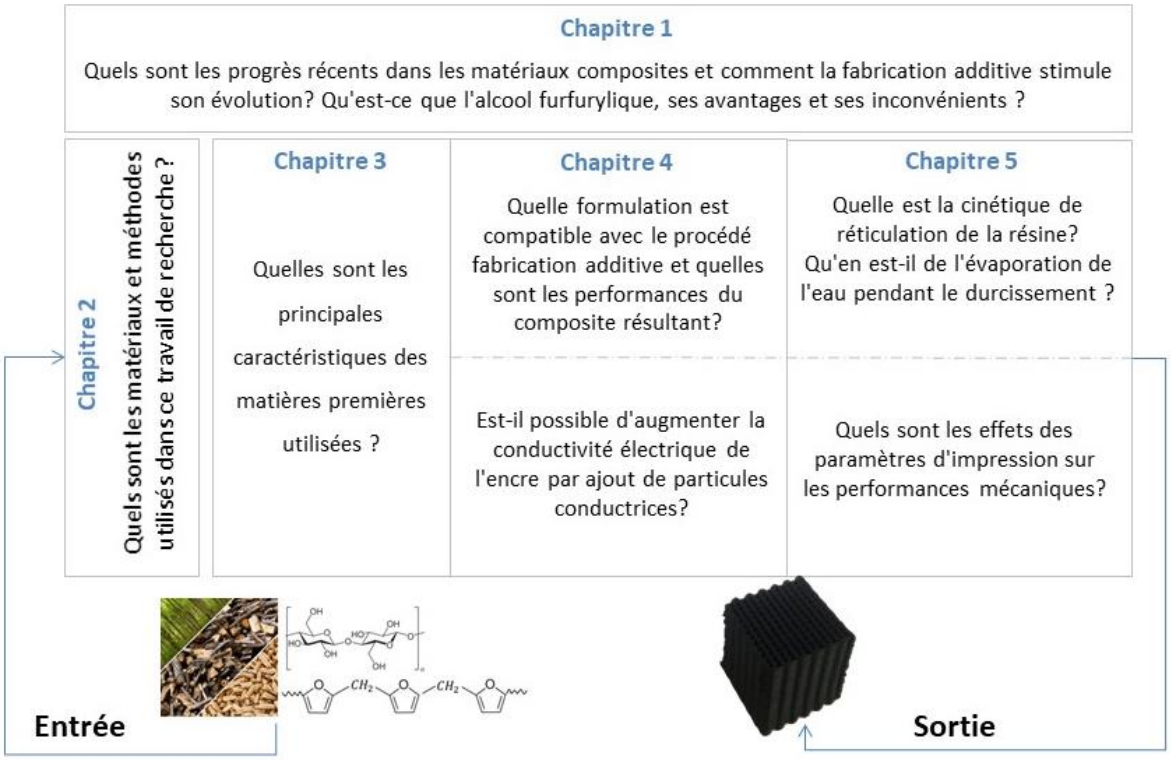

Figure R-0-2 : Représentation schématique du plan du manuscrit de thèse.

Résumé des travaux de thèse

[Chapitre 2 et 3] Matériaux et méthodes

Pour la formulation de ce biocomposite, une résine biosourcée commerciale d'alcool polyfurfurylique (Furolite) avec un catalyseur latent ont été utilisés et ont été gracieusement fournis par Transfurans Chemicals (Belgique). Cette résine commerciale contient 7,5 % d'eau et moins de 1 % de monomères libres. Pour la phase de renfort, une poudre de cellulose commerciale a été utilisée. Cette poudre est

fournie par Rossow. Pour la formulation de l'encre fonctionnelle, des nanotubes de carbone (CNT) commerciaux (Nanoamor) de différentes morphologies ont été ajoutés dans le but d'augmenter la conductivité électrique. Une caractérisation exhaustive de la résine furanique et des particules de cellulose a été faite. Ces analyses ont révélé, d'une part, que l'on peut considérer les charges cellulosiques utilisées comme des microparticules chimiquement inertes en forme de bâtonnets ; d'autre part, que l'on peut considérer l'oligomère Furolite commerciale comme un enchaînement d'une moyenne de 2 à 5 des noyaux aromatiques furaniques reliés majoritairement par des ponts éther et se terminant par des groupements hydroxyles rendant donc la résine plutôt soluble dans l'eau.

Le procédé d'impression 3D par écriture directe de l'encre a été réalisé grâce à l'utilisation d'une imprimante 3D à fil fondu commerciale modifiée. La tête d'extrusion du fil fondu a été remplacée par une extrudeuse à vis permettant l'extrusion et le dépôt de la pâte à froid. Après impression ou moulage des formulations, les objets sont réticulés dans un four à 90°C durant une nuit et puis post-réticulés à haute température (130°C).

[Chapitre 4] Développement et caractérisation de nouveaux matériaux biosourcés pour l'impression 3D par extrusion à froid

Dans la fabrication additive (FA) par extrusion de matière, on remarque la prédominance des thermoplastiques qui sont majoritairement petro-sourcés. Dans le cadre des préoccupations environnementales croissantes, de nombreux travaux de recherche ont été menés pour trouver un substitut à l'utilisation des thermoplastiques. Parmi les matériaux proposés on peut citer la cellulose et, plus généralement, les matériaux lignocellulosiques. Ce matériau biosourcé est particulièrement intéressant pour l'impression 3D car il est disponible, renouvelable, économique et léger. Cependant, ces avantages s'accompagnent d'une limitation majeure : la cellulose ne peut pas être fondue. Les chercheurs ont donc proposé plusieurs formulations utilisant différentes formes de cellulose pour l'impression par extrusion à froid, notamment des aérogels de NFC, MFC et CNC compatibles avec cette technique de FA. Néanmoins, l'utilisation de ces aérogels, et dans certains cas de suspensions et de solutions, a soulevé des défis et des limites supplémentaires à son imprimabilité, comme un retrait important au séchage en raison d'une teneur limitée en matière sèche dans la formulation, ou comme une étape de séchage et solidification compliquée et onéreuse.

D'un point de vue technique, les thermoplastiques ont une stabilité thermique limitée, rendant l'utilisation des pièces imprimées en 3D limitée aux environnements à basse température. En dépit de filaments techniques imprimables thermiquement stables, comme le PEEK et le PEI, ces matériaux demeurent coûteux (jusqu'à 790 $/kg) et plutôt compliqués à imprimer. Pour pallier ces limitations,

plusieurs articles ont été publiés sur des formulations compatibles avec la FA par extrusion de composites en utilisant des résines thermodurcissables avec de meilleures performances thermiques et mécaniques. Néanmoins, la majorité des composites proposés sont encore d'origine fossile. Pour surmonter ces défis, on propose dans ce travail le développement d'un matériau imprimable en 3D par FA par extrusion à froid utilisant des fibres de cellulose comme charge biosourcée et rentable ainsi qu'une résine thermodurcissable biosourcée jouant le rôle de liant avec d'excellentes performances thermiques. Ce mélange donnerait un composite imprimable entièrement biosourcé avec des performances dépassant les matériaux actuellement existants. Cependant, une étape d'optimisation doit être effectuée pour définir les proportions appropriées pour obtenir une « encre » imprimable et des performances optimales du composite polymérisé, ce qui est l'objectif principal de ce chapitre. Deux « encres » différentes sont développées dans ce travail :

- Une encre structurale à base de particules cellulosiques et d'oligomères PFA et éventuellement d'un solvant.
- Une encre électriquement conductrice à base de particules conductrices, de cellulose et d'oligomères PFA.

Les deux types de formulation d'encres imprimables par extrusion ont été développés et les composites polymérisés résultants ont été caractérisés.

En premier lieu, pour développer l'encre structurale, une étude rhéologique de différentes pâtes à base de résine furanique et poudre de cellulose a été menée. Les données rhéologiques ont révélé deux formulations d'encre avec un potentiel pour l'impression 3D. Ces deux formulations contiennent de 25 à 28 wt% de poudre de cellulose, respectivement appelées PFA-cell25-B et PFA-cell28-B. En effet, ces deux formulations présentaient un comportement rhéofluidifiant, une limite d'élasticité satisfaisante et un comportement thixotrope, qui sont des paramètres cruciaux pour une impression 3D réussie par extrusion à froid, ce qui est mis en évidence sur la Figure R-0-3.

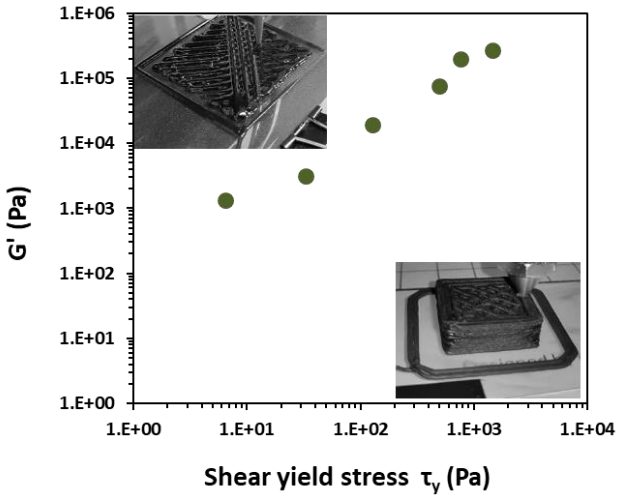

Figure R-0-3: Evolution de la contrainte seuil d'écoulement et du module de stockage en fonction de l'ajout de poudre de cellulose.

Les matériaux composites obtenus après réticulation ont été caractérisés pour mieux comprendre leurs propriétés physiques et mécaniques. Les modules de traction et de flexion des composites ont augmenté avec l'accroissement de la teneur en cellulose, pour atteindre respectivement 2,9 GPa et 4,3 GPa. D'autre part, après l'ajout de particules de cellulose, les contraintes à la rupture ont diminué par rapport au PFA pur en raison de la forte porosité causée par l'inclusion d'air lors des étapes de mélange et de moulage des composites. Les résistances à la traction et à la flexion du composite PFA-cell28-B sont respectivement de 40 et 20 MPa.

Le retrait est un autre paramètre important pour l'impression 3D, notamment lors de l'utilisation de polymères amorphes. Les expériences réalisées dans ce travail ont montré que le PFA pur a un retrait dimensionnel de 2,9% qui a été réduit de près de 40% pour le PFA-cell28-B (contenant 30% cellulose).

En outre, l'ajout des particules cellulosique a amélioré les propriétés thermomécaniques du composite avec un module de stockage supérieur à 5 GPa à température ambiante. A haute température (200°C), le module ne baisse que de 20% et reste stable pendant plusieurs heures comme le montrent les résultats de DMA présentés Figure R-0-4. De plus, la stabilité thermique du composite a été évaluée par des tests TGA, qui ont montré une dégradation thermique limitée, avec une perte en point inférieure à 10% pour des températures inférieures à 300°C.

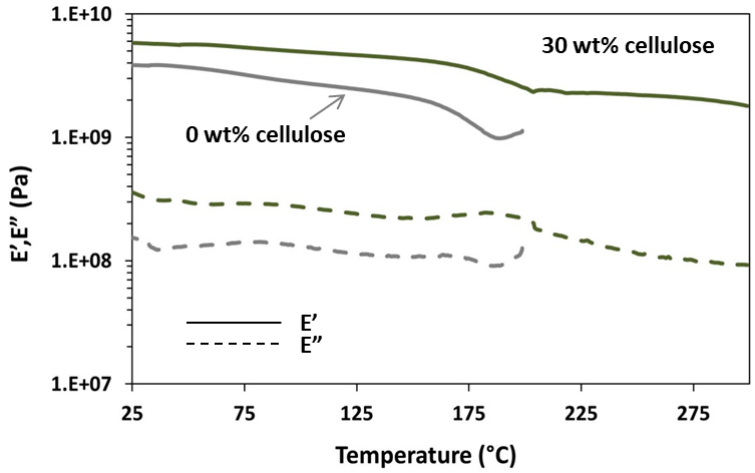

Figure R-0-4: Evolution des modules elastique (E') et plastique (E'') en fonction de la température pour le PFA pur et le composite.

Le développement de l'encre conductrice a commencé par la caractérisation de la rhéologie de suspensions de différents types de nanotubes de carbone (CNT), qui a révélé une meilleure dispersion et donc un meilleur comportement rhéologique des CNTs ayant le plus faible facteur de forme.

La formulation contenant 4 wt% en poids de MWNT-short et 15 wt% de poudre de cellulose a montré les meilleures performances rhéologiques, une meilleure imprimabilité et une conductivité électrique d'au moins 2 10^{-2} S/m.

De plus, la carbonisation des deux composites différents (conducteur et structurel) a encore augmenté la conductivité électrique, grâce à la formation d'une structure vitreuse-carbone. De plus, la carbonisation du composite contenant les CNT a résulté en un composite carbone/carbone ayant une conductivité électrique a minima égale à 4,7 10^{3} S/m, ce qui est mis en évidence sur la Figure R-0-5.

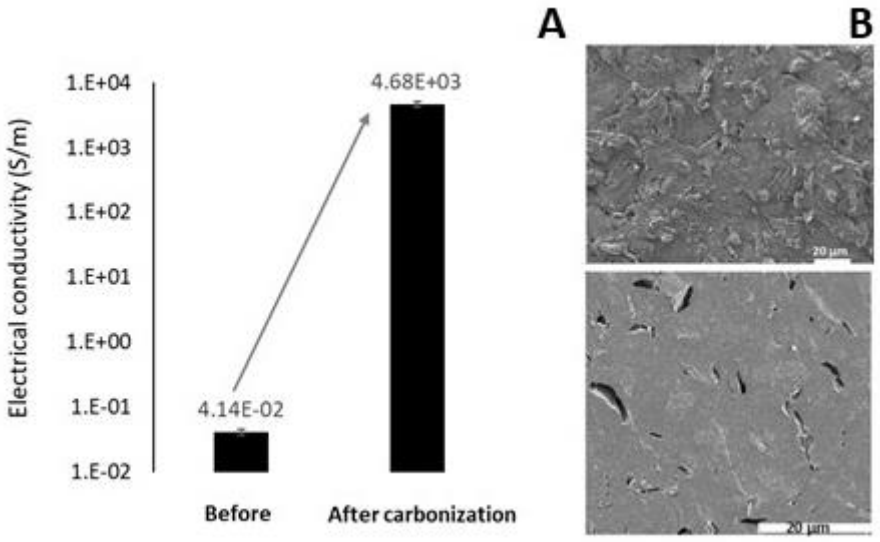

Figure R-0-5: (A) Conductivité électrique des composites avant et après carbonisation (B) des images MEB de section d'un filament contenant des CNT avant (haut) et après (bas) étape de carbonisation.

Une encre optimisée pour la fabrication additive LDM n'est pas suffisante pour obtenir un objet imprimé solidifié sans défaut. L'optimisation et l'analyse à la fois du processus d'impression 3D et de l'étape de réticulation demeure cruciale.

Les résultats les plus significatifs du chapitre 5 sont résumés dans le Figure R-0-6.

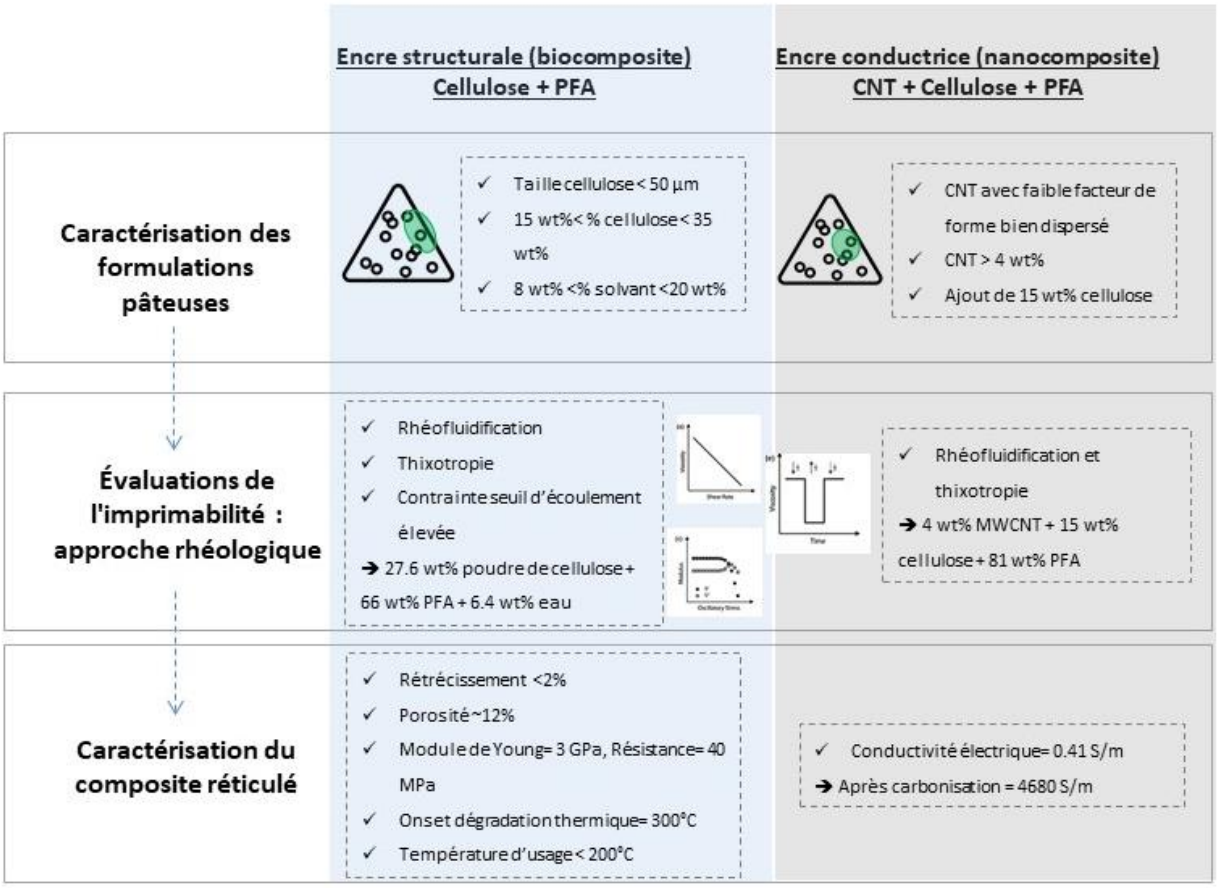

Figure R-0-6: Résumé des résultats du chapitre 4.

[Chapitre 5] Optimisation et étude de procédé

L'objectif de ce chapitre est d'étudier les étapes d'impression et de solidification de la pâte PFA/cellulose dans le but d'optimiser le procédé et les performances du composite. Par conséquent, le chapitre est divisé en deux parties distinctes complémentaires. La première partie est dédié à la compréhension de la cinétique de réticulation de la résine de PFA utilisée, ainsi qu'à l'étape d'évaporation de l'eau. Ces connaissances permettraient de mieux programmer l'étape de solidification pendant ou après le procédé d'impression, afin d'obtenir un composite entièrement réticulé et sans défaut. Dans la deuxième partie, on étudie l'étape d'impression 3D. Afin de maîtriser cette étape, plusieurs paramètres clés doivent être maîtrisés. L'effet des principaux paramètres d'impression a donc été évalué pour mieux quantifier l'imprimabilité et les limites du matériau utilisé. Enfin, une imprimante personnalisée a été développée.

À l'issue de ce dernier chapitre, la meilleure compréhension du processus d'impression et de séchage de la formulation d'encre qui a été développée a permis une meilleure optimisation du procédé d'impression et de solidification.

Tout d'abord, 5 wt% de catalyseur ont été fixés pour une réaction de réticulation adéquate de la résine. On a de plus constaté que la cellulose avait peu d'effet sur la réaction de réticulation. En

outre, l'évolution de la réticulation a été étudiée avec l'ajout d'un taux fixe de catalyseur (5%) à différentes températures. Il a été constaté que la vitesse de réticulation était proportionnelle à la température de traitement. D'autre part, il a été montré que la réticulation à des températures élevées provoque le moussage et la formation de bulles dans le matériau. Par conséquent, une réticulation à des températures plus basses est privilégiée. Le programme suivant de solidification (Figure R-0-7) a été recommandé en conséquence :

1. Phase de pré-réticulation : évaporer l'eau à une température inférieure à 90°C jusqu'à atteindre le point de gélification ;
2. Étape de réticulation : atteindre un degré de réticulation élevé sous 90°-100°C permettant la manipulation de l'objet imprimé ;
3. Étape de post-réticulation : maximiser la réticulation du polymère sous 150°C-200°C.

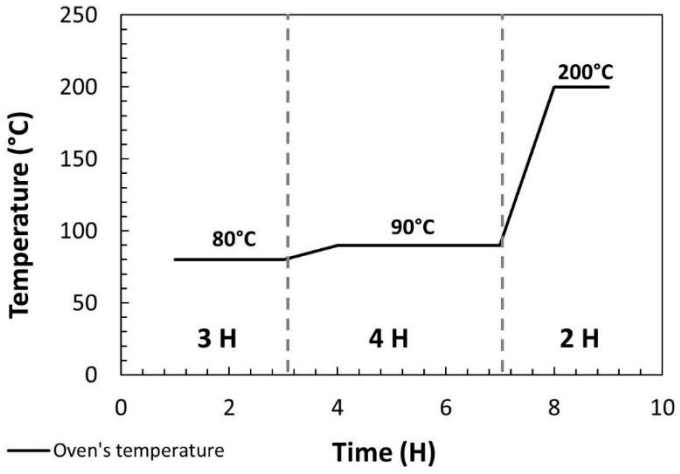

Figure R-0-7 : Programme de réticulation proposé.

L'étape d'extrusion a été optimisée en calibrant la tête d'impression pour la faire correspondre au débit d'extrusion calculé par le logiciel. Cet étalonnage a été effectué en fixant : un multiplicateur d'extrusion spécifique à chaque formulation, une forme de buse, une taille de buse, et une vitesse d'alimentation. Le flux d'extrusion optimisé garantissait un dépôt continu et précis, et une bonne qualité d'impression.

De plus, l'effet de la hauteur de la couche, de la largeur de la trame, de l'angle de trame et du flux d'extrusion sur les performances mécaniques a été abordé. Il a été constaté que ces paramètres n'ont pas d'effet significatif sur les propriétés mécaniques des éprouvettes testées. Cependant, il est recommandé de limiter l'épaisseur de couche, de ne pas dépasser la taille de la buse pour la largeur de la trame, et d'augmenter au maximum de 10% le débit d'extrusion pour garantir une bonne qualité d'impression et des performances mécaniques optimisées. L'adhérence inter-couches et inter-filamentaires s'est avérée optimale, ce qui a éliminé les problèmes de délaminage. En effet, les

tests de flexion avec des éprouvettes ayant les trames perpendiculaire (0°) ou parallèle (90°) au sens de la sollicitation ont montré des propriétés en flexion similaires, comme montré sur la Figure R-0-8. Plus généralement, indépendamment des paramètres d'impression, les éprouvettes imprimées présentaient un module de flexion allant de 3 à 3,5 GPa et une résistance à la rupture entre 40 et 50 MPa.

Les résultats les plus significatifs du chapitre 6 sont résumés dans le Figure R-0-9.

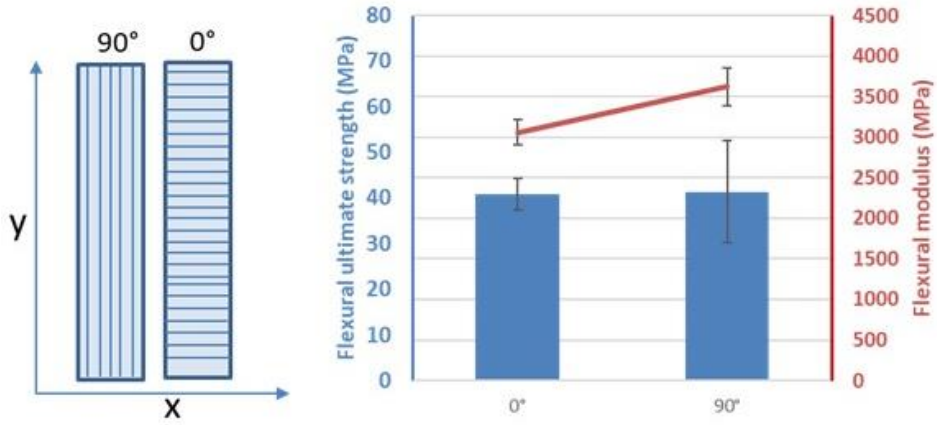

Figure R-0-8: Propriété mécanique en flexion des éprouvettes imprimées ayant différentes orientations de trame.

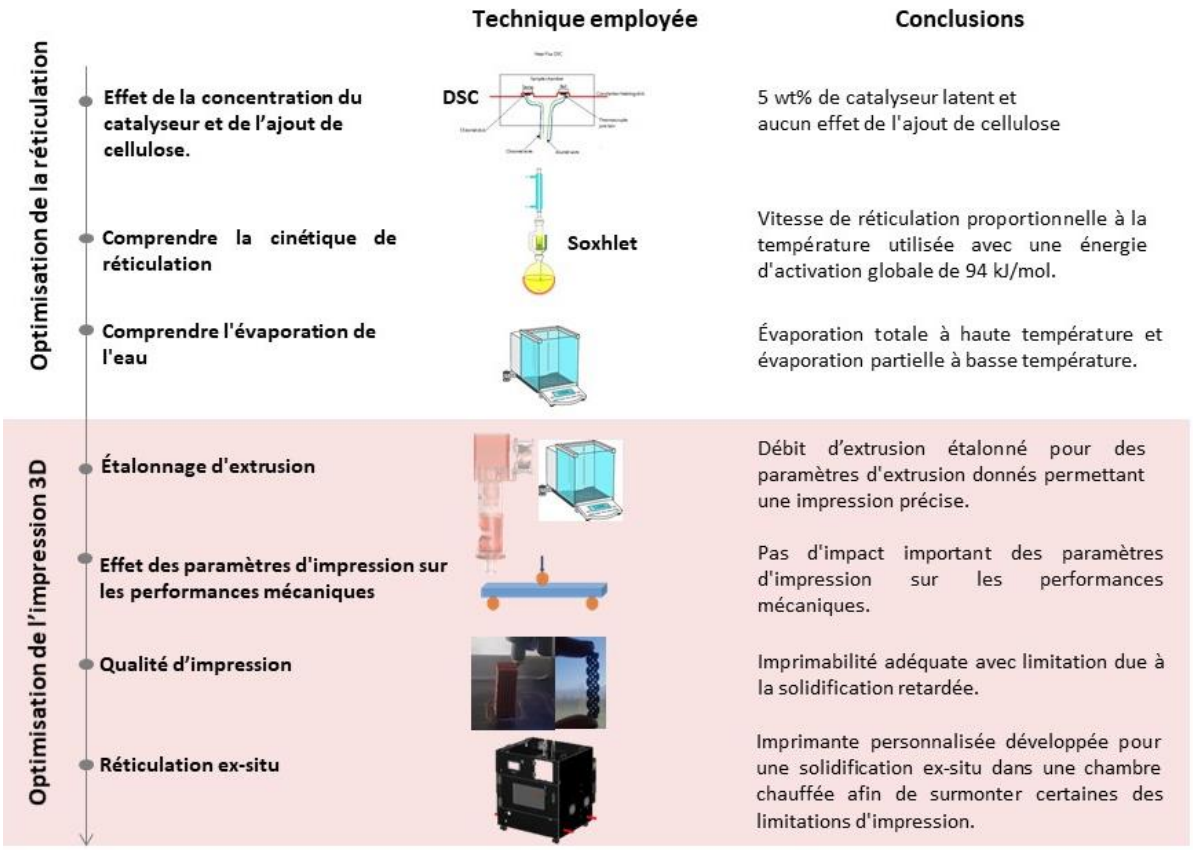

Figure R-0-9 : Résumé des résultats du chapitre 5.

Conclusions générales

L'écriture directe à l'encre (DIW) de composites à base de résines thermodurcissables est une approche d'impression 3D relativement récente permettant de produire de nouveaux matériaux à hautes performances. Néanmoins, cette approche était et demeure à ce jour sous-explorée. Dans le présent travail de thèse, un nouveau matériau pour la fabrication additive à base d'une résine thermodurcissables et d'une poudre de cellulose durables biosourcés a été développé. Par ailleurs, cette thèse portait sur la compréhension de l'effet de la formulation de l'encre sur sa rhéologie et son imprimabilité. En outre, l'effet de différents paramètres du procédé sur la qualité d'impression et les performances du matériau ont été étudiés.

En premier lieu, la préparation et caractérisation de la formulation des encres imprimables pour la fabrication additive a été réalisée. Une encre structurale optimisée contenant plus de 25 wt% de poudre de cellulose et d'une résine biosourcée présente un comportement rhéologique compatible avec le procédé DIW. Postérieurement, le composite réticulé a été caractérisé ce qui a révélé une que l'ajout de cellulose a permis d'améliorer la stabilité thermomécanique du composite avec un

module stable élastique stable jusqu'à 200°C. Une deuxième formulation avec 4 wt% de nanotubes de carbone (CNT) courts à parois multiples et de la poudre de cellulose a été développée pour une éventuelle impression d'un matériau conducteur avec une conductivité électrique d'au moins 2 10^{-2} S /m. Pour améliorer davantage la conductivité électrique, la carbonisation des deux matériaux développés a été testée, ce qui a donné une conductivité électrique d'au moins 4,7 10^{3} S/m.

D'autre part, une étude et optimisation du procédé d'impression 3D et de réticulation ont été effectué. En conséquent, une solidification étape par étape a été suggéré commençant par une réticulation partielle à faible température pour éviter le moussage de la résine. Par ailleurs, l'effet des paramètres d'impression sur la qualité et les performances mécaniques du matériau a été analysé. Il a été constaté que ces paramètres n'ont pas d'effet significatif sur les propriétés du matériau imprimé ce qui montre une bonne adhésion inter-filamentaire et inter-couche. Toutefois, plusieurs challenges ont été identifiés pour l'impression du matériau développé. Pour surmonter ces défis, une imprimante 3D personnalisée a été développée pour une solidification *in situ*.

Références

Kariz, M., Sernek, M., Kuzman, M.K., 2016. Use of wood powder and adhesive as a mixture for 3D printing. European Journal of Wood and Wood Products 74, 123–126. https://doi.org/10.1007/s00107-015-0987-9

Kucherov, F.A., Gordeev, E.G., Kashin, A.S., Ananikov, V.P., 2017. Three-Dimensional Printing with Biomass-Derived PEF for Carbon-Neutral Manufacturing. Angewandte Chemie International Edition 56, 15931–15935. https://doi.org/10.1002/anie.201708528

Li, Y., Zhu, H., Wang, Y., Ray, U., Zhu, S., Dai, J., Chen, C., Fu, K., Jang, S.-H., Henderson, D., Li, T., Hu, L., 2017. Cellulose-Nanofiber-Enabled 3D Printing of a Carbon-Nanotube Microfiber Network. Small Methods 1, 1700222. https://doi.org/10.1002/smtd.201700222

Liu, J., Sun, L., Xu, W., Wang, Q., Yu, S., Sun, J., 2019. Current advances and future perspectives of 3D printing natural-derived biopolymers. Carbohydrate Polymers 207, 297–316. https://doi.org/10.1016/j.carbpol.2018.11.077

Montalvo Navarrete, J.I., Hidalgo-Salazar, M.A., Escobar Nunez, E., Rojas Arciniegas, A.J., 2018. Thermal and mechanical behavior of biocomposites using additive manufacturing. Int J Interact Des Manuf 12, 449–458. https://doi.org/10.1007/s12008-017-0411-2

Nguyen, N.A., Barnes, S.H., Bowland, C.C., Meek, K.M., Littrell, K.C., Keum, J.K., Naskar, A.K., 2018. A path for lignin valorization via additive manufacturing of high-performance sustainable composites with enhanced 3D printability. Science Advances 4, eaat4967. https://doi.org/10.1126/sciadv.aat4967

Peerzada, M., Abbasi, S., Lau, K.T., Hameed, N., 2020. Additive Manufacturing of Epoxy Resins: Materials, Methods, and Latest Trends. Industrial & Engineering Chemistry Research 59, 6375–6390. https://doi.org/10.1021/acs.iecr.9b06870

Tao, Y., Wang, H., Li, Z., Li, P., Shi, S.Q., 2017. Development and Application of Wood Flour-Filled Polylactic Acid Composite Filament for 3D Printing. Materials 10, 339. https://doi.org/10.3390/ma10040339

Wang, Q., Sun, J., Yao, Q., Ji, C., Liu, J., Zhu, Q., 2018. 3D printing with cellulose materials. Cellulose 25, 4275–4301. https://doi.org/10.1007/s10570-018-1888-y

Yang, J., An, X., Liu, L., Tang, S., Cao, H., Xu, Q., Liu, H., 2020. Cellulose, hemicellulose, lignin, and their derivatives as multi-components of bio-based feedstocks for 3D printing. Carbohydrate Polymers 250, 116881. https://doi.org/10.1016/j.carbpol.2020.116881

Résumé

Au cours des deux dernières décennies, la fabrication additive est devenue une technologie révolutionnaire. Historiquement, la stéréolithographie est la première technique utilisée en fabrication additive donnant plus tard naissance à de nombreuses nouvelles techniques basées sur différentes approches. L'écriture directe à l'encre est l'une de ces techniques. Elle est utilisée pour imprimer différents matériaux comme la céramique, les pâtes de ciment et, plus récemment, les résines thermodurcissables petro-sourcées. Dans un contexte où le développement durable devient un sujet clé, une nouvelle encre imprimable biosourcée a été développée en utilisant cette nouvelle approche de FA dans cette thèse. L'encre développée est constituée d'un mélange d'une résine furanique biosourcée avec des charges cellulosiques et éventuellement de nanotubes de carbone. La résine thermodurcissable assure la stabilité dimensionnelle, les particules de cellulose permettent la modification des propriétés rhéologiques, et les nanotubes de carbone une augmentation de la conductivité électrique. Au préalable, les propriétés rhéologiques ont été optimisées pour aboutir une encre imprimable, compatible avec la technique d'écriture directe à l'encre, caractérisée par un comportement rheofluidifiant et un seuil d'écoulement élevé supérieure à 10^5 Pa. A posteriori, les composites réticulés résultants ont été largement caractérisés, mettant en évidence une stabilité thermomécanique élevée permettant d'atteindre une température de mise en œuvre du matériau pouvant atteindre les 200°C. Le procédé DIW et l'étape de réticulation ont été étudiés et optimisés pour une meilleure qualité d'impression avec une excellente cohésion intercouche. Enfin, une stratégie de réticulation in-situ en cours d'impression a été proposée pour surmonter certains des défis rencontrés en cours de l'impression de la pâte. Cette stratégie a été implémentée sur une imprimante 3D conçue dans le cadre de ce travail de thèse et équipée d'une chambre d'impression thermoregulable entre 30 et 250°C.

Mots-clés: Fabrication Additive, Biocomposite, Furan, Cellulose, DIW

Abstract

In the last two decades, additive manufacturing has emerged as a revolutionary and influential technology. Historically, stereolithography is the first technique used in additive manufacturing giving later birth to many new techniques based on different approaches. Direct ink writing, is one such technique, used to print different materials like ceramics, concrete, and more recently fossil-based thermosetting resins. In the context of the increasing interest in sustainable development, in this thesis, a new bio-based printable ink was developed using the aforementioned AM approach. The developed ink consists of a blend of bio-based furanic resin and cellulosic fillers and eventually carbon nanotubes. The thermosetting resin provides dimensional stability, the cellulose particles enable the tuning of the rheological properties and the carbon nanotubes permit an increase in the electrical conductivity. First, the rheological requirements for a printable ink compatible with the direct ink writing technique, were studied and displayed a shear-thinning behavior and a yield stress superior to 10^5 Pa. Later the ensuing crosslinked composites were extensively characterized highlighting high thermomechanical stability permitting to reach a material processing temperature of up to 200°C. The DIW process and the curing step were thoroughly studied and optimized in order to obtain a better printing quality and excellent interlayer cohesion. Lastly, an in-situ curing strategy was suggested to overcome some of the challenges encountered in the paste DIW. This strategy was implemented on a 3D printer designed as part of this thesis work and equipped with a thermoregulated printing chamber between 30 and 250°C.

Key-words: *Additive Manufacturing, Biocomposite, Furan, Cellulose, DIW*